UNIVERSIDADE FEDERAL DE PERNAMBUCO
PROGRAMA DE PÓS-GRADUAÇÃO EM CIÊNCIAS BIOLÓGICAS
CENTRO DE BIOCIÊNCIAS

PAULO EUZÉBIO CABRAL FILHO

DESENVOLVIMENTO DE SONDAS MULTIMODAIS BASEADAS EM PONTOS QUÂNTICOS PARA APLICAÇÕES BIOMÉDICAS

Recife
2016

PAULO EUZÉBIO CABRAL FILHO

DESENVOLVIMENTO DE SONDAS MULTIMODAIS BASEADAS EM PONTOS QUÂNTICOS PARA APLICAÇÕES BIOMÉDICAS

Tese de Doutorado apresentada à Coordenação do Programa de Pós-graduação em Ciências Biológicas da Universidade Federal de Pernambuco, como parte dos requisitos à obtenção do grau de Doutor em Ciências Biológicas, área de concentração: Biotecnologia.

Orientação: Profª. Drª. Adriana Fontes

Coorientação: Profª. Drª. Giovannia A. L. Pereira

Recife
2016

Catalogação na fonte
Elaine Barroso
CRB 1728

Cabral Filho, Paulo Euzébio
Desenvolvimento de sondas multimodais baseadas em pontos quânticos para aplicações biomédicas / Paulo Euzébio Cabral Filho– Recife: O Autor, 2016.

173 folhas: il., fig., tab.
Orientadora: Adriana Fontes
Coorientadora: Giovannia A.L. Pereira
Tese (doutorado) – Universidade Federal de Pernambuco. Centro de Biociências. Biotecnologia, 2016.
Inclui referências e anexos

1. Nanotecnologia 2. Câncer 3. Marcadores biológicos I. Fontes, Adriana (orientadora) II. Pereira, Giovannia A.L. (coorientadora) III. Título

620.5 CDD (22.ed.) UFPE/CCB-2016-330

PAULO EUZÉBIO CABRAL FILHO

DESENVOLVIMENTO DE SONDAS MULTIMODAIS BASEADAS EM PONTOS QUÂNTICOS PARA APLICAÇÕES BIOMÉDICAS

Tese de Doutorado apresentada à Coordenação do Programa de Pós-graduação em Ciências Biológicas da Universidade Federal de Pernambuco (UFPE), como parte dos requisitos à obtenção do grau de Doutor em Ciências Biológicas, área de concentração: Biotecnologia.

Aprovado em: 15 de julho de 2016.

BANCA EXAMINADORA

_____

Profª Drª Adriana Fontes (Presidente)
Departamento de Biofísica e Radiobiologia – CB – UFPE

_____

Drª Claudilene Ribeiro Chaves
Departamento de Física da Universidade Federal de Minas Gerais - UFMG

_____

Prof. Dr. Fernando Hallwass
Departamento de Química Fundamental – CCEN – UFPE

_____

Profª Drª Maria Tereza dos Santos Correia
Departamento de Bioquímica – CB – UFPE

_____

Prof. Drª Maria Danielly Lima de Oliveira
Departamento de Bioquímica – CB – UFPE

À Joselita, Joseíza, Alzira e Adriana Fontes.

Palavras são insuficientes, poucas e pequenas
para expressar tão grande amor, alegria, compreensão e gratidão.

AGRADECIMENTOS

A todos que me ajudaram nesta caminhada que termina, pois não posso deixar de agradecer aqueles que foram os responsáveis pela realização de um sonho, que agora se tornou uma realidade, ser Doutor. Vocês são muito especiais e serão sempre lembrados;

À minha orientadora, Profª Drª Adriana Fontes por ter aceitado me conduzir no desenvolvimento deste trabalho, pela amizade, carinho, dedicação e o entendimento nas horas de dificuldades encontradas no desenvolvimento deste trabalho;

Às minhas co-orientadoras, Profª Drª Giovannia A. Pereira e a Profª Drª Beate Saegesser, pela valiosa contribuição e também aos professores do Laboratório de Biofísica Química: Profª Drª Cláudia, Profª Drª Lêda e ao Prof. Dr. Ricardo;

A todos do Laboratório de Biofísica Química, em especial a minha "filha-irmã-científica" Maria Isabela, por me dar o prazer de ensinar, à minha "prima-cientifica" e a amiga Camila Galvão pela motivação e confiança, as filhas científicas deste período de doutorado Camila Pereira e Ana Paula e aos demais membros que não irei citar nomes, para não correr risco de esquecimento, pois todos tiveram sua parcela de contribuição neste trabalho, seja ajudando com a "mão na massa", ou escutando meu falatório e risadas dentro do laboratório;

À Universidade Federal de Pernambuco e a Universidade de Coimbra pelo espaço cedido para desenvolver este trabalho, bem como as agências de fomento em especial a CAPES pela bolsa cedida e ao Instituto Nacional de Ciência e Tecnologia em Fotônica - INFo pelo apoio nas viagens e pela aquisição de alguns equipamentos necessários ao desenvolvimento desse trabalho;

A todos os professores da pós-graduação;

A todos os amigos que fiz em Coimbra, em especial, aos Professores que me receberam de braços abertos em seus laboratórios; Profª. Drª Conceição Pedroso de Lima, Profª Drª Margarida Castro, Prof. Dr. Carlos Geraldes, Drª Ana Luísa Cardoso e a todos os

colegas de laboratório de terapia gênica, em especial Pedro Cunha e Raquel Costa, não posso deixar de lembrar e ser eternamente grato aos que convivi durante quatro meses dividindo casa; Luisa Abrahão, Luisa Dall'Agnese, Carolina Bassani, Gabriel do Vale, Luan Martins, por fazerem dos dias cansativos uma festa e pelos exemplos magníficos de vida;

Aos meus tios, em especial; à Joseíza Saraiva, Joseilton Saraiva, Antônio Saraiva e José Joseli pela ajuda essencial na minha formação;

Aos meus primos, em especial a minha irmã Talina, e também aos que moram mais próximo, pelo apoio e por dividir o fardo de atividades, correria e dias estressados durante esses três anos de doutorado, ao meu irmão de sangue Walberto pelo apoio incondicional;

À minha mãe, Joselita e à minha avó Alzira, os alicerces fundamentais da minha vida, das quais me orgulho, pois me apoiaram a conseguir esse pilar na minha formação de vida;

À minha namorada, Nathália Emanuelle, que dividiu durante esses três anos o cansaço e superou a distância, na certeza de que juntos somos mais fortes e em Deus superamos todas as dificuldades, o meu muito e eterno obrigado;

A todos os meus familiares que diretamente e indiretamente me ajudaram a conquistar mais essa vitória na minha vida;

Aos meus amigos, em especial aos amigos-irmãos Ewerton, Priscila e Rosângela pelo apoio e carinho, e aos demais amigos que me ajudam nas horas de dificuldades e a dividir momentos de alegrias;

E, sobretudo, a Deus pelo dom da vida e por ter me dado forças para conseguir subir mais um degrau na minha formação, além de colocar-me ao lado de pessoas especiais como essas;

os meus sinceros agradecimentos.

RESUMO

Os pontos quânticos ou *quantum dots* (QDs) são nanocristais fluorescentes de semicondutores com propriedades ópticas únicas, tendo como principais vantagens: (1) alta resistência à fotodegradação, possibilitando o acompanhamento de eventos biológicos em tempo real e, (2) superfície ativa, permitindo a conjugação a biomoléculas que vão propiciar especificidade às marcações, além de possibilitar também sua ligação a outras nanopartículas. Com isso, é possível quantificar uma variedade de biomoléculas em células e tecidos e desenvolver nanossondas bimodais (magnético-fluorescentes) baseadas em QDs. O desenvolvimento de nanopartículas bimodais pode aliar as vantagens das técnicas baseadas em fluorescência com as de imagem por ressonância magnética (IRM). Entretanto, a obtenção de sondas bimodais é ainda um desafio, pois durante a conjugação devem ser mantidas as propriedades fluorescentes e magnéticas das nanopartículas, e com isso ainda há poucos trabalhos que façam aplicações em sistemas biológicos. O objetivo desta tese se caracteriza pelo desenvolvimento de sondas com propriedades multimodais baseadas em QDs de Telureto de Cádmio (CdTe) associadas a nanopartículas magnéticas de óxido de ferro como marcadores sítio-específicos em células cancerígenas. Inicialmente os QDs foram conjugados covalentemente à transferrina (Tf) [QDs-Tf] para a quantificação específica de seus receptores (TfRs) em células HeLa e em duas linhagens de glioblastoma (U87 e DBTRG). Através de ensaios de saturação do TfR, foi possível inferir sobre a taxa de renovação deste receptor nessas células. Os resultados mostraram que as células HeLa e as DBTRG possuem uma maior quantidade do TfR quando comparadas às U87. As DBTRG apresentaram maior taxa de renovação do TfR, quando comparadas aos outros dois tipos, demonstrando que os conjugados QDs-Tf são potenciais ferramentas para o estudo da biologia celular do câncer. Posteriormente, nanossondas bimodais (QDs-MNPs), baseadas em QDs associados a nanopartículas magnéticas de óxido de ferro, foram obtidas por conjugação covalente. De acordo com as caracterizações, QDs-MNPs mantiveram suas propriedades ópticas e magnéticas e apresentaram-se como potenciais sondas inespecíficas para fluorescência e para aquisição de imagens por RM ponderadas em T_2 (tempo de relaxação nuclear transversal). A conjugação prévia dos QDs a Tf, além de fornecer informações sobre a biologia do câncer, auxiliou também na padronização da marcação específica do TfR em células cancerígenas e no estabelecimento de protocolos de conjugação das sondas bimodais a Tf. Por fim, as QDs-MNPs foram conjugadas covalentemente a Tf e essa nova sonda multimodal [(QDs-MNPs)-Tf] reconheceu especificamente os TfR em células HeLa. As caracterizações indicaram que o sistema multimodal não apresentou alteração significativa nas propriedades ópticas e exibiu uma maior relaxividade transversal (r_2), se mostrando igualmente potencial sonda para análise por fluorescência e IRM ponderada em T_2. Neste trabalho foram obtidas nanossondas promissoras para serem aplicadas na compreensão da biologia celular do câncer, além de auxiliar em métodos diagnósticos e terapêuticos para essa doença.

Palavras-chaves: *quantum dots,* transferrina, sistemas bimodais, receptor.

ABSTRACT

Quantum dots (QDs) are fluorescent semiconductor nanocrystals with unique optical properties, which have as major advantages: (1) the high resistance to photobleaching, making possible to monitor biological events in real-time and, (2) active surface, allowing the conjugation not only with biomolecules for specific labeling, but also to other nanoparticles. Thus, it would be possible to quantify a variety of biomolecules in cells and tissues, as well as to develop bimodal nanoprobes (fluorescent-magnetic) [BNPs] based on QDs. The development of BNPs can help to combine the advantages of the fluorescence with the resonance magnetic imaging techniques. However, the preparation of bimodal probes can still be considered a challenge, since the fluorescent and magnetic nanoparticles' properties need to be preserved after conjugation. Therefore, there are still few works applying BNPs in biological studies. The aim of this thesis was to develop nanoprobes, with multimodal properties, based on cadmium telluride (CdTe) QDs conjugated with iron oxide magnetic nanoparticles (MNPs), for site-specific labeling in cancer cells. For this, initially, QDs were covalently coupling to transferrin (Tf) [QDs-Tf] and used to quantify the transferrin receptor (TfRs) in HeLa cells as well as in two glioblastoma lines (U87 and DBTRG). Furthermore, by a TfR saturation assay, it was possible to study the recycling rate of this receptor in cells studied. The results showed that HeLa and DBTRG cells present a higher amount of TfRs when compared to U87. DBTGR showed a higher TfR recycling rate, when compared to the other two lineages, demonstrating that QDs-Tf conjugates are potential tools to study the cancer cell biology. BNPs, based on the conjugation of QDs with MNPs (QDs-MNPs), were obtained by covalent coupling. According to characterizations, the BNPs remained with their optical and magnetic properties preserved and showed to be potential unspecific probes for fluorescence analysis and for T_2-weighted magnetic resonance imaging (MRI) acquisition. The conjugation of QDs to Tf, performed previously, was a valuable step not only to provide us information about the biology of cancer cells, but also for the standardization of TfR specific labeling and the establishment of protocol to conjugate the BNPs with Tf. Therefore, QDs-MNPs were also covalently coupling to Tf and this new multimodal nanotool [(QDs-MNPs)-Tf] was also able to recognize specifically TfRs in HeLa cells. The multimodal nanosystems presented their fluorescent properties practically unchanged and also exhibited a higher transversal relaxivity (r_2), when compared to bare BNPs, showing likewise potential to be used for fluorescence and T_2-weighted MRI analyses. In this work, it was developed promising nanoprobes, able to be applied for the cancer cell biology comprehension, and with potential for helping in the improvement of diagnostic and therapeutic methods for this disease.

Keywords: quantum dots, transferrin, multimodal systems, receptor.

LISTA DE ILUSTRAÇÕES DO REFERENCIAL TEÓRICO

LISTA DE ILUSTRAÇÕES DO ARTIGO PUBLICADO

LISTA DE ILUSTRAÇÕES DO ARTIGO A SER SUBMETIDO À REVISTA *"JOURNAL OF MATERIALS CHEMISTRY B"*

LISTA DE ILUSTRAÇÕES DO ARTIGO EM PREPARAÇÃO PARA SER SUBMETIDO À REVISTA *"COLLOIDS AND SURFACES B: BIOINTERFACES"*

LISTA DE ILUSTRAÇÕES DO CAPÍTULO SUBMETIDO À "*ENCYCLOPEDIA OF NANOSCIENCE AND NANOTECHNOLOGY*"

LISTA DE ABREVIATURAS E SIGLAS

ACs	Agentes de contraste
AH	Ácido hialurônico
AMA	Ácido mercaptoacético
AMACR	Alfa-metilacil-coenzima A racemase
AMP	Ácido mercaptopropiônico
AMS	Ácido mercaptossuccínico
B_0	Campo magnético externo
BC	Banda de Condução
BFP	Proteína Fluorescente Azul
BNPs	Nanopartículas bimodais
BV	Banda de Valência
CEACAM8/ CD67	Receptores de antígenos carcinoembrionários relacionado à adesão da molécula 8
CdTe	Telureto de Cádmio
QDs	*Quantum dots* ou pontos quânticos
UV	Ultravioleta
NIR	Infravermelho próximo
CdSe	Seleneto de Cádmio
CdS	Sulfeto de Cádmio
CIS	L-cisteína
CISAM	Cisteamina
DDA	Dodecil amina
DMT1	Transportador de metais bivalentes
FWHM	Largura a meia altura
HeLa	Células de adenocarcinoma cervical humano
ICP	Plasma acoplado indutivamente
IRM	Imagem por ressonância magnética
EDC	1-etil-3-(3-dimetilaminopropil) carbodiimida
EGF	Fator de crescimento epidermal
EGFR	Receptor do fator de crescimento epidermal

FAAS	Espectrometria de absorção atômica de chama
FDA	Órgão de controle de administração de alimentos e remédios
GFP	Proteína Fluorescente Verde
GSH	Glutationa
ICP	Plasma acoplado indutivamente
M_0	Magnetização resultante
Ms	Magnetização de saturação
PAR1	Receptor ativador de protease 1
RMN	Ressonância Magnética Nuclear
SPIONs	Nanopartículas magnéticas de óxido de ferro superparamagnéticas
TGA	Ácido Tioglicólico
Sulfo-NHS	N-hidroxisulfosuccinimida
T_1	Tempo de relaxação longitudinal
T_2	Tempo de relaxação transversal
Tf	Transferrina
YFP	Proteína fluorescente amarela
r_1	Relaxividade longitudinal
r_2	Relaxividade transversal

LISTA DE SÍMBOLOS E UNIDADES

nm	Nanômetro
m	Metro
Eg	*band gap* de energia
Ev	Elétron-volt
H	Constante de Planck
υ	Frequência da luz
λ	Comprimento de onda
a_0	Raio de Bohr
Å	Angstron
kDa	Kilodaltons
V	Volts
µM	Micromolar
u.a.	Unidades arbitrárias

SUMÁRIO

1 INTRODUÇÃO

Um dos objetivos fundamentais em biologia é entender a complexa interação de biomoléculas tanto a nível celular quanto em organismos inteiros. Para estudar essas interações, pesquisadores comumente utilizam a fluorescência, pois técnicas de análise baseadas nesse fenômeno são altamente sensíveis, apresentam especificidade bioquímica e permitem o acompanhamento da dinâmica dos eventos biológicos em tempo real, além da quantificação e visualização da distribuição de biomoléculas na superfície ou no interior das células (Giepmans *et al.*, 2006). No entanto, para que determinadas estruturas biológicas possam ser estudadas, é necessária a utilização de marcadores fluorescentes, pois através da conjugação destes as biomoléculas de reconhecimento advém a especificidade bioquímica (por exemplo: os reconhecimentos antígenos-anticorpos ou proteínas-receptores). Além disso, alguns marcadores fluorescentes possuem especificidade química por alguma região específica na célula. Dessa forma, estes marcadores propiciam uma maior sensibilidade às técnicas de análises baseadas em fluorescência. Por essa razão, a aplicação eficiente dessas técnicas está intrinsecamente relacionada à ação do fluoróforo empregado.

Os nanocristais fluorescentes de semicondutores, chamados de pontos quânticos ou *quantum dots* (QDs) estão cada vez mais ganhando espaço frente aos tradicionais corantes orgânicos luminescentes. Isso se deve a algumas vantagens fundamentais apresentadas pelos QDs, tais como: (1) sintonização da fluorescência com o tamanho, assim um QD de mesma composição química pode emitir em diferentes regiões do espectro eletromagnético em função apenas do seu tamanho; (2) QDs apresentam estreitos espectros de emissão, que permitem múltiplas marcações simultâneas; (3) o efeito de fotodegradação da fluorescência é cerca de 100 vezes menor nos QDs do que nos corantes orgânicos, permitindo que amostras sejam expostas à luz e os estudos biológicos possam ser monitorados em tempo real; (4) QDs são eletrodensos, permitindo sua localização por microscopia eletrônica e (5) QDs possuem uma superfície ativa permitindo conjugações com moléculas ou até mesmo outras nanopartículas (Bruchez *et al.*, 1998; Chan, W. C. W. e Nie, S., 1998; Santos *et al.*, 2008; Santos, B. S. *et al.*, 2008; Wegner e Hildebrandt, 2015).

QDs conjugados a biomoléculas para reconhecimento específico vêm sendo cada vez mais aplicados para: aquisição de imagens *in vitro* de células e tecidos; aquisição de

imagens *in vivo* de pequenos animais (ratos e camundongos), o diagnóstico do câncer e outras doenças, biodetecção por imunoensaios, biossensores, estudos por citometria de fluxo e, até mesmo em terapia fotodinâmica (Yaghini *et al.*, 2009). Além disso, recentemente tem surgido também a associação de QDs a outros sistemas com a finalidade de se gerar nanopartículas bimodais com propriedades ópticas e magnéticas (Jin *et al.*, 2008; Stasiuk *et al.*, 2011; Shen *et al.*, 2012). Dentre os sistemas paramagnéticos/superparamagnéticos mais utilizados para esse fim, estão os quelatos contendo íons paramagnéticos, como o gadolínio (Gd^{3+}) os quais geram imagens ponderadas em T_1, e as nanopartículas de óxido de ferro que geram imagens ponderadas em T_2 (Etgar *et al.*, 2007; Liu, X. *et al.*, 2010; Geszke *et al.*, 2011). Além da aplicação clássica como agentes de contraste (AC) para aquisição de imagens por ressonância magnética (IRM), as nanopartículas de óxido de ferro também podem ser utilizadas para biosseparação, para biorreatores baseados em enzimas digestivas e também para terapia por hipertermia (Wang *et al.*, 2004; Wang *et al.*, 2010; Shen *et al.*, 2012).

A técnica de IRM é baseada nos princípios da ressonância magnética nuclear (RMN) e, sendo assim, as imagens são obtidas a partir da resolução espacial dos sinais RMN dos prótons (^1H) das moléculas de água existentes nos tecidos, obtidas por uso de gradientes de campo magnético, na qual a intensidade dos elementos de imagem ("voxels") depende, entre outros parâmetros, da densidade local de prótons e principalmente dos tempos de relaxação (longitudinal e transversal) do spin nuclear (T_1 e T_2, respectivamente). Os tempos de relaxação do spin nuclear refletem a mobilidade local das moléculas de água presentes nos tecidos e são afetados pela vizinhança permitindo assim visualizar e distinguir as variadas estruturas presentes nos organismos vivos (Merbach *et al.*, 2013). O papel principal dos ACs na IRM é potencializar a diferença entre as intensidades das imagens de estruturas patológicas e normais, ou seja, melhorar o contraste entre as mesmas. Essa capacidade dos ACs é consequência da diminuição dos tempos de relaxação T_1 e/ou T_2 dos prótons das moléculas de água que estão à sua volta (Caravan *et al.*, 1999; Geraldes, C. F. e Laurent, S., 2009).

O crescente interesse nessas nanopartículas híbridas (magnéticas e fluorescentes) surge devido às suas propriedades complementares que podem suprir as respectivas deficiências de cada uma, potencializando sua aplicação não só para imagenologia, para fins de compreensão de processos biológicos e diagnóstico, como até mesmo em terapia. Dessa forma, o desenvolvimento e a utilização dessas nanopartículas bimodais poderão, por exemplo, permitir: (1) a localização de moléculas alvos, através da

aquisição de imagens em tempo real com especificidade bioquímica propiciada pela fluorescência, associada à localização espacial, rica em detalhes anatômicos realçados, fornecidos pela IRM, especialmente para ensaios *in vivo*; (2) o monitoramento, através das propriedades fluorescentes, da terapia por hipertermia gerada através das propriedades magnéticas das nanopartículas de óxido de ferro e (3) possibilitar a biosseparação de células alvo (Figueiredo *et al.*, 2011; Norek e Peters, 2011).

Apesar de já existirem trabalhos sobre sistemas bimodais, contendo QDs e nanopartículas magnéticas, a grande maioria destes, são voltados para o aprimoramento da síntese dessas nanopartículas (Du *et al.*, 2006; Jie-Mei *et al.*, 2012; Ahmed *et al.*, 2013). Mesmo assim, há ainda poucos sistemas desenvolvidos, e ainda não há muitos trabalhos que destaquem alguma aplicação biomédica de sistemas bimodais sítio-específicos, também denominados como multimodais. Devido à importância e à necessidade de se suprir as deficiências inerentes, principalmente, às técnicas ópticas e magnéticas de aquisição de imagens, a obtenção de nanopartículas multimodais, que propiciem a formação de imagens com alta sensibilidade espacial e temporal, especificidade bioquímica e que investiguem fenômenos biológicos em tempo real estão sempre em foco e podem contribuir para a compreensão da biologia celular e molecular de diversas doenças. A exemplo destas tem-se o câncer, uma vez que ainda é um desafio a sua compreensão para fins de desenvolvimento de diagnósticos rápidos e eficientes, e principalmente de tratamentos mais eficazes (Wegner e Hildebrandt, 2015).

Assim, para que haja especificidade bioquímica, e melhor contraste localizado na IRM, as sondas bimodais devem ser conjugadas a biomoléculas que propiciem às mesmas um direcionamento específico, formando nanossondas multimodais. Dentre as biomoléculas de interesse para esse fim está a transferrina, proteína responsável pelo transporte de ferro para o meio intracelular. A transferrina (Tf) se liga ao seu receptor (TfR) que está localizado na superfície das células e após essa ligação o complexo (transferrina-receptor) é endocitado como forma de captação intracelular de íons Fe^{3+}, o qual é um importante íon para o metabolismo celular (Li e Qian, 2002; Daniels *et al.*, 2012). Em especial, células com elevada taxa metabólica, como as células tumorais, podem expressar maiores quantidades desses receptores de transferrina. Dessa forma, o receptor de transferrina pode ser então um alvo interessante não só para a compreensão da biologia celular do câncer, como também para o aprimoramento de métodos de diagnósticos e terapêuticos para esta doença.

Assim, neste trabalho, primeiramente QDs de Telureto de Cádmio (CdTe) foram conjugados à Tf para o estudo da distribuição e da quantificação de TfRs em células cancerígenas, para posteriormente servir de modelo no desenvolvimento de sondas multimodais. Para tanto, a primeira etapa foi conjugar QDs a nanopartículas de óxido de ferro, formando uma sonda bimodal com propriedades magnético-fluorescentes. Essas sondas bimodais mostraram-se eficientes na marcação inespecífica de células por fluorescência e com potencial AC para aquisição de imagens ponderadas em T_2 por ressonância magnética. Por fim, estas sondas bimodais foram então conjugadas à Tf e aplicadas para reconhecimento específico dos TfR de células cancerígenas, originando assim sondas multimodais. Portanto, essas novas nanossondas desenvolvidas nessa tese podem ajudar a ampliar a compreensão da biologia celular do câncer, além de auxiliar em métodos diagnósticos e terapêuticos para essa doença.

2 OBJETIVOS

2.1 OBJETIVO GERAL

Desenvolver sondas com propriedades multimodais baseadas em QDs de Telureto de Cádmio (CdTe) associadas a nanopartículas magnéticas de óxido de ferro para aplicações em células cancerígenas.

2.2 OBJETIVOS ESPECÍFICOS

- Sintetizar e caracterizar opticamente QDs de CdTe carboxilados;
- Conjugar os QDs à Tf, confirmar a conjugação e caracterizar o conjugado (QDs-Tf) opticamente.
- Aplicar os conjugados de QDs-Tf no estudo de TfR em células cancerígenas e também como modelo de padronização para a preparação da sonda multimodal;
- Sintetizar e caracterizar estruturalmente e magneticamente as nanopartículas de óxido de ferro (MNPs);
- Conjugar os QDs de CdTe às nanopartículas de óxido de ferro e caracterizar esse sistema bimodal opticamente, estruturalmente e magneticamente;
- Aplicar os sistemas bimodais para marcação inespecífica de células tumorais e estudar a interação nanopartículas/sistemas biológicos através de fluorescência;
- Conjugar os sistemas bimodais com a transferrina e caracterizar essas novas sondas multimodais opticamente e relaxometricamente;
- Aplicar os sistemas multimodais para marcação por fluorescência do TfR em células tumorais;
- Elaborar um capítulo de revisão abordando as aplicações de sistemas bimodais e multimodais em Ciências da Vida.

3 REFERÊNCIAL TEÓRICO

Este trabalho destaca o uso e a caracterização de processos físicos relacionados à emissão de luz por nanopartículas de semicondutores, este fenômeno é chamado de fluorescência, um tipo de luminescência.

3.1 LUMINESCÊNCIA

O processo de luminescência envolve duas etapas: a excitação de elétrons para níveis de maior energia e o retorno desses elétrons para níveis de menor energia que resulta na emissão de fótons, ou seja, de luz. A luminescência pode ser classificada de acordo com o modo no qual os elétrons são excitados para geração de fótons, por exemplo: bioluminescência e quimiluminescência - os elétrons são excitados através de reações bioquímicas e químicas, tal como: a emissão de luz pelo vagalume; eletroluminescência - a excitação dos elétrons é induzida pela corrente elétrica; catodoluminescência - excitação a partir da colisão de elétrons do meio com elétrons livres originados de descargas elétricas (é o caso das lâmpadas fluorescentes); e termoluminescência - onde há liberação de elétrons presos em níveis de armadilhas pelo calor, promovendo seu decaimento (Goldberg e Dean, 1966; Preusser *et al.*, 2008; Cesar *et al.*, 2010). Além dessas, também há a fotoluminescência que é um dos fenômenos estudados nesse trabalho.

3.1.1 Fotoluminescência

A fotoluminescência é um processo no qual os elétrons são excitados por fótons e quando os elétrons retornam ao estado fundamental, fótons (luz) também são emitidos. A fluorescência e fosforescência são processos englobados pela fotoluminescência. A fluorescência é um processo rápido que ocorre na ordem de 10^{-9} a 10^{-7} segundos. Já a fosforescência é lenta, podendo durar de 10^{-3} a 100 segundos (Cesar *et al.*, 2010). Em outras palavras, a fluorescência só ocorre enquanto a amostra estiver sendo excitada, e a fosforescência persiste por um determinado tempo depois que a excitação da amostra é finalizada.

Em 1852, o físico e matemático escocês, George Stokes foi o primeiro a descrever o fenômeno da fluorescência (Cesar *et al.*, 2010). Apesar da descoberta ter acontecido por volta de 1852, somente por volta de 1930, com a invenção dos corantes orgânicos como marcadores fluorescentes, é que a fluorescência passou a ser amplamente utilizada nas Ciências da Vida.

Quase todo tecido biológico, devido à presença dos aminoácidos aromáticos, tais como: tirosina, triptofano e fenilalanina (Figura 1 A-C, respectivamente), é autofluorescente, pois quando excitados por luz, principalmente na região do UV ao verde, fluorescem naturalmente em quase todo espectro visível (do azul ao vermelho) sem necessitar da adição de substâncias exógenas. A autofluorescência é um fenômeno indesejado em muitos casos, pois se sobrepõe à fluorescência emitida pelos fluoróforos convencionais. Por outro lado, a autofluorescência pode ser valiosa para estudos de processos celulares *in vivo*, nos quais a marcação exógena deve ser evitada (Ntziachristos, 2006; Cesar *et al.*, 2010).

Figura 1 – Estrutura dos aminoácidos (A) Tirosina, (B) Triptofano e (C) Fenilalanina. Tirosina é um aminoácido polar neutro. Já o Triptofano e a Fenilalanina são aminoácidos apolares.

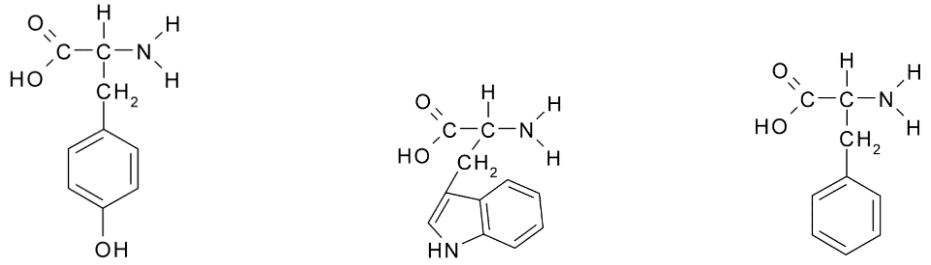

(A) (B) (C)

Fonte: O autor.

A fluorescência acontece somente se a molécula for excitada com luz. Essa excitação só ocorre se o comprimento de onda da luz incidente (λ_i) estiver dentro de um intervalo chamado de banda de absorção, ou banda de excitação (Figura 2). A luz é então emitida em outro comprimento de onda (λ_e), formando a banda de emissão (Figura 2). O deslocamento entre os máximos da excitação (absorção) e da emissão é chamado de *Stokes - shift* (Figura 2). Vale a pena ressaltar que, a banda de emissão é deslocada em relação à banda de excitação na direção de comprimentos de onda maiores (menor energia).

Figura 2 – Espectros de absorção e emissão de corante orgânico.

Fonte: O autor

Para entendermos melhor o *Stokes shift* é importante visualizarmos parte do diagrama de Jablonski, apresentado na Figura 3. As moléculas possuem níveis eletrônicos de energia e cada nível eletrônico possui níveis vibracionais. Quando uma molécula absorve um fóton, ganha energia e o elétron passa para um nível eletrônico e vibracional mais excitado. Então, o elétron decai não radiativamente para níveis vibracionais de menor energia, e posteriormente para um nível eletrônico de menor energia, liberando então esse excesso de energia na forma de fótons (Cesar *et al.*, 2010; Lakowicz, 2013). No entanto, para que haja fluorescência é necessário que a transição do elétron ocorra entre níveis eletrônicos de energia, caso essa transição ocorra entre os níveis vibracionais da molécula, haverá perda de energia apenas de forma não radiativa. Portanto a diferença da energia entre o fóton emitido (menor energia) e o fóton absorvido (maior energia) é chamada de *Stokes Shift.*

Figura 3 – Esquema da emissão de fluorescência através do diagrama de Jablonski.

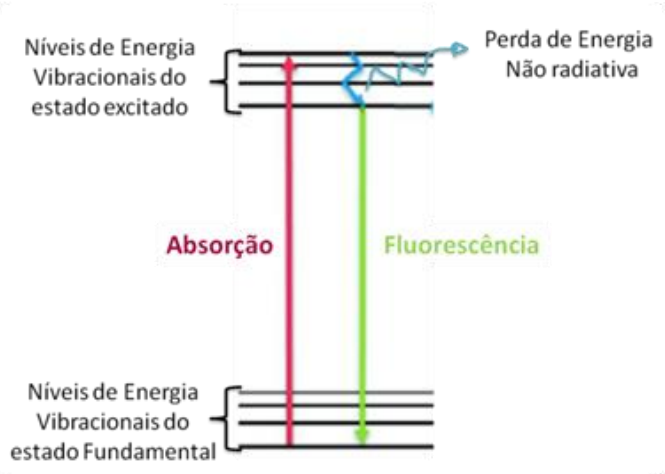

Fonte: Adaptada de Cesar *et al.* (2010).

Análises baseadas em fluorescência têm especificidade bioquímica e alta sensibilidade. As sondas fluorescentes mais utilizadas são moléculas orgânicas, convencionalmente chamadas de corantes orgânicos. Existe atualmente uma grande diversidade desses corantes orgânicos disponíveis comercialmente. Porém, como em geral esses marcadores, quando utilizados sozinhos, não apresentam especificidade por determinadas biomoléculas, muitas aplicações fazem usos destas sondas ligadas a anticorpos (Giepmans *et al.*, 2006).

Nas últimas décadas, as proteínas fluorescentes vêm também sendo bastante utilizadas como marcador de células e organismos. Elas são produzidas a partir de modificações genéticas, que permitem obter imagens de células vivas e organismos, de forma não invasiva, desde que eles expressem um gene de interesse ligado a essas proteínas. Inicialmente foi descoberta, clonada e expressa a proteína fluorescente verde (GFP) da água viva. Tal descoberta consagrou um prêmio Nobel de Química de 2008 a três pesquisadores americanos Osamu Shimomura, Martin Chalfie e Roger Y. Tsien (Giepmans *et al.*, 2006). Atualmente, já existem outras proteínas fluorescentes como a proteína fluorescente amarela (YFP), a azul (BFP), dentre outras variações (Wachter *et al.*, 1998).

No entanto, tanto os corantes orgânicos como as proteínas fluorescentes possuem algumas limitações, tais como a fotodegradação dos corantes e a necessidade de laboriosas manipulações genéticas das proteínas fluorescentes. Por isso, há um considerável interesse no emprego de *quantum dots* ou pontos quânticos como sondas fluorescentes para Ciências da Vida. Isso se deve ao fato deles apresentarem significativas vantagens fotofísicas em relação aos marcadores fluorescentes usados convencionalmente, o que possibilita se melhorar não só a qualidade das imagens obtidas por fluorescência, como também a compreensão de processos biológicos (Fontes *et al.*, 2012, Lira *et al.*, 2011, Cabral Filho, *et al.* 2015).

3.2 PONTOS QUÂNTICOS OU *QUANTUM DOTS* (QDs)

3.2.1 Fundamentos

Pontos quânticos ou *quantum dots* (QDs) são cristais de semicondutores fluorescentes em escala nanométrica (nanocristais). Apresentam diâmetros da ordem de

1,5 a 10 nm (1 nm = 10^{-9} m ou um bilionésimo do metro). Os QDs são constituídos de poucas centenas a poucos milhares de átomos, exibindo propriedades ópticas, que são significativamente diferentes, quando comparadas aos mesmos cristais em escala macroscópica "*bulk*" (Michalet *et al.*, 2005; Michalet *et al.*, 2008; Santos *et al.*, 2008).

Os QDs podem ser feitos de vários tipos de materiais semicondutores e são classificados como sendo nanocristais dos tipos: II - VI, III - V ou IV - VI, com base em combinações de elementos pertencentes às antigas famílias da tabela periódica (Sukhanova e Nabiev, 2008). Atualmente, a tabela periódica não tem subdivisão de famílias, apenas grupos de 1 a 18, no entanto, a subdivisão das famílias ainda é bastante utilizada (Figura 4). Dessa forma, nanocristais de CdTe (Telureto de Cádmio), por exemplo, são do tipo II-VI, pois são formados pelo Cádmio, pertencente a antiga família IIB (atual grupo 12) e o Telúrio da família VIA (atual grupo 16) (Figura 4).

Figura 4 – Tabela periódica dos elementos químicos. Em destaque os elementos das antigas Famílias IIB e VIA, atuais grupos 12 e 16, respectivamente.

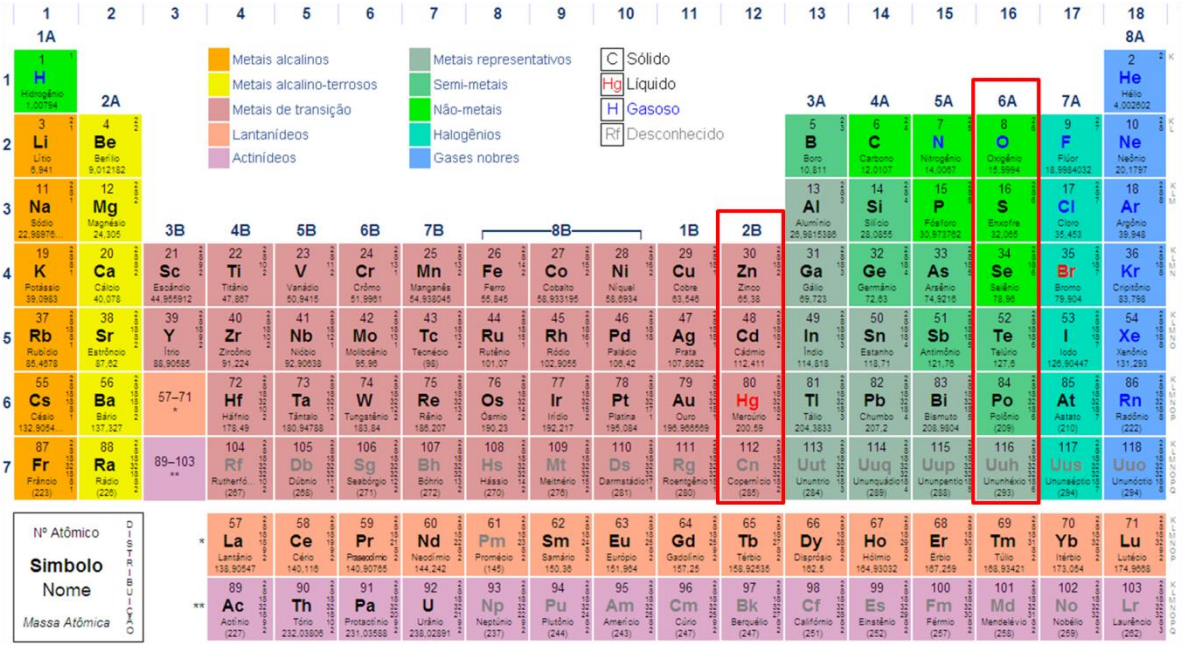

Fonte: Adaptada de http://www.tabelaperiodicacompleta.com/.

Os semicondutores são sólidos que apresentam uma banda de valência (BV) totalmente ocupada por elétrons, a qual está separada de uma banda de condução (BC) por uma banda de energia proibida ou *band gap* (Eg), Figura 5. Para que os elétrons passem da BV para a BC, eles precisam receber energias iguais ou maiores que a

energia da Eg. Em semicondutores, a Eg normalmente é menor que 3 eV[1], o que permite por exemplo, que a luz no ultravioleta (UV) ou visível possa ser utilizada para promover elétrons para a BC em temperatura ambiente. Por outro lado, um sólido também pode ser isolante ou condutor. Os isolantes caracterizam-se por apresentarem elevadas Eg, que em temperatura ambiente, impossibilitam o elétron de passar por essa barreira de energia e chegar a BC. Já nos condutores há presença de bandas semipreenchidas ou ainda a BV e a BC podem estar sobrepostas formando uma banda contínua, fazendo com que não haja resistência à passagem dos elétrons entre as bandas (Smith *et al.*, 2004).

Figura 5 – Diferença na energia do *band gap* (Eg) para diferentes classes de materiais em sólidos.

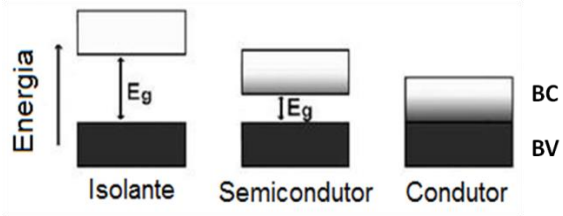

Fonte: Adaptada de Smith *et al.*, (2004).

Quando os semicondutores recebem energia externa através de fótons, elétrons da BV, de menor energia, passam para a BC, de maior energia, gerando um par elétron-buraco, também chamado de éxciton (Figura 6). O éxciton formado possui uma vida de alguns nanosegundos e o processo de decaimento energético para a BV é denominado de recombinação excitônica. A recombinação dos elétrons excitados (localizados na BC) com os buracos da BV dá origem à emissão característica (fluorescência) tanto em regime macroscópico quanto nanométrico. Porém, quando em nanoescala, os elétrons e buracos sofrem um forte confinamento quântico, modificando as propriedades ópticas desses materiais.

[1] eV: quantidade de energia cinética de um elétron quando acelerado por uma diferença de potencial elétrico de 1 Volt, no vácuo.

Figura 6 – Esquema de formação de um éxciton. No qual, h^+ representa o buraco gerado na banda de valência, pela excitação do elétron e^-, hv a energia de um fóton excitando a amostra, E = hv, h é a constante de Planck e v é a frequência da luz.

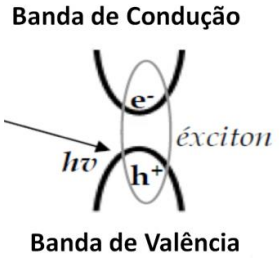

Fonte: Adaptado de Chaves, (2006).

O confinamento quântico é um fenômeno bastante importante para materiais semicondutores. No caso do semicondutor macroscópico (*bulk*), o elétron pode ocupar uma variedade de estados energéticos que estão distribuídos de modo contínuo. Quando uma das dimensões do material torna-se fisicamente menor que o raio de Bohr[2] característico deste material, dizemos que essa estrutura encontra-se em confinamento quântico. Essa barreira limita o movimento dos elétrons em uma ou mais direções x, y ou z, e isso leva a uma mudança na distribuição dos estados de energia nesse material (Brus, 1984).

Se, por exemplo, limitarmos os três lados de um cubo (ou seja, três das dimensões do material são menores que o raio de Bohr), dizemos que o movimento dos elétrons fica limitado tridimensionalmente. Nesse caso, temos um confinamento quântico em três dimensões e a formação de níveis de energia discretos, que também podem ser ocupados por elétrons. É nessa situação, quando o confinamento quântico é tridimensional, que temos os chamados QDs e é por essa razão que esses nanocristais também são chamados de átomos artificiais, porque apresentam estados energéticos discretos, assim como os átomos (Figura 7). Dessa forma, se, por exemplo, o raio de Bohr para o *bulk* do semicondutor CdSe (Seleneto de Cádmio) é 5,0 nm, quando o nanocristal for menor que 5,0 nm ele está em confinamento quântico e é chamado de QD (Santos *et al.*, 2008).

[2] O par elétron-buraco pode se mover pelo material macroscópico (já que os estados são contínuos) e uma força atrativa os mantém movendo-se juntos existindo sempre uma distância média entre eles chamada raio de Bohr, em alusão ao átomo de hidrogênio. O raio de Bohr é característico de cada semicondutor e é calculado analisando o material em escala macroscópica (*bulk*).

Figura 7 – Redução do tamanho de partículas semicondutoras dentro do regime de confinamento quântico comparando os QDs ao *bulk* (cristal macroscópico) do mesmo material. Também se pode observar que com a diminuição do tamanho das partículas há discretização dos níveis energéticos e aumento do *band gap.*

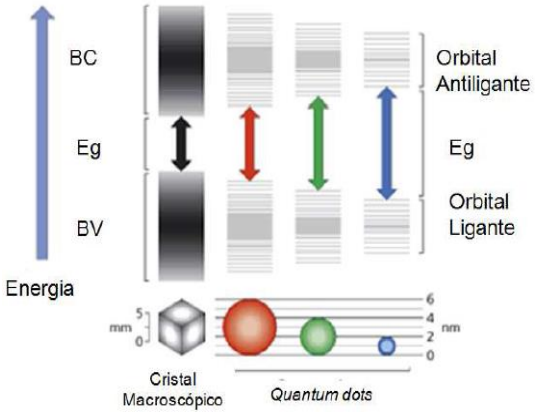

Fonte: Adaptado de Cox, (2003).

Além da discretização dos estados energéticos, o confinamento quântico também faz com que seja possível controlar em que região do espectro eletromagnético um QD irá emitir, através do controle do seu tamanho, isto é o que chamamos de sintonização do comprimento de onda de emissão em função do tamanho do nanocristal. Essa propriedade ocorre devido ao fato de que, em confinamento quântico, a Eg aumenta ou diminui de acordo com o tamanho da nanopartícula, quando ela é formada pelo mesmo material (Figura 7).

Como $Eg \alpha 1/d^2$ (onde d é o diâmetro das nanopartículas) e $E \alpha 1/\lambda$ (energia E é inversamente proporcional ao comprimento de onda de emissão - λ), quanto menor a partícula de um dado semicondutor, maior é a Eg e mais para a região do azul do espectro eletromagnético (menores comprimentos de onda) é sua emissão. Enquanto para partículas maiores, menor é Eg e mais para o vermelho devem apresentar luminescência (Santos *et al.*, 2008)

Portanto, essas novas características que materiais (já bem conhecidos na escala macroscópica) adquirem quando escalonados nanometricamente é que fazem os QDs terem grande potencial para aplicações em diferentes áreas da pesquisa, desde a microeletrônica às Ciências da Vida. Isso se deve principalmente às novas propriedades ópticas que são alcançadas controlando o tamanho desses nanomateriais (Santos *et al.*, 2008).

Os QDs vêm cada vez mais sendo utilizados como marcadores biológicos fluorescentes em Ciências da Vida. Isso ocorre devido ao fato destes apresentarem

consideráveis vantagens em relação aos marcadores convencionais (principalmente os corantes orgânicos), tais como: (1) largo espectro de absorção, uma única fonte de luz pode excitar a luminescência das nanopartículas, as quais podem (2) emitir luz em diferentes regiões do espectro variando-se apenas o tamanho da partícula (corantes orgânicos exigem mais de uma fonte de luz de excitação), como pode ser visto na Figura 8; (3) o efeito de fotodegradação da luminescência é cerca de 100 vezes menor nos QDs do que nos corantes orgânicos (isso permite que amostras com QDs sejam expostas à luz, as imagens sejam obtidas com maior intensidade de luminescência e que estudos de processos em função do tempo possam ser realizados, como podemos observar na Figura 9) e (4) os QDs são eletrodensos, permitindo localização subcelular das nanopartículas por microscopia eletrônica de transmissão como pode ser observado na Figura 10 (Alivisatos, 2004; Medintz *et al.*, 2005; Michalet *et al.*, 2005; Sukhanova e Nabiev, 2008).

Figura 8 – Espectros de emissão e absorção dos QDs comparados com corante orgânico. O QD por possuir um largo espectro de absorção pode ser excitado em vários comprimentos de onda, no entanto cada corante convencional necessita da excitação em comprimento de onda específico.

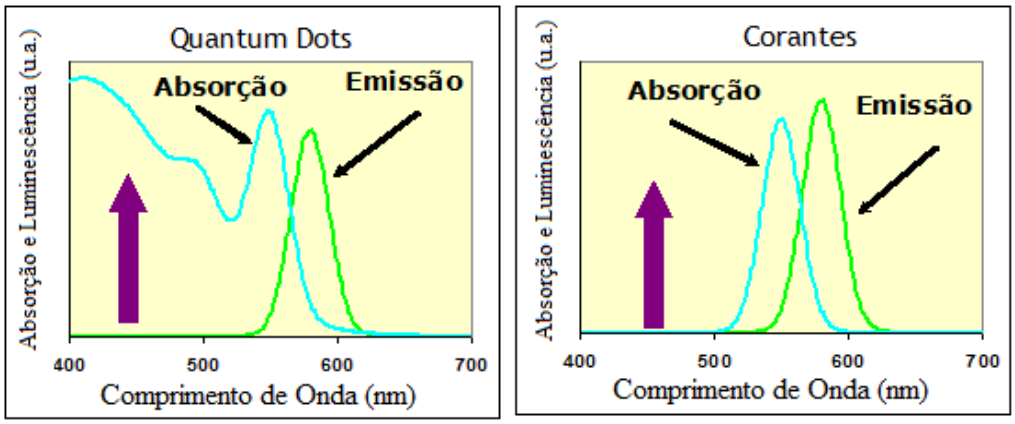

Fonte: Adaptada de De Farias, (2007).

Figura 9 – Fotodegradação em função do tempo: antígenos nucleares corados com Alexa Fluor 488 e microtúbulos corados com QD 605 - CdSe (Tempos observados: 0 s, 20 s, 60 s, 120 s e 180 s).

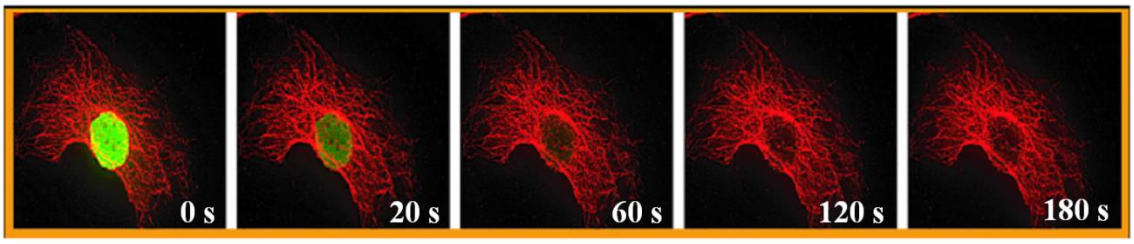

Fonte: Adaptada de Alivisatos, (2004).

Figura 10 – Imagens da localização intracelular de QDs por microscopia eletrônica de transmissão. Em (A) QDs condensados no endossoma de células epiteliais de adenocarcinoma mamário humano (MCF-7), em (B) imagens de QDs no citostoma de *Trypanosoma cruzi.*

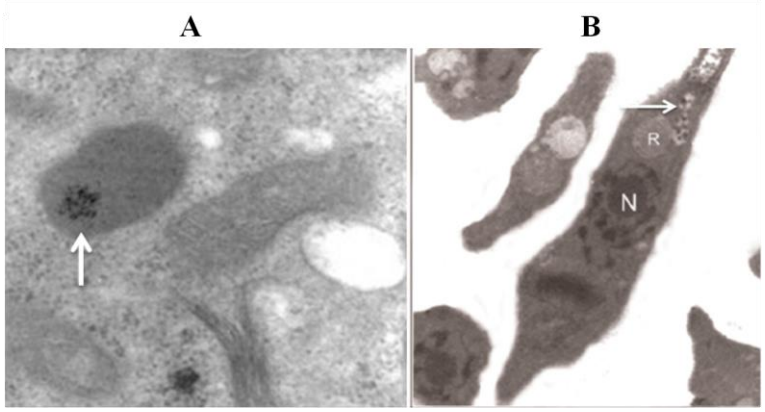

Fonte: (A) Adaptada de Xiao *et al.,* (2010); (B) Adaptada de Chaves *et al.,*(2008).

A redução do volume da partícula resulta em um aumento da relação área/volume, no entanto, a elevada área superficial aumenta a contribuição dos defeitos de superfície dos nanocristais (átomos da superfície do cristal que tem ligações não compartilhadas) resultando no decréscimo da eficiência da emissão de luz pelas nanopartículas. Isso ocorre porque os defeitos levam à formação de níveis intermediários entre a BV e a BC, e ao invés do elétron ir diretamente da BC para a BV, ele vai perdendo energia aos poucos nesses níveis intermediários, levando a uma baixa eficiência de luminescência. Uma maneira de contornar esses problemas é crescer uma "casca" (camada de passivação), de umas poucas camadas de átomos, de um material semicondutor, geralmente com um *band gap* maior do que o do semicondutor do núcleo da nanopartícula. Esse processo da formação da "casca" é denominado passivação e as nanopartículas resultantes apresentam uma estrutura física do tipo *core/shell* (núcleo/casca) (Fontes *et al.*, 2012).

3.2.2 Síntese coloidal

Os QDs são geralmente sintetizados por métodos de química coloidal, sendo considerados coloides. Um coloide é uma mistura de pelo menos duas substâncias em fases diferentes: a fase dispersa, que pode ser sólida, líquida ou gasosa, e deve ser finamente dividida, com pelo menos uma das dimensões entre 1 µm e 1 nm; e a fase contínua (dispersante), que também pode ser sólida, líquida ou gasosa e é denominada

meio de dispersão. No caso dos QDs, a fase dispersa é sólida e a dispersante é líquida. Os métodos de síntese química coloidal é baseado numa reação de precipitação controlada feita em água ou em solventes orgânicos. A síntese em água de nanopartículas de CdTe passivadas com CdS (Sulfeto de Cádmio) para produção de QDs, é bastante utilizada para aplicações como marcadores celular, pois os QDs produzidos por esse método são hidrofílicos e, portanto, compatíveis com os sistemas biológicos (Pankiewicz *et al.*, 2015).

Simplificadamente, a síntese em meio aquoso é dividida em três etapas (Figura 11). Em uma primeira etapa, é feita uma solução aquosa, em pH e temperatura controlados, contendo um sal de um metal de transição (do atual grupo 12 ou da antiga família IIB da tabela periódica) e um agente estabilizante, cujo papel é controlar o crescimento do núcleo inicial e evitar a aglomeração das nanopartículas. Em uma segunda etapa, ocorre a redução de um calcogênio e na terceira etapa, o calcogênio reduzido é então adicionado à solução da etapa 1 e a reação continua ao longo do tempo, em temperatura controlada, até que se tenha o tamanho de nanopartícula desejado (Santos *et al.*, 2008).

Figura 11 – Esquema de síntese de QDs em meio aquoso.

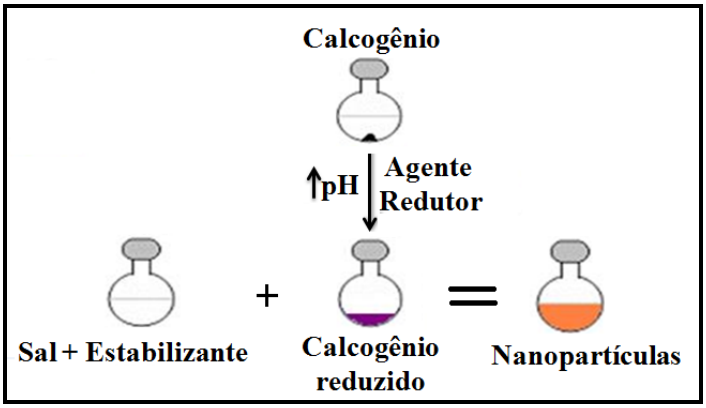

Fonte: O autor.

Os estabilizantes comumente utilizados em QDs coloidais apresentam grupamento tiol (–SH). Moléculas contendo esses grupamentos são ótimos estabilizantes de nanopartículas, pois o enxofre ajudará a compor a camada de passivação e o restante da molécula conferirá cargas (positivas ou negativas) às partículas, mantendo-as afastadas em suspensão. Dentre os agentes estabilizantes mais utilizados, destacam-se o ácido mercaptoacético (AMA) ou ácido tioglicólico (TGA), o

ácido 3-mercaptopropiônico (AMP), o ácido mercaptosuccínico (AMS), a L-cisteína (CIS) e a cisteamina (CISAM) (Rogach *et al.*, 2007; Idowu *et al.*, 2008; Zhang *et al.*, 2011; Chang *et al.*, 2012; Silva *et al.*, 2012; Ribeiro *et al.*, 2013), cujas estruturas químicas são observadas na Figura 12.

Figura 12 – Fórmulas estruturais dos agentes estabilizantes comumente utilizados para obtenção de QDs: (A) ácido mercaptoacético (AMA) ou ácido tioglicólico (TGA), (B) ácido 3-mercaptopropiônico (AMP), (C) ácido mercaptosuccínico (AMSAMS), (D) cisteína (CIS) e (E) cisteamina (CISAM).

.

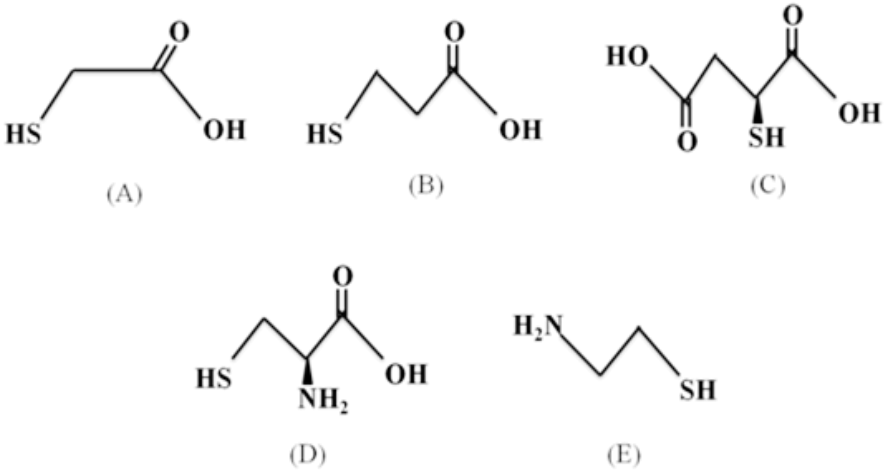

Fonte: O autor.

Como pode ser observado na Figura 12, além do grupamento tiol essas partículas apresentam grupamentos funcionais (ácidos carboxílicos ou aminas), que além de conferir cargas superficiais aos QDs, possibilitam a ligação dos QDs a biomoléculas ou a outras nanopartículas e por isso os agentes estabilizantes são também chamados de funcionalizantes (Ribeiro *et al.*, 2013). Os agentes estabilizantes também ajudam a compor a camada de passivação.

3.2.3 Aplicações biológicas

Os primeiros trabalhos envolvendo aplicação biológica de QDs foram publicados em 1998 na *Science* simultaneamente por dois grupos de pesquisadores distintos Bruchez e colaboradores (1998) e por Chan e Nie (1998). A partir de então uma infinidade de trabalhos foram publicados envolvendo primeiramente a utilização de QDs como sondas inespecíficas (Smith e Giorgio, 2009; Lira *et al.*, 2012). Estes estudos

envolvendo marcação inespecífica de células foram importantes para entender os mecanismos de interação dessas nanopartículas com diversos tipos de células e também para avaliar os QDs como possíveis sondas fluorescentes para aplicação biológica (Clift e Stone, 2012). As marcações inespecíficas podem ser obtidas, por exemplo, através da interação eletrostática de grupos positivos/negativos presentes na superfície dos QDs com grupos de carga contrária presentes nos sistemas biológicos. Como as membranas celulares são negativas, esse tipo de interação inespecífica em geral é observado quando QDs estabilizados com cisteamina, os quais têm a superfície positiva, são utilizados. Essa interação eletrostática já foi utilizada, por exemplo, para estudar a carga da membrana de hemácias utilizando QDs (Huang *et al.*, 2011). Por outro lado, células que tem alta taxa metabólica, como por exemplo, linhagens de células cancerígenas e macrófagos, podem também ser marcadas inespecificamente devido à sua alta capacidade endocítica (Yong *et al.*, 2009; Zhang *et al.*, 2009).

A superfície ativa dos QDs oferece a possibilidade de conjugá-los a várias biomoléculas de interesse, tais como anticorpos ou enzimas, que podem torná-los sondas específicas para compreender processos bioquímicos, auxiliar no diagnóstico baseado em fluorescência e também para terapia. Além disso, os QDs também podem ser conjugados a fármacos ou até mesmo a outras nanopartículas (Wegner e Hildebrandt, 2015). A conjugação de QDs a biomoléculas pode ser feita através de adsorção (interação eletrostática) ou por ligação covalente entre os sistemas. Atualmente, as principais estratégias de conjugação covalente são realizadas utilizando reagentes que proporcionam a reação entre grupamentos carboxilas-aminas como o EDC (1-etil-3-(3-dimetilaminopropil)carbodiimida) e o Sulfo-NHS (*N*-hidroxisulfosuccinimida), entre amina-amina utilizando o glutaraldeído, através da ligação estreptavidina-biotina e por ponte entre sulfetos (Hermanson, 2008; Guan *et al.*, 2012). Apesar de existir várias metodologias já publicadas de técnicas de conjugação, vários desafios sempre são encontrados, como por exemplo: (I) o processo de conjugação não pode desnaturar a biomolécula e não pode afetar as propriedades das nanopartículas; (II) sempre é preciso padronizar a quantidade de agentes de acoplamento, pois a mesma depende do tipo da biomolécula e da nanopartícula a ser utilizada; (III) a conjugação deve ser eficiente de modo que as interações inespecíficas sejam minimizadas ao máximo e (IV) deve haver reprodutibilidade na conjugação (Jin e Hildebrandt, 2012).

Entretanto, com a evolução das técnicas de conjugação de QDs a biomoléculas vários trabalhos envolvendo a marcação específica de células *in vitro* e *in vivo* têm sido publicados. Muitos deles envolvem a conjugação de QDs a biomoléculas para estudos *in vitro* da expressão de proteínas na superfície das células (Guan *et al.*, 2012; Schieber *et al.*, 2012; Zhang *et al.*, 2012), bem como marcação de células *in vivo*, principalmente em pequenos animais (Chen, K. *et al.*, 2008; Chen, Z. *et al.*, 2008; Fitzpatrick *et al.*, 2009; Ho *et al.*, 2013; Tang *et al.*, 2013). Além de sua extensa aplicabilidade em diagnóstico por imagens ópticas, os QDs também têm sido recentemente investigados na terapêutica, sendo utilizados para ensaios de terapia fotodinâmica (Samia *et al.*, 2006; Qi *et al.*, 2011; Malik *et al.*, 2012; Viana *et al.*, 2015).

Vários estudos *in vitro* têm sido conduzidos para o desenvolvimento de novos métodos auxiliares de diagnóstico (Zhang *et al.*, 2012; Tenório *et al.*, 2015; Andrade et. al., 2013). Além disso, os QDs aliados às técnicas de fluorescência são potenciais ferramentas para também colaborar para o entendimento da biologia celular de diversas doenças, tais como o câncer (Jin e Hildebrandt, 2012; Pisanic Ii *et al.*, 2014; Wegner e Hildebrandt, 2015). Por exemplo, Fang e colaboradores (2013), investigaram os processos de metástase do câncer. Através das imagens utilizando QDs conjugados a diferentes anticorpos, os autores investigaram a dinâmica do colágeno tipo IV, identificando que o aumento do colágeno tem relação direta com a invasão e metástase do câncer.

Em outro trabalho, Guan *et al.* (2012) utilizaram três diferentes métodos de conjugação de QDs a transferrina para avaliar qual dos conjugados eram mais eficientes na quantificação do receptor de transferrina em células HeLa. Os autores utilizaram a conjugação (1) por adsorção (interação eletrostática entre o QD e a transferrina), (2) conjugação covalente utilizando apenas o EDC e (3) desnaturando a transferrina com um agente redutor, o boridreto de sódio. Através dos resultados de citometria, os autores definiram que a conjugação utilizando o EDC marcou mais células HeLa que os outros dois métodos de conjugação utilizados. Portanto, os autores sugeriram que o uso do EDC seria um método simples para conjugação de QDs à transferrina.

Atualmente tem se aumentado o interesse em marcações múltiplas envolvendo QDs conjugados a várias biomoléculas para investigação do perfil de biomarcadores relacionados ao câncer. Através desse painel de QDs conjugados é possível a diferenciação dos alvos celulares com acurácia, devido aos diferentes perfis de emissão dessas nanopartículas. Liu *et al.* (2010), utilizando quatro biomarcadores proteicos

conjugados a QDs (com emissão em verde, vermelho, azul) em glândulas prostáticas, distinguiu células cancerígenas em tumores de próstata. Os resultados mostraram uma boa distinção da heterogeneidade molecular e celular nesses tipos de tecido. Na Figura 13, podemos observar proteínas da glândula prostática marcadas por um painel de QDs conjugados a anticorpos secundários. Observamos as marcações das proteínas: caderina-E (em verde), citoqueratina de alto peso molecular (em branco), p63 (em vermelho) e alfa-metilacil-coenzima A racemase - AMACR (em azul).

Figura 13 – Marcação múltipla de células tumorais de uma glândula prostática utilizando QDs conjugados a proteínas biomarcadores caderina-E (em verde), citoqueratina de alto peso molecular (em branco), p63 (em vermelho) e AMACR (em azul).

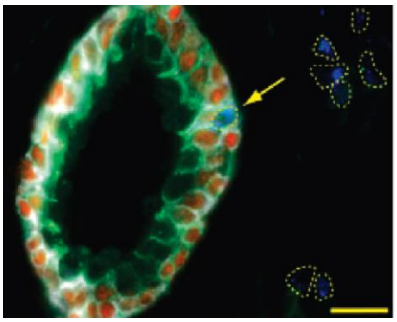

Fonte: Adaptada de Liu *et al.* (2010).

Sempre que os pesquisadores obtêm êxito na pesquisa *in vitro* de um novo marcador específico, é natural que posteriormente sejam realizados testes *in vivo.* As primeiras publicações de QDs *in vivo* apareceram no começo deste milênio (Åkerman *et al.*, 2002; Dubertret *et al.*, 2002) e desde então o número de artigos tem aumentado consideravelmente. Deve notar-se que as aplicações *in vivo* de QDs têm sido limitadas a pequenos animais. Esta limitação está relacionada com a profundidade de penetração da luz nos tecidos dificultando a geração de imagens de fluorescência em tecidos profundos. Além disso, os QDs ainda não foram aprovados para uso em humanos pela FDA (Órgão de controle de administração de alimentos e remédios dos Estados Unidos).

Os estudos *in vivo* têm também sido direcionados para a avaliação da toxicidade dos QDs (Ma-Hock *et al.*, 2012) e para estudos de biodisponibilidade e biodistribuição nos organismos vivos (Wegner e Hildebrandt, 2015). Estudos realizados por Praetner *et al.* (2010), indicam que QDs aniônicos permanecem pouco tempo na circulação e preferem acumular-se nos órgãos. Para driblar esses mecanismos de acumulação, vários

pesquisadores que estudam a interação dos QDs *in vivo*, recobriram os mesmos com uma camada de polímero, tais como o polietileno glicol, para evitar essa interação e sua consequente acumulação nos órgãos, melhorando a eliminação via renal dos QDs pelos sistemas vivos (Choi *et al.*, 2007; Choi *et al.*, 2010; Ho *et al.*, 2013).

Junto a isso, os desafios relacionados à compreensão (mecanismos associados aos processos de metástase), melhoramento das técnicas auxiliares de diagnóstico e de terapia do câncer faz com que as investigações *in vivo*, por fluorescência, sejam um campo de pesquisa que também está em foco (Wegner e Hildebrandt, 2015). Sendo assim, vários estudos têm sido conduzidos nessas áreas, como, por exemplo, os estudos promovidos por Diagaradjane *et al.* (2008) os quais investigaram a interação de QDs com emissão no infravermelho próximo (NIR) conjugados ao fator de crescimento epidermal (EGF) para marcação do receptor do fator de crescimento epidermal (EGRF) em tumores de ratos xenográficos. Os autores foram capazes de distinguir três fases da nanosonda: dentro do influxo do tumor cerca de 3 minutos após a injeção, eliminação dentro de 60 minutos e o aumento da acumulação em cerca de 1-6 horas. Não só o tráfico de células para a corrente sanguínea, mas também a interação com as membranas são fatores significativos para o entendimento do processo de metástase (Diagaradjane *et al.*, 2008).

Bhang *et al.* (2009) utilizando QDs conjugados ao ácido hialurônico (AH) conseguiu identificar a presença das nanopartículas em vasos linfáticos, logo após a injeção, por imagens de fluorescência *in vivo*, como pode ser observado na Figura 14. Além disso, esses mesmos autores apresentam uma série de confirmação da localização dos QDs conjugados por testes histológicos. De acordo com os resultados, QDs-AH apresentam endocitose mediada por essa molécula. Além disso, os autores observaram um aumento do tempo de retenção dos QDs nos vasos linfáticos, e o relacionaram ao aumento do tamanho do complexo, ou seja QDs-AH, quando comparados aos QDs sozinhos. Por fim, Bang et al. (2009) consideram esse modelo em pequenos animais (ratos) e o uso de QDs-AH, como um grande avanço para estudos *in vivo* ao longo do tempo.

Figura 14 – Imagem de orelhas de ratos sob luz UV após injeção subcutânea de QDs-HA em dois locais distintos, que estão indicados pelos (asteriscos) na figura. Após 30 min da administração foi possível observar a presença de QDs-HA dentro de vasos linfáticos indicados pelas (setas em amarelo).

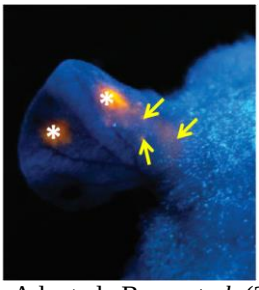

Fonte: Adaptada Bang *et al.* (2009).

Em geral, para uma melhor compreensão das doenças e uma visão mais abrangente sobre as mesmas, se faz necessário o uso de sondas auxiliares versáteis que preferencialmente possam ser aplicadas em mais de uma modalidade de imagem. Isso é interessante, pois as diferentes técnicas de imagens podem dar informações complementares sobre os processos biológicos. Por exemplo, a microscopia por fluorescência fornece imagens com especificidade química e alta resolução. Já a ressonância magnética fornece imagens de quaisquer regiões do organismo vivo, até mesmo das regiões mais profundas com bom contraste. Além disso, a IRM não é invasiva e não é prejudicial aos sistemas biológicos, apesar de propiciar imagens com menor resolução e não fornecer especificidade química, quando comparada às microscopias. Por isso, o desenvolvimento de sondas multimodais pode possibilitar e auxiliar a aquisição de imagens que formem um conjunto mais completo de informações biológicas contendo especificidade, ótima localização espacial e temporal, detalhes morfológicos e resolução ao nível celular e molecular (Wegner e Hildebrandt, 2015). Dentro desse contexto a preparação de sondas bimodais (magnéticas e fluorescentes) baseadas em QDs tem sido bastante discutida e vários estudos têm sido realizados, a fim de se obter nanopartículas multifuncionais estáveis e versáteis para marcação de sistemas biológicos (Jin e Hildebrandt, 2012; Wegner e Hildebrandt, 2015).

3.3 IMAGEM POR RESSONÂNCIA MAGNÉTICA (IRM)

Imagem por ressonância magnética (IRM) é uma das mais importantes e poderosas técnicas de diagnóstico desenvolvidas. Esta técnica é baseada nos princípios

da ressonância magnética nuclear (RMN) sendo, portanto, uma técnica não invasiva e que produz imagens com bastante detalhes morfológicos. A IRM apresenta diversas vantagens, quando comparada a outras técnicas de diagnóstico, principalmente às baseadas em raios-X, raios gama e ultrassom. Por exemplo, a IRM não utiliza radiação ionizante, sendo esta uma de suas mais importantes vantagens, além de propiciar imagens com melhor resolução em comparação com as técnicas mencionadas acima (*ca*. 0,5 mm), e ser capaz de diferenciar tecidos normais e patológicos (Pereira, G. e Geraldes, C., 2007; Merbach *et al.*, 2013).

Desde 1946 a RMN é uma técnica bastante utilizada por cientistas para obter informações químicas e físicas de moléculas. No entanto, só em 1971 que essa técnica foi empregada por Raymond Vahan Damadian para distinguir tecidos normais e tumorais (Damadian, 1971; Pereira, G. e Geraldes, C., 2007), uma vez que os tempos de relaxação dos spins nucleares foram distintos nesses dois tipos de tecidos possibilitando a sua diferenciação através do contraste. Em 1973, Paul Lauterbur e Mansfield foram os primeiros a demonstrarem uma imagem por ressonância magnética. Essas imagens são obtidas a partir da resolução espacial dos sinais RMN dos prótons (^{1}H) das moléculas de água existentes nos tecidos. A escolha do monitoramento dos prótons da água é devido à abundância desse elemento no nosso corpo, cerca de 70% do peso corporal de um adulto jovem é composto por água (Merbach e Tóth, 2001; Pereira, G. e Geraldes, C., 2007).

Os tempos de relaxação de spin nuclear refletem a mobilidade local das moléculas de água presentes nos tecidos e são afetados pela vizinhança permitindo assim visualizar e distinguir as variadas estruturas presentes nos organismos vivos (Merbach *et al.*, 2013). Em tecidos anormais, os quais apresentam alterações morfológicas e/ou metabólicas (Damadian, 1971; Lauterbur, 1973; Buxton, 2009), os valores dos tempos de relaxação magnética nuclear (T_1 e T_2) mudam e, consequentemente alteram a imagem obtida. A sensibilidade dos prótons ^{1}H ao campo magnético é que possibilita a detecção dessas alterações em tecidos anormais.

No processo de relaxação magnética, quando os prótons dos átomos de hidrogênio (^{1}H) estão na presença de um campo magnético externo (B_0) ocorre um alinhamento dos spins, gerando uma magnetização resultante (M_0), a qual é paralela e proporcional ao B_0 (Figura 15). Em equilíbrio $M_0 = M_z$, onde z é o eixo longitudinal. Para poder medir a M_0 é necessário aplicar um pulso oscilante de radiofrequência na frequência de Larmor (ou frequência de precessão) dos prótons de ^{1}H com a finalidade

de deslocar M_0 aos planos transversais (xy). Posteriormente, os prótons liberam a energia absorvida (na região de radiofrequência) retornando ao estado de equilíbrio, sendo este processo conhecido como relaxação (Pereira e Geraldes, 2007; Hage e Iwasaki, 2009; Doan *et al.*, 2013).

O processo de relaxação é modulado por duas constantes exponenciais de tempo, T_1 e T_2, os quais dependem das propriedades físicas e químicas dos tecidos. Como pode ser observado na Figura 15, T_1 reflete o retorno do equilíbrio no eixo z (longitudinal), ou seja, é o tempo referente a recuperação da magnetização M_0 em z. Enquanto, T_2 reflete o desaparecimento do sinal no plano xy (transversal) (Doan *et al.*, 2013). Na prática, isto resulta nas diferenças de imagens geradas pelas diferenças químicas e morfológicas do ambiente (Landini *et al.*, 2005; Pereira e Geraldes, 2007; Lam *et al.*, 2013).

Figura 15 - Representação esquemática dos tempos e processos de relaxação em T_1 e T_2.

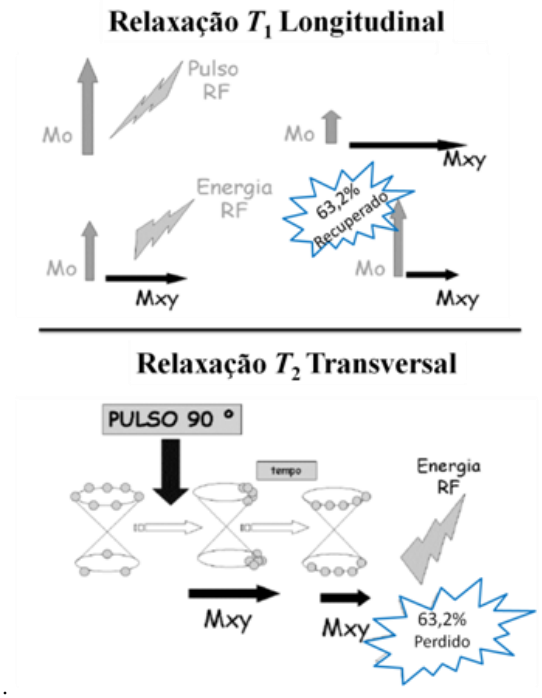

Fonte: Adaptada de Hage e Iwasaki (2009) e Doan *et al.* (2013).

Para melhorar a qualidade da geração de imagens podem ser administrados agentes de contrastes (ACs) em procedimentos clínicos. Estes ACs para IRM devem conter substâncias paramagnéticas ou superparamagnéticas. A maioria desses ACs aprovados para uso clínico pela FDA são baseados em quelatos paramagnéticos contendo íons lantanídeos, tais como o Gadolínio (Gd^{3+}), além destes, o uso de

partículas de óxido de ferro também é aprovado (Edelman e Warach, 1993). Entretanto, o melhoramento da imagem só é alcançado quando um dos tecidos tem alta afinidade pelos ACs ou é mais vascularizado que os tecidos próximos. Os tumores são metabolicamente diferentes e apresentam consequentemente uma maior captação dos ACs, resultando em um aumento do contraste na imagem.

A eficiência dos ACs é medida em termos de relaxividade ($r_{i,}$ em $s^{-1}.mM^{-1}$, i = 1,2), a qual indica a habilidade do AC em diminuir os tempos de relaxação dos prótons de hidrogênio na água por unidade de concentração (mM) do íon ou elemento paramagnético. Altos valores de r_1 e r_2 correspondem a menores valores de T_1 e T_2, respectivamente. As relaxividades longitudinal e transversal (r_1 e $r_{2,}$ respectivamente), são geralmente diferentes, dependem do B_0 e podem ser definidas como o aumento provocado nas taxas de relaxação dos prótons da água por 1 $mmol.L^{-1}$ de íons, ou elementos, para- ou superparamagnéticos. Geralmente, a água apresenta tempos de relaxação longitudinal (T_1) por volta dos 3000 ms (milissegundos) e seu tempo de relaxação transversal (T_2) é de aproximadamente 2500 ms. Enquanto materiais que apresentam contraste em T_1 geram imagens com contraste hiperintenso (branco – contraste positivo – Figura 16B), materiais que apresentam contraste em T_2 apresentam contraste hipointenso (preto – contraste negativo – Figura 16D) (Koole *et al.*, 2008). ACs contendo íons paramagnéticos (Gd^{3+}; Mn^{2+}) apresentam comumente contraste em $T_{1,}$ enquanto partículas de óxido de ferro apresentam contraste em T_2 (Jing *et al.*, 2014). Entretanto, como T_1 e T_2 não são processos independentes nenhum AC apresenta contraste exclusivamente positivo ou negativo (Koole *et al.*, 2008). Nas Figuras 16A e 16C podem ser observadas IRM sem a administração do AC, sendo difícil visualizar a delimitação do tumor.

Figura 16 – IRM antes e após a aplicação de agentes de contraste com ponderação em T1 e em T2. Em (A) antes da aplicação do agente de contraste e, em (B) após aplicação do agente de contraste atuante em T_1, em (C) controle e em (D) após aplicação de um agente de contraste atuante em T_2. IRM antes e após a aplicação de agentes de contraste em T_1 e em T_2**.**

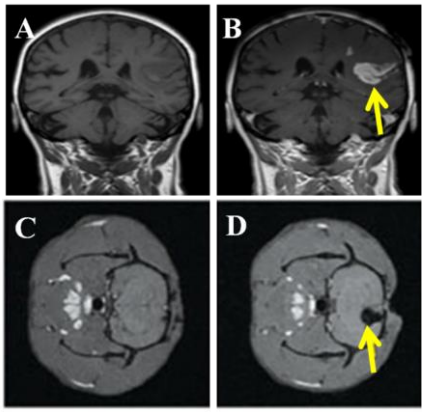

Fonte: Adaptada de Mamani *et al.*(2012).

No caso dos ACs serem baseados em quelatos, o contraste alcançado ainda é limitado porque requer uma alta concentração de moléculas de quelatos contendo íons paramagnéticos dentro ou na superfície das células. Entretanto, considerando a estrutura molecular dos quelatos, uma alta concentração no local desejado é difícil de ser obtida. Recentemente, para vencer essa limitação pesquisadores têm adotado o uso de nanosistemas baseados em ACs, os quais são capazes de aumentar a concentração local de íons paramagnéticos (Geraldes e Laurent, 2009; Na *et al.*, 2009). Vários nanossistemas têm sido empregados no desenvolvimento agentes de contraste, tais como: nanotubos de carbono (Sitharaman *et al.*, 2005; Na *et al.*, 2009), lipossomas (Mulas *et al.*, 2014; Zhang *et al.*, 2014), nanopartículas poliméricas (Turner *et al.*, 2005; Mouffouk *et al.*, 2015), nanopartículas de ouro (Zeng *et al.*, 2014). Portanto, observa-se que de forma geral os sistemas nanoparticulados podem ser ferramentas interessantes para o desenvolvimento de agentes de contraste específicos para IRM (Gossuin *et al.*, 2009) e é também dentro desse contexto que os QDs vêm sendo explorados.

3.4 SONDAS BIMODAIS BASEADAS EM *QUANTUM DOTS*

Na tentativa de vencer as limitações impostas pelas técnicas de aquisição de imagens através de fluorescência e pela IRM, o desenvolvimento de nanossondas

bimodais baseadas em QDs para imagens ópticas e por ressonância magnética é ainda recente. Por isso, os estudos têm se baseado no *design* e melhorias na preparação de materiais que apresentem ambas as propriedades, fluorescente e magnética. Sendo assim, a maioria destes trabalhos, tem como meta a obtenção de nanossondas bimodais com maior estabilidade físico-química, alta intensidade de fluorescência, resposta magnética/relaxométrica eficiente, e elevada especificidade bioquímica (López-Cebral *et al.*, 2014), originando sondas multimodais. Na tentativa de obter novas sondas bimodais com elevadas propriedades magnético-fluorescentes para aplicações biológicas, este trabalho destaca a associação dos QDs às nanopartículas de óxido de ferro.

3.4.1 Quantum dots e nanopartículas de óxido de ferro

QDs associados às nanopartículas magnéticas (MNPs) têm despertado grande interesse como nova classe de materiais, pois esta associação pode fornecer uma combinação das propriedades ópticas dos QDs com as propriedades magnéticas das nanopartículas magnéticas em um mesmo material, tornando-os capaz de propiciar não só imagens ópticas e magnéticas simultaneamente, como também separação de células e terapia por hipertermia (Yang *et al.*, 2008; Liu *et al.*, 2011). Há poucos exemplos de imagens multimodais contendo nanopartículas magnéticas, sendo as nanopartículas de óxido de ferro superparamagnéticas as mais usadas, uma vez que são aprovadas pela FDA como agentes de contraste para IRM (Santhosh e Ulrih, 2013).

O material macroscópico (*bulk*) de óxido de ferro é classificado como um material ferromagnético, porque apresenta magnetização permanente, mesmo na ausência do campo magnético externo (Gupta e Gupta, 2005; Koktysh *et al.*, 2011). Ao diminuir o tamanho das partículas da escala macroscópica para a nanoescala suas propriedades físicas e químicas são alteradas. Quando as partículas de óxido de ferro são reduzidas a poucos nanômetros (*ca.* 1 – 100 nm), suas propriedades magnéticas são alteradas, devido ao efeito do confinamento quântico e ao aumento da área superficial, tornando-as superparamagnética, sendo chamadas de nanopartículas de óxido de ferro superparamagnéticas (SPIONs) (Liu *et al.*, 2008; Weinstein *et al.*, 2010; Koktysh *et al.*, 2011). As SPIONs possuem um estado de magnetização uniforme, o que significa que após a remoção do campo magnético externo elas perdem a magnetização, fazendo com

que se tornem novamente dispersas no meio, diminuindo, consequentemente, sua tendência em aglomerar-se (Yang *et al.*, 2008). As SPIONs possuem um núcleo de óxido de ferro, o qual é responsável pela sua propriedade magnética. Os núcleos mais comuns de óxido de ferro são a magnetita (Fe_3O_4) e sua forma oxidada, a maguemita (γ-Fe_2O_3). A magnetita é a mais utilizada porque tem uma resposta ferromagnética melhor, podendo apresentar uma magnetização de saturação (*Ms*) de aproximadamente 92-100 $emu.g^{-1}$ a 25 ºC ou 300 K, enquanto a maguemita apresenta valores de *Ms* menores em torno de 60 – 80 $emu.g^{-1}$ (Gupta e Gupta, 2005). O núcleo é geralmente coberto com um polímero biocompatível que protege o mesmo do meio e permite que a nanopartícula esteja funcionalizada possibilitando a ligação das SPIONs a outras partículas ou até mesmo moléculas (Teja e Koh, 2009).

Há várias rotas sintéticas para produção das SPIONs, podendo ser: co-precipitação de sais de ferro, microemulsão, processos hidrotermais, deposição via eletroquímica, processos sol-gel, dentre outros. A metodologia mais utilizada é a co-precipitação de sais de ferro, isto porque é um método simples, eficiente e de baixo custo. Nessa metodologia, sais de ferro em ambos os estados de oxidação (íons férrico e ferroso em uma proporção molar de 2:1, respectivamente) são adicionados a uma solução alcalina, em atmosfera inerte, e as SPIONs são então obtidas pela precipitação (Liu *et al.*, 2008; Teja e Koh, 2009; Mahmoudi *et al.*, 2011).

Atualmente, MNPs têm atraído muito a atenção dos pesquisadores devido a sua versatilidade de aplicações, que compreendem desde a aplicação em Ciências dos Materiais até as Ciências da Vida. Essas nanopartículas têm sido utilizadas em Ciências da Vida devido a sua grande versatilidade para aplicações *in vivo* como, por exemplo sendo agentes de contraste em IRM, para terapias via hipertermia e até mesmo carreadores de drogas. Entretanto, para serem aplicados, várias caracterizações devem ser realizadas, tais como medidas de magnetização de saturação (*Ms*), a qual indica a magnitude de magnetização do material quando submetido a um campo magnético externo. Os valores de *Ms* indicam quão grande é a magnetização do material, significando que todos os domínios (núcleos) respondem ao campo, ou seja, estão alinhados ao campo magnético externo (Ito *et al.*, 2005; Jurgons *et al.*, 2006; Weissleder, 2006; Gupta *et al.*, 2007; Frimpong e Hilt, 2010).

A eficiência dos ACs é geralmente medida em termos de relaxividade, como discutido anteriormente na seção de IRM. Muitos pesquisadores, no entanto, só apresentam valores de *Ms* como método de caracterização de SPIONs. Embora não haja

uma correlação entre essas medidas, o que se sabe é que quanto maior a *Ms* mais haverá um aumento do campo magnético local, afetando os prótons da água que estão a sua volta melhorando o sinal das imagens por ressonância magnética. Dessa forma, os mesmos fatores que afetam a magnetização também afetarão na redução de T_2. Normalmente é necessário revestir as SPIONs com um polímero para torná-las mais biocompatíveis, e até mesmo possibilitar a associação com moléculas ou outras nanopartículas. Entretanto, a *Ms* está também relacionada com a espessura da camada de revestimento da superfície do nanomaterial, uma vez que as propriedades magnéticas podem ser atenuadas na superfície. Isto acontece, pois, quanto mais próximos as moléculas de água do meio externo (bulk) estiverem do núcleo da nanopartícula, melhor é a capacidade em reduzir T_2. Em outras palavras, quanto menor a espessura da camada de revestimento da SPION maior a *Ms* e consequentemente maior a capacidade em reduzir T_2. Dessa forma, o revestimento da superfície das nanopartículas de óxido de ferro podem também afetar a eficiência na geração de imagens e tem sido observado que o contraste em T_2 diminui com o aumento da largura da camada de revestimento, para as nanopartículas de óxido de ferro. Quando os trabalhos fazem medidas de relaxividade, é necessário saber as quantidades e quais os constituintes presentes na suspensão, sendo, portanto, realizadas análises de ICP-OES (espectrometria de emissão ótica com plasma acoplado indutivamente) ou de FAAS (espectrometria de absorção atômica de chama) (Jaganathan e Ivanisevic, 2011; Jańczewski *et al.*, 2011; Merbach *et al.*, 2013).

3.4.1.1 Técnicas de conjugação e aplicações de QDs-SPIONs

Já foi demonstrado anteriormente a associação de QDs a SPIONs com o objetivo de gerar nanopartículas bimodais (Wang *et al.*, 2004; Wang *et al.*, 2005; Chen *et al.*, 2014). Entretanto ainda há vários desafios a serem vencidos para se obter nanopartículas com alta eficiência, estabilidade e capazes de gerar imagens duais e até realizar terapia. Na tentativa de vencer essas dificuldades na produção dessas novas nanossondas, usando QDs e SPIONs, muitos pesquisadores tem se preocupado com o melhoramento da ligação entre estas nanopartículas. Dessa forma, os estudos incluem metodologias para inserir QDs e SPIONs em esferas de sílica (Lu *et al.*, 2007; Pinho *et al.*, 2010), micelas (Insin *et al.*, 2008), nanoesferas poliméricas (Ruan *et al.*, 2012), interações

eletrostáticas (Thakur *et al.*, 2009; Kale *et al.*, 2011; Santhosh e Ulrih, 2013), por ligação covalente, mediada por agentes de acoplamento, como mostra a Figura 17 (Ruan *et al.*, 2010; Song *et al.*, 2011). A partir de então, a conjugação covalente será mais discutida, pois foi a estratégia utilizada nesta tese, para obtenção de nanopartículas bimodais.

Figura 17 – Representação da obtenção de sistemas bimodais a partir da conjugação covalente entre nanopartículas magnéticas representada pelas SPIONs e QDs.

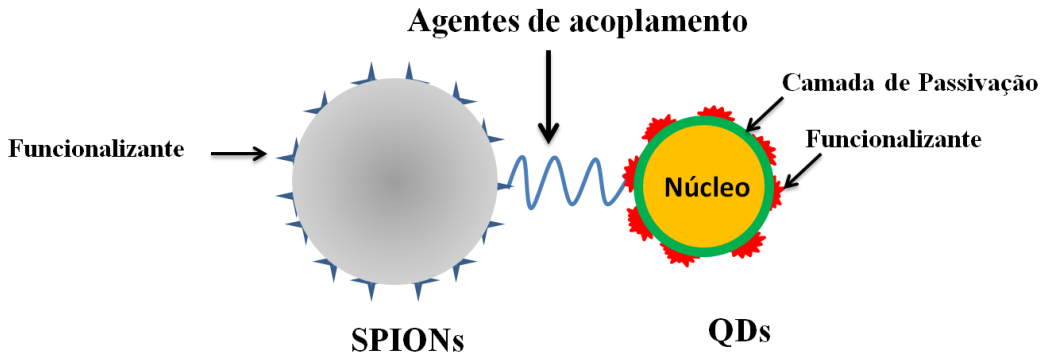

.

Fonte: O autor.

O primeiro trabalho que descreveu a formação de sistemas bimodais utilizando conjugação covalente foi reportado por Wang em (2004). Em seu trabalho, Wang utilizou QDs de Seleneto de Cádmio/Sulfeto de Zinco (CdSe/ZnS) e maguemita (γ-Fe_2O_3) como núcleo das SPIONs. A partir de então, vários trabalhos têm sido relatados para produção de nanopartículas bimodais, na tentativa de diminuir ainda mais os tempos de relaxação magnética possibilitando imagens com um maior contraste. Entretanto, ainda são poucos os trabalhos que aplicaram essas nanoparticulas bimodais em sistemas biológicas.

Sun e colaboradores (2009) utilizaram o mesmo método de conjugação para associar QDs de Telureto de Cádmio (CdTe) a magnetita (Fe_3O_4). Neste trabalho os QDs foram funcionalizados/estabilizados com ácido tioglicólico (TGA) e foram ligados a SPIONs revestidas com sílica (SPIONs@SiO_2). O sistema bimodal resultante apresentou emissão similar aos QDs originais e uma medida de *Ms* = 2,26 meu.g^{-1}, a qual foi menor que a *Ms* das nanopartículas de Fe_3O_4 originais (*Ms* = 49,97 meu.g^{-1}). O tamanho final foi de aproximadamente 30 nm. Em seguida o sistema bimodal (Fe_3O_4@SiO_2-CdTe) foi conjugado, utilizando *N*-hidroxisuccinimida (NHS), ao anticorpo anti-CEACAM8, o qual reconhece receptores de antígenos carcinogênico-

embrionário relacionado a adesão celular da molécula 8 do complexo de histocompatibilidade principal. Este receptor, o CEACAM8, também é conhecido como CD67. Utilizando essas nanossondas bimodais conjugadas ao anti-CEACAM8 foi possível estudar o receptor CEACAM8 em células de adenocarcinoma cervical humano (células HeLa).

Kale e colaboradores (2011) também preparam nanopartículas bimodais utilizando CdTe, só que funcionalizados com ácido mercaptopropiônico (AMP) e nanopartículas magnéticas (Fe_3O_4) utilizando a dodecil amina (DDA) como um agente de acoplamento. Para isto, os QDs foram preparados na presença da magnetita funcionalizadas com DDA. O sistema bimodal apresentou um rendimento quântico aproximado de 18% em água. CdTe-Fe_3O_4 apresentaram uma *Ms* = 44 $emu.g^{-1}$, enquanto que a magnetita apresentava antes da conjugação uma *Ms* = 62 $emu.g^{-1}$. As nanopartículas bimodais (CdTe-Fe_3O_4) foram posteriormente conjugadas com anticorpo anti-EGFR (anti – receptor do fator de crescimento epidermal) e o sistema multimodal foi então utilizado para separação específica e para obtenção de imagem de linfócitos T leucêmicos (Molt-4), utilizando uma suspensão de células mistas composta por Molt-4 e células leucemia mielogênica (K562). Esta separação específica foi possível uma vez que o receptor do fator de crescimento epidermal é altamente expresso nas células Molt-4, enquanto que as células de origem mielóide não expressam esse receptor. Os resultados mostraram que estas nanopartículas bimodais mostraram um excelente potencial para separação magnética e aquisição de imagens fluorescentes para um tipo específico de células, as Molt-4.

Koktysh e colaboradores (2011) prepararam nanopartículas bimodais utilizando QDs funcionalizados com glutationa (GSH) e Fe_3O_4 funcionalizadas com Dextran, o qual é biocompatível e comumente utilizado para aumentar a retenção de ACs no sangue. Os pesquisadores utilizaram dois tipos de QDs, o CdTe/CdS com emissão no visível (600 nm) e CdHgTe/CdS com emissão no infravermelho próximo (NIR – 800 nm). De acordo com as imagens de microscopia eletrônica de transmissão, as nanopartículas bimodais apresentaram tamanho aproximado de 7,8 nm. Além disso, análises da composição do material por plasma acoplado indutivamente (ICP) confirmaram a presença de Fe > 80% e Cd > 13% e a caracterização óptica não indicou alterações significativas no perfil espectroscópico. Os autores indicaram não haver toxicidade das partículas em ratos. As imagens *ex-vivo* mostraram que as partículas se acumularam no pulmão e subsequentemente nos linfonodos. No fim, os autores

afirmaram que essas nanopartículas bimodais são um sistema combinado que pode ser usado simultaneamente para imagens por ressonância magnética e ópticas.

Vários trabalhos relatam uma diminuição da *Ms* após a conjugação dos QDs às nanopartículas bimodais, como detalhado na Tabela 1, na qual podemos observar as estratégias de conjugação, o tamanho da nanossonda bimodais e as medidas de *Ms*. Vale a pena ressaltar que a maioria destes trabalhos, encontrados na Tabela 1, não aplicaram esses sistemas em Ciências da Vida, entretanto apresentaram esses sistemas como sondas potenciais para serem aplicados em nessa área. Por outro lado, alguns trabalhos que aplicaram biologicamente os sistemas bimodais não apresentaram valores de *Ms*.

Tabela 1 – Valores de *Ms* das MNPs antes e após a conjugação covalente com QDs.

Estratégia de síntese	**Composição das nanoparticulas bimodais**	**Tamanho (nm)**	***Ms* das MNPs (emu.g^{-1}) [a]**	***Ms* da nanopartícula bimodal (emu.g^{-1})[a]**	**Citação**
Ligação covalente	Fe_3O_4@SiO_2-CdSe/ZnS	25	67.7	2.38	(Zhang *et al.*, 2008)
	Fe_3O_4@SiO_2-CdTe	30	40.97	2.26	(Sun *et al.*, 2009)
	SPION-CdS	100	55	9.5	(Thakur *et al.*, 2009)
	Fe_3O_4- CdTe/CdS	11	62	44	(Kale *et al.*, 2011)

3.5 TRANSFERRINA

Desde que a transferrina foi descoberta, cerca de 50 anos atrás, várias pesquisas têm sido realizadas para entender como essa biomolécula medeia a internalização do ferro nas células de vertebrados (Li e Qian, 2002; Li *et al.*, 2002). A transferrina é uma glicoproteína do tipo β-globina, da família das proteínas ligantes de ferro, possui cerca de 600-700 aminoácidos e tem peso molecular de 80 KDa, aproximadamente (Chung, 1984; Li e Qian, 2002). Ela está presente no plasma sanguíneo, controlando os níveis de ferro nos sistemas biológicos, pois se ligam com alta afinidade, mas reversivelmente a esses íons (Fe^{3+}). Entretanto, quando a transferrina não está ligada a íons Fe^{3+} é conhecida como Apotransferrina (Apo-Tf), e não tem afinidade pelo seu receptor, por

outro lado quando está ligada a íons Fe^{3+} a transferrina recebe o nome de holo transferrina (Holo-Tf) e possui alta afinidade pelo seu receptor.

O receptor de transferrina (TfR) também conhecido como CD71, o qual promove a entrada intracelular da Holo-Tf (Daniels *et al.*, 2012), tem sido encontrado em vários tipos celulares, como em hemácias, hepatócitos, monócitos, células cerebrais, em alguns insetos e bactérias (Schryvers *et al.*, 1998). O receptor de transferrina tem sido identificado através de estudos utilizando anticorpos monoclonais e já foi bastante caracterizado a partir de inúmeras técnicas bioquímicas e de biologia molecular. O primeiro receptor a ser identificado (TfR1) está relacionado com a captação intracelular de ferro e com a regulação do crescimento celular, sendo sua expressão acentuada em células com alta taxa de proliferação. Já o segundo receptor identificado (TfR2) é expresso principalmente em tecidos responsáveis pelo metabolismo do ferro, tal como no fígado e intestino (Tortorella e Karagiannis, 2014).

Como mencionado no parágrafo anterior, o TfR1 tem sua expressão acentuada em células com alta taxa proliferativa (Tortorella e Karagiannis, 2014). Dessa forma, células cancerígenas podem ter uma maior expressão desse receptor, atribuída aos altos níveis metabólicos e de crescimento celular (Huebers e Finch, 1987). Parece haver também uma correlação entre os níveis de expressão do TfR e o nível de malignidade do tumor. Isto já foi determinado em vários tipos de cânceres, tais como mama, linfoma Hodking e leucemia linfocítica crônica (Singh *et al.*, 2011). Esta alta expressão em células cancerígenas faz com que esse receptor seja bastante estudado (Daniels *et al.*, 2012).

Este receptor é sintetizado no retículo endoplasmático (Li e Qian, 2002; Qian *et al.*, 2002) e expresso na membrana celular. Após a ligação da Holo-Tf ao TfR este é endocitado. O principal mecanismo de captação do ferro é feito por endocitose mediada via clatrina (proteína de membrana responsável pela formação de vesículas membranosas em células de vertebrados) (Tortorella e Karagiannis, 2014). Após a endocitose, e em pH ácido, o Fe^{3+} é reduzido a Fe^{2+} e é, portanto, liberado pela Holo-Tf e externalizado do endossoma pelo transportador de metais bivalentes (DMT1). Estudos realizados (Mayle *et al.*, 2012; Tortorella e Karagiannis, 2014) identificaram que após a endocitose o TfR pode ter duas vias distintas. A primeira delas envolve a reexpressão (*recycling*) deste receptor na membrana das células. A outra via afirma que o receptor pode ser degradado por complexos lisossomais (Tortorella e Karagiannis, 2014). Entretanto a Apo-Tf retorna a membrana celular externa, e ao encontrar íons Fe^{3+}, em

pH próximo do neutro, ligam-se a estes se iniciando um novo ciclo (Qian *et al.*, 2002), como pode ser observado na Figura 18.

Com o avanço da nanotecnologia, o TfR tem sido bastante utilizado como potencial via para melhoramento da terapia e dos procedimentos diagnósticos relacionados ao câncer, pois este receptor pode ser uma via de entrada de fármacos dentro das células cancerígenas. Para a entrega dos fármacos, os sistemas mais empregados são lipossomas (Li *et al.*, 2002; Zhai *et al.*, 2010), nanopartículas metálicas (Wiley *et al.*, 2013; Dixit *et al.*, 2015) e nanopartículas magnéticas (Ding e Guo, 2013). Estes sistemas têm sido funcionalizados com transferrina para ligar-se especificamente ao seu receptor e melhorar técnicas de diagnóstico, bem como, a eficiência dos quimioterápicos, uma vez que as células cancerígenas podem ter a expressão desse receptor aumentada na membrana. Portanto, estudos relacionados ao TfR podem fornecer um melhor entendimento da biologia celular do câncer e também ajudar a melhorar o tratamento dessa doença.

Figura 18 – Captação do ferro pelas células de vertebrados.

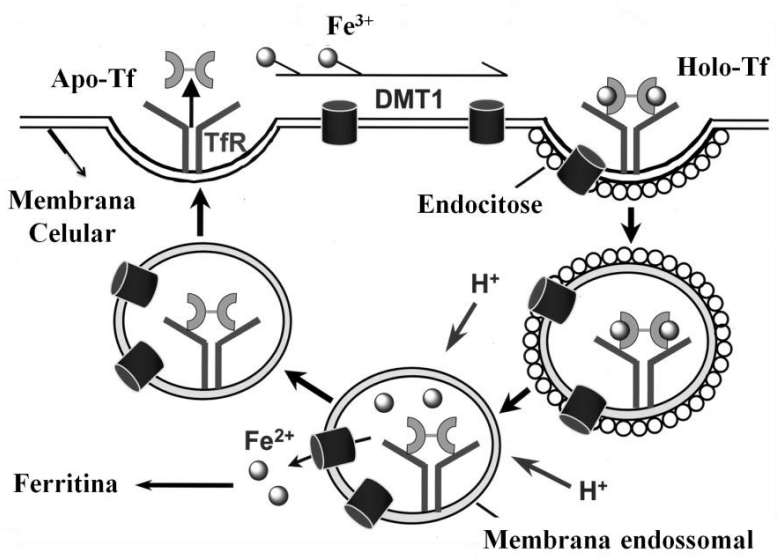

Fonte: Adaptada de Qian *et al.*, (2002).

A maioria dos trabalhos que envolvem o estudo desse receptor utilizam métodos de biologia molecular para identificá-lo e investigar a sua expressão nos mais diversos tipos de células. Entretanto, através dessa técnica não é possível estudar a internalização desse receptor, nem o tráfego no interior das células, nem a sua quantificação na membrana (Ponka e Lok, 1999; Yoon *et al.*, 2009). Isso é possível através de técnicas baseadas em fluorescência, pois possibilitam a identificação, quantificação e a

investigação da distribuição intracelular do TfR com alta especificidade e sensibilidade complementando as análises de biologia molecular (Jing *et al.*, 2014).

Dentro desse contexto, a transferrina pode ser conjugada aos QDs para quantificar e estudar o tráfego desse receptor em diversos tipos de células cancerígenas. Além disso, esta proteína pode ser utilizada como molécula direcionadora no desenvolvimento de agentes de contraste multimodais. Dessa forma, esses estudos podem servir como guia para fins diagnósticos e também terapêuticos, que utilizem o TfR como porta para a entrega intracelular de fármacos (Cabral Filho *et al.*, 2016).

REFERÊNCIAS DA REVISÃO BIBLIOGRÁFICA

AHMED, S. R. et al. Quantum dots incorporated magnetic nanoparticles for imaging colon carcinoma cells. Journal of nanobiotechnology, v. 11, n. 1, p. 28, 2013. ISSN 1477-3155.

ÅKERMAN, M. E. et al. Nanocrystal targeting in vivo. Proceedings of the National Academy of Sciences, v. 99, n. 20, p. 12617-12621, 2002. ISSN 0027-8424.

ALIVISATOS, P. The use of nanocrystals in biological detection. Nat Biotech, v. 22, n. 1, p. 47-52, 2004. ISSN 1087-0156. Disponível em: < http://dx.doi.org/10.1038/nbt927 >.

ANDRADE, C. G. et al. Evaluation of glycophenotype in breast cancer by quantum dot-lectin histochemistry. International journal of nanomedicine, v. 8, p. 4623, 2013.

BHANG, S. H. et al. Hyaluronic Acid−Quantum Dot Conjugates for In Vivo Lymphatic Vessel Imaging. Acs Nano, v. 3, n. 6, p. 1389-1398, 2009/06/23 2009. ISSN 1936-0851. Disponível em: < http://dx.doi.org/10.1021/nn900138d >.

BRUCHEZ, M. et al. Semiconductor Nanocrystals as Fluorescent Biological Labels. Science, v. 281, n. 5385, p. 2013-2016, September 25, 1998 1998. Disponível em: < http://www.sciencemag.org/content/281/5385/2013.abstract >.

BRUS, L. E. Electron–electron and electron-hole interactions in small semiconductor crystallites: The size dependence of the lowest excited electronic state. The Journal of chemical physics, v. 80, n. 9, p. 4403-4409, 1984. ISSN 0021-9606.

BUXTON, R. B. Introduction to functional magnetic resonance imaging: principles and techniques. Cambridge university press, 2009. ISBN 1139481304.

CABRAL FILHO, P. E. et al. CdTe quantum dots as fluorescent probes to study transferrin receptors in glioblastoma cells. Biochimica et Biophysica Acta (BBA) - General Subjects, v. 1860, n. 1, Part A, p. 28-35, 2016. ISSN 0304-4165. Disponível em: < http://www.sciencedirect.com/science/article/pii/S0304416515002639 >.

CARAVAN, P. et al. Gadolinium (III) chelates as MRI contrast agents: structure, dynamics, and applications. Chemical Reviews, v. 99, n. 9, p. 2293-2352, 1999. ISSN 0009-2665.

CESAR, C. L. et al. Fluorescencia. Rio de Janeiro: Sociedade Brasileira de Microscopia e Microanálises, 2010. ISBN 978-85-98460-08-6.

CHAN, W. C. W.; NIE, S. Quantum Dot Bioconjugates for Ultrasensitive Nonisotopic Detection. Science, v. 281, n. 5385, p. 2016-2018, September 25, 1998 1998. Disponível em: < http://www.sciencemag.org/content/281/5385/2016.abstract >.

CHANG, S. et al. The combined influence of surface modification, size distribution, and interaction time on the cytotoxicity of CdTe quantum dots in PANC-1 cells. Acta biochimica et biophysica Sinica, p. gmr126, 2012. ISSN 1672-9145.

CHAVES, C. Síntese e caracterização de nanopartículas de sulfeto de cádmio: aplicação biomédicas. 2006. 111 f. 2006. Dissertação de Mestrado em Ciências de Materiais

CHAVES, C. et al. Application of core–shell PEGylated CdS/Cd (OH) 2 quantum dots as biolabels of Trypanosoma cruzi parasites. Applied Surface Science, v. 255, n. 3, p. 728-730, 2008. ISSN 0169-4332.

CHEN, K. et al. Dual-modality optical and positron emission tomography imaging of vascular endothelial growth factor receptor on tumor vasculature using quantum dots. European Journal of Nuclear Medicine and Molecular Imaging, v. 35, n. 12, p. 2235-2244, 2008/12/01 2008. ISSN 1619-7070. Disponível em: < http://dx.doi.org/10.1007/s00259-008-0860-8 >.

CHEN, O. et al. Magneto-fluorescent core-shell supernanoparticles. Nat Commun, v. 5, 2014. Disponível em: < http://dx.doi.org/10.1038/ncomms6093 >.

CHEN, Z. et al. Bio-distribution and metabolic paths of silica coated CdSeS quantum dots. Toxicology and applied pharmacology, v. 230, n. 3, p. 364-371, 2008. ISSN 0041-008X.

CHOI, H. S. et al. Design considerations for tumour-targeted nanoparticles. Nature nanotechnology, v. 5, n. 1, p. 42-47, 2010. ISSN 1748-3387.

CHOI, H. S. et al. Renal clearance of quantum dots. Nature biotechnology, v. 25, n. 10, p. 1165-1170, 2007. ISSN 1087-0156.

CHUNG, M. Structure and function of transferrin. Biochemical Education, v. 12, n. 4, p. 146-154, 1984. ISSN 1879-1468.

CLIFT, M. J. D.; STONE, V. Quantum Dots: An Insight and Perspective of Their Biological Interaction and How This Relates to Their Relevance for Clinical Use. Theranostics, Sydney, v. 2, n. 7, p. 668-680, 2012. ISSN 1838-7640. Disponível em: < http://www.ncbi.nlm.nih.gov/pmc/articles/PMC3418927/ >.

COX, J. A quantum paintbox. CHEMISTRY IN BRITAIN, v. 39, n. 9, p. 21-25, 2003. ISSN 0009-3106.

DAMADIAN, R. Tumor Detection by Nuclear Magnetic Resonance. Science, v. 171, n. 3976, p. 1151-1153, March 19, 1971 1971. Disponível em: < http://www.sciencemag.org/content/171/3976/1151.abstract >.

DANIELS, T. R. et al. Transferrin receptors and the targeted delivery of therapeutic agents against cancer. Biochimica et biophysica acta, v. 1820, n. 3, p. 291-317, 2012. ISSN 0006-3002. Disponível em: < http://www.ncbi.nlm.nih.gov/pmc/articles/PMC3500658/ >.

DE FARIAS, P. et al. Highly fluorescent semiconductor core–shell CdTe–CdS nanocrystals for monitoring living yeast cells activity. Applied Physics A, v. 89, n. 4, p. 957-961, 2007. ISSN 0947-8396.

DIAGARADJANE, P. et al. Imaging epidermal growth factor receptor expression in vivo: pharmacokinetic and biodistribution characterization of a bioconjugated quantum dot nanoprobe. Clinical Cancer Research, v. 14, n. 3, p. 731-741, 2008. ISSN 1078-0432.

DING, W.; GUO, L. Immobilized transferrin Fe(3)O(4)@SiO(2) nanoparticle with high doxorubicin loading for dual-targeted tumor drug delivery. International journal of nanomedicine, v. 8, p. 4631-4639, 2013. ISSN 1176-9114
1178-2013. Disponível em: < http://www.ncbi.nlm.nih.gov/pmc/articles/PMC3857267/ >.

DIXIT, S. et al. Transferrin receptor-targeted theranostic gold nanoparticles for photosensitizer delivery in brain tumors. Nanoscale, v. 7, n. 5, p. 1782-1790, 2015. ISSN 2040-3364. Disponível em: < http://dx.doi.org/10.1039/C4NR04853A >.

DOAN, B.-T.; MEME, S.; BELOEIL, J.-C. General Principles of MRI. The Chemistry of Contrast Agents in Medical Magnetic Resonance Imaging, Second Edition, editors André Merbach, Lothar Helm and Éva Tóth., p. 1-23, 2013. ISSN 1118503651.

DU, G. H. et al. Fe3O4/CdSe/ZnS magnetic fluorescent bifunctional nanocomposites. Nanotechnology, v. 17, n. 12, p. 2850, 2006. ISSN 0957-4484.

DUBERTRET, B. et al. In vivo imaging of quantum dots encapsulated in phospholipid micelles. Science, v. 298, n. 5599, p. 1759-1762, 2002. ISSN 0036-8075.

EDELMAN, R. R.; WARACH, S. Magnetic Resonance Imaging. New England Journal of Medicine, v. 328, n. 10, p. 708-716, 1993. Disponível em: < http://www.nejm.org/doi/full/10.1056/NEJM199303113281008 >.

ETGAR, L.; LIFSHITZ, E.; TANNENBAUM, R. Hierarchical conjugate structure of γ-Fe2O3 nanoparticles and PbSe quantum dots for biological applications. The Journal of Physical Chemistry C, v. 111, n. 17, p. 6238-6244, 2007. ISSN 1932-7447.

FANG, M. et al. Quantum dots-based in situ molecular imaging of dynamic changes of collagen IV during cancer invasion. Biomaterials, v. 34, n. 34, p. 8708-8717, 2013/11// 2013. ISSN 0142-9612. Disponível em: < http://europepmc.org/abstract/MED/23932291
http://dx.doi.org/10.1016/j.biomaterials.2013.07.069 >.

FIGUEIREDO, S. et al. Yeast cell wall particles: a promising class of nature-inspired microcarriers for multimodal imaging. Chemical Communications, v. 47, n. 38, p. 10635-10637, 2011.

FITZPATRICK, J. A. et al. Long-term persistence and spectral blue shifting of quantum dots in vivo. Nano Letters, v. 9, n. 7, p. 2736-2741, 2009. ISSN 1530-6984.

FONTES, A. et al. Quantum Dots in Biomedical Research. In: HUDAK, R. (Ed.). Biomedical Engineering - Technical Applications in Medicine: InTech, 2012. cap. 12, ISBN 978-953-51-0733-0.

FRIMPONG, R. A.; HILT, J. Z. Magnetic nanoparticles in biomedicine: synthesis, functionalization and applications. Nanomedicine, v. 5, n. 9, p. 1401-1414, 2010. ISSN 1743-5889.

GERALDES; LAURENT. Classification and basic properties of contrast agents for magnetic resonance imaging. Contrast Media & Molecular Imaging, v. 4, n. 1, p. 1-23, 2009. ISSN 1555-4317. Disponível em: < http://dx.doi.org/10.1002/cmmi.265 >.

GERALDES, C. F.; LAURENT, S. Classification and basic properties of contrast agents for magnetic resonance imaging. Contrast media & molecular imaging, v. 4, n. 1, p. 1-23, 2009. ISSN 1555-4317.

GESZKE, M. et al. Folic acid-conjugated core/shell ZnS: Mn/ZnS quantum dots as targeted probes for two photon fluorescence imaging of cancer cells. Acta biomaterialia, v. 7, n. 3, p. 1327-1338, 2011. ISSN 1742-7061.

GIEPMANS, B. N. G. et al. The Fluorescent Toolbox for Assessing Protein Location and Function. Science, v. 312, n. 5771, p. 217-224, April 14, 2006 2006. Disponível em: < http://www.sciencemag.org/content/312/5771/217.abstract >.

GOLDBERG, P.; DEAN, P. J. Luminescence of inorganic solids. Academic Press New York, 1966.

GONDA, K. et al. In Vivo Nano-imaging of Membrane Dynamics in Metastatic Tumor Cells Using Quantum Dots. The Journal of Biological Chemistry, 9650 Rockville Pike, Bethesda, MD 20814, U.S.A., v. 285, n. 4, p. 2750-2757, 2010. ISSN 0021-9258 1083-351X. Disponível em: < http://www.ncbi.nlm.nih.gov/pmc/articles/PMC2807330/ >.

GOSSUIN, Y. et al. Magnetic resonance relaxation properties of superparamagnetic particles. Wiley Interdiscip Rev Nanomed Nanobiotechnol, v. 1, n. 3, p. 299-310, 2009. ISSN 1939-0041. Disponível em: < http://dx.doi.org/10.1002/wnan.36 >.

GUAN, L.-Y. et al. Characterization of CdTe/CdSe quantum dots-transferrin fluorescent probes for cellular labeling. Analytica Chimica Acta, v. 741, n. 0, p. 86-92, 2012. ISSN 0003-2670. Disponível em: < http://www.sciencedirect.com/science/article/pii/S0003267012009634 >.

GUPTA, A. K.; GUPTA, M. Synthesis and surface engineering of iron oxide nanoparticles for biomedical applications. Biomaterials, v. 26, n. 18, p. 3995-4021, 6// 2005. ISSN 0142-9612. Disponível em: < http://www.sciencedirect.com/science/article/pii/S0142961204009317 >.

GUPTA, A. K. et al. Recent advances on surface engineering of magnetic iron oxide nanoparticles and their biomedical applications. Nanomedicine, v. 2, n. 1, p. 23-39,

2007/02/01 2007. ISSN 1743-5889. Disponível em: < http://dx.doi.org/10.2217/17435889.2.1.23 >. Acesso em: 2015/05/29.

HAGE, M. C. F. N. S.; IWASAKI, M. Imagem por ressonância magnética: princípios básicos. Ciência Rural, 2009. ISSN 0103-8478.

HERMANSON, G. T. Chapter 7 - Dendrimers and Dendrons. In: HERMANSON, G. T. (Ed.). Bioconjugate Techniques (Second Edition). New York: Academic Press, 2008. p.346-390. ISBN 978-0-12-370501-3.

HO, C.-C. et al. Quantum dot 705, a cadmium-based nanoparticle, induces persistent inflammation and granuloma formation in the mouse lung. Nanotoxicology, v. 7, n. 1, p. 105-115, 2013. ISSN 1743-5390.

HUANG, Y.-X. et al. Human red blood cell aging: correlative changes in surface charge and cell properties. Journal of Cellular and Molecular Medicine, Oxford, UK, v. 15, n. 12, p. 2634-2642, 2011. ISSN 1582-1838
1582-4934. Disponível em: < http://www.ncbi.nlm.nih.gov/pmc/articles/PMC4373432/ >.

HUEBERS, H. A.; FINCH, C. A. The physiology of transferrin and transferrin receptors. 1987. 520-582 Disponível em: < http://physrev.physiology.org/physrev/67/2/520.full.pdf >.

IDOWU, M.; LAMPRECHT, E.; NYOKONG, T. Interaction of water-soluble thiol capped CdTe quantum dots and bovine serum albumin. Journal of Photochemistry and Photobiology A: Chemistry, v. 198, n. 1, p. 7-12, 2008. ISSN 1010-6030.

INSIN, N. et al. Incorporation of iron oxide nanoparticles and quantum dots into silica microspheres. Acs Nano, v. 2, n. 2, p. 197-202, 2008. ISSN 1936-0851.

ITO, A. et al. Medical application of functionalized magnetic nanoparticles. Journal of bioscience and bioengineering, v. 100, n. 1, p. 1-11, 2005. ISSN 1389-1723.

JAGANATHAN, H.; IVANISEVIC, A. Nanostructured Materials for Improved Magnetic Resonance Imaging. In: SITHARAMAN, B. (Ed.). Nanobiomaterials Handbook: CRC Press, 2011. cap. 19, p.1-17. ISBN 978-1-4200-9466-4.

JAŃCZEWSKI, D. et al. Bimodal magnetic–fluorescent probes for bioimaging. Microsc ResTech, v. 74, n. 7, p. 563-576, 2011. ISSN 1097-0029. Disponível em: < http://dx.doi.org/10.1002/jemt.20912 >.

JIE-MEI, L. et al. Preparation and Characterization of Bimodal Magnetofluorescent Nanoprobes for Biomedical Application. Chinese Physics Letters, v. 29, n. 9, p. 097803, 2012. ISSN 0256-307X.

JIN, T. et al. Gd3+-functionalized near-infrared quantum dots for in vivo dual modal (fluorescence/magnetic resonance) imaging. Chem. Commun., n. 44, p. 5764-5766, 2008. ISSN 1364-548X.

JIN, Z.; HILDEBRANDT, N. Semiconductor quantum dots for in vitro diagnostics and cellular imaging. Trends in biotechnology, v. 30, n. 7, p. 394-403, 2012. ISSN 0167-7799.

JING, L. et al. Magnetically Engineered Semiconductor Quantum Dots as Multimodal Imaging Probes. Advanced Materials, v. 26, n. 37, p. 6367-6386, 2014. ISSN 1521-4095. Disponível em: < http://dx.doi.org/10.1002/adma.201402296 >.

JURGONS, R. et al. Drug loaded magnetic nanoparticles for cancer therapy. Journal of Physics: Condensed Matter, v. 18, n. 38, p. S2893, 2006. ISSN 0953-8984.

KALE, A. et al. Magnetite/CdTe magnetic–fluorescent composite nanosystem for magnetic separation and bio-imaging. Nanotechnology, v. 22, n. 22, p. 225101, 2011. ISSN 0957-4484.

KOKTYSH, D.; BRIGHT, V.; PHAM, W. Fluorescent magnetic hybrid nanoprobe for multimodal bioimaging. Nanotechnology, v. 22, n. 27, p. 275606, 2011. ISSN 0957-4484.

KOOLE, R. et al. Paramagnetic Lipid-Coated Silica Nanoparticles with a Fluorescent Quantum Dot Core: A New Contrast Agent Platform for Multimodality Imaging. Bioconjugate Chemistry, v. 19, n. 12, p. 2471-2479, 2008/12/17 2008. ISSN 1043-1802. Disponível em: < http://dx.doi.org/10.1021/bc800368x >.

LAKOWICZ, J. R. Principles of fluorescence spectroscopy. Springer Science & Business Media, 2013. ISBN 1475730616.

LAM, T. et al. Superparamagnetic iron oxide based nanoprobes for imaging and theranostics. Advances in Colloid and Interface Science, v. 199–200, n. 0, p. 95-113, 2013. ISSN 0001-8686. Disponível em: < http://www.sciencedirect.com/science/article/pii/S0001868613000730 >.

LANDINI, L.; POSITANO, V.; SANTARELLI, M. Advanced image processing in magnetic resonance imaging. Taylor & Francis group, LLC, 2005. ISBN 0824725425.

LAUTERBUR, P. C. Image formation by induced local interactions: examples employing nuclear magnetic resonance. Nature, v. 242, n. 5394, p. 190-191, 1973. Disponível em: < http://www.nature.com/physics/looking-back/lauterbur/index.html >.

LI, H.; QIAN, Z. M. Transferrin/transferrin receptor-mediated drug delivery. Medicinal research reviews, v. 22, n. 3, p. 225-250, 2002. ISSN 1098-1128.

LI, H.; SUN, H.; QIAN, Z. M. The role of the transferrin–transferrin-receptor system in drug delivery and targeting. Trends in Pharmacological Sciences, v. 23, n. 5, p. 206-209, 2002. ISSN 0165-6147. Disponível em: < http://www.sciencedirect.com/science/article/pii/S0165614702019892 >.

LIRA, R. B. et al. Non-specific interactions of CdTe/Cds Quantum Dots with human blood mononuclear cells. Micron, v. 43, n. 5, p. 621-626, 2012. ISSN 0968-4328.

Disponível em: < http://www.sciencedirect.com/science/article/pii/S0968432811002150 >.

LIU, B. et al. Preparation and characterization of magnetic luminescent nanocomposite particles. Materials Letters, v. 62, n. 17–18, p. 3014-3017, 2008. ISSN 0167-577X. Disponível em: < http://www.sciencedirect.com/science/article/pii/S0167577X08001419 >.

LIU, J. et al. Molecular mapping of tumor heterogeneity on clinical tissue specimens with multiplexed quantum dots. Acs Nano, v. 4, n. 5, p. 2755-2765, 2010. ISSN 1936-0851.

LIU, X. et al. Formation of Surface Traps on Quantum Dots by Bidentate Chelation and Their Application in Low-Potential Electrochemiluminescent Biosensing. Chemistry-A European Journal, v. 16, n. 35, p. 10764-10770, 2010. ISSN 1521-3765.

LIU, Y. et al. Fluorescence-enhanced gadolinium-doped zinc oxide quantum dots for magnetic resonance and fluorescence imaging. Biomaterials, v. 32, n. 4, p. 1185-1192, February 2011. ISSN 0142-9612. Disponível em: < http://www.sciencedirect.com/science/article/pii/S0142961210013116 >.

LÓPEZ-CEBRAL, R. et al. Progress in the characterization of bio-functionalized nanoparticles using NMR methods and their applications as MRI contrast agents. Progress in nuclear magnetic resonance spectroscopy, v. 79, n. 0, p. 1-13, 5// 2014. ISSN 0079-6565. Disponível em: < http://www.sciencedirect.com/science/article/pii/S0079656514000120 >.

LU, A.-H.; SALABAS, E. L.; SCHÜTH, F. Magnetic Nanoparticles: Synthesis, Protection, Functionalization, and Application. Angewandte Chemie International Edition, v. 46, n. 8, p. 1222-1244, 2007. ISSN 1521-3773. Disponível em: < http://dx.doi.org/10.1002/anie.200602866 >.

MA-HOCK, L. et al. Short term inhalation toxicity of a liquid aerosol of CdS/Cd (OH) 2 core shell quantum dots in male Wistar rats. Toxicology letters, v. 208, n. 2, p. 115-124, 2012. ISSN 0378-4274.

MAHMOUDI, M. et al. Superparamagnetic iron oxide nanoparticles (SPIONs): Development, surface modification and applications in chemotherapy. Advanced Drug Delivery Reviews, v. 63, n. 1–2, p. 24-46, 1// 2011. ISSN 0169-409X. Disponível em: < http://www.sciencedirect.com/science/article/pii/S0169409X1000133X >. Acesso em: 2011/2//.

MALIK, M. A.; WANI, M. Y.; HASHIM, M. A. Microemulsion method: A novel route to synthesize organic and inorganic nanomaterials: 1st Nano Update. Arabian Journal of Chemistry, v. 5, n. 4, p. 397-417, 2012. ISSN 1878-5352. Disponível em: < http://www.sciencedirect.com/science/article/pii/S1878535210002005 >.

MAMANI, J. B. et al. In vivo magnetic resonance imaging tracking of C6 glioma cells labeled with superparamagnetic iron oxide nanoparticles. Einstein (São Paulo), v. 10, p. 164-170, 2012. ISSN 1679-4508. Disponível em: <

http://www.scielo.br/scielo.php?script=sci_arttext&pid=S1679-45082012000200009&nrm=iso >.

MAYLE, K. M.; LE, A. M.; KAMEI, D. T. The Intracellular Trafficking Pathway of Transferrin. Biochimica et biophysica acta, v. 1820, n. 3, p. 264-281, 2012. ISSN 0006-3002. Disponível em: < http://www.ncbi.nlm.nih.gov/pmc/articles/PMC3288267/ >.

MEDINTZ, I. L. et al. Quantum dot bioconjugates for imaging, labelling and sensing. Nat Mater, v. 4, n. 6, p. 435-446, 2005. ISSN 1476-1122. Disponível em: < http://dx.doi.org/10.1038/nmat1390 >.

MERBACH, A.; HELM, L.; TÓTH, É., Eds. The Chemistry of Contrast Agents in Medical Magnetic Resonance Imaging. Chichester, UK: John Wiley & Sons, Ltd, Second Edition ed. 2013.

MERBACH, A. E.; TÓTH, É. The chemistry of contrast agents in medical magnetic resonance imaging. Wiley Online Library, 2001.

MICHALET, X.; BENTOLILA, L. A.; WEISS, S., Eds. Molecular Imaging: Physics and Bioapplications of Quantum Dots. ADVANCES IN MEDICAL PHYSICS, ADVANCES IN MEDICAL PHYSICSed. 2008.

MICHALET, X. et al. Quantum Dots for Live Cells, in Vivo Imaging, and Diagnostics. Science, v. 307, n. 5709, p. 538-544, January 28, 2005 2005. ISSN 0036-8075. Disponível em: < http://www.sciencemag.org/content/307/5709/538.abstract >.

MOUFFOUK, F. et al. Self-assembled polymeric nanoparticles as new, smart contrast agents for cancer early detection using magnetic resonance imaging. International journal of nanomedicine, v. 10, p. 63-76, 2015. ISSN 1176-9114 1178-2013. Disponível em: < http://www.ncbi.nlm.nih.gov/pmc/articles/PMC4275056/ >.

MULAS, G. et al. Insights on the relaxation of liposomes encapsulating paramagnetic Ln-based complexes. Magnetic Resonance in Medicine, p. n/a-n/a, 2014. ISSN 1522-2594. Disponível em: < http://dx.doi.org/10.1002/mrm.25412 >.

NA, H. B.; SONG, I. C.; HYEON, T. Inorganic Nanoparticles for MRI Contrast Agents. Advanced Materials, v. 21, n. 21, p. 2133-2148, 2009. ISSN 1521-4095. Disponível em: < http://dx.doi.org/10.1002/adma.200802366 >.

NOREK, M.; PETERS, J. A. MRI contrast agents based on dysprosium or holmium. Progress in nuclear magnetic resonance spectroscopy, v. 59, n. 1, p. 64-82, 2011. ISSN 0079-6565.

NTZIACHRISTOS, V. Fluorescence molecular imaging. Annu. Rev. Biomed. Eng., v. 8, p. 1-33, 2006. ISSN 1523-9829.

PANKIEWICZ, C. et al. Characterization of the Dynamics of Photoluminescence Degradation in Aqueous CdTe/CdS Core-Shell Quantum Dots. Journal of fluorescence, v. 25, n. 5, p. 1389-1395, 2015. ISSN 1053-0509.

PEREIRA; GERALDES. Design and optimization of gadolinium based contrast agents for magnetic resonance imaging. Ann Magn Reson, v. 6, n. 1, p. 1-33, 2007. Disponível em: < http://www.auremn.org.br/Annals/2007-vol6-num1/AMRn122007_p1-33.pdf >.

PEREIRA, G.; GERALDES, C. Design and optimization of gadolinium based contrast agents for magnetic resonance imaging. Ann Magn Reson, v. 6, n. 1, p. 1-33, 2007.

PINHO, S. L. C. et al. Fine Tuning of the Relaxometry of γ-Fe2O3@SiO2 Nanoparticles by Tweaking the Silica Coating Thickness. ACS Nano, v. 4, n. 9, p. 5339-5349, 2010/09/28 2010. ISSN 1936-0851. Disponível em: < http://dx.doi.org/10.1021/nn101129r >.

PISANIC II, T.; ZHANG, Y.; WANG, T. Quantum dots in diagnostics and detection: principles and paradigms. Analyst, v. 139, n. 12, p. 2968-2981, 2014.

PONKA, P.; LOK, C. N. The transferrin receptor: role in health and disease. The International Journal of Biochemistry & Cell Biology, v. 31, n. 10, p. 1111-1137, 1999. ISSN 1357-2725. Disponível em: < http://www.sciencedirect.com/science/article/pii/S1357272599000709 >.

PRAETNER, M. et al. The contribution of the capillary endothelium to blood clearance and tissue deposition of anionic quantum dots in vivo. Biomaterials, v. 31, n. 26, p. 6692-6700, 2010. ISSN 0142-9612.

PREUSSER, F. et al. Luminescence dating: basics, methods and applications. Quaternary Science Journal, v. 57, n. 1-2, p. 95-149, 2008.

QI, Z.-D. et al. Biocompatible CdSe quantum dot-based photosensitizer under two-photon excitation for photodynamic therapy. Journal of Materials Chemistry, v. 21, n. 8, p. 2455-2458, 2011.

QIAN, Z. M. et al. Targeted drug delivery via the transferrin receptor-mediated endocytosis pathway. Pharmacological reviews, v. 54, n. 4, p. 561-587, 2002. ISSN 1521-0081.

RIBEIRO, R. T. et al. Electrochemical synthetic route for preparation of CdTe quantum-dots stabilized by positively or negatively charged ligands. Green Chemistry, v. 15, n. 4, p. 1061-1066, 2013.

ROGACH, A. L. et al. Aqueous Synthesis of Thiol-Capped CdTe Nanocrystals: State-of-the-Art. The Journal of Physical Chemistry C, v. 111, n. 40, p. 14628-14637, 2007/10/01 2007. ISSN 1932-7447. Disponível em: < http://dx.doi.org/10.1021/jp072463y >.

RUAN, G. et al. Simultaneous Magnetic Manipulation and Fluorescent Tracking of Multiple Individual Hybrid Nanostructures. Nano Letters, v. 10, n. 6, p. 2220-2224, 2010/06/09 2010. ISSN 1530-6984. Disponível em: < http://dx.doi.org/10.1021/nl1011855 >.

RUAN, J. et al. Fluorescent magnetic nanoparticle-labeled mesenchymal stem cells for targeted imaging and hyperthermia therapy of in vivo gastric cancer. Nanoscale Research Letters, v. 7, n. 1, p. 1-12, 2012. ISSN 1931-7573.

SAMIA, A.; DAYAL, S.; BURDA, C. Quantum Dot-based Energy Transfer: Perspectives and Potential for Applications in Photodynamic Therapy. Photochemistry and photobiology, v. 82, n. 3, p. 617-625, 2006. ISSN 1751-1097.

SANTHOSH, P. B.; ULRIH, N. P. Multifunctional superparamagnetic iron oxide nanoparticles: Promising tools in cancer theranostics. Cancer Letters, v. 336, n. 1, p. 8-17, 8/9/ 2013. ISSN 0304-3835. Disponível em: < http://www.sciencedirect.com/science/article/pii/S0304383513003662 >.

SANTOS; FARIAS; FONTES. Semiconductor Quantum Dots for Biological Applications. In: HENINI, M. (Ed.). Handbook of Self Assembled Semiconductor Nanostructures for Novel Devices in Photonics and Electronics. Amsterdam: Elsevier, 2008. p.773-798. ISBN 978-0-08-046325-4.

SANTOS, B. S. et al. New highly fluorescent biolabels based on II–VI semiconductor hybrid organic–inorganic nanostructures for bioimaging. Applied Surface Science, v. 255, n. 3, p. 790-792, 2008. ISSN 0169-4332.

SCHIEBER, C. et al. Conjugation of Transferrin to Azide-Modified CdSe/ZnS Core–Shell Quantum Dots using Cyclooctyne Click Chemistry. Angewandte Chemie International Edition, v. 51, n. 42, p. 10523-10527, 2012. ISSN 1521-3773. Disponível em: < http://dx.doi.org/10.1002/anie.201202876 >.

SCHRYVERS, A. et al. Bacterial Lactoferrin Receptors. In: SPIK, G.;LEGRAND, D., *et al* (Ed.). Advances in Lactoferrin Research: Springer US, v.443, 1998. cap. 15, p.123-133. (Advances in Experimental Medicine and Biology). ISBN 978-1-4757-9070-2.

SHEN, J.-M. et al. Luminescent/magnetic hybrid nanoparticles with folate-conjugated peptide composites for tumor-targeted drug delivery. Bioconjugate Chemistry, v. 23, n. 5, p. 1010-1021, 2012. ISSN 1043-1802.

SILVA, F. O. et al. Effect of surface ligands on the optical properties of aqueous soluble CdTe quantum dots. Nanoscale Research Letters, v. 7, n. 1, p. 1-10, 2012. ISSN 1931-7573.

SINGH, M. et al. Differential expression of transferrin receptor (TfR) in a spectrum of normal to malignant breast tissues: implications for in situ and invasive carcinoma. Applied Immunohistochemistry & Molecular Morphology, v. 19, n. 5, p. 417-423, 2011. ISSN 1062-3345.

SITHARAMAN, B. et al. Superparamagnetic gadonanotubes are high-performance MRI contrast agents. Chemical Communications, n. 31, p. 3915-3917, 2005. ISSN 1359-7345. Disponível em: < http://dx.doi.org/10.1039/B504435A >.

SMITH, A. M.; GAO, X.; NIE, S. Quantum Dot Nanocrystals for In Vivo Molecular and Cellular Imaging¶. Photochemistry and photobiology, v. 80, n. 3, p. 377-385, 2004. ISSN 1751-1097.

SMITH, R.; GIORGIO, T. Quantitative measurement of multifunctional quantum dot binding to cellular targets using flow cytometry. Cytometry Part A, v. 75, n. 5, p. 465-474, 2009. ISSN 1552-4930.

SONG, E.-Q. et al. Fluorescent-magnetic-biotargeting multifunctional nanobioprobes for detecting and isolating multiple types of tumor cells. Acs Nano, v. 5, n. 2, p. 761-770, 2011. ISSN 1936-0851.

STASIUK, G. J. et al. Cell-Permeable Ln(III) Chelate-Functionalized InP Quantum Dots As Multimodal Imaging Agents. Acs Nano, v. 5, n. 10, p. 8193-8201, 2011/10/25 2011. ISSN 1936-0851. Disponível em: < http://dx.doi.org/10.1021/nn202839w >.

SUKHANOVA, A.; NABIEV, I. Fluorescent nanocrystal quantum dots as medical diagnostic tools. Expert Opinion on Medical Diagnostics, v. 2, n. 4, p. 429-447, 2008/04/01 2008. ISSN 1753-0059. Disponível em: < http://dx.doi.org/10.1517/17530059.2.4.429 >. Acesso em: 2015/03/06.

SUN, P. et al. Preparation and characterization of Fe3O4/CdTe magnetic/fluorescent nanocomposites and their applications in immuno-labeling and fluorescent imaging of cancer cells. Langmuir, v. 26, n. 2, p. 1278-1284, 2009. ISSN 0743-7463.

TANG, Y. et al. The role of surface chemistry in determining in vivo biodistribution and toxicity of CdSe/ZnS core–shell quantum dots. Biomaterials, v. 34, n. 34, p. 8741-8755, 2013. ISSN 0142-9612.

TEJA, A. S.; KOH, P.-Y. Synthesis, properties, and applications of magnetic iron oxide nanoparticles. Progress in Crystal Growth and Characterization of Materials, v. 55, n. 1–2, p. 22-45, 3// 2009. ISSN 0960-8974. Disponível em: < http://www.sciencedirect.com/science/article/pii/S0960897408000168 >. Acesso em: 2009/6//.

TENÓRIO, D. P. L. A. et al. CdTe quantum dots conjugated to concanavalin A as potential fluorescent molecular probes for saccharides detection in Candida albicans. Journal of Photochemistry and Photobiology B: Biology, v. 142, n. 0, p. 237-243, 2015. ISSN 1011-1344. Disponível em: < http://www.sciencedirect.com/science/article/pii/S1011134414003649 >.

THAKUR, D. et al. pH sensitive CdS–iron oxide fluorescent–magnetic nanocomposites. Nanotechnology, v. 20, n. 48, p. 485601, 2009. ISSN 0957-4484.

TORTORELLA, S.; KARAGIANNIS, T. Transferrin Receptor-Mediated Endocytosis: A Useful Target for Cancer Therapy. The Journal of Membrane Biology, v. 247, n. 4, p. 291-307, 2014/04/01 2014. ISSN 0022-2631. Disponível em: < http://dx.doi.org/10.1007/s00232-014-9637-0 >.

TURNER, J. L. et al. Synthesis of Gadolinium-Labeled Shell-Crosslinked Nanoparticles for Magnetic Resonance Imaging Applications. Advanced Functional Materials, v. 15, n. 8, p. 1248-1254, 2005. ISSN 1616-3028. Disponível em: < http://dx.doi.org/10.1002/adfm.200500005 >.

VIANA, O. S. et al. Comparative Study on the Efficiency of the Photodynamic Inactivation of Candida albicans Using CdTe Quantum Dots, Zn (II) Porphyrin and Their Conjugates as Photosensitizers. Molecules, v. 20, n. 5, p. 8893-8912, 2015.

WACHTER, R. M. et al. Structural basis of spectral shifts in the yellow-emission variants of green fluorescent protein. Structure, v. 6, n. 10, p. 1267-1277, 1998. ISSN 0969-2126.

WANG, D. et al. Superparamagnetic Fe2O3 Beads−CdSe/ZnS Quantum Dots Core−Shell Nanocomposite Particles for Cell Separation. Nano Letters, v. 4, n. 3, p. 409-413, 2004/03/01 2004. ISSN 1530-6984. Disponível em: < http://dx.doi.org/10.1021/nl035010n >. Acesso em: 2014/05/28.

WANG, G.-P. et al. Biofunctionalization of fluorescent-magnetic-bifunctional nanospheres and their applications. Chemical Communications, n. 34, p. 4276-4278, 2005. ISSN 1359-7345. Disponível em: < http://dx.doi.org/10.1039/B508075D >.

WANG, H. et al. Synthesis and characterization of multifunctional CdTe/Fe 2 O 3@ SiO 2 core/shell nanosensors for Hg2+ ions detection. New Journal of Chemistry, v. 34, n. 12, p. 2996-3003, 2010.

WEGNER, K. D.; HILDEBRANDT, N. Quantum dots: bright and versatile in vitro and in vivo fluorescence imaging biosensors. Chemical Society Reviews, 2015. ISSN 0306-0012. Disponível em: < http://dx.doi.org/10.1039/C4CS00532E >.

WEINSTEIN, J. S. et al. Superparamagnetic iron oxide nanoparticles: diagnostic magnetic resonance imaging and potential therapeutic applications in neurooncology and central nervous system inflammatory pathologies, a review. Journal of Cerebral Blood Flow and Metabolism: Official Journal of the International Society of Cerebral Blood Flow and Metabolism, v. 30, n. 1, p. 15-35, 2010. ISSN 0271-678X
1559-7016. Disponível em: < http://www.ncbi.nlm.nih.gov/pmc/articles/PMC2949106/ >.

WEISSLEDER, R. Molecular imaging in cancer. Science, v. 312, n. 5777, p. 1168-1171, 2006. ISSN 0036-8075.

WILEY, D. T. et al. Transcytosis and brain uptake of transferrin-containing nanoparticles by tuning avidity to transferrin receptor. Proceedings of the National Academy of Sciences of the United States of America, v. 110, n. 21, p. 8662-8667, 2013. ISSN 0027-8424
1091-6490. Disponível em: < http://www.ncbi.nlm.nih.gov/pmc/articles/PMC3666717/ >.

XIAO, Y. et al. Research Dynamics and mechanisms of quantum dot nanoparticle cellular uptake. Journal of nanobiotechnology, p. 8-13, 2010.

YAGHINI, E.; SEIFALIAN, A. M.; MACROBERT, A. J. Quantum dots and their potential biomedical applications in photosensitization for photodynamic therapy. 2009. ISSN 1743-5889.

YANG, J. et al. Ultrasensitive detection and molecular imaging with magnetic nanoparticles. Analyst, v. 133, n. 2, p. 154-160, 2008.

YONG, K.-T. et al. Imaging Pancreatic Cancer Using Bioconjugated InP Quantum Dots. Acs Nano, v. 3, n. 3, p. 502-510, 2009/03/24 2009. ISSN 1936-0851. Disponível em: < http://pubs.acs.org/doi/abs/10.1021/nn8008933 >.

YOON, D. J. et al. Genetically engineering transferrin to improve its in vitro ability to deliver cytotoxins. Journal of controlled release : official journal of the Controlled Release Society, v. 133, n. 3, p. 178-184, 2009. ISSN 0168-3659
1873-4995. Disponível em: < http://www.ncbi.nlm.nih.gov/pmc/articles/PMC2681226/ >.

ZENG, C. et al. Colloids containing gadolinium-capped gold nanoparticles as high relaxivity dual-modality contrast agents for CT and MRI. Colloids and Surfaces B: Biointerfaces, v. 123, n. 0, p. 130-135, 11/1/ 2014. ISSN 0927-7765. Disponível em: < http://www.sciencedirect.com/science/article/pii/S0927776514004755 >.

ZHAI, G. et al. A transferrin receptor-targeted liposomal formulation for docetaxel. Journal of Nanoscience and Nanotechnology, v. 10, n. 8, p. 5129-5136, 2010. ISSN 1533-4880.

ZHANG, F. et al. Facile synthesis of functional gadolinium-doped CdTe quantum dots for tumor-targeted fluorescence and magnetic resonance dual-modality imaging. Journal of Materials Chemistry B, v. 2, n. 41, p. 7201-7209, 2014. ISSN 2050-750X. Disponível em: < http://dx.doi.org/10.1039/C4TB00920G >.

ZHANG, H. et al. L-Cysteine capped CdTe–CdS core–shell quantum dots: preparation, characterization and immuno-labeling of HeLa cells. Luminescence, v. 26, n. 2, p. 86-92, 2011. ISSN 1522-7243.

ZHANG, M.-Z. et al. Targeted quantum dots fluorescence probes functionalized with aptamer and peptide for transferrin receptor on tumor cells. Nanotechnology, v. 23, n. 48, p. 485104, 2012. ISSN 0957-4484. Disponível em: < http://stacks.iop.org/0957-4484/23/i=48/a=485104 >.

ZHANG, S. et al. Size-Dependent Endocytosis of Nanoparticles. Advanced materials (Deerfield Beach, Fla.), v. 21, p. 419-424, 2009. ISSN 0935-9648
1521-4095. Disponível em: < http://www.ncbi.nlm.nih.gov/pmc/articles/PMC2709876/ >.

ZHANG, Y. et al. Self-assembly multifunctional nanocomposites with Fe3O4 magnetic core and CdSe/ZnS quantum dots shell. Journal of Biomedical Materials Research Part A, v. 85A, n. 3, p. 840-846, 2008. ISSN 1552-4965. Disponível em: < http://dx.doi.org/10.1002/jbm.a.31609 >.

4 ARTIGO PUBLICADO

Biochimica et Biophysica Acta 1860 (2016) 28–35

Contents lists available at ScienceDirect

Biochimica et Biophysica Acta

journal homepage: www.elsevier.com/locate/bbagen

CdTe quantum dots as fluorescent probes to study transferrin receptors in glioblastoma cells

Paulo E. Cabral Filho [a], Ana L.C. Cardoso [b], Maria I.A. Pereira [a], Ana P.M. Ramos [a], Fernando Hallwass [c], M. Margarida C.A. Castro [d,e], Carlos F.G.C. Geraldes [d,e], Beate S. Santos [f], Maria C. Pedroso de Lima [b], Giovannia A.L. Pereira [c], Adriana Fontes [a,*]

[a] Biophysics and Radiobiology Department, Federal University of Pernambuco, Recife, PE, Brazil
[b] CNC- Center for Neuroscience and Cell Biology, University of Coimbra, Coimbra, Portugal
[c] Department of Fundamental Chemistry, Federal University of Pernambuco, Recife, PE, Brazil
[d] Department of Life Sciences, Faculty of Science and Technology, University of Coimbra, Coimbra, Portugal
[e] Coimbra Chemistry Center, University of Coimbra, Coimbra, Portugal
[f] Department of Pharmaceutical Sciences, Federal University of Pernambuco, Recife, PE, Brazil

ARTICLE INFO

Article history:
Received 30 June 2015
Received in revised form 18 September 2015
Accepted 30 September 2015
Available online 3 October 2015

Keywords:
Nanoparticles
Cancer cells
Transferrin
Receptors
Bioconjugation
Covalent binding

ABSTRACT

Background: Overexpression of transferrin receptors (TfRs), which are responsible for the intracellular uptake of ferric transferrin (Tf), has been described in various cancers. Although molecular biology methods allow the identification of different types of receptors in cancer cells, they do not provide features about TfRs internalization, quantification and distribution on cell surface. This information can, however, be accessed by fluorescence techniques. In this work, the quantum dots (QDs)' unique properties were explored to strengthen our understanding of TfRs in cancer cells.
Methods: QDs were conjugated to Tf by covalent coupling and QDs-(Tf) bioconjugates were applied to quantify and evaluate the distribution of TfRs in two human glioblastoma cells lines, U87 and DBTRG-05MG, and also in HeLa cells by using flow cytometry and confocal microscopy.
Results: HeLa and DBTRG-05MG cells showed practically the same TfR labeling profile by QDs-(Tf), while U87 cells were less labeled by bioconjugates. Furthermore, inhibition studies demonstrated that QDs-(Tf) were able to label cells with high specificity.
Conclusions: HeLa and DBTRG-05MG cells presented a similar and a higher amount of TfR than U87 cells. Moreover, DBTRG-05MG cells are more efficient in recycling the TfR than the other two cells types.
General significance: This is the first study about TfRs in human glioblastoma cells using QDs. This new fluorescent tool can contribute to our understanding of the cancer cell biology and can help in the development of new therapies targeting these receptors.

1. Introduction

Transferrin (Tf) is a β-globin with approximately 670–700 amino acids, which binds to a cell surface receptor (TfR) expressed by most proliferating cells with particularly high expression on tumor cells, being one of the biomolecules most applied to cancer cell targeting [1]. The TfR is also known as CD71 and promotes the cellular uptake of ferric Tf [2], by clathrin-mediated endocytosis [3]. Nanotechnology approaches have taken advantage of the potential use of the TfRs to improve therapy and diagnostic procedures related to cancer. The most common systems employed for these purposes are liposomes [4,5], metallic nanoparticles [6,7] and magnetic nanoparticles [3]. These nanosystems have been functionalized with Tf to target the TfR in order to improve diagnostic methods, as well as the efficacy of chemotherapeutics, since cancer cells and tissues overexpress TfR on their surface with respect to normal cells. Zhai et al. [4], for instance, used TfRs as targets of liposomes conjugated to Tf and loaded with docetaxel, showing that these nanocarriers are a promising chemotherapeutic delivery vehicle for cancer therapeutics, when compared to liposomes lacking Tf. Therefore, studies related to the TfR can provide a better understanding of the cell biology of cancer and also help to improve its treatment.

TfRs have been widely studied by molecular biology approaches, which proved to be a valuable tool in the identification of different types of receptors in cancer cells [8–10]. However, molecular biology methods do not provide information about the cellular internalization of the receptor, its quantification and distribution. Fluorescence-based techniques have high sensitivity to quantify biomolecules with

* Corresponding author at: Av. Prof. Moraes Rego, S/N. Departamento de Biofísica e Radiobiologia, CCB, UFPE, 50670-901, Recife, PE, Brazil.
E-mail address: adriana.fontes.biofisica@gmail.com (A. Fontes).

http://dx.doi.org/10.1016/j.bbagen.2015.09.021
0304-4165/

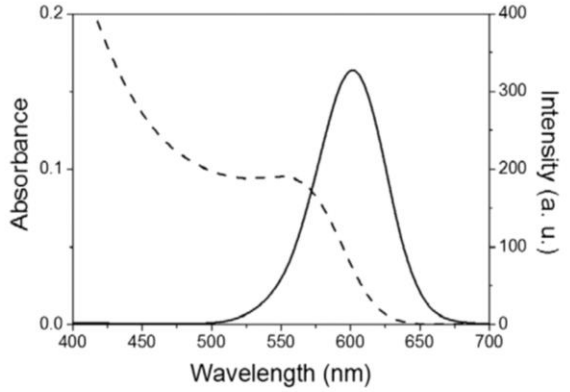

Fig. 1. Optical characterization of CdTe QDs aqueous colloidal suspension: absorption (dashed line) and emission (solid line) spectra. The excitation wavelength (λ_{exc}) for the emission spectrum was 365 nm.

high specificity and thus can be used as innovative and attractive methods to investigate receptor intracellular trafficking and distribution, complementing molecular biology studies [11]. Among the most promising probes that can be applied in fluorescence-based research are the quantum dots (QDs), which are semiconductor fluorescent nanoparticles that have great potential for biological research due to their unique optical and chemical properties. QDs present exceptional resistance to photobleaching, enabling long-term studies, and their active surface allows their functionalization with biomolecules in order to reach biological targets with a high specificity [12–15]. These QDs' features can be employed to strengthen our understanding of cellular receptors, such as the TfR.

The aim of this work was to apply CdTe QDs conjugated to Tf (QDs-Tf) as probes to study the TfRs in human glioblastoma cells, by using the complementary analyzes provided by fluorescence confocal microscopy and flow cytometry. The TfR was quantified and its distribution was analyzed in two different human glioma cells lines, U87 (glioblastoma) and DBTRG-05MG (recurrent glioblastoma). HeLa cells (human epithelial cervical carcinoma) were used as a control cellular model in this work, since QDs associated to Tf have already been applied to study the TfR in these cells [16–19]. However, the specificity of such conjugates has not been fully proved in those previous works. Here, the bioconjugation procedure of QDs to Tf was improved and the specificity of the labeling was demonstrated by TfR saturation assays. Moreover, to our knowledge, this is the first study that not

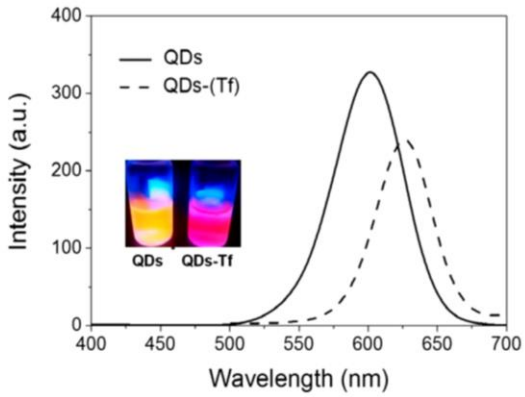

Fig. 2. Emission spectra of bare QDs (solid line) and QDs-(Tf) (dashed line). Pictures of the QDs (orange emission) and the bioconjugates (red emission) show their fluorescence under UV–Vis excitation (λ_{exc} = 365 nm).

Table 1
Fluorescence Microplate Assay results obtained from the average signal of fluorescence intensities (controls and bioconjugates) and percentage of relative fluorescence intensity of the bioconjugates.

Systems	Average of signal 4 days	RF (%) 4 days	Average of signal 10 days	RF (%) 10 days
Transferrin	151.6	–	122.6	–
QDs	212.0	–	258.0	–
QDs-(Tf)	698.0	283.9	41,615.0	21,764.0

only investigates the TfR in these two glioblastoma cell lines, but also compares the amount and the distribution of TfRs on these types of tumor cells, using the HeLa cell line as reference.

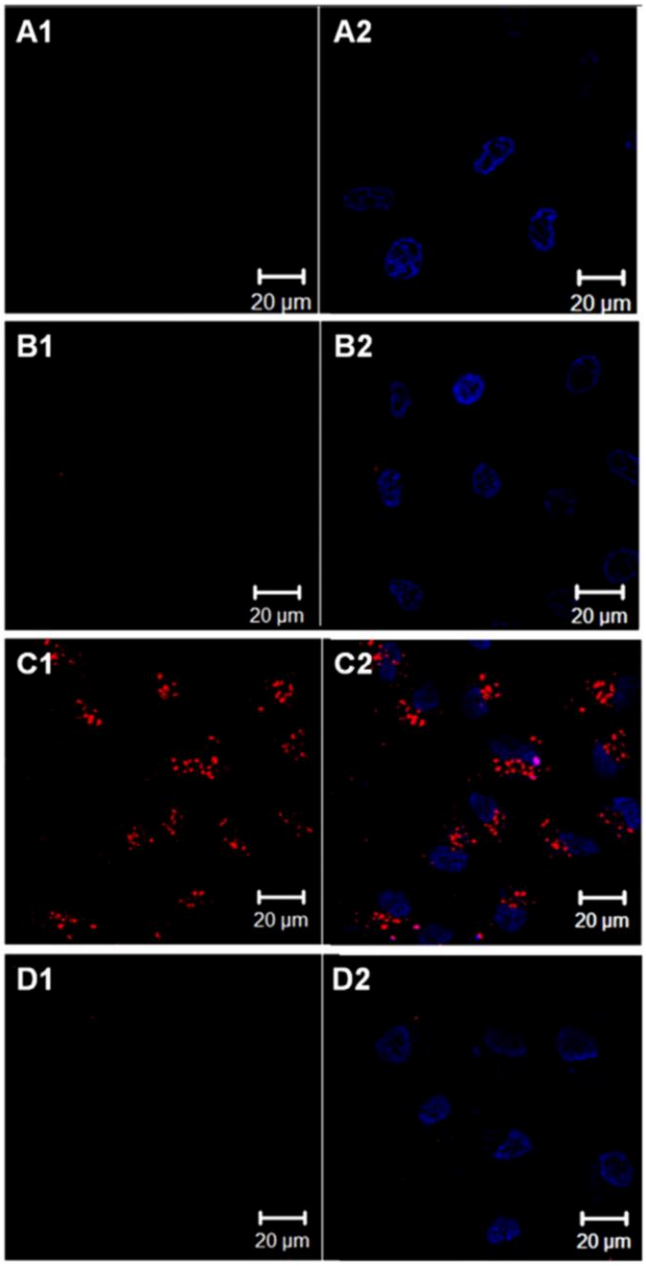

Fig. 3. Confocal microscopy images of HeLa cells labeled by QDs-(Tf). (A) Control HeLa cells, (B) HeLa cells incubated with bare QDs, (C) HeLa cells incubated with QDs-(Tf) and (D) HeLa cells incubated with QDs-(Tf) after TfR saturation. The identification (1) refers to the confocal emission channel LP 565 nm and the identification (2) refers to the overlap of LP 565 nm and Hoechst emission channel (BP 420-480 nm). Scale Bar: 20 μm.

2. Experimental procedures

2.1. Synthesis and characterization of CdTe-MSA QDs

CdTe-MSA QDs were synthesized as an aqueous colloidal dispersion according to a previously reported method, with some modifications [20]. Briefly, QDs were prepared by adding Te^{2-} ions to a $Cd(ClO_4)_2$ solution at pH > 10 in the presence of MSA (mercaptosuccinic acid) as stabilizing agent in a molar ratio of 5:1:6 (Cd:Te:MSA, respectively). The Te^{2-} aqueous solution was prepared by reducing metallic tellurium with $NaBH_4$ at a high pH and under nitrogen saturated inert atmosphere. The reaction proceeded under constant stirring and heating at 90 °C during 5 h.

After their synthesis, QDs were optically characterized by absorption and emission spectroscopy carried out on a spectrophotometer Evolution 600 UV–Vis (Thermo Scientific) and on spectrometer LS 55 (PerkinElmer, at $\lambda_{exc} = 365$ nm), respectively.

2.2. CdTe-MSA QDs conjugation to transferrin

CdTe-MSA QDs were conjugated with human holo transferrin (Tf) (Sigma Aldrich) by using N-ethyl-3-(3-dimethylaminopropyl)carbo diimide hydrochloride (EDC — Fluka) and N-hydroxysulfosuccinimide sodium salt (Sulfo-NHS — Sigma Aldrich) as coupling reagents.

First, the pH of 2 mL of the CdTe-MSA QDs dispersion (at 0.84 μM) was adjusted to 5.5 by using MSA at 4.9% (*w*/*v*). Then, 1 mL of EDC (at 4 $mg \cdot mL^{-1}$) was added and after 5 min, 1 mL of Sulfo-NHS (at 5.5 $mg \cdot mL^{-1}$) was also added to the QDs aqueous suspension [21,22]. Then, 15 min later, 194 μL of Tf (at 1 $mg \cdot mL^{-1}$) was added to reach a ratio of QDs:Tf 1:2 (particle:molecule).

Before cell labeling, the QDs-(Tf) conjugated system was incubated with 50 μL of TRIS base (at 1 mM) for 2 h under slow agitation. This procedure was used to quench the free carboxyl groups of non-conjugated QDs in order to minimize unspecific labeling. QDs-(Tf) were optically characterized by emission spectroscopy at $\lambda_{exc} = 365$ nm by using the same spectrometer mentioned above (LS 55, PerkinElmer).

2.3. Confirmation of conjugation QDs-(Tf) by Fluorescence Microplate Assay (FMA)

To confirm the efficiency of the bioconjugation process, we employed the Fluorescence Microplate Assay (FMA) [23]. Briefly, all the systems (Tf, bare QDs and QDs-(Tf)) were placed in a polystyrene microplate (black 96-well Optiplate F HB microplates — PerkinElmer) in triplicates, at the same concentration used for the bioconjugation assay. The plate was maintained for 2 h in an incubator (water bath, humid chamber) at 37 °C. After this period, the plate was washed three times with a phosphate buffered saline solution, PBS 1× (from now on named as PBS). We analyzed the conjugates as a function of time by evaluating the QDs-(Tf) samples at 4th and 10th days after the initial bioconjugation assay.

Fluorescence measurements were performed on a WALLAC 1420 Plate Reader, equipped with the software Victor² (PerkinElmer). The excitation band pass filter used was the BP 405 nm ± 2.5 nm and the emission band pass filter was the BP 595 nm ± 15 nm. The acquisition time was 1 s, the lamp was set to 20,000 and normal slits were used for the excitation of samples and for collecting the emission.

2.4. Cell culture

HeLa cells (human epithelial cervical carcinoma) were obtained from the American Type Culture Collection (Manassas, VA, USA) and the U87 (human glioblastoma) and DBTRG-05MG (human recurrent glioblastoma) cells were kindly provided by Dr. Peter Canoll (Columbia University, New York, NY) and Dr. Massimiliano Salerno (Siena Biotech, Italy). HeLa and U87 cells were cultured in Dulbecco's modified Eagle's medium with high glucose (DMEM — Sigma Aldrich) supplemented with 10% of fetal bovine serum (FBS — Gibco), 100 $mg \cdot mL^{-1}$ streptomycin and 100 units $\cdot mL^{-1}$ penicillin (Sigma Aldrich) at 37 °C in a humidified atmosphere with 5% CO_2. DBTRG-05MG cells were cultured in Roswell Park Memorial Institute (RPMI — Sigma Aldrich) 1640 medium supplemented with 10% of FBS, 100 $mg \cdot mL^{-1}$streptomycin and 100 units $\cdot mL^{-1}$ penicillin at 37 °C in a humidified atmosphere with 5% CO_2. When HeLa cells reached 90% confluence in the culture

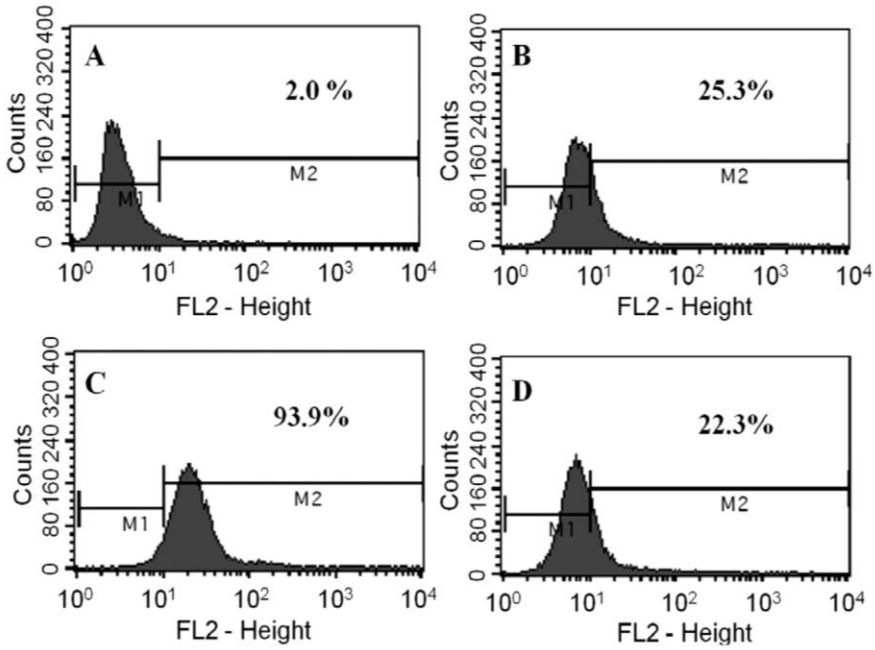

Fig. 4. Flow cytometry analysis of HeLa cells. In (A) HeLa cells in PBS, (B) HeLa cells incubated with bare QDs (C) HeLa cells incubated with QDs-(Tf) and (D) HeLa cells incubated with QDs-(Tf) after Tf-receptor saturation.

flask, they were detached with 0.25% of trypsin (Sigma Aldrich) in Dissociation Buffer (Gibco). Detachment of U87 and DBTRG cells was performed exclusively with Dissociation Buffer. The cells were then seeded onto a 6-well plate (1.5 x 10^5 cells/well — Thermo Scientific™ BioLite) and incubated for 24 h for flow cytometry studies and in an 8-well plate (2.0 × 10^4 cells/well — μSlide IbiTreat, Germany) for confocal microscopy analysis. At this time point, cells exhibited a confluence of around 80–90% in the wells.

2.5. Labeling cancer cells with QDs-(Tf)

After incubation for 24 h in 6-well or 8-well plates, the cells were washed with PBS and the following experimental conditions were assayed: (I) control cells with PBS; (II) PBS and bare QDs (1:1 *v*/*v*); (III) PBS and QDs-(Tf) (1:1 *v*/*v*). After 1 h of incubation at 37 °C, the cells were washed with PBS before flow cytometry and confocal microscopy analysis to remove any residual labeling on the cell surface by bare QDs.

The percentage of labeled cells was determined by flow cytometry (FACSCalibur™, Becton Dickinson). In these studies, HeLa cells were detached from the 6-well plate upon incubation with trypsin 0.25% in Dissociation Buffer followed by trypsin inactivation with DMEM and then placed in suspension. U87 and DBTRG cells were detached exclusively with Dissociation Buffer. The cell suspensions were washed 3 times with PBS and pelleted by centrifugation at 1200 ×*g*, 30 s (MiniSpin — Eppendorf). Around 20,000 events were acquired for each experimental condition following excitation at 488 nm. The emission was detected with the band pass filter 585/20 nm and the collected data were processed by the Cell Pro Software (Cell Quest™, Becton-Dickinson).

For confocal analysis, and following the establishment of different experimental conditions, the cells plated onto 8-well plates were washed three times with PBS. The cell nuclei were stained for 5 min with the fluorescent DNA-binding dye Hoechst 33,342 (at a final concentration of 1 μg·mL^{-1}), and the cells were washed with PBS three times before being observed under a confocal microscope (Zeiss LSM 510 META).

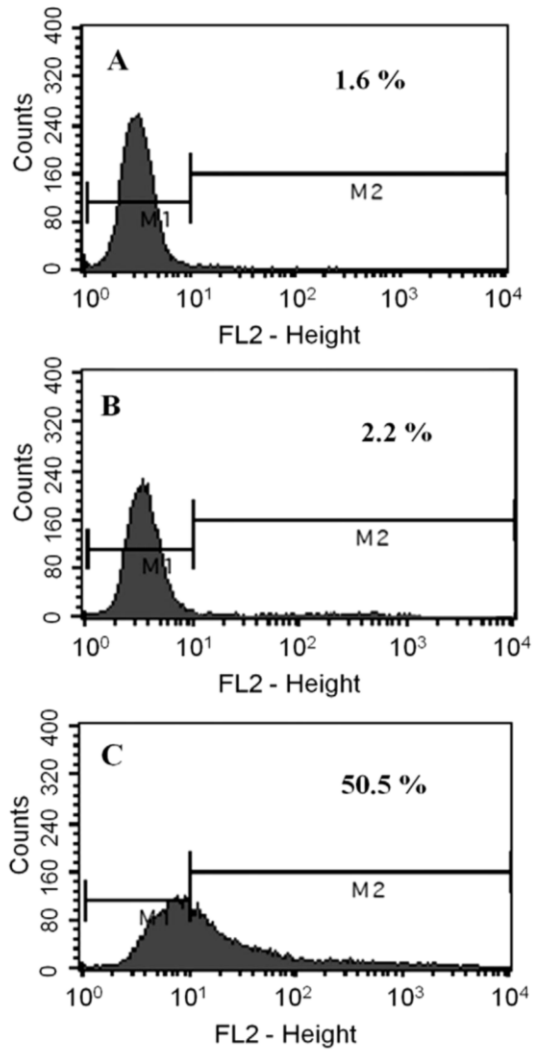

Fig. 5. Flow cytometry analysis of HeLa cells following incubation at 4 °C. (A) HeLa cells in PBS, (B) HeLa cells incubated with bare QDs, and (C) HeLa cells incubated with QDs-(Tf).

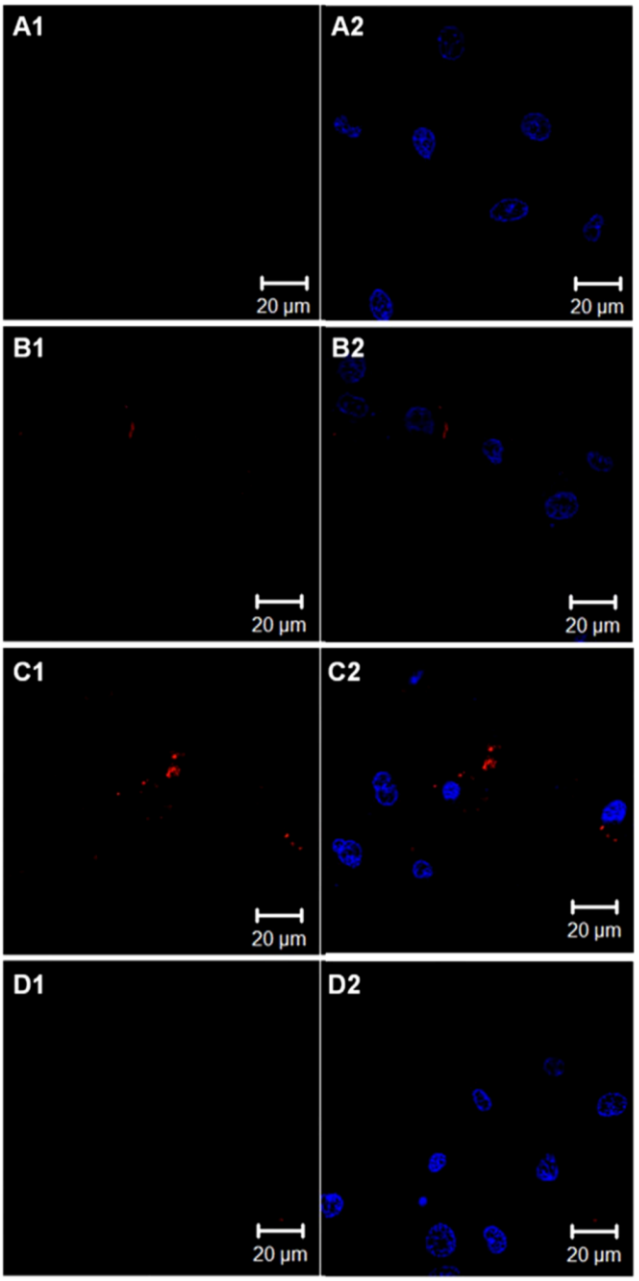

Fig. 6. Confocal microscopy images of U87 cells labeled by QDs-(Tf). (A) Control U87 cells, (B) U87 cells incubated with bare QDs, (C) U87 cells incubated with QDs-(Tf) and (D) U87 cells incubated with QDs-(Tf) after TfR saturation. The identification (1) refers to the confocal emission channel LP 565 nm and the identification (2) refers to the overlap of LP 565 nm and Hoechst emission channel (BP 420-480 nm). Scale Bar: 20 μm.

In order to confirm the specificity of the labeling, as well as the efficiency of the bioconjugation, cells were also incubated with excess of free human holo transferrin (at a final concentration of 10 mg·mL^{-1}) for 1 h at 37 °C, aiming at saturating the TFRs [24], before the confocal analysis. After this period, the cells were incubated with QDs-(Tf) for 1 additional hour at a final QDs-(Tf): free Tf ratio of 1:1 (*v*/*v*).

3. Results and discussion

3.1. Characterization of CdTe QDs and bioconjugates

According to optical characterizations, MSA QDs aqueous suspension presented a first maximum absorption peak at 548 nm, as can be observed in Fig. 1. By using the Dagtepe et al. [25] equation and the Rogach et al. [26] approximation, we estimated an average diameter of approximately 3.1 nm for these nanoparticles. Furthermore, taking into account the absorbance at the first maximum absorption peak, the CdTe QDs molar extinction coefficient proposed by Yu et al., [27] and the Lambert-Beer equation, we also estimated the QDs concentration as approximately 4.8 μM. The QDs colloidal suspension showed an emission maximum at 602 nm and a full width at a half maximum (FWHM) of about 58 nm, indicating a narrow emission spectrum (Fig. 1) which is ascribed to the exciton recombination.

Bare QDs and QDs-(Tf) (bioconjugates) exhibited similar emission spectra profiles for emission spectra (Fig. 2, $\lambda_{exc} = 365$ nm), however QDs-(Tf) showed a maximum emission at 626 nm. The observed red shift for the QDs-(Tf) suggests modifications on the QDs surface due to the bioconjugation process. The same behavior was observed in previous works using hydrophilic QDs conjugated to Concanavalin A [28] and to *Ulex europaeus* lectins [29]. In both cases the red shift of the emission peak was observed. Despite the red shift, QDs bioconjugates suspension remained highly fluorescent, as shown in Fig. 2.

3.2. Fluorescence Microplate Assay

The *FMA* results are presented in Table 1 as the average of the fluorescent signal of triplicate wells for controls and conjugates. The data analysis was carried out according to Carvalho et al. [23]. The relative fluorescence (RF) results for QDs-(Tf) were 283.9% and 21,764.0%, for the 4th and 10th days after bioconjugation, respectively. According to Carvalho et al. [23] the bioconjugation process is efficient when the bioconjugates show a RF higher than 100%. Therefore, our results (Table 1) indicate that the bioconjugation was efficient after four days and improved over time. The Sigma Aldrich product information indicates that Tf should remain active at 4 °C for 5–10 days after dilution.

3.3. Labeling HeLa cells by using QDs-(Tf)

As shown in Fig. 3, efficient and specific labeling of the TfR was observed in HeLa cells using QDs-(Tf) (Fig. 3, C1 and C2). HeLa cells, incubated with bare QDs (Fig. 3, B1 and B2), as well as after TfR saturation by free Tf (Fig. 3, D1 and D2), did not show considerable labeling, resulting in an image profile similar to the one obtained for control (in the absence of QDs) HeLa cells (Fig. 3, A1 and A2). The use of the DNA-binding dye Hoechst allowed to detect the intracellular localization of the receptor, indicating that 1 h of cell incubation with the QDs-(Tf) was sufficient to promote the internalization of the TfR by HeLa cells.

The confocal microscopy results were confirmed by flow cytometry analysis. As shown in Fig. 4C, about 94% of HeLa cells were labeled by QDs-(Tf), while incubation of the cells with bare QDs (Fig. 4B) or after inhibiting the specific interaction of QDs-(Tf) with TfRs (Fig. 4D), resulted in less than 26% of cell labeling. The residual labeling, less than 26%, may be attributed to QDs internalization by a TfR-independent pathway. This type of unspecific interaction between the cells and nanoparticles has been previously reported [30–32].

These results were confirmed by incubating the cells at 4 °C (Fig. 5), under which conditions endocytosis is compromised [33]. As shown in Fig. 5B, HeLa cells labeling by bare QDs was inhibited. On the other hand, QDs-(Tf) labeled 50.5% of HeLa cells (Fig. 5C) corresponding to the labeling of TfRs that remained on the cell surface, since the receptors cannot be internalized at this temperature, resulting in a decrease of labeled cells of approximately 43%, when compared to what was observed at 37 °C (Fig. 4C). Therefore, our results demonstrated specific

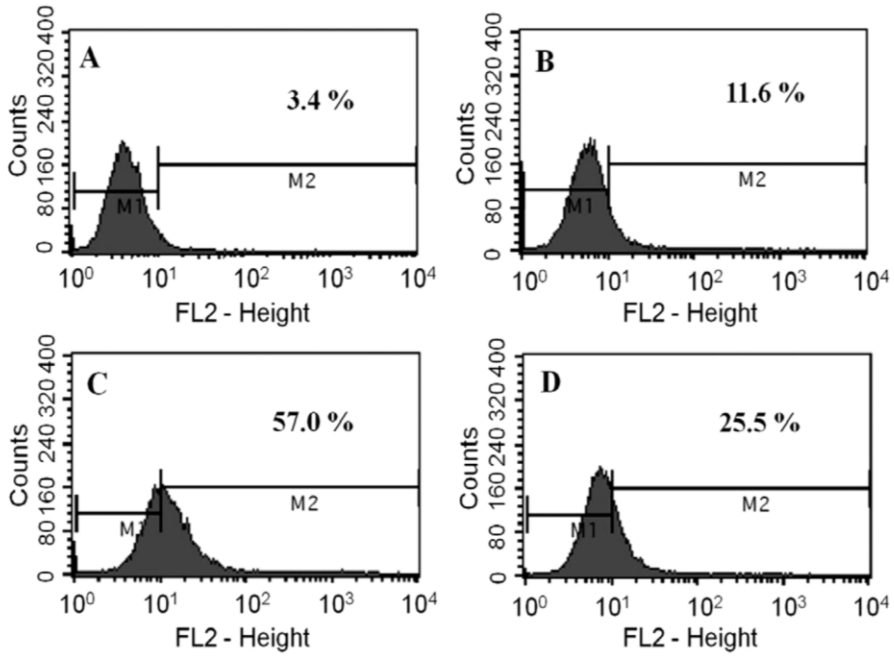

Fig. 7. Flow cytometry analysis of U87 cells. (A) U87 cells in PBS, (B) U87 cells incubated with bare QDs (C) U87 cells incubated with QDs-(Tf) and (D) U87 cells incubated with QDs-(Tf) after TfR saturation.

interaction of QDs- (Tf) with TfRs, which promoted cellular internalization of the QDs-(Tf).

In this work, HeLa cells were used as a model cell system and experimental approaches involving the blocking of TfR or inhibition of TfR-mediated endocytosis were employed to confirm the efficiency and specificity of QDs-(Tf) conjugates. Indeed, although the TfR has been studied by fluorescence assays with QDs [16,18,34,35], the targeting specificity of such conjugates has not been fully demonstrated. Sahoo et al. used polymeric nanoparticles (NPs) conjugated to Tf and showed that when NPs-Tf were incubated with an excess of Tf (50 μg), the percentage of labeled MCF-7 cells (a breast cancer cell line) was similar to that obtained when the cells were incubated with bare NPs [36]. These results are in agreement with our findings showing the specificity of the TfR labeling by QDs-Tf in HeLa cells. In this regard, less than 23% of HeLa cells were labeled after TfR saturation (Fig. 4D), this labeling being most likely attributed to QDs-(Tf) non-specific endocytosis, consistent with the results observed when HeLa cells were incubated with bare QDs, which do not exhibit affinity to TfR (Fig. 4B). To our knowledge, this is the first study addressing TfR saturation through competitive inhibition experiments with free Tf to confirm that the cell internalization of QDs-(Tf) bioconjugates is specific for TfRs.

Our results showed that 1 h of incubation with QDs-(Tf) was sufficient to promote their internalization through specific interaction with TfRs in HeLa cells. These achievements agree with those presented by Chan et al. and Tekle et al. that applied QDs-(Tf) to label specifically the TfR in HeLa cells [16,19]. Guan et al. carried out three different types of conjugations by using QDs and Tf, and showed that the most efficient was the one using EDC as coupling agent [18]. The authors demonstrated that approximately 85.5% of cells were labeled by QDs-Tf. Our results using EDC and Sulfo-NHS presented an improvement relative to these previous studies, showing a labeling percentage of about 93%. To our best knowledge, this is the first work that used EDC and Sulfo-NHS simultaneously as coupling agents to conjugate MSA-QDs to Tf. According to Hermanson [22], the simultaneous use of these coupling agents improves the bioconjugation process by minimizing the generation of reactive species, when compared to the individual use of EDC for bioconjugation purposes.

3.4. Labeling glioblastoma cells by using QDs-(Tf)

In studies addressing the TfR in glioblastoma cells, we employed the U87 human glioblastoma cell line, extensively reported as a relevant glioblastoma cellular model and the DBTRG-05MG cell line, established from a glioblastoma patient treated with local brain irradiation and multidrug chemotherapy. Confocal microscopy images of U87 cells, displayed in Fig. 6, show that the TfR is present in a minimal amount, since a very small amount of labeling could be observed following incubation with QDs-(Tf) (Fig. 6, C1 and C2). Blocking Tf-receptor by adding excess of free Tf decreased even further the cell labeling (Fig. 6, D1 and D2), and similar results were obtained after cell incubation with bare QDs (Fig. 6, B1 and B2).

The confocal microscopy results were confirmed by quantitative flow cytometry analysis of U87 cells, as illustrated in Fig. 7. Fig. 7C shows that 57.0% of U87 cells were labeled when incubated with QDs-(Tf). On the other hand, only 25.5% of cells were labeled after TfR saturation (Fig. 7D).

According to Dixit et al. [7], when U87 cells were incubated with gold nanoparticles functionalized by the Tf peptide, an accumulation of these nanostructures was observed inside the cells after 1 h, which increased until 24 h. The results of that study indicated that the endocytic activity of U87 cells occurs at a slower rate when compared to that of LN299 cells, another human glioma cell line, with an uptake plateau after 1 h. In agreement with the findings reported by Dixit et al., our results showed that U87 cells internalize QDs-(Tf) at a low extent which also seem to have a small amount of TfRs at the plasma membrane.

In contrast with U87 cells, confocal microscopy images of DBTRG-05MG cells incubated with QDs-(Tf) (Fig. 8, C1 and C2) showed that TfR internalization was very effective in these cells. After 1 h incubation with QDs-(Tf), DBTRG-05MG cells showed a similar profile to that in HeLa cells, regarding the presence of the TfR (Fig. 8C and Fig. 3C, respectively). Furthermore, when DBTRG-05MG cells were incubated with bare QDs (Fig. 8, B1 and B2) no significant unspecific labeling was observed. However, when these cells were incubated with QDs-(Tf), after TfR saturation with free Tf (Fig. 8, D1 and D2), fluorescent labeling in some cells was detected.

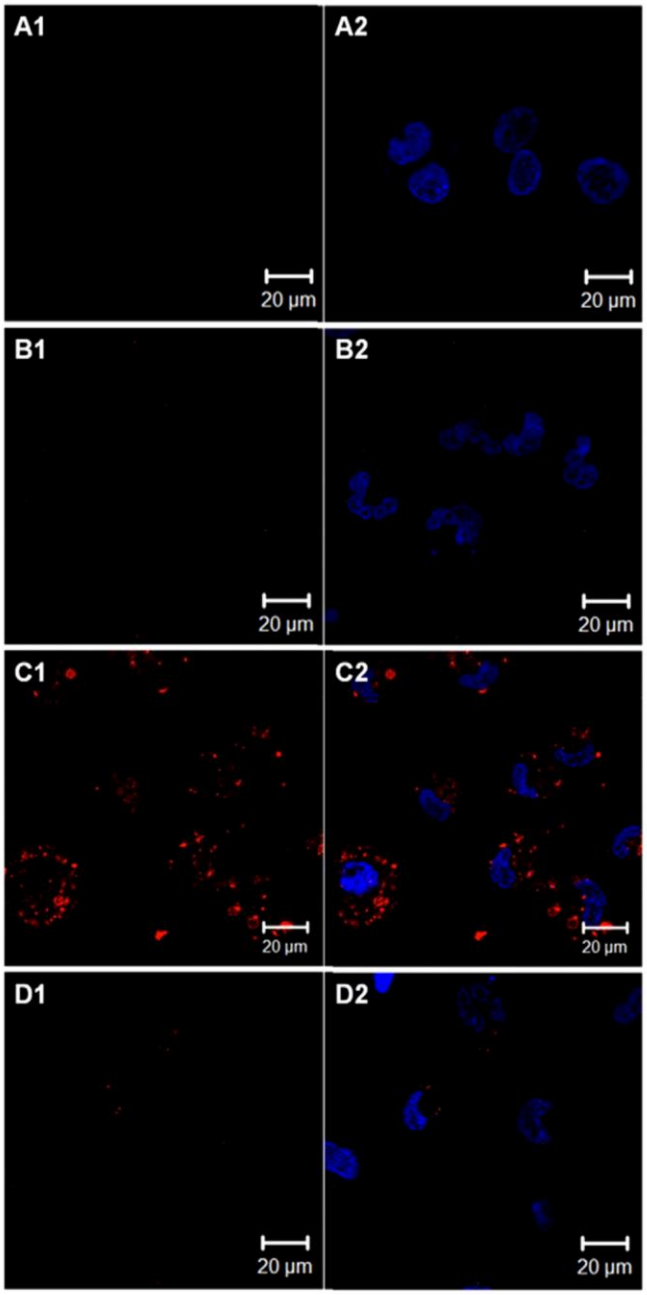

Fig. 8. Confocal microscopy images of DBTRG-05MG cells labeled by QDs-(Tf). (A) Control DBTRG-05MG cells (B) DBTRG-05MG cells incubated with bare QDs, (C) DBTRG-05MG cells incubated with QDs-(Tf) and (D) DBTRG-05MG cells incubated with QDs-(Tf) after TfR saturation. The identification (1) refers to the confocal emission channel LP 565 nm and the identification (2) refers to the overlap of LP 565 nm and Hoechst emission channel (BP 420-480 nm). Scale Bar: 20 μm.

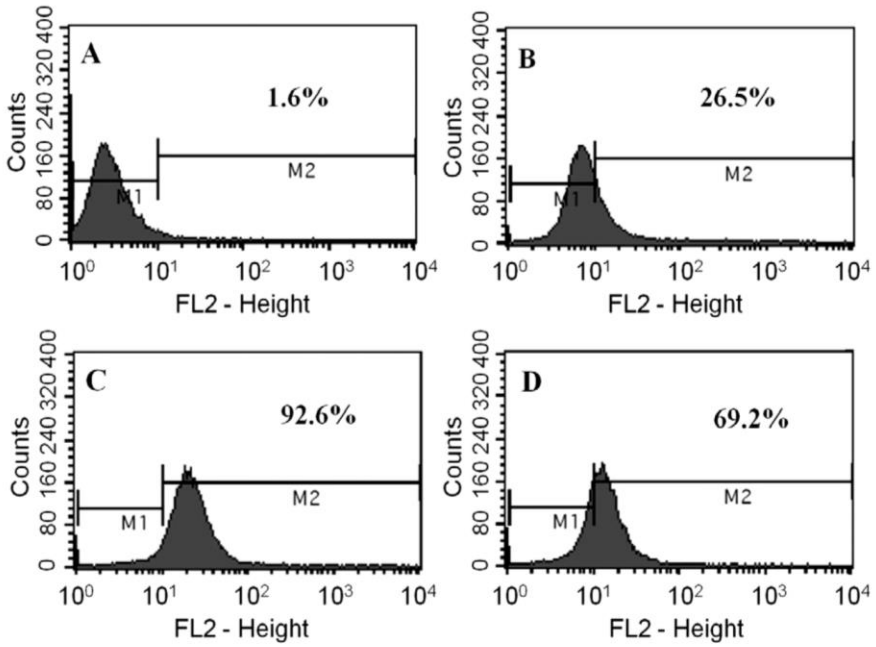

Fig. 9. Flow cytometry analysis in DBTRG-05MG cells. (A) DBTRG-05MG cells in PBS, (B) DBTRG-05MG cells incubated with bare QDs, (C) DBTRG-05MG cells incubated with QDs-(Tf) and (D) DBTRG-05MG cells incubated with QDs-(Tf) after TfR saturation.

These results obtained by confocal microscopy were confirmed through flow cytometry analysis (Fig. 9). Approximately 93% of DBTRG-05MG cells were positively labeled after 1 h incubation with QDs-(Tf) (Fig. 9C), indicating that these cells express a high amount of TfRs. However, when the cells were incubated with bare QDs, a significant decrease in the percentage of labeled cells was observed to about 26% (Fig. 9B). Furthermore, when the TfR was blocked by addition of excess free Tf, 69.2% of DBTRG-05MG cells still presented labeling by QDs-(Tf) (Fig. 9D), corroborating the observations made by confocal microscopy. Taken together, these results denote a more efficient TfR recycling in these cells as compared to U87 or HeLa cells, which can be attributed to a higher metabolic activity of DBTRG-05MG cells [37].

As mentioned before, the DBTRG-05MG cell line was originated from the tumor tissue of a patient owing a recurrent glioblastoma that has been treated with irradiation and chemotherapy [38]. This variant of glioblastoma is more aggressive and resistant to current chemotherapy when compared to that originated from U87 cells [39–41], which can also justify the high metabolic rate and the probably faster recycling of the TfR observed in DBTRG-05MG cells.

Moreover, our results demonstrate that HeLa and DBTRG-05MG cells express and internalize comparable amounts of TfRs, showing 94% and 93% of cells labeled by QDs-(Tf), respectively, while U87 cells present a lower quantity of TfRs, associated to a lower extent of internalization of these receptors, resulting in 57% of cells labeled by QDs-(Tf).

Fig. 10 shows comparative confocal microscopy images of the three cell lines, HeLa (Fig. 10A), U87 (Fig. 10B) and DBTRG-05MG (Fig. 10C), after incubation with QDs-(Tf). As observed, after 1 h of incubation, TfRs are accumulated inside HeLa and DBTRG-05MG cells in endocytic vesicles, indicating an efficient uptake of these receptors. This kind of internalization profile has already been reported previously in HeLa cells [16,19,35]. On the other hand, U87 cells (Fig. 10B) present a lower amount of TfRs, and the conjugates seem to be preferentially located at the cell membrane level, suggesting a lower endocytosis extent when compared to HeLa or DBTRG-05MG cells.

4. Conclusions

QDs-(Tf) were used in this work to quantify the expression and study the traffic of the TfRs in different types of mammalian cancer cells. HeLa and DBTRG-05MG cells present a similar amount of TfR, while U87 cells demonstrated to have a lower quantity of this receptor, when compared to the other two cell lines. Furthermore, DBTRG-05MG cells were more efficient in promoting the recycling of TfRs than HeLa or U87 cells. Therefore, this work suggests that a specific chemotherapeutic drug delivery

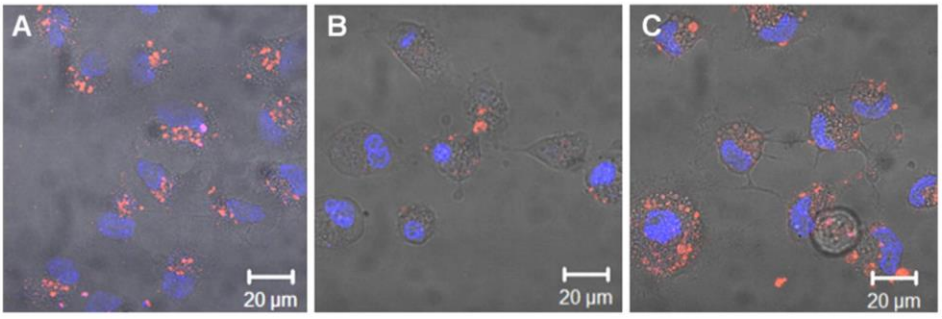

Fig. 10. Confocal microscopy images comparing HeLa, U87 and DBTRG-05MG cells following labeling by QDs-(Tf). These micrographs are overlaps of the confocal filters: LP 565, BP 420–480 nm emission and DIC. (A) HeLa cells, (B) U87 cells and (C) DBTRG-05MG cells. Scale bar: 20 nm.

system targeting TfRs could be more effective in DBTRG-05MG and HeLa cancer cells than in U87. This is an interesting result, particularly taking into consideration the fact that DBTRG-05MG cells are originated from a recurrent glioblastoma, while U87 cells derive from a primary tumor, which suggests that TfRs may play an important role in cancer cell maintenance in recurrent situations.

Overall, the results presented in this study illustrate that QDs-(Tf) can be applied to quantify TfR expression and also to study the dynamics of this receptor in different types of cancer cells. Therefore, we believe that this biophotonic tool can be of great value in future studies in cancer cell biology. The understanding of the molecular aspects of cancer cell biology can help to develop new and effective therapies for this disease, such as those targeting TfRs as a specific and efficient entry pathway for chemotherapeutic drugs.

Author contributions

PECF participated in all experiments involved in the study; MIAP and APMR synthesized and characterized the QDs and conjugates; GALP, MMC and FH analyzed and discussed the bioconjugation; ALC, MCPL, PECF and AF interpreted the microscopy and flow cytometry results; AF, BSS, GALP and CFGCG conceived and designed the experiments. All authors read and approved the final manuscript.

Disclosure

The authors confirm that there are no conflicts of interest in this work.

Acknowledgments

This work was supported by the Brazilian agencies: the Coordination for the Improvement of Higher Education Personnel (CAPES), through the Transnational Cooperation Program CAPES/FCT (331/13), the National Council for Scientific and Technological Development (CNPq), and the Foundation for Science and Technology of Pernambuco (FACEPE). This work is also linked to the National Institute of Photonics (INFo).

Transparency document

The Transparency document associated with this article can be found in the online version.

References

[1] H. Li, Z.M. Qian, Transferrin/transferrin receptor-mediated drug delivery, Med. Res. Rev. 22 (2002) 225–250.
[2] T.R. Daniels, E. Bernabeu, J.A. Rodríguez, S. Patel, M. Kozman, D.A. Chiappetta, E. Holler, J.Y. Ljubimova, G. Helguera, M.L. Penichet, Transferrin receptors and the targeted delivery of therapeutic agents against cancer, Biochim. Biophys. Acta 1820 (2012) 291–317.
[3] W. Ding, L. Guo, Immobilized transferrin Fe(3)O(4)@SiO(2) nanoparticle with high doxorubicin loading for dual-targeted tumor drug delivery, Int. J. Nanomedicine 8 (2013) 4631–4639.
[4] G. Zhai, J. Wu, B. Yu, C. Guo, X. Yang, R.J. Lee, A transferrin receptor-targeted liposomal formulation for docetaxel, J. Nanosci. Nanotechnol. 10 (2010) 5129–5136.
[5] H. Li, H. Sun, Z.M. Qian, The role of the transferrin–transferrin-receptor system in drug delivery and targeting, Trends Pharmacol. Sci. 23 (2002) 206–209.
[6] D.T. Wiley, P. Webster, A. Gale, M.E. Davis, Transcytosis and brain uptake of transferrin-containing nanoparticles by tuning avidity to transferrin receptor, Proc. Natl. Acad. Sci. U. S. A. 110 (2013) 8662–8667.
[7] S. Dixit, T. Novak, K. Miller, Y. Zhu, M.E. Kenney, A.-M. Broome, Transferrin receptor-targeted theranostic gold nanoparticles for photosensitizer delivery in brain tumors, Nanoscale 7 (2015) 1782–1790.
[8] D.J. Yoon, D.S.H. Chu, C.W. Ng, E.A. Pham, A.B. Mason, D. Hudson, V.C. Smith, R.T.A. MacGillivray, D.T. Kamei, Genetically engineering transferrin to improve its in vitro ability to deliver cytotoxins, J. Control. Release 133 (2009) 178–184.
[9] P. Ponka, C.N. Lok, The transferrin receptor: role in health and disease, Int. J. Biochem. Cell Biol. 31 (1999) 1111–1137.
[10] E.W. Müllner, L.C. Kühn, A stem-loop in the 3′ untranslated region mediates iron-dependent regulation of transferrin receptor mRNA stability in the cytoplasm, Cell 53 (1988) 815–825.
[11] L. Jing, K. Ding, S.V. Kershaw, I.M. Kempson, A.L. Rogach, M. Gao, Magnetically engineered semiconductor quantum dots as multimodal imaging probes, Adv. Mater. 26 (2014) 6367–6386.
[12] A. Sukhanova, I. Nabiev, Fluorescent nanocrystal quantum dots as medical diagnostic tools, Expert Opinion on Medical Diagnostics, 2 2008, pp. 429–447.
[13] I.L. Medintz, H.T. Uyeda, E.R. Goldman, H. Mattoussi, Quantum dot bioconjugates for imaging, labelling and sensing, Nat. Mater. 4 (2005) 435–446.
[14] X. Michalet, F.F. Pinaud, L.A. Bentolila, J.M. Tsay, S. Doose, J.J. Li, G. Sundaresan, A.M. Wu, S.S. Gambhir, S. Weiss, Quantum dots for live cells, in vivo imaging, and diagnostics, Science 307 (2005) 538–544.
[15] P. Alivisatos, The use of nanocrystals in biological detection, Nat. Biotechnol. 22 (2004) 47–52.
[16] W.C.W. Chan, S. Nie, Quantum dot bioconjugates for ultrasensitive nonisotopic detection, Science 281 (1998) 2016–2018.
[17] C. Schieber, A. Bestetti, J.P. Lim, A.D. Ryan, T.-L. Nguyen, R. Eldridge, A.R. White, P.A. Gleeson, P.S. Donnelly, S.J. Williams, P. Mulvaney, Conjugation of transferrin to azide-modified CdSe/ZnS core–shell quantum dots using cyclooctyne click chemistry, Angew. Chem. Int. Ed. 51 (2012) 10523–10527.
[18] L.-Y. Guan, Y.-Q. Li, S. Lin, M.-Z. Zhang, J. Chen, Z.-Y. Ma, Y.-D. Zhao, Characterization of CdTe/CdSe quantum dots-transferrin fluorescent probes for cellular labeling, Anal. Chim. Acta 741 (2012) 86–92.
[19] C. Tekle, B.v. Deurs, K. Sandvig, T.-G. Iversen, Cellular trafficking of quantum dot-ligand bioconjugates and their induction of changes in normal routing of unconjugated ligands, Nano Lett. 8 (2008) 1858–1865.
[20] C.G. Andrade, P.E. Cabral Filho, D.P.L. Tenório, B.S. Santos, E.I.C. Beltrão, A. Fontes, L.B. Carvalho, Evaluation of glycophenotype in breast cancer by quantum dot-lectin histochemistry, Int. J. Nanomedicine 8 (2013) 4623–4629.
[21] J. Wang, X. Huang, F. Zan, C.-g. Guo, C. Cao, J. Ren, Studies on bioconjugation of quantum dots using capillary electrophoresis and fluorescence correlation spectroscopy, Electrophoresis 33 (2012) 1987–1995.
[22] G.T. Hermanson, Chapter 3 — zero-length crosslinkers, in: G.T. Hermanson (Ed.), Bioconjugate Techniques, second editionAcademic Press, New York 2008, pp. 213–233.
[23] K.H.G. Carvalho, A.G. Brasi, P.E.C. Filho, D.P.L.A. Tenorio, A.C.A. de Siqueira, E.S. Leite, A. Fontes, B.S. Santos, Fluorescence plate reader for quantum dot-protein bioconjugation analysis, J. Nanosci. Nanotechnol. 14 (2014) 3320–3327.
[24] A.L.C. Cardoso, S. Simões, L.P. de Almeida, N. Plesnila, M.C. Pedroso de Lima, E. Wagner, C. Culmsee, Tf-lipoplexes for neuronal siRNA delivery: a promising system to mediate gene silencing in the CNS, J. Control. Release 132 (2008) 113–123.
[25] P. Dagtepe, V. Chikan, J. Jasinski, V.J. Leppert, Quantized growth of CdTe quantum dots; observation of magic-sized CdTe quantum dots, J. Phys. Chem. C 111 (2007) 14977–14983.
[26] A.L. Rogach, T. Franzl, T.A. Klar, J. Feldmann, N. Gaponik, V. Lesnyak, A. Shavel, A. Eychmüller, Y.P. Rakovich, J.F. Donegan, Aqueous synthesis of thiol-capped CdTe nanocrystals: state-of-the-art, J. Phys. Chem. C 111 (2007) 14628–14637.
[27] W.W. Yu, L. Qu, W. Guo, X. Peng, Experimental determination of the extinction coefficient of CdTe, CdSe, and CdS nanocrystals, Chem. Mater. 15 (2003) 2854–2860.
[28] J.-H. Wang, Y.-Q. Li, H.-L. Zhang, H.-Q. Wang, S. Lin, J. Chen, Y.-D. Zhao, Q.-M. Luo, Bioconjugation of concanavalin and CdTe quantum dots and the detection of glucose, Colloids Surf. A Physicochem. Eng. Asp. 364 (2010) 82–86.
[29] P.E. Cabral Filho, M.I.A. Pereira, H.P. Fernandes, A.A. de Thomaz, C.L. Cesar, B.S. Santos, M.L. Barjas-Castro, A. Fontes, Blood groups antigens studies using CdTe quantum dots and flow cytometry, Int. J. Nanomedicine 10 (2015) 4393–4404.
[30] S. Zhang, J. Li, G. Lykotrafitis, G. Bao, S. Suresh, Size-Dependent Endocytosis of Nanoparticles, Advanced materials (Deerfield Beach, Fla.), 21 2009, pp. 419–424.
[31] K.-T. Yong, H. Ding, I. Roy, W.-C. Law, E.J. Bergey, A. Maitra, P.N. Prasad, Imaging pancreatic cancer using bioconjugated InP quantum dots, ACS Nano 3 (2009) 502–510.
[32] D. Chen, G. Xu, B.A. Ali, K.-T. Yong, C. Zhou, X. Wang, J. Qu, P.N. Prasad, H. Niu, Uptake of transferrin-conjugated quantum dots in single living cells, Chin. Opt. Lett. 8 (2010) 940–943.
[33] V. Biju, T. Itoh, M. Ishikawa, Delivering quantum dots to cells: bioconjugated quantum dots for targeted and nonspecific extracellular and intracellular imaging, Chem. Soc. Rev. 39 (2010) 3031–3056.
[34] P.R. Sager, P.A. Brown, R.D. Berlin, Analysis of transferrin recycling in mitotic and interphase hela cells by quantitative fluorescence microscopy, Cell 39 (1984) 275–282.
[35] M.-Z. Zhang, R.-N. Yu, J. Chen, Z.-Y. Ma, Y.-D. Zhao, Targeted quantum dots fluorescence probes functionalized with aptamer and peptide for transferrin receptor on tumor cells, Nanotechnology 23 (2012) 485104.
[36] S.K. Sahoo, V. Labhasetwar, Enhanced antiproliferative activity of transferrin-conjugated paclitaxel-loaded nanoparticles is mediated via sustained intracellular drug retention, Mol. Pharm. 2 (2005) 373–383.
[37] N.-M. Tsai, S.-Z. Lin, C.-C. Lee, S.-P. Chen, H.-C. Su, W.-L. Chang, H.-J. Harn, The antitumor effects of angelica sinensis on malignant brain tumors in vitro and in vivo, Clin. Cancer Res. 11 (2005) 3475–3484.
[38] C.A. Kruse, D.H. Mitchell, B.K. Kleinschmidt-DeMasters, W.A. Franklin, H.G. Morse, E.B. Spector, K.O. Lillehei, Characterization of a continuous human glioma cell line DBTRG-05MG: growth kinetics, karyotype, receptor expression, and tumor suppressor gene analyses, In Vitro Cell. Dev. Biol. Anim. 28 (1992) 609–614.
[39] M.M. Zulkifli, R. Ibrahim, A.M. Ali, I. Aini, H. Jaafar, S.S. Hilda, N.B. Alitheen, J.M. Abdullah, Newcastle diseases virus strain V4UPM displayed oncolytic ability against experimental human malignant glioma, Neurol. Res. 31 (2009) 3–10.
[40] P.-C. Lin, T.-W. Chiou, H.-J. Harn, An evidence-based perspective of Angelica Sinensis (Chinese Angelica) for cancer patients, in: W.C.S. Cho (Ed.), Evidence-based Anticancer Materia Medica, Springer, Netherlands 2011, pp. 131–153.
[41] R. Wondergem, J.W. Bartley, Menthol increases human glioblastoma intracellular Ca(2+), BK channel activity and cell migration, J. Biomed. Sci. 16 (2009) 90-90.

5 ARTIGO A SER SUBMETIDO AO *JOURNAL OF MATERIALS CHEMISTRY B*

Journal of Materials Chemistry B

ARTICLE

Preparation and characterization of highly fluorescent superparamagnetic nanoparticles for biomedical applications

Mariana P. Cabrera[a,b], Paulo E. Cabral Filho[a], Camila M. C. M. Silva[b], Rita M. Oliveira[c], Carlos F. G. C. Geraldes[c], M. Margarida C.A. Castro[c], Benilde F. O. Costa[d], Marta S. C. Henriques[d], José A. Paixão[d], Luiz B. Carvalho Jr[e], Beate S. Santos[f], Fernando Hallwass[b], Adriana Fontes[a]†, Giovannia A. L. Pereira [b]†.

Received 00th January 20xx,
Accepted 00th January 20xx

DOI: 10.1039/x0xx00000x

www.rsc.org/MaterialsB

This work reports a simple and efficient method for the preparation of new bimodal nanoparticles (BNPs) with small dimensions (*ca.* 17 nm), designed for fluorescence and magnetic applications, consisting of superparamagnetic iron oxide nanoparticles (SPIONs) covalently bound to eight small (*ca.* 3 nm) CdTe quantum dots. The chemical structure of the magnetic part of BNPs is predominantly magnetite, with minor goethite and maghemite contributions, as shown by Mössbauer spectroscopy, which is compatible with the X-ray diffraction data. Their size evaluation by different techniques showed that the SPIONs derivatization process, in order to produce the BNPs, does not lead to a large size increase. The BNPs saturation magnetization (M_s), when corrected for the organic content of the sample, is close to that of the bulk magnetite, indicating that the SPIONs surface functionalization does not change considerably the magnetic properties. The BNPs aqueous suspensions presented stable, highly fluorescent, with a high r_2/r_1 relaxivity ratio and labeled HeLa cells trough fluorescence analysis. These BNPs' properties point to their applications as fluorescent probes as well as negative T_2-weighted MRI contrast agents. Moreover, their potential magnetic response can also be used for fast bioseparation applications.

Introduction

Nowadays, the development of magnetic/fluorescent bimodal nanoparticles (BNPs) has been increasingly motivating the interest of researches[1-7], since this kind of nanomaterials can be versatile for many applications, such as magnetic separation, clinical diagnostics and therapies, optical imaging and nanodevices.[8] Superparamagnetic iron oxide nanoparticles (SPIONs) and fluorescent semiconductor nanocrystals, also called as quantum dots (QDs), are nanosystems that have been greatly studied due to their significant potential applications came from their unique magnetic and optical properties, respectively. Pure iron oxide nanoparticles such as magnetite (Fe_3O_4), maghemite (γ-Fe_2O_3) and hematite (α-Fe_2O_3), with a core diameter between 10 nm and 100 nm, belong to the SPIONs type materials. The superparamagnetic behaviour of these nanoparticles is observed when they are attracted to an external magnetic field and, after its removal, the magnetic system presents no residual magnetism.[9] This interesting feature of SPIONs is related to the proper dispersion/stability of superparamagnetic particles propitiated by their surface modification, *e.g*, coating with silica.[10] It is well known that their application such as contrast and/or therapeutic agents, for example, are directly associated with their chemical structure and size distribution.[9] On the other hand, QDs have also played significant roles in photonic and biomedical applications due to their broad absorption band, narrow emission spectra, high photoluminescence intensity, high photostability and active surface.[11] Due to the wide range of possible QDs biological applications as fluorescent probes with chemical specificity, different synthetic routes, and conjugation strategies, have been reported by some of us.[11-13]

A deeper study of the synthesis, functionalization and conjugation processes involved in BNPs preparation, could lead to the better comprehension of their properties focusing the improvement of potential applications for these nanoplatforms. Although much research has been devoted to this goal, laborious procedures with many steps, and/or the challenges to preserving the fluorescent and magnetic properties, have been reported and also motivated new studies. Among the most commonly used BNPs preparation techniques one can mention procedures using biomolecules as cross-linker,[4, 14-19] coating with silica layers,[2, 20-25] encapsulation of the BNPs,[26-30] reverse microemulsion,[5, 6, 31] and electrostatic interactions.[3, 32-34]

In this context, here, we present a simple and efficient process to produce BNPs from the covalent conjugation of amine-functionalized SPIONs with carboxyl-coated hydrophilic CdTe QDs (Fig. 1). A complete physical-chemical characterization of the BNPs was also performed to evaluate their magnetic and fluorescent properties, as well as to prove the success of the conjugation

[a]*Biophysics and Radiobiology Department, UFPE, Recife, Pernambuco, Brazil*
[b]*Fundamental Chemistry Department, UFPE, Recife, Pernambuco, Brazil*
[c]*Department of Life Sciences, Faculty of Science and Technology, and Coimbra Chemistry Center, UC, Coimbra, Portugal.*
[d] *CFisUC, Department of Physics, Faculty of Science and Technology, UC, Portugal.*
[e] *Biochemistry Department and Laboratory of Immunopathology Keizo Asami, UFPE, Recife, Pernambuco, Brazil.*
[f] *Pharmaceutical Science Department, UFPE, Recife, Pernambuco, Brazil.*

**These authors contributed equally to this work.*

† Corresponding authors: Adriana Fontes, Av. Prof. Moraes Rego, S/N, Biophysics and Radiobiology Department, CCB, UFPE, 50670-901 Recife, PE, Brazil. Tel.: +558121267818, e-mail: adriana.fontes.biofisica@gmail.com; Giovannia A. L. Pereira, Av. Prof. Moraes Rego, S/N, Fundamental Chemistry Department, CCEN, UFPE, 50670-901 Recife, PE, Brazil. Tel.: +558121267412, e-mail: giovannia_pereira@yahoo.com.br;

Electronic Supplementary Information (ESI) available: [details of any supplementary information available should be included here]. See DOI: 10.1039/x0xx00000x

process. Moreover, the potential of BNPs as fluorescent probe was confirmed through the labeling of HeLa cells, by confocal microscopy and flow cytometry; and as MRI contrast agent, by relaxometric analyses. We believe that we developed BNPs with valuable properties to be applied as promising nanosystems for optical and magnetic techniques, such as probes for fluorescence analysis and/or contrast agents for magnetic resonance imaging (MRI).

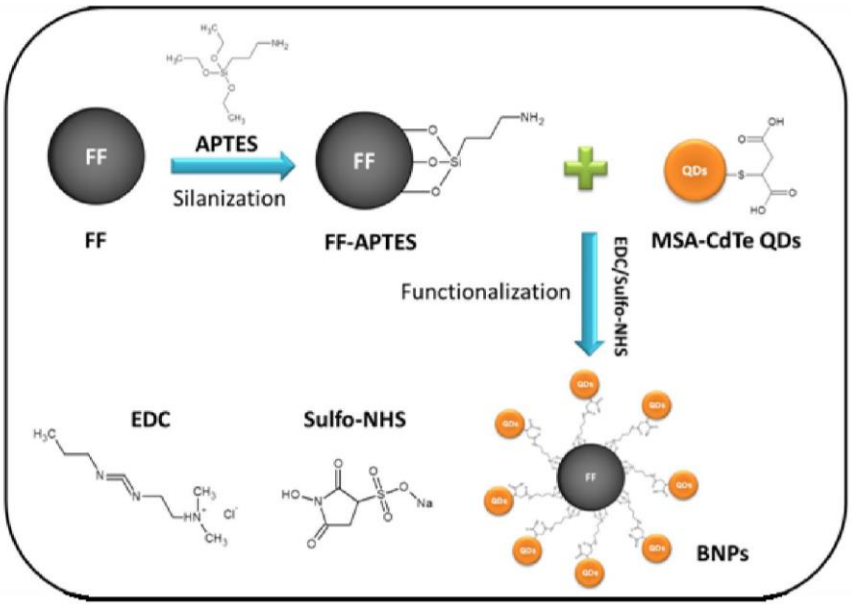

Fig. 1 Schematic representation of bimodal nanoparticles (BNPs) synthetic procedure.

Materials and Methods

Materials

The reagents $FeCl_2 \cdot 4H_2O$, $FeCl_3 \cdot 6H_2O$, NH_4OH, 3-aminopropyltriethoxysilane (APTES), 3-mercaptossuccinic acid (MSA), cadmium perchlorate, metallic tellurium, sodium borohydride, N-hydroxysulfosuccinimide sodium salt (Sulfo-NHS), Dulbecco's modified Eagle's medium with high glucose (DMEM), penicillin and trypsin were purchased from Sigma-Aldrich. N-ethyl-3-(3-dimethylaminopropyl) carbodiimide hydrochloride (EDC) was obtained from Fluka. Furthermore, Gibco products such as fetal bovine serum (FBS) and Dissociation Buffer were also used. All other chemicals were of the highest purity available commercially. All reagents were used without further purification.

Preparation of nanosystems

Synthesis and functionalization of the ferrofluid

The aqueous magnetic ferrofluid (FF) was synthesized by the alkaline co-precipitation of Fe^{2+} and Fe^{3+} salts. Briefly, $FeCl_2 \cdot 4H_2O$ and $FeCl_3 \cdot 6H_2O$ (2:3 molar ratio) were dissolved in 2 M HCl aqueous solution and submitted under vigorous stirring at room temperature (RT). Then, 50 mL of ammonium hydroxide (7 M) was added to the solution containing the iron chloride mixture under vigorous stirring. The magnetic preparation was heated at 50 °C in an ultrasound bath for 30 min. The resulting suspension was cooled to RT and washed with ultrapure water. The washing process was performed by magnetic decantation using a super-strong neodymium magnet, also known as NdFeB.

The functionalization process was carried out with 3-aminopropyltriethoxysilane (APTES), a coupling silane agent that allows the functionalization of the magnetic surface with amine groups. For this, the bare ferrofluid solution (*ca.* 35 µM - forty-fold diluted) was treated with APTES (2.5 % v/v prepared in acetone) for 2 h at RT under stirring. After this, the ferrofluid functionalized with APTES (FF-APTES) was washed with ultrapure water as described above.[35]

Synthesis of MSA capped CdTe QDs

MSA-CdTe QDs suspension was synthesized in aqueous solution by a method previously described by some of us.[12, 36] After the synthesis procedure, QDs were optically characterized by electronic absorption (UV-1800 UV/Vis spectrophotometer, Shimadzu) and emission spectroscopy (LS 55, PerkinElmer) at 365 nm excitation.

Preparation of the bimodal nanoparticles (BNPs)

The bimodal system was obtained by covalent binding of QDs and FF-APTES nanoparticles. For this, carboxyl coated MSA-CdTe QDs (1 mL, *ca.* 0.8 µM) were activated by EDC (4.4 mg mL^{-1}) and Sulfo-NHS (5.5 mg mL^{-1}). Then, FF-APTES nanoparticles (0.5 mL, *ca.* 0.1 µM) were added into the activated QDs' suspension. The resulting mixture composed of fluorescent and magnetic nanoparticles (8:1) was then kept overnight under stirring at RT. After this, BNPs were collected by NdFeB magnet, washed and redispersed in ultrapure water. Optical characterizations of BNPs were also carried out by electronic absorption and emission spectroscopy, as described previously.

Physico-chemical characterization

Scanning electron microscopy coupled with energy dispersive X-ray spectroscopy (SEM/EDX)

The morphology of the FF and FF-APTES nanosystems, as well as BNPs, was investigated by scanning electron microscopy (SEM, Evo SL15, Zeiss). Energy dispersive X-ray (EDX) spectroscopy coupled to SEM was also used to identify the elemental composition of the nanosystems. The EDX analysis was performed by the system INCA (Oxford Instruments). Samples were prepared by coating the nanosystems with a thin gold layer under reduced pressure (Q150T ES).

Transmission electron microscopy (TEM)

TEM images were acquired with an FEI Tecnai G2 microscope operating at an accelerating voltage of 200 kV. Samples were dispersed in a sodium acetate aqueous solution under sonication, spotted by the drip of a carbon grid (400 mesh) and subsequent air-drying at RT. Average particle sizes (D_{TEM}) were calculated by analysing more than 150 particles randomly selected from TEM micrographs.

X-ray diffraction (XRD)

Powder XRD measurements were performed at room temperature over the 2θ range of 20–130°, and a scanning step width 0.005° in a Bruker AXS D8 Advance diffractometer equipped with Ni-filtered Cu Kα radiation (λ = 1.5406 Å) and a Lynxeye detector (operated with a narrow energy window for discrimination against Fe fluorescence background). Average particle sizes (D_{XRD}) were estimated from the width of the diffraction lines using the Debye-Scherrer equation. The analysis of the XRD patterns was also performed by full pattern profile refinement (Pawley method) using the computer program TOPAS.[37] The fundamental parameters (FP) approach was used to model the reflection profiles. The instrumental resolution was calculated from a full modelling of the X-ray optics.

Mössbauer spectroscopy (MS)

^{57}Fe Mössbauer spectra were recorded at RT in a conventional transmission geometry spectrometer using a triangular driving, with 30 mCi Co/Rh source. The spectra were analyzed by using the least squares method assuming Lorentzian line shapes and also by a hyperfine field distribution with the NORMOS program,[38] WissEl GmbH, Germany. The isomer shifts obtained in the fitting procedures are relative to α-Fe at RT. Powder samples were measured in acrylic holders of 1.5 mm diameter, covering all the surface area. When necessary, the samples were mixed with boron nitride to be able to cover the whole surface.

Magnetization measurements

Magnetic properties were measured using a vibrating sample magnetometer (Quantum Design Dynacool PPMS-9T system). The magnetization was studied as a function of applied magnetic field [$M(H)$] and temperature [$M(T)$]. Hysteresis cycles were measured at 2 K and 298 K up to 5 T. The thermal dependence of the magnetization was measured in ZFC (zero field cooling) and FC (field cooling) cycles from 2 K to 350 K under applied field of 1000 Oe.

Fourier transform infrared (FTIR)

FTIR spectra were recorded (Spotlight^{TM} 400, PerkinElmer) in the 400–4000 cm^{-1} range, at RT. The spectra of dried samples were obtained using KBr pellets method (Aldrich, FT-IR spectroscopy grade) containing 1 wt% of the nanosystems.

Thermogravimetric analysis (TGA)

TGA was carried out on a Perkin-Elmer STA6000 simultaneous (DSC/TG) system, in the temperature range of 50 – 900 °C at a heating rate of 10 °C min^{-1} under a nitrogen flow (20 mL min^{-1}).

Zeta potential (ζ) measurements

The ζ measurements of FF, FF-APTES, and BNPs, to evaluate changes on FF charge surfaces before and after conjugation with QDs, were carried out in a NanoZS equipment (Malvern) and data were analyzed by the *Technology Software 7.01*. All samples were washed using ultrapure water. The **ζ** was measured at RT in a pH of *ca.* 6.0.

Flame atomic absorption spectrometry (FAAS)

The iron concentration of the colloidal dispersions was determined by FAAS using an atomic absorption spectrometer (SpectrAA 220 IFS, Varian) equipped with an air-acetylene flame (air and acetylene flow rate: 13.5 and 2.0 L min^{-1}, respectively). For the analysis, the following conditions were used: iron hollow-cathode lamp as the radiation source, the wavelength at 372.0 nm, the lamp current of 5.0 mA and a slit width of 0.2 nm.

Nuclear relaxation measurements

T_1 and T_2 proton relaxation times of aqueous nanosystems dispersions were measured at 298 K by magnetic resonance relaxometry (Bruker Minispec mq20 relaxometer operating at a magnetic field of 0.47 T, corresponding to a proton Larmor frequency of 20 MHz). T_1 values were measured using an inversion recovery pulse sequence, while T_2 values were measured using a Carr–Purcell–Meiboom–Gill (CPMG) pulse sequence and by varying the time interval between two consecutive refocusing pulses in a train of 180° applied pulses.

A linear dependence between the inverse proton relaxation times (*i.e.* the water proton relaxation rates $1/T_i$, i = 1, 2) and the iron concentration was obtained for the three magnetic nanomaterials, in accordance with the following equation:

$$\frac{1}{T_{i,obs}} = \frac{1}{T_{i,0}} + r_i[\mathrm{Fe}] \qquad \text{Equation 1}$$

where $T_{i,obs}$ (i = 1, 2) is the relaxation time measured experimentally in the presence of the magnetic nanomaterial, $T_{i,0}$ is the relaxation time of pure water in the absence of the contrast agent, [Fe] is the iron concentration (mM) in the contrast agent and r_i is the longitudinal (i = 1) or transverse (i = 2) relaxivity (*i.e.* proton relaxation rate enhancement *per* mM Fe).

Cell studies

HeLa cells (human epithelial cervical carcinoma) were used as a model to evaluate the labeling by the bimodal systems. Cells were cultured according to a previously procedure described by some of us.[12] Cells were then seeded into a 6-well plate (2.0 x 10^5 cells/well - Thermo Scientific^{TM} BioLite) for flow cytometry studies and in an 8-well plate (2.0 x 10^4 cells/well - µSlide IbiTreat, Germany) for confocal microscopy analysis. After 24 h of incubation in a 6-well or 8-well plate culture, cells were washed with phosphate-buffered saline (PBS 1X, from now on named as PBS) and the following experimental conditions were assayed: (I) control cells and (II) cells with BNPs (1:1 v/v). Systems were incubated for 90 min.

For flow cytometry (FACSCalibur™, Becton Dickinson) analysis, HeLa cells, after incubation time, were detached with 0.25 % of trypsin in Dissociation Buffer followed by trypsin inactivation with DMEM containing FBS. Cell suspensions were then washed three times with PBS and pelleted by centrifugation 1,200 x g, 30 s (MiniSpin - Eppendorf). Around 20,000 events were acquired for each experimental condition (I and II) at 488 nm excitation. The emission was detected with the long pass filter 670 nm (FL3) and the data were processed by the Cell Pro Software (Cell Quest™, Becton-Dickinson).

For confocal analysis, cells plated in 8-well plates were washed three times with PBS, after the incubation time. Cells were also stained, for 5 min, with the fluorescent DNA-binding dye Hoechst 33342 (at a final concentration of 1 μg mL^{-1}) before being evaluated under a fluorescence confocal microscope (Zeiss LSM 510 META). The dye Hoechst fluorescence was excited at 365 nm and collected by a band pass filter (BP 420-480 nm), while, the labeling by BNPs was excited at 530 nm and evaluated by a long pass filter 565 nm.

Results and Discussion

Physico-chemical characterization

Fourier transform infrared (FTIR)

The FTIR spectra of the bare FF, FF-APTES, and BNPs (Fig. S1) suggested that APTES molecules were present onto the surface of the FF magnetic nanoparticles and that MSA-CdTe QDs were conjugated to FF-APTES and form BNPs. More information about these results can be found in the Supporting Information.

XRD, SEM/EDX and TEM

The three magnetic systems were characterized by XRD, SEM/EDX, and TEM in order to provide information about their crystalline structure, morphology, composition and particle size.

X-ray diffraction profiles of all samples (Fig. 2) exhibit the typical Bragg reflections of ferrites, indicating that the nanomaterials present a cubic spinel structure (space group $Fd\bar{3}m$) and are crystalline. In order to identify the nature of the iron oxides, the diffractograms were fitted using the Pawley method, considering a single phase of maghemite (γ-Fe_2O_3) or magnetite (Fe_3O_4). Fig. 2 also allows observing similar peaks for all magnetic systems after the treatment processes (silanization and conjugation with QDs) when compared to bare FF, indicating that the treatments did not affect the crystalline structure of the nanomaterials. Nevertheless, it is not possible to state that no change has taken place in the magnetic systems. The oxidation processes (*e.g.* addition of functionalizing molecules) can take to more than one iron oxide phase in the samples[39], due to high oxygen sensitivity of magnetite (Fe_3O_4).[40] XRD results do not allow distinguishing between magnetite and maghemite because of XRD parameters were very close (Table S1). Recently, one of the authors of this report studied SPIONs obtained by thermolysis methods.[41] In that study, it was also not possible to distinguish magnetite from maghemite by XRD analyses. Only Mössbauer measurements permitted to distinguish magnetite and maghemite oxides. In addition, magnetite, non-stoichiometric magnetite, and maghemite were also not distinguished by XRD analyses, in a magnetic fluorescent nanocomposite obtained from magnetite and CdTe, using dodecyl-amine (DDA) as cross-linker, for bio-imaging.[42]

Average particle sizes (D_{XRD}) in the examined samples were fitted in the full profile model using the Debye-Scherrer equation:

$$FWHM = k\lambda / D_{XRD} \cos\theta \qquad \text{Equation 2}$$

where the Debye-Scherrer constant is k = 1, FWHM is the full width at half-maximum of the XRD peak, λ is the incident X-ray wavelength and θ is the diffraction angle. The volume-weighted thickness, L_v, of the crystallite domains perpendicular to the diffraction planes as determined by the integral breadth of the Lorentzian contribution to reflection profiles are also shown in the Supporting Information (Table S1). This parameter will be used later to compare the size of nanosystems obtained through the magnetization measurements. The bare FF and BNPs systems exhibited an average particle size of about 15.0(1) nm. After the silanization process, a slight and barely increase in size for the FF-APTES, 15.3(1) nm, was observed. The number between parentheses represents the error, which is associated with the uncertainty corresponding to the last number of the measurement.

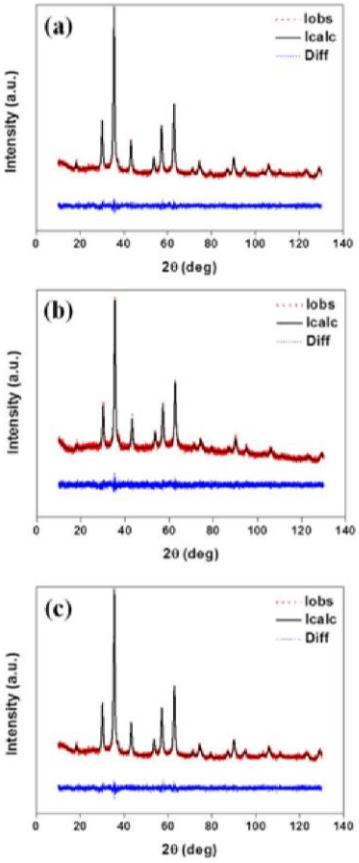

Fig. 2 X-ray diffraction profiles (red lines) of magnetic systems (a) bare FF, (b) FF-APTES and (c) BNPs and their respective Pawley refinement. The black line represents the model obtained from Pawley refinement and the blue line represents the difference between the experimental data and the fit.

The studies by SEM allowed assessing the effect of surface modifications on morphological changes in the investigated samples, showing that there are no significant modifications on their morphologies after the silanization and conjugation procedures. Fig. 3 shows the SEM images and the respective qualitative chemical composition of the samples obtained by EDX analysis. On the other hand, EDX analysis showed changes in the elemental composition of samples. The bare FF, being an iron oxide, presented only peaks of O and Fe. After silanization treatment with APTES, Si and N peaks also appeared, while for the bimodal system peaks related to Cd, Te and S were also observed. The peaks observed at 1.7, 2.2, 8.5, 9.7, 10.3 and 11.6 keV, corresponding to the Au element, while that one at 0.3 keV is attributed to the carbon, which came from the sample preparation procedures for the SEM analysis.

TEM images (Fig. 4) reveal that all the iron oxide nanomaterials exhibit a quasi-spherical shape. The bare FF presented an average diameter *ca.* 11(2) nm. After silanization and conjugation processes, the FF-APTES and BNPs systems exhibited a size of *ca.* 15(2) and 17(2) nm, respectively. The low variation in average diameter of the magnetic systems can be related to the small size of the QDs. The TEM result is not sufficient to affirm that the silanization and conjugation process were responsible for any variation in the dimensions of the systems. On the other hand, it is possible to confirm the success of these processes by the EDX results (Fig. 3).

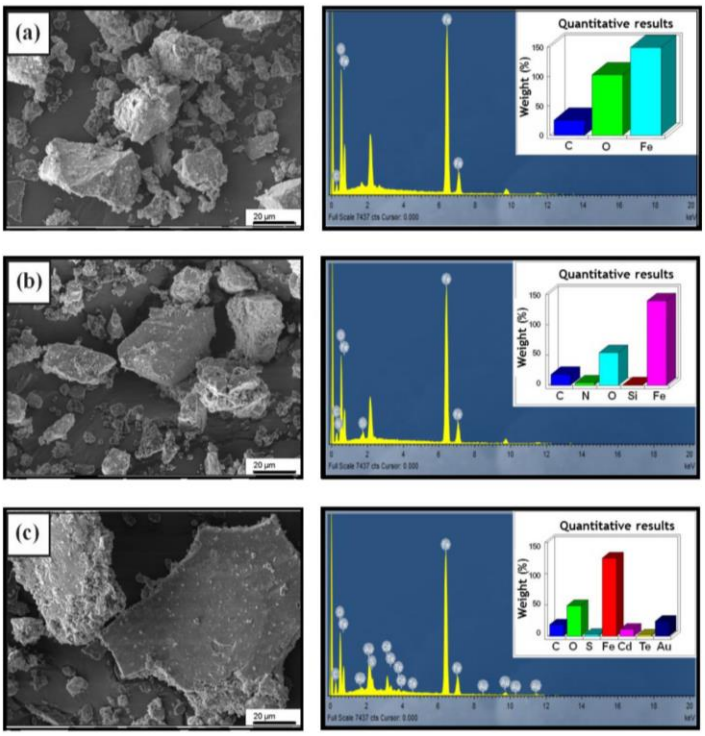

Fig. 3 Representative SEM images at magnification x1,500 (left column, scale bar = 20 µm) and EDX analysis (right column) for all magnetic nanosystems: (a) bare FF, (b) FF-APTES and (c) BNPs. The inset graphs at the right column represent an estimative of the amounts of chemical elements present in the samples.

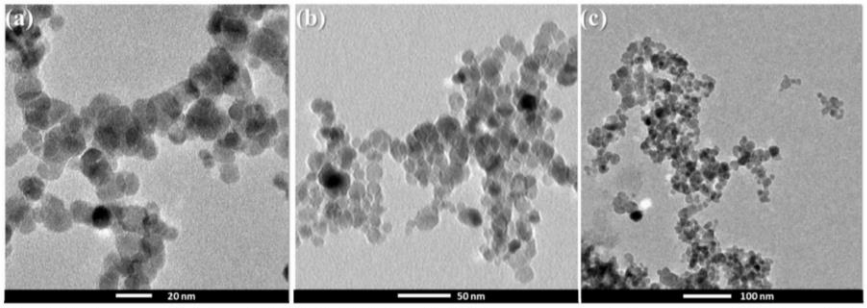

Fig. 4 Representative TEM images of (a) bare FF, (b) FF-APTES and (c) BNPs system. Scale bars: 20 nm (a), 50 nm (b) and 100 nm (c).

Mössbauer spectroscopy

Mössbauer spectra (^{57}Fe) were performed at RT for the three samples and showed the presence of sextets in all spectra (Fig. 5). Parameters including isomer shift (IS), quadrupole splitting (QS), hyperfine magnetic field (B_{hf}), line width at half maximum (Γ) and relative area (Area) were obtained through fitting of the spectra (Table 1). Some degree of superparamagnetism is possible to exist as the sextets have large line widths, Γ. This is supported by the hyperfine field distributions (Fig. S2), where small values of B_{hf} are seen. The spectrum recorded for bare FF is ascribed to nanosized magnetite with two sextets belonging to site A (Fe^{3+} ions) with B_{hf} = 48.5(1) T and IS = 0.33(1) mm s^{-1}, and to the site B (mixed Fe^{2+} and Fe^{3+} ions) with B_{hf} = 44.0(1) T and IS = 0.34(1) mm s^{-1}, respectively.[43] The line width obtained for the sextet of the B-site is quite large, Γ = 1.38(1) mm s^{-1}, possibly due to particle size distribution and presence of different iron environments leading to intermediate iron oxidation states. A crystalline bulk magnetite has B_{hf} = 49.2 T and IS = 0.26 mm s^{-1} for site A and B_{hf} = 46.1 T and IS = 0.67 mm s^{-1} for site B and a ratio of 1:2 for site A:site B.[44] Magnetite has an inverse-spinel structure, in which the A sites (tetrahedral sites) are occupied by Fe^{3+} ions and B sites (octahedral sites) by Fe^{2+} and Fe^{3+}.[44, 45] For nanoparticulate systems, the Mössbauer interpretation is more complex due to the coexistence of a few iron oxide phases or even due to surface and size effects. Kalska-Szostko et al.[46] described that for nanosystems, the broad component with the lowest value of the hyperfine magnetic field is due to relaxation effect characteristics. We have obtained similar values, but IS for the second sextet is significantly lower, possibly indicating the presence of some other iron mineral such as maghemite or goethite. As observed by the broad line widths obtained and the broad hyperfine field distribution, the components of the spectrum are not fully resolved and there may be more than two sextets presented in the spectrum. The deviation from the ideal ratio (1:2) of the iron in tetrahedral and octahedral positions obtained from the sub-spectra area is due to the smaller particle size compared to their bulk in counterpart.[47] Nonstoichiometric magnetite is characterized by the presence of vacancies at the octahedral sites and may be represented as $(Fe^{3+})_A(Fe^{2+}_{1-3x}Fe^{3+}_{1+2x}\delta_x)_BO_4$ where A and B are the tetrahedral and octahedral sites respectively and δ represents a vacancy.[46] The degree of non-stoichiometry (X) can be estimated from the area ratio of the sextets corresponding to Fe ions in the A and B sites using the empirical formula.[48]

$$X = \frac{(2-r)}{(6+5r)} \qquad \text{Equation 3}$$

where r = A_B/A_A (A_A and A_B being the area of the sextets corresponding to A and B sites).

The spectrum recorded for FF-APTES also shows a sextet with parameters ascribed to goethite. Crystalline bulk goethite has B_{hf} = 38.0 T and IS = 0.37 mm s^{-1}.[44] The parameters determined in our fitting procedure and ascribed to goethite, were B_{hf} = 40.2(1) T and IS= 0.38(1) mm s^{-1}. For this sample, the line width was very large, 1.43(1) mm s^{-1}. The line widths obtained for the magnetite sextets are also very large, in particular for the second sextet, being also valid the assumption of the existence of other non-resolved sextets, possibly maghemite (the IS of the second sextet is also too small when compared to IS = 0.67 mm s^{-1} for site B of magnetite). The hyperfine field distribution corresponding to the spectrum of FF-APTES was broad and showed low fields, which indicated the presence of possible superparamagnetism. This distribution gave a B_{hf} equal to 42.8(1) T and σ equal to 9.4(1) T.

For BNPs, the recorded spectrum showed about 15% of crystalline maghemite, with parameters of B_{hf} = 50.2(1) T and IS = 0.35(1) mm s^{-1}.[44] However, this percentage must be underestimated, because as discussed before, the line widths of magnetite and goethite were very large and IS of the second sextet of magnetite is very low. Also, the presence of superparamagnetism should not be disregarded, as a broad hyperfine field distribution is obtained together with low values of hyperfine fields. For this sample, a mean hyperfine field of $\langle B_{hf} \rangle$ = 42.1(1) T and a standard deviation of σ = 10.0(1) T was obtained.

The degree of non-stoichiometry was estimated from Equation 3 for all samples, and X = 0.090, 0.0436 and -0.0206 were obtained for FF, FF-APTES, and BNPs respectively. It is important to mention that the presence of goethite and maghemite (probably in low quantity) did not affect the magnetic properties of the bimodal system. Thus, we can consider that the magnetite was the major constituent of all the systems.

Table 1. Room temperature Mössbauer parameters obtained for the samples. IS - isomer shift, QS - quadrupole splitting, B_{hf} - hyperfine field, Γ- Lorentzian width at half maximum.

Sample	IS[b] (mm s^{-1})	QS (mm s^{-1})	B_{hf} (T)	Γ (mm s^{-1})	Area (%)	Site	Iron oxide phases[c]
FF	0.33(1)	0.00(1)	48.5(1)	0.68(1)	49.9	Site 1	Magnetite Fe_3O_4 (A)
	0.34(1)	-0.03(1)	44.0(1)	1.38(1)	50.1	Site 2	Magnetite Fe_3O_4 (B)
FF-APTES	0.34(1)	0.00(1)	49.5(1)	0.53(1)	29.6	Site 1	Magnetite Fe_3O_4 (A)
	0.34(1)	-0.03(1)	46.3(1)	0.82(1)	42.2	Site 2	Magnetite Fe_3O_4 (B)
	0.38(1)	-0.05(1)	40.2(1)	1.43(1)	28.2	Site 3	Goethite α-FeOOH
BNPs[a]	0.34(1)	-0.002(1)	48.2(1)	0.53(1)	19.8	Site 1	Magnetite Fe_3O_4 (A)
	0.35(1)	-0.02(1)	44.8(1)	1.11(1)	46.8	Site 2	Magnetite Fe_3O_4 (B)
	0.46(1)	-0.30(1)	38.5(1)	1.59(1)	18.6	Site 3	Goethite α-FeOOH
	0.35(1)	0.000(1)	50.2(1)	0.41(1)	14.8	Site 4	Maghemite γ-Fe_2O_3

[a]BNPs synthesized from FF-APTES and MSA-CdTe QDs.

[b] The isomer shift is relative to α-Fe at RT.

[c] The sites are named after that the number of sextet sites was determined by fitting procedure (Fig. 5).

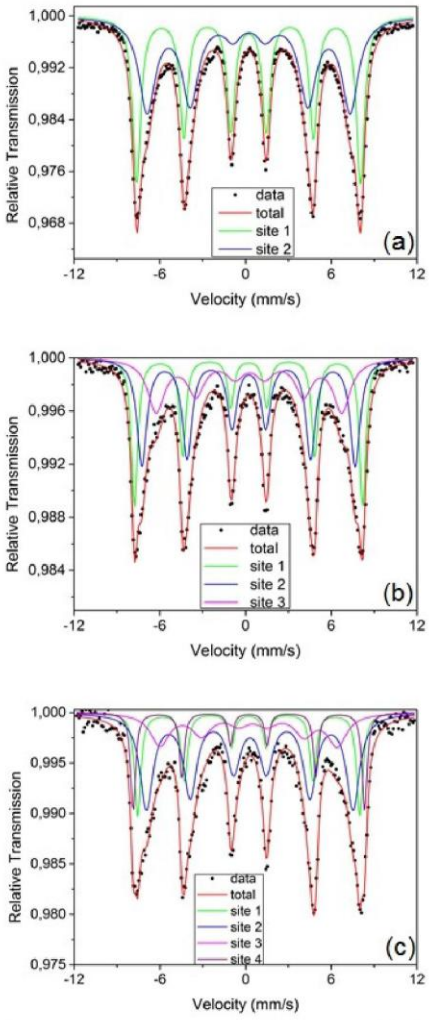

Fig. 5 Mössbauer spectra of samples (a) bare FF, (c) FF-APTES and (d) BNPs.

Magnetic properties

A detailed study on the magnetization (*M*) of the iron oxide nanoparticles as a function of applied magnetic field (*H*) and temperature (*T*) was performed by magnetometry.

Magnetization (H)

Fig. 6 and Fig. S3 show the *M*(*H*) behaviour of bare FF, FF-APTES, and BNPs systems obtained from ferrofluid functionalized with APTES and conjugated to MSA-CdTe QDs, measured at 298 K and 2 K, respectively. All systems showed a typical superparamagnetic behaviour at both temperatures with hysteresis loops in the *M*(*H*) curves with the typical Langevin-like shape. The main magnetic properties of all systems studied obtained from the fitting of the experimental *M*(*H*) curves performed at 298 K are shown in Table 2. The saturation magnetization (M_s) obtained for the bare FF (72.5 emu g^{-1}) at 298 K is lower than the typical value for the bulk magnetite (91 emu g^{-1}) and for bulk maghemite (78 emu g^{-1}).[49] The functionalization and conjugation processes with APTES and MSA-CdTe QDs, respectively did not significantly affect the magnetic properties of the iron oxide nanoparticles. The FF-APTES and BNPs systems showed M_s at 298 K of 70.2 and 78.1 emu g^{-1}, respectively. A decrease of about 16% of the magnetization relative to the bulk magnetite was observed for the M_s of the BNPs. However, when these values were corrected to the non-oxide content of the samples, as determined from the TGA analysis (See SI, Fig. S4), the magnetization values attained 72.9 and 91.8 emu g^{-1}, respectively, the latter value being equal to that reported for bulk magnetite. The preservation of the magnetic properties of the iron oxide nanoparticles after the conjugation indicates that this process did not affect considerably the chemical composition (formation of some non-magnetic iron oxide) of the BNPs. To the best of our knowledge, several researchers published the synthesis of bimodal nanoparticles with M_s values lower than 45 emu g^{-1}.[2, 3, 5, 16, 17, 24, 25, 28, 42, 50-52] Only Ahmed *et al.*[53] prepared BNPs with an M_s value of 65 emu g^{-1} by a layer-by-layer method, where Fe_3O_4 nanoparticles were dispersed in an organic solvent and green CdTe QDs were conjugated by electrostatic interaction. Even if a lower M_s values would be expected for nano-sized systems, it is not clear whether such reported low values of magnetization are not due to use of raw masses uncorrected for the organic content of the samples. The M_s values measured at 2 K showed only a small increase with respect to the room temperature values, as expected (Fig. S3).

Remanent magnetization (M_r) and coercivity (H_c) values are also shown in Table 2. It can be observed that coercivity values did not change for the bare FF and the BNPs. These results indicate that the process used to conjugate iron oxide nanoparticles to MSA-CdTe QDs did not affect the magnetic dipole coupling interaction of the magnetic nanoparticles. The superparamagnetic behaviour is clearly shown in the *M*(*H*) curves and it is also reflected in the low M_r/M_s ratio, as well as in the small H_c values.

Magnetization (T)

The thermal dependence of the magnetization was measured in ZFC and FC curves under applied field of 1000 Oe (Fig. 7), which provide important information to better understand the magnetic properties of the systems under study. The blocking temperature (T_B), irreversibility temperature (T_{irr}) and distribution profile of nanoparticles diameters can be obtained from those curves. T_B was obtained as the temperature where the magnetization is maximum in the ZFC curve, whereas T_{irr} was determined as the temperature where ZFC and FC curves coalesce. The ferrofluid functionalized with APTES showed a similar T_B value (~ 120 K) when compared with the bare FF (~ 100 K). The T_{irr} for the FF-APTES was lower (~ 235 K) than for the ferrofluid untreated with silane agent (~ 315 K). In addition, the BNPs displayed a T_B value at ~ 160 K and T_{irr} value at ~ 250 K. This thermal parameter marks the transition from a kinetically responsive magnetic moment to a kinetically unresponsive moment with decreasing of temperature, i.e. the transition between a blocked and a superparamagnetic systems.[54] On the other hand, T_{irr} is usually associated with the blockage of larger particles in the system, assuming the existence of a distribution of particle sizes. Therefore, a large difference between T_{irr} and T_B indicates a larger distribution of particle sizes. For BNPs system (Fig. 7c), it is possible to observe close values for both parameters, which indicates the existence of a narrow particle size distribution. By comparison of ZFC-FC curves of bare FF and BNPs, it was clear that functionalization and conjugation processes with APTES and CdTe-MSA QDs, respectively, avoided strong aggregation and decreased dipolar interactions.

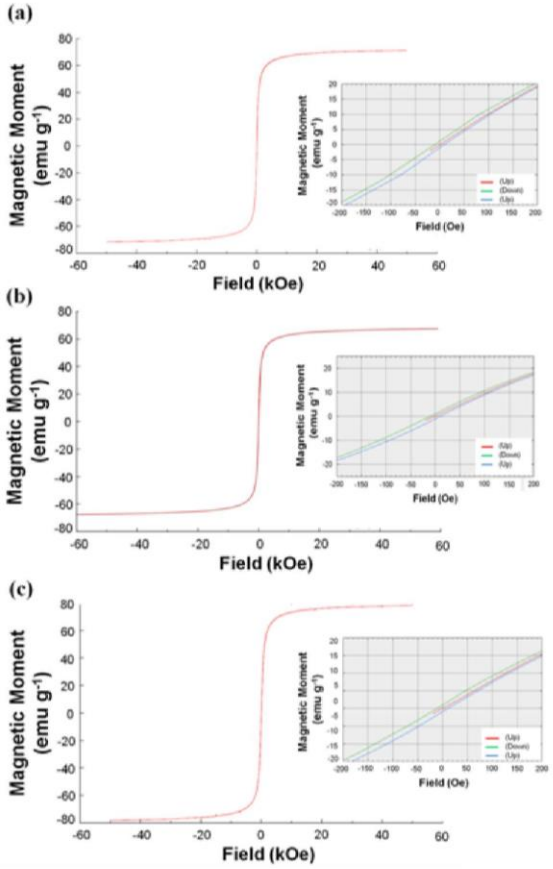

Fig. 6 *M*(*H*) loops between - 50 kOe and + 50 kOe at 298 K of the (a) bare FF, (b) FF-APTES and (c) BNPs; inset: magnified *M(H)* curves near the coercive field. The magnetization values of the curves are raw data, not yet corrected for the small organic content of the samples.

Table 2. Main magnetic properties of all systems studied obtained from the *M*(*H*) curves performed at 298 K. Saturation magnetization values are normalized to mass values of both uncorrected (M_s) and corrected values (M_s^c) for the small organic content of the samples.

	M_s (emu g^{-1})	M_s^c (emu g^{-1})	M_r (emu g^{-1})	Remanence M_r/M_s	H_c (Oe)
Bare FF	72.5	75.3	1.0	0.0138	10
FF-APTES	70.2	72.9	1.0	0.0142	10
BNPs[a]	78.1	91.8	1.0	0.0128	10

[a] BNPs synthesized from FF-APTES and MSA-CdTe QDs.

Size determination of superparamagnetic nanoparticles from magnetization curves

The hysteresis curves were analyzed by fitting a Langevin function and assuming a lognormal distribution of particle sizes, according to Chen et al.[55] Two models were tested: a uniform model, and a model with a magnetite ferromagnetic core and a paramagnetic shell (core-shell model). The results of these fits are shown in Table 3. Parameters μ and σ are the mean and the standard deviation of ln*v* (assuming a lognormal distribution of particle sizes, *v* = particle volume). D_0 and [illegible] are the core diameter and paramagnetic shell thickness. These parameters refer to the particle-volume-weighted average diameter (D_{vd}) of the nanoparticles. These fits have been performed with magnetization normalized to the iron oxide content of the samples, this content being determined from the mass of the samples corrected by the organic fraction determined from the TGA experiments (Fig. S4). According to Table 3, we can conclude that size of magnetic nanosystems determinate through two models was *ca.* 10 nm in the examined samples. Moreover, the fits using the core-shell model provide a small paramagnetic shell thickness values of 0.30 and 0.33 nm for FF and FF-APTES respectively, and no paramagnetic shell for the bimodal system (BNPs). The fits also showed that the width of particle size distribution, as gauged by the σ parameter, was narrower for the BNPs compared to the other two systems, in agreement with the observation that for BNPs the values of T_{irr} and T_B are closer to each other (Fig. 7).

In order to compare the experimental size values obtained from different techniques (XRD, TEM and magnetization), the results were summarized in Table 4. Firstly, we would emphasize that neither D_{XRD} nor L_v can strictly be compared to the average particle

size as determined by e.g. TEM (D_{TEM}). Because a proper interpretation of these values depends on *i*) the shape of the particles and crystallite domains and *ii*) the statistical size distribution (log-normal or otherwise). However, D_{vd} determined from magnetization curves are directly comparable to L_v determined from XRD for magnetite as they use similar weighting schemes. Thus, the numbers for D_{vd} and L_v are very close as showed in Table 4. In addition, the particle size of magnetic nanosystems was around 10 nm as result of two models tested. The D_{vd}, L_v and D_{XRD} are more related to the core size of the nanosystems, while D_{TEM} corresponds to all contributions.

Zeta Potential Analyzes

According to the ζ results for FF and FF-APTES, the functionalization using APTES was effective, because there was a change in the ζ from a negative value for the FF system (ζ = –23(5) mV), to a positive value for the FF-APTES system (ζ = + 23(4) mV). Therefore, the positive charge indicates the presence of the amino groups when FF was functionalized by APTES (FF-APTES). On the other hand, when FF-APTES was conjugated with MSA-CdTe QDs to obtain BNPs, these new nanoparticles showed a negative zeta potential (ζ = – 27(5) mV) indicating an efficient conjugation. In this case, the negative charge comes from the carboxyl groups of MSA present on the QDs surface. Moreover, according to previously published work, systems that have a zeta potential higher than 20 mV *in modulus* can be considered chemically stable suspensions.[56, 57]

Relaxometric characterization

To evaluate the potential of the prepared iron oxide nanomaterials as MRI contrast agents (CAs), their relaxometric properties were studied. For each iron oxide sample, the longitudinal and transverse water proton relaxation times (T_1 and T_2, respectively) of the aqueous dispersions at different iron concentrations were measured at 298 K and at a magnetic field of 0.47 T (Larmor frequency of 20 MHz).

The relaxivity values obtained at 20 MHz for the different systems are summarized in Table 5. The r_1 values obtained are much lower than those reported for commercially available standards consisting of magnetite or maghemite nanoparticles coated with dextran or other polysaccharides reported in the literature.[58-60] Values of r_1 are usually interpreted through the use of the outer-sphere Curie relaxation theory, where the accessibility of water molecules to the surface of the nanoparticle is a dominant factor, represented by the distance of closest approach.[61, 62] This r_1 decrease for FF-APTES and BNPs relative to bare FF is attributed to a very significant reduction in the accessibility of water molecules to the surface of the nanoparticle because of their coating.

The r_2 value of the FF nanoparticles is quite high, possibly due to clustering in solution, as large r_2 values are usually related with a large magnetization of the iron oxide nanocrystals and therefore with their size.[61] As the maximum relaxivity for ultra-small superparamagnetic iron oxide nanoparticles (USPIONs) is only expected by theory at a particles size of 25-27 nm,[63] high r_2 values can only be achieved through clustering of USPIONs to larger clusters. Large r_2 increases have been achieved for commercially available products, such as Resovist or Endorem,[58-60] due to the collective magnetic effects of the nanoparticle assemblies. However, the r_2 value for the covalently coated FF-APTES is quite small, which could result from the efficient coating of their USPIONs with 10-15 nm size, which efficiently hinders their clustering and water accessibility. For the BNPs system was not observed an r_2 value so low (~ 90 s^{-1} mM^{-1}) and it can be ascribed to good stability of BNPs system as well as to a satisfactory preservation of magnetization. The representative plots of BNPs are shown in Fig. S6.

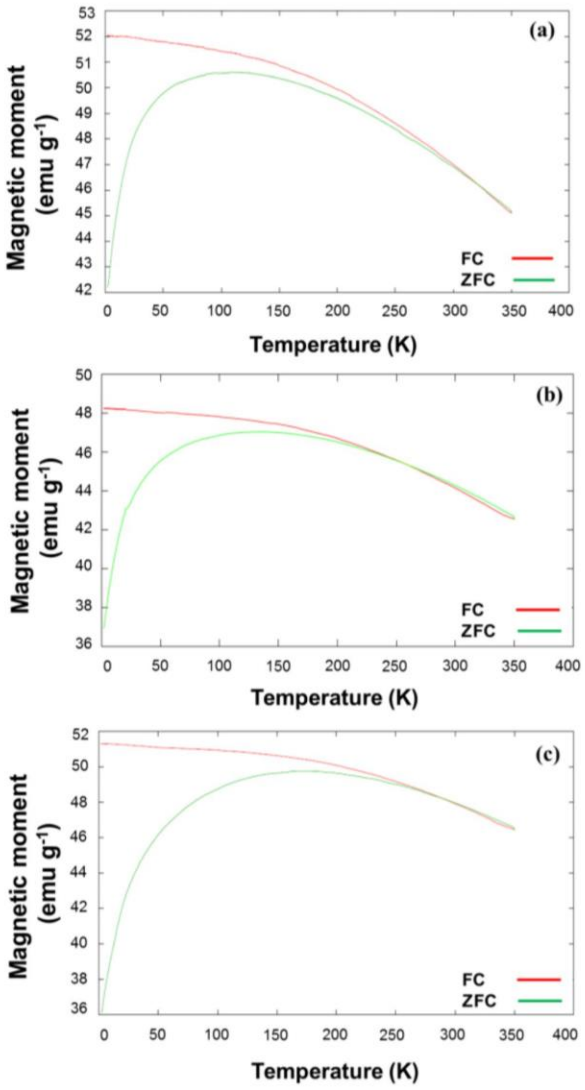

Fig. 7 Temperature dependence of the magnetization over the range of 1.8 – 350 K with *H* = 1000 Oe in the ZFC and FC regimes for (a) bare FF, (b) FF-APTES and (c) BNPs.

Table 3 Magnetization curves fits results by a (A) uniform model and a (B) core-shell model. M_s - saturation magnetization, χ_{pm} - paramagnetic susceptibility, μ - mean of ln *v* (*v* = particle volume), σ - standard deviation of ln *v*, D_0 - core diameter, δ-paramagnetic shell thickness, D_{vd} - particle-volume-weighted average diameter.

A - Uniform model						
Sample	M_s (emu g^{-1})	M	χ_{pm} (emu g^{-1} Oe^{-1})	σ (nm)	D_0 (nm)	D_{vd} (nm)
FF	73.74(1)	6.000(1)	$2.32(1)\times10^{-5}$	0.760(3)	9.17(1)	9.46(1)
FF-APTES	71.64(1)	6.090(2)	$2.17(2)\times10^{-5}$	1.054(3)	9.45(1)	10.05(1)
BNPs	88.69(3)	5.518(2)	$6.39(8)\times10^{-5}$	0.693(4)	7.81(1)	8.02(1)
B- Core-shell model (Fe_3O_4, μ_0B_s = 0.6 T, M_s = 91.0 emu g^{-1})						
Sample	μ	χ_{pm} (emu g^{-1} Oe^{-1})	σ (nm)	D_0 (nm)	δ (nm)	D_{vd} (nm)
FF	5.928(1)	$1.21(1)\times10^{-4}$	0.713(3)	8.95(1)	0.297(1)	9.21(1)
FF-APTES	5.968(2)	$9.99(9)\times10^{-5}$	0.986(4)	9.07(1)	0.333(1)	9.57(1)

Table 4 Average particle sizes of the nanostructured magnetic systems by different methods.

Sample	Particle size			
	D_{XRD} (nm)	L_V (nm)	D_{TEM} (nm)	D_{vd}[a] (nm)
FF	15.0(1)	9.56(4)	11(2)	9.21(1)
FF-APTES	15.3(1)	9.75(6)	15(2)	9.57(1)
BNPs	15.0(1)	9.57(4)	17(2)	8.02(1)

[a] Values obtained from B core-shell model with exception for the BNPs system.

The relaxivity ratio, r_2/r_1, is another important parameter to evaluate the efficiency of T_2-type contrast agents, which increases with the value of this ratio by limiting T_1-weighting effects. The r_2/r_1 ratios of the magnetic nanosystems studied were above 20, making these systems potentially efficient T_2 MRI contrast agents. It is worthwhile to mention, that the BNPs presented the highest relaxivity ratio. And this finding could be a suitable evidence to suggest that BNPs is a promising system as MRI CAs.

Few studies about magnetic and fluorescent nanoparticles used as imaging probes have reported the relaxivity ratio.[64] An interesting system composed of magnetite and fluorescent polymers; with r_2/r_1 equal to 3.8, sizes of the 20 nm and low aggregation; revealed to be an efficient probe for *in vivo* and *in vitro applications*. [65] Generally, efficiency of the systems under study as MRI CAs is compared with the Resovist®, a commercial preparation widely used as contrast agent for liver/spleen imaging (r_2/r_1 value of the 11.3).[66] Recently, Ma *et al.*[64] have reported a novel magnetic composite with a potential features (r_2/r_1 value around 40) to be used as negative MRI CAs when compared with the Resovist®. In our work, we obtained a BNPs system with relaxivity ratio equal to 59.6 making it a promising T_2 MRI contrast agent.

Optical characterization of the BNPs system

Fig. 8 shows the absorption and emission spectra of the MSA-CdTe QDs and BNPs system. Using the first absorption peak (Fig. 8a) at about 552 nm, the diameter of QDs was estimated as *ca.* 3 nm [67,68]. Furthermore, according to the Lambert-Beer equation and using the molar extinction coefficient of CdTe QDs proposed by Yu et al.,[69] the original concentration of CdTe QDs was about 4.8 μM. The emission spectrum of the QDs is consisted of a narrow peak with a maximum at about 593 nm and a FWHM of about 45 nm.[70]

Table 5 Longitudinal (r_1) and transverse (r_2) relaxivities and relaxivity ratios (r_2/r_1), obtained from relaxometry measurements, for all systems (20 MHz, 298 K, 0.47 T).

Sample	r_1 (s^{-1}.mM^{-1})	r_2 (s^{-1}.mM^{-1})	r_2/r_1
FF	4.1(2)	111(2)	27.1
FF-APTES	0.54(2)	15(2)	27.7
BNPs	1.5(2)	88(8)	59.6

The BNPs system showed a red shift of about 30 nm in their emission wavelength (λ_{em} = 623 nm) relative to the bare MSA-CdTe QDs (Fig. 8b). Despite the red shift, the BNPs system remained highly fluorescent. The red shift probably results from the QDs surface modification promoted by covalent coupling. These findings have already been previously reported for QDs conjugation.[13, 71] After BNPs washing using an NdFeB magnet, the absorption spectrum of the supernatant did not present any peak characteristic of the QDs suspension (Fig. 8c), indicating that practically all QDs were conjugated to FF-APTES. Fig. 8d demonstrates the magnetic attraction of the BNPs to the applied magnetic field.

To the best of our knowledge, this was the first work of BNPs that evaluated the absorption peaks of the supernatant as an additional procedure to confirm the QDs' conjugation to FF-APTES. In previously published works the authors confirmed the conjugation by emission spectra of the supernatant[34] and others only showed the supernatant without fluorescence using the attraction by NdFeB as showed by our system in Fig. 8d.[2, 19, 42, 72] Thus, our BNPs system presented bright fluorescence intensity and suitable magnetic properties making them ideal systems to be used for dual images modality (fluorescence and MRI) to biological applications. It is worth to mention that an important feature of BNPs was their preservation of magnetic and fluorescent properties when were stored at 4 °C for more than one year.

Labeling HeLa Cancer Cells with BNPs

Confocal microscopy images of HeLa cells before and after incubating with BNPs are displayed in Fig. 9. HeLa cells were highly labeled after incubation with BNPs (Fig. 9B), as compared to the images before incubation (Fig. 9A). DNA-binding by Hoechst was

used to detect the intracellular labeling more easily. Therefore, through this method, we observed that some BNPs were internalized by cells, while other BNPs were found at the cell's membrane. The binding of BNPs to cells was promoted by QDs' carboxyl groups previously activated by coupling agents during the conjugation of these nanocrystals with magnetic nanoparticles.

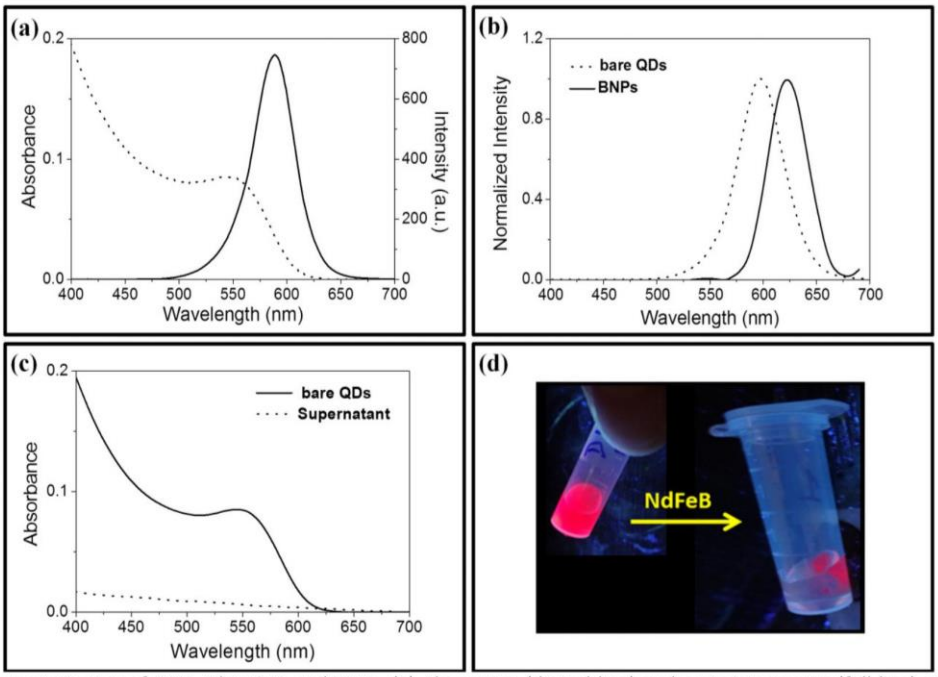

Fig. 8 Optical characterization of MSA-CdTe QDs and BNPs. (a) Absorption (dotted line) and emission spectra (full line) of bare QDs, (b) emission spectra of bare QDs (dotted line) and BNPs (full line), (c) absorption spectrum of QDs (full line) and supernatant after conjugation (dotted line) and (d) BNPs before and after being subjected to the presence of an external magnetic field (NdFeB magnet). The emission experiments were acquired using λ_{exc} = 365 nm.

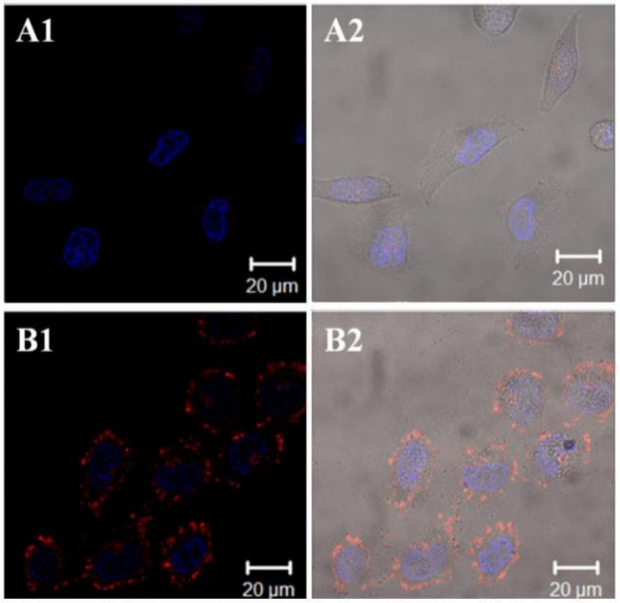

Fig. 9 Confocal microscopy images of HeLa cells before and after incubation with BNPs. (A) HeLa cells and (B) HeLa cells after incubation with BNPs. The identification (1) refers to the overlap of the confocal emission channel LP 565 nm and Hoechst emission channel (BP 420 – 480 nm) and (2) refers to the overlap of the confocal emission filters described in (1) and differential interference contrast (DIC). Scale bar: 20 µm.

The results obtained by confocal microscopy were confirmed by flow cytometry analysis (Fig. 10 and Fig. 11). BNPs labeled efficiently approximately 80% of cells (Fig. 10b). The unspecific interaction of cancer cells and nanoparticles depends on several factors, such as metabolic rate of the cells lines, as reported previously.[73, 74] This can also justify the interaction of BNPs and their cell internalization.

In Fig. 11, from flow cytometry analysis, the y-axis represents the side scatter (SSC) parameter, which evaluates the cells' internal complexity, while the x-axis corresponds to the forward scatter (FSC) parameter that represents the cells size. Therefore, in Fig. 11c a higher internal complexity was observed after incubation of HeLa cells with BNPs, while the cells size showed no considerable changes. The control cells (Fig. 11a) and cells incubated with bare QDs (Fig. 11b) did not show any changes in size and internal complexity. These results suggest that BNPs were internalized by the cells, without change cells' size.

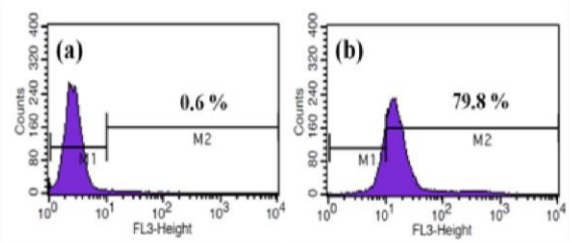

Fig. 10 Flow cytometry analysis by histogram of HeLa cells before (a) and after (b) incubation with BNPs.

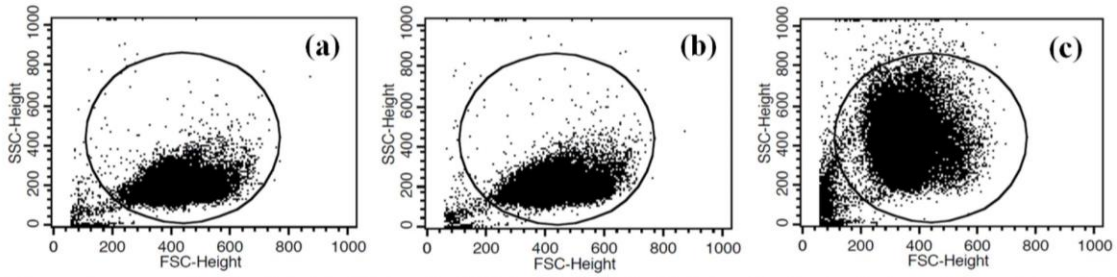

Fig. 11. Flow cytometry analysis by dot plot of HeLa cells. (a) HeLa control cells, (b) HeLa cells after incubation with bare QDs and (c) HeLa cells incubated with BNPs. The delimited region represents the HeLa cells population collected for fluorescence histogram generation.

Conclusions

A new BNP of small dimensions, designed for fluorescence and magnetic analysis, consisting of SPIONs (~15 nm diameter) covalently bound to eight small (3 nm diameter) CdTe QDs, was reported. The BNPs preparation is simple and efficient; consisting of covalently conjugating of the amine functionalized APTES-coated FF with the carboxylic groups of MSA CdTe QDs, using EDC and Sulfo-NHS. Their chemical composition and morphology, as well as of their precursors, FF and FF-APTES, were systematic characterized using a combination of SEM/EDX, TEM, XRD and Mössbauer spectroscopy techniques. The BNPs nanocrystals have a predominant magnetite structure, with minor goethite and maghemite contributions, as shown by Mössbauer spectroscopy, which are compatible with the XRD data. The derivatization of the SPIONs (FF system) with APTES and the formation of the BNPs do not lead to a large size increase. Although the average particle sizes obtained by the different techniques cannot be directly compared, TEM data shows that BNPs presented a diameter of ca. 17 nm. The magnetizations studies of the systems showed that the BNPs have a superparamagnetic behaviour following closely a Langevin M(H,T) function, with small coercivity and a quite high saturation magnetization value, close to that of bulk magnetite, indicating that the SPIONs surface functionalization did not lead to a significant surface paramagnetic dead layer.

The BNPs show high aqueous colloidal stability, with a quite high r2/r1 relaxivity ratio indicating their potential as T2-weighted MRI contrast agents, and high fluorescence at 623 nm showing also to be potential optical probes. BNPs also labeled efficiently HeLa cancer cells, as shown by fluorescence confocal microscopy and flow cytometry results. Their valuable magnetic, optical and relaxometric properties indicate that the BNPs developed here can be used as promising optical labels and negative MRI contrast agents for in vitro and in vivo applications. The BNPs can also offer other potential applications, including rapid bioseparation and hyperthermia, due to their very suitable exhibited magnetic response.

Acknowledgements

This work was supported by the Brazilian agencies: the Coordination for the Improvement of Higher Education Personnel (CAPES), through the Transnational Cooperation Program CAPES / FCT (331/13), the National Council for Scientific and Technological Development (CNPq), and the Foundation for Science and Technology of Pernambuco (FACEPE). This work is also linked to the National Institute of Photonics (INFo). Access to TAIL-UC facility funded under QREN-Mais Centro project ICT_2009_02_012_1890 is also gratefully acknowledged.

Disclosure

The authors confirm that there are no conflicts of interest in this work.

References

1. V. G. Demillo, M. Liao, X. Zhu, D. Redelman, N. G. Publicover and K. W. Hunter Jr, *Colloids and Surfaces A: Physicochemical and Engineering Aspects*, 2015,

464, 134-142.
2. O. Chen, L. Riedemann, F. Etoc, H. Herrmann, M. Coppey, M. Barch, C. T. Farrar, J. Zhao, O. T. Bruns, H. Wei, P. Guo, J. Cui, R. Jensen, Y. Chen, D. K. Harris, J. M. Cordero, Z. Wang, A. Jasanoff, D. Fukumura, R. Reimer, M. Dahan, R. K. Jain and M. G. Bawendi, *Nat Commun*, 2014, **5**.
3. L. Jie-Mei, X. Xiao-Liang, L. Ling, Y. Nai-Qiang and Z. Li-Xin, *Chinese Physics Letters*, 2012, **29**, 097803.
4. K. Anup, K. Sonia, Y. Prasad, G. Haribhau, P. Renu, J. P. Jog, L. Benoit, H. Béatrice, S. Padma and O. Satishchandra, *Nanotechnology*, 2011, **22**, 225101.
5. R. He, X. You, J. Shao, F. Gao, B. Pan and D. Cui, *Nanotechnology*, 2007, **18**, 315601.
6. J. Ruan, J. Ji, H. Song, Q. Qian , K. Wang , C. Wang and D. Cui, *Nanoscale Research Letters* 2012, **7**
7. H.-D. Oh and S.-W. Lee, *Materials Research Bulletin*, 2013, **48**, 2191-2195.
8. K. D. Mahajan, Q. Fan, J. Dorcéna, G. Ruan and J. O. Winter, *Biotechnology Journal*, 2013, **8**, 1424-1434.
9. M. Mahmoudi, S. Sant, B. Wang, S. Laurent and T. Sen, *Advanced Drug Delivery Reviews*, 2011, **63**, 24-46.
10. H.-H. Yang, S.-Q. Zhang, X.-L. Chen, Z.-X. Zhuang, J.-G. Xu and X.-R. Wang, *Analytical Chemistry*, 2004, **76**, 1316-1321.
11. K. H. G. Carvalho, A. G. Brasi, P. E. C. Filho, D. P. L. A. Tenorio, A. C. A. de Siqueira, E. S. Leite, A. Fontes and B. S. Santos, *Journal of Nanoscience and Nanotechnology*, 2014, **14**, 3320-3327.
12. P. E. Cabral Filho, A. L. C. Cardoso, M. I. A. Pereira, A. P. M. Ramos, F. Hallwas, M. M. C. A. Castro, C. F. G. C. Geraldes, B. S. Santos, M. C. Pedroso de Lima, G. A. L. Pereira and A. Fontes, *Biochimica et Biophysica Acta (BBA) - General Subjects*, 2016, **1860**, 28-35.
13. P. E. Cabral Filho, M. I. A. Pereira, H. P. Fernandes, A. A. de Thomaz, C. L. Cesar, B. S. Santos, M. L. Barjas-Castro and A. Fontes, *International Journal of Nanomedicine*, 2015, **10**, 4393-4404.
14. D. Wang, J. He, N. Rosenzweig and Z. Rosenzweig, *Nano Letters*, 2004, **4**, 409-413.
15. Z. Rosenzweig, D. Wang, L. M. Rossi, Y. A. Barnakov and L. Shi, 2004.
16. Y. Zhang, S.-N. Wang, S. Ma, J.-J. Guan, D. Li, X.-D. Zhang and Z.-D. Zhang, *Journal of Biomedical Materials Research Part A*, 2008, **85A**, 840-846.
17. P. Sun, H. Zhang, C. Liu, J. Fang, M. Wang, J. Chen, J. Zhang, C. Mao and S. Xu, *Langmuir*, 2010, **26**, 1278-1284.
18. T. Dhananjay, D. Shuang, B. Thierno and O. W. Jessica, *Nanotechnology*, 2009, **20**, 485601.
19. K. Dmitry, B. Vanessa and P. Wellington, *Nanotechnology*, 2011, **22**, 275606.
20. D. K. Yi, S. T. Selvan, S. S. Lee, G. C. Papaefthymiou, D. Kundaliya and J. Y. Ying, *Journal of the American Chemical Society*, 2005, **127**, 4990-4991.
21. V. Salgueiriño-Maceira, M. A. Correa-Duarte, M. Spasova, L. M. Liz-Marzán and M. Farle, *Advanced Functional Materials*, 2006, **16**, 509-514.
22. W. Qiangbin, L. Yan, L. Chenxiang and Y. Hao, *Nanotechnology*, 2007, **18**, 405604.
23. S. T. Selvan, P. K. Patra, C. Y. Ang and J. Y. Ying, *Angewandte Chemie International Edition*, 2007, **46**, 2448-2452.
24. B. Liu, W. Xie, D. Wang, W. Huang, M. Yu and A. Yao, *Materials Letters*, 2008, **62**, 3014-3017.
25. L. Li, E. S. G. Choo, Z. Liu, J. Ding and J. Xue, *Chemical Physics Letters*, 2008, **461**, 114-117.
26. G.-P. Wang, E.-Q. Song, H.-Y. Xie, Z.-L. Zhang, Z.-Q. Tian, C. Zuo, D.-W. Pang, D.-C. Wu and Y.-B. Shi, *Chemical Communications*, 2005, 4276-4278.
27. T. R. Sathe, A. Agrawal and S. Nie, *Analytical Chemistry*, 2006, **78**, 5627-5632.
28. L. Li, D. Chen, Y. Zhang, Z. Deng, X. Ren, X. Meng, F. Tang, J. Ren and L. Zhang, *Nanotechnology*, 2007, **18**, 405102.
29. T. Chifeng, Y. Yunhua and G. Mingyuan, *Nanotechnology*, 2008, **19**, 105601.
30. E.-Q. Song, J. Hu, C.-Y. Wen, Z.-Q. Tian, X. Yu, Z.-L. Zhang, Y.-B. Shi and D.-W. Pang, *Acs Nano*, 2011, **5**, 761-770.
31. D. Cui, Y. Han, Z. Li, H. Song, K. Wang, R. He, B. Liu, H. Liu, C. Bao, P. Huang, J. Ruan, F. Gao, H. Yang, H. S. Cho, Q. Ren and D. Shi, *Nano Biomedicine and Engineering*, 2009, **1**, 61-74.
32. X. Hong, J. Li, M. Wang, J. Xu, W. Guo, J. Li, Y. Bai and T. Li, *Chemistry of Materials*, 2004, **16**, 4022-4027.
33. Y. Xiaogang, H. Rong, G. Feng, S. Jun, P. Bifeng and C. Daxiang, *Nanotechnology*, 2007, **18**, 035701.
34. S. Ahmed, J. Dong, M. Yui, T. Kato, J. Lee and E. Park, *Journal of Nanobiotechnology*, 2013, **11**, 28.
35. M. Cabrera, J. C. Maciel, J. Quispe-Marcatoma, B. Pandey, D. F. M. Neri, F. Soria, E. Baggio-Saitovitch and L. B. de Carvalho, Jr., *Hyperfine Interact*, 2014, **224**, 197-204.
36. C. G. Andrade, P. E. Cabral Filho, D. P. Tenório, B. S. Santos, E. I. Beltrão, A. Fontes and L. B. Carvalho Jr, *International journal of nanomedicine*, 2013, **8**, 4623.
37. A. Coelho, *Journal of Applied Crystallography*, 2000, **33**, 899-908.
38. R. A. Brand, *Nuclear Instruments and Methods in Physics Research Section B: Beam Interactions with Materials and Atoms*, 1987, **28**, 398-416.
39. G. Thomas, F. Demoisson, O. Heintz, N. Geoffroy, L. Saviot and N. Millot, *RSC Advances*, 2015, **5**, 78614-78624.
40. R. A. Bini, R. F. C. Marques, F. J. Santos, J. A. Chaker and M. Jafelicci Jr, *Journal of Magnetism and Magnetic Materials*, 2012, **324**, 534-539.
41. A. S. Gaspar, F. E. Wagner, V. S. Amaral, S. A. Costa Lima, V. A. Khomchenko, J. G. Santos, B. F. O. Costa and L. Durães, *Spectrochimica Acta Part A: Molecular*

and Biomolecular Spectroscopy.

42. A. Kale, S. Kale, P. Yadav, H. Gholap, R. Pasricha, J. P. Jog, B. Lefez, B. Hannoyer, P. Shastry and S. Ogale, *Nanotechnology*, 2011, **22**, 225101.
43. J. Korecki, B. Handke, N. Spiridis, T. Ślęzak, I. Flis-Kabulska and J. Haber, *Thin Solid Films*, 2002, **412**, 14-23.
44. E. Murad, *Hyperfine Interact*, 1998, **111**, 251-259.
45. M. P. Pasternak, W. M. Xu, G. K. Rozenberg, R. D. Taylor and R. Jeanloz, *Journal of Magnetism and Magnetic Materials*, 2003, **265**, L107-L112.
46. B. Kalska-Szostko, U. Wykowska and D. Satuła, *Applied Surface Science*, 2014, **306**, 7-15.
47. L. Cabrera, S. Gutierrez, N. Menendez, M. P. Morales and P. Herrasti, *Electrochimica Acta*, 2008, **53**, 3436-3441.
48. A. Roychowdhury, S. P. Pati, S. Kumar and D. Das, *Powder Technology*, 2014, **254**, 583-590.
49. A. Durdureanu-Angheluta, L. Pricop, I. Stoica, C.-A. Peptu, A. Dascalu, N. Marangoci, F. Doroftei, H. Chiriac, M. Pinteala and B. C. Simionescu, *Journal of Magnetism and Magnetic Materials*, 2010, **322**, 2956-2968.
50. B. Zhang, J. Cheng, X. Gong, X. Dong, X. Liu, G. Ma and J. Chang, *Journal of Colloid and Interface Science*, 2008, **322**, 485-490.
51. D. Thakur, S. Deng, T. Baldet and J. O. Winter, *Nanotechnology*, 2009, **20**, 485601.
52. A. W. H. Lin, C. Yen Ang, P. K. Patra, Y. Han, H. Gu, J.-M. Le Breton, J. Juraszek, H. Chiron, G. C. Papaefthymiou, S. Tamil Selvan and J. Y. Ying, *Journal of Solid State Chemistry*, 2011, **184**, 2150-2158.
53. S. R. Ahmed, J. Dong, M. Yui, T. Kato, J. Lee and E. Y. Park, *Journal of nanobiotechnology*, 2013, **11**, 28.
54. B. D. Plouffe, D. K. Nagesha, R. S. DiPietro, S. Sridhar, D. Heiman, S. K. Murthy and L. H. Lewis, *Journal of Magnetism and Magnetic Materials*, 2011, **323**, 2310-2317.
55. D.-X. Chen, A. Sanchez, E. Taboada, A. Roig, N. Sun and H.-C. Gu, *Journal of Applied Physics*, 2009, **105**, 083924.
56. R. B. Lira, M. A. Seabra, A. L. Matos, J. V. Vasconcelos, D. P. Bezerra, E. de Paula, B. S. Santos and A. Fontes, *Journal of Materials Chemistry B*, 2013, **1**, 4297-4305.
57. F. Quemeneur, M. Rinaudo, G. Maret and B. Pepin-Donat, *Soft Matter*, 2010, **6**, 4471-4481.
58. C. F. Geraldes and S. Laurent, *Contrast media & molecular imaging*, 2009, **4**, 1-23.
59. Y.-X. J. Wang, S. M. Hussain and G. P. Krestin, *European radiology*, 2001, **11**, 2319-2331.
60. C. Pereira, A. M. Pereira, M. Rocha, C. Freire and C. F. Geraldes, *Journal of Materials Chemistry B*, 2015, **3**, 6261-6273.
61. S. Laurent, D. Forge, M. Port, A. Roch, C. Robic, L. Vander Elst and R. N. Muller, *Chemical Reviews*, 2008, **108**, 2064-2110.
62. A. Roch, R. N. Muller and P. Gillis, *The Journal of chemical physics*, 1999, **110**, 5403-5411.
63. P. Gillis, F. Moiny and R. A. Brooks, *Magnetic resonance in medicine*, 2002, **47**, 257-263.
64. X. Ma, A. Gong, B. Chen, J. Zheng, T. Chen, Z. Shen and A. Wu, *Colloids and Surfaces B: Biointerfaces*, 2015, **126**, 44-49.
65. G. Wang, X. Zhang, Y. Liu, Z. Hu, X. Mei and K. Uvdal, *Journal of Materials Chemistry B*, 2015, **3**, 3072-3080.
66. H.-l. Ma, X.-r. Qi, Y. Maitani and T. Nagai, *International Journal of Pharmaceutics*, 2007, **333**, 177-186.
67. P. Dagtepe, V. Chikan, J. Jasinski and V. J. Leppert, *The Journal of Physical Chemistry C*, 2007, **111**, 14977-14983.
68. A. L. Rogach, T. Franzl, T. A. Klar, J. Feldmann, N. Gaponik, V. Lesnyak, A. Shavel, A. Eychmüller, Y. P. Rakovich and J. F. Donegan, *The Journal of Physical Chemistry C*, 2007, **111**, 14628-14637.
69. W. W. Yu, L. Qu, W. Guo and X. Peng, *Chemistry of Materials*, 2003, **15**, 2854-2860.
70. R. B. Lira, M. B. Cavalcanti, M. A. B. L. Seabra, D. C. N. Silva, A. J. Amaral, B. S. Santos and A. Fontes, *Micron*, 2012, **43**, 621-626.
71. J.-H. Wang, Y.-Q. Li, H.-L. Zhang, H.-Q. Wang, S. Lin, J. Chen, Y.-D. Zhao and Q.-M. Luo, *Colloids and Surfaces A: Physicochemical and Engineering Aspects*, 2010, **364**, 82-86.
72. D. Jańczewski, Y. Zhang, G. K. Das, D. K. Yi, P. Padmanabhan, K. K. Bhakoo, T. T. Y. Tan and S. T. Selvan, *Microscopy Research and Technique*, 2011, **74**, 563-576.
73. S. Zhang, J. Li, G. Lykotrafitis, G. Bao and S. Suresh, *Advanced materials (Deerfield Beach, Fla.)*, 2009, **21**, 419-424.
74. K.-T. Yong, H. Ding, I. Roy, W.-C. Law, E. J. Bergey, A. Maitra and P. N. Prasad, *Acs Nano*, 2009, **3**, 502-510.

Supporting Information

Preparation and characterization of highly fluorescent superparamagnetic nanoparticles for biomedical applications

Mariana P. Cabrera[a,b], Paulo E. Cabral Filho[a], Camila M. C. M. Silva[b], Rita M. Oliveira[c], Carlos F. G. C. Geraldes[c], M. Margarida C.A. Castro[c], Benilde F. O. Costa[d], Marta S. C. Henriques[d], José A. Paixão[d], Luiz B. Carvalho Jr[e], Beate S. Santos[f], Fernando Hallwass[b], Adriana Fontes[a]†, Giovannia A. L. Pereira [b]†.

[1] Biophysics and Radiobiology Department, Federal University of Pernambuco, Recife, Pernambuco, Brazil

[2] Fundamental Chemistry Department, Federal University of Pernambuco, Recife, Pernambuco, Brazil

[3] Department of Life Sciences, Faculty of Science and Technology, and Coimbra Chemistry Center, University of Coimbra, Coimbra, Portugal.

[4] CFisUC, Department of Physics, Faculty of Science and Technology, University of Coimbra, Coimbra, Portugal.

[5] Biochemistry Department and Laboratory of Immunopathology Keizo Asami, Federal University of Pernambuco, Recife, Pernambuco, Brazil.

[6] Pharmaceutical Science Department, Federal University of Pernambuco, Recife, Pernambuco, Brazil

1. Fourier Transform Infrared (FTIR)

The FTIR spectra of all the magnetic nanomaterials are presented in Figure S1. The absorption bands at around 625 and 580 cm^{-1} are characteristic of the Fe-O bond.[1] and the bands near 3383 and 1620 cm^{-1} are ascribed to the OH-stretching bands of water adsorbed on the surface.[2] The addition of APTES molecules onto the surface of magnetic nanoparticles was confirmed by the presence of a band at 1010 cm^{-1} (broad) that corresponds to siloxane (Si-O-Si) stretching. The bands near 1111 and 1049 cm^{-1} which are related with the Si-O-Si and SiO-H groups were not observed [1]. It's important to mention that the main band responsible for the covalent binding between APTES and iron oxide nanoparticles cannot be observed in Figure S1. The reason for this is the overlap of the bands for the Fe-O-Si bonds (584 cm^{-1}) and the Fe-O bonds (580 cm^{-1}) of iron oxide nanoparticles.[3, 4] In addition, N-H stretching vibration and NH_2 stretching were also observed at 3362 and 1621 cm^{-1}, respectively.[5] The FTIR spectrum profile of the MSA-CdTe QDs conjugated onto iron oxide nanoparticles (Fig. S1c) was very similar to the other magnetic systems (Fig. S1a and b).

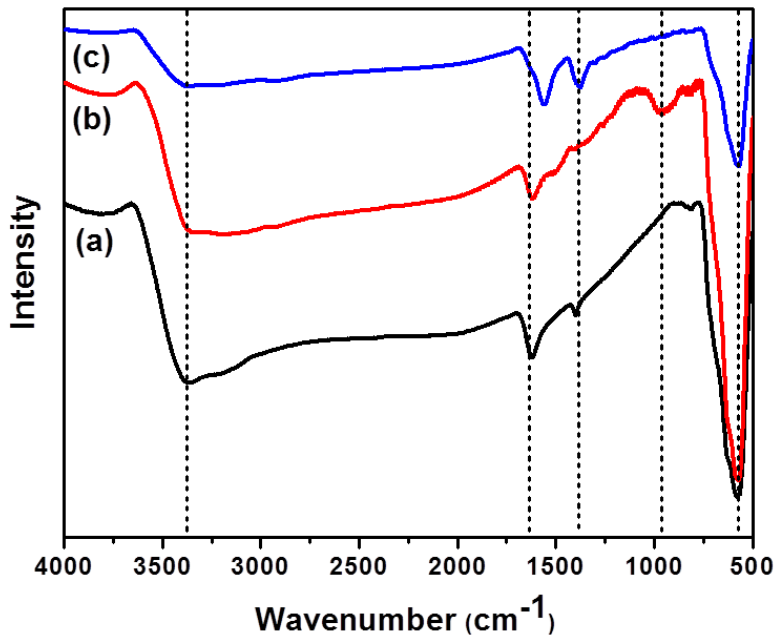

Fig. S1 FTIR spectra of (a) bare FF, (b) FF-APTES and (c) BNPs system; highlighting characteristic vibration bands of the magnetic nanomaterials with short dash lines.

2. Mössbauer spectroscopy

The Fig. S2 shows the hyperfine field distributions for all magnetic nanosystems.

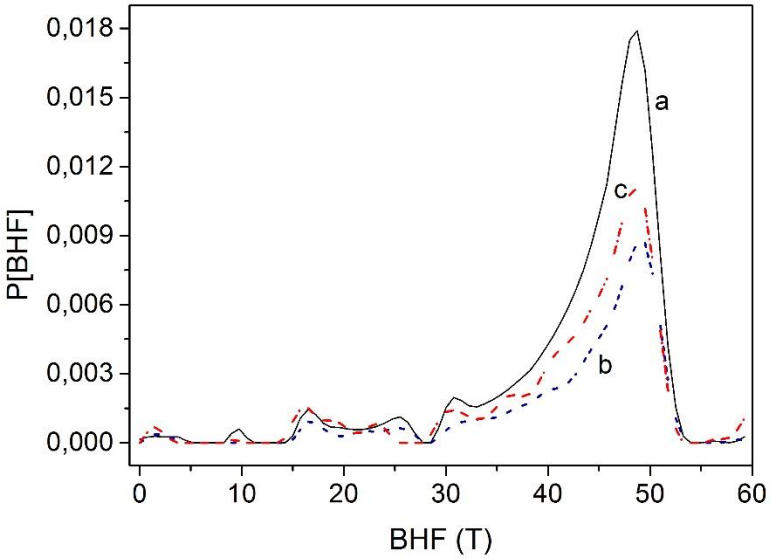

Fig. S2 Hyperfine magnetic field distributions resulting from the fitting to spectra shown in Fig. 4. Curves (a), (b) and (c) correspond to samples: bare FF, FF-APTES and BNPs, respectively.

3. Magnetization (H)

The Fig. S3 presents the saturation magnetization for all magnetic samples at 2 K.

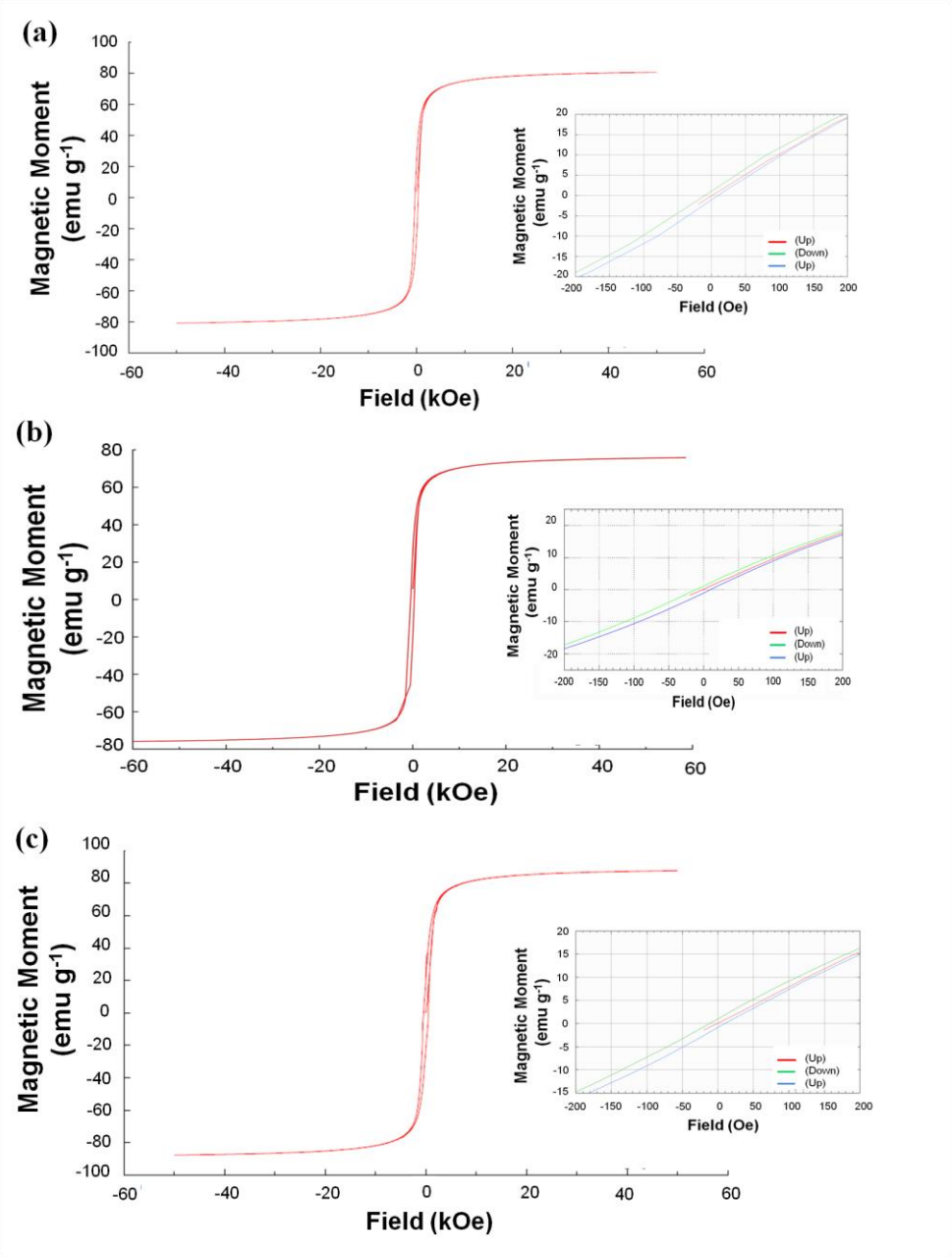

Fig. S3 M(*H*) loops between -50 kOe and +50 kOe at 2 K of the (a) bare FF, (b) FF-APTES and BNPs; inset: magnified M(*H*) curves near the coercive field. The magnetization values of the curves are raw data, not yet corrected for the small organic content of the samples.

4. Thermogravimetric analysis (TGA)

The amount of ligands adsorbed on the nanomaterials surface was quantified by TGA. The thermograms of the three samples (Fig. S4) reveal the existence of several main weight loss steps. For the FF system, a continuous small weight loss was observed upon heating up to 550ºC (3.7% weight loss), the mass remaining constant from 550ºC up to 900 ºC. For the FF-APTES, a continuous small weight loss was observed upon heating up to 550ºC (4.5% weight loss), the mass increasing slightly (0.5%) from 550ºC up to 900 ºC. For the BNPs system there are three steps: (i) the first occurs in the range of 50–160 ºC and is related with the removal of physisorbed water and surface hydroxyl groups; (ii) the second and most significant weight loss occurs in the range of 160-400 ºC being assigned to the depletion of physisorbed ligands; and (iii) the third weight loss occurs up to 800 ºC being ascribed to the thermal decomposition of molecules chemically bound to the particles surface.

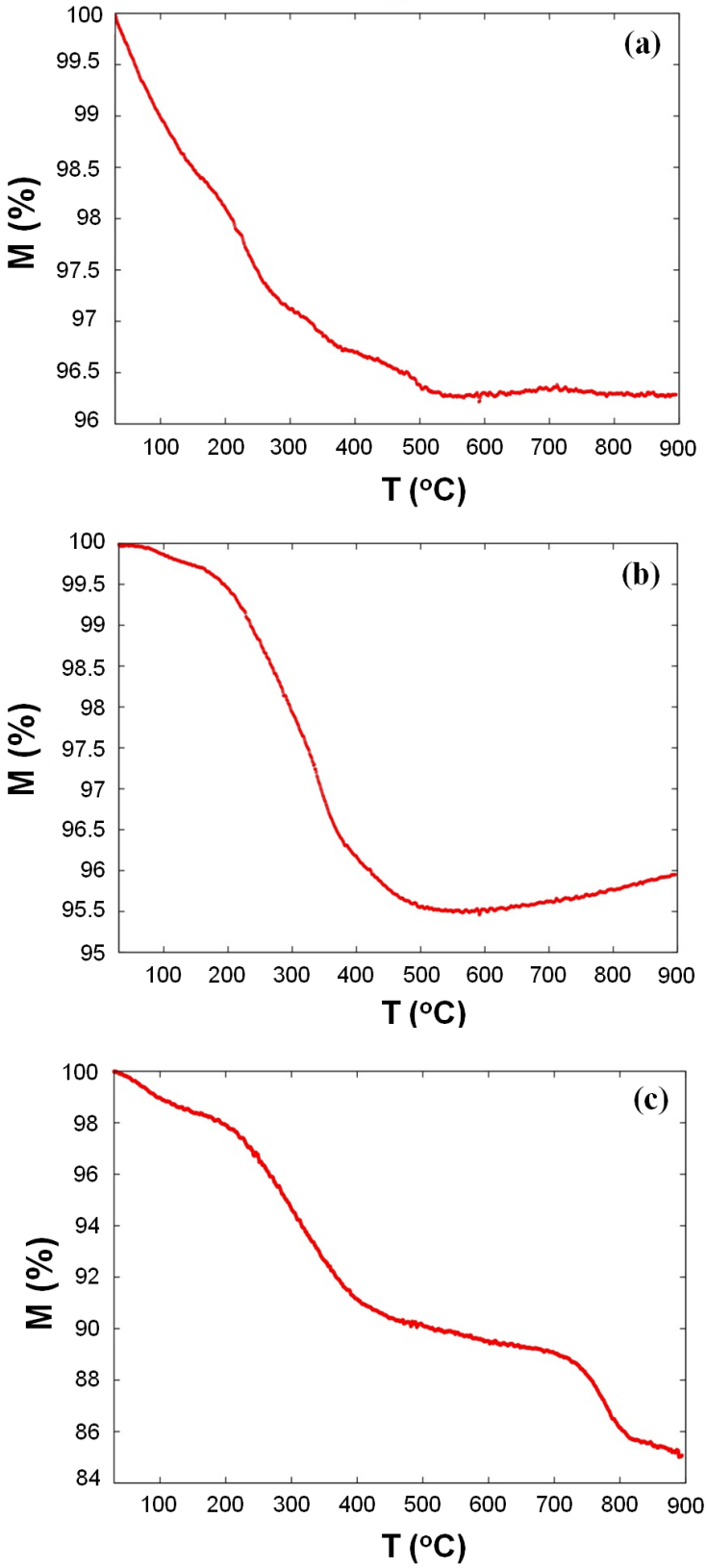

Fig. S4 Thermogravimetric curves of (a) FF, (b) FF-APTES and (c) BNPs performed under N_2 atmosphere.

5. Relaxometric characterization for the BNPs system

The Fig. S5 shows a linear dependence between the inverse proton relaxation times and the iron concentration.

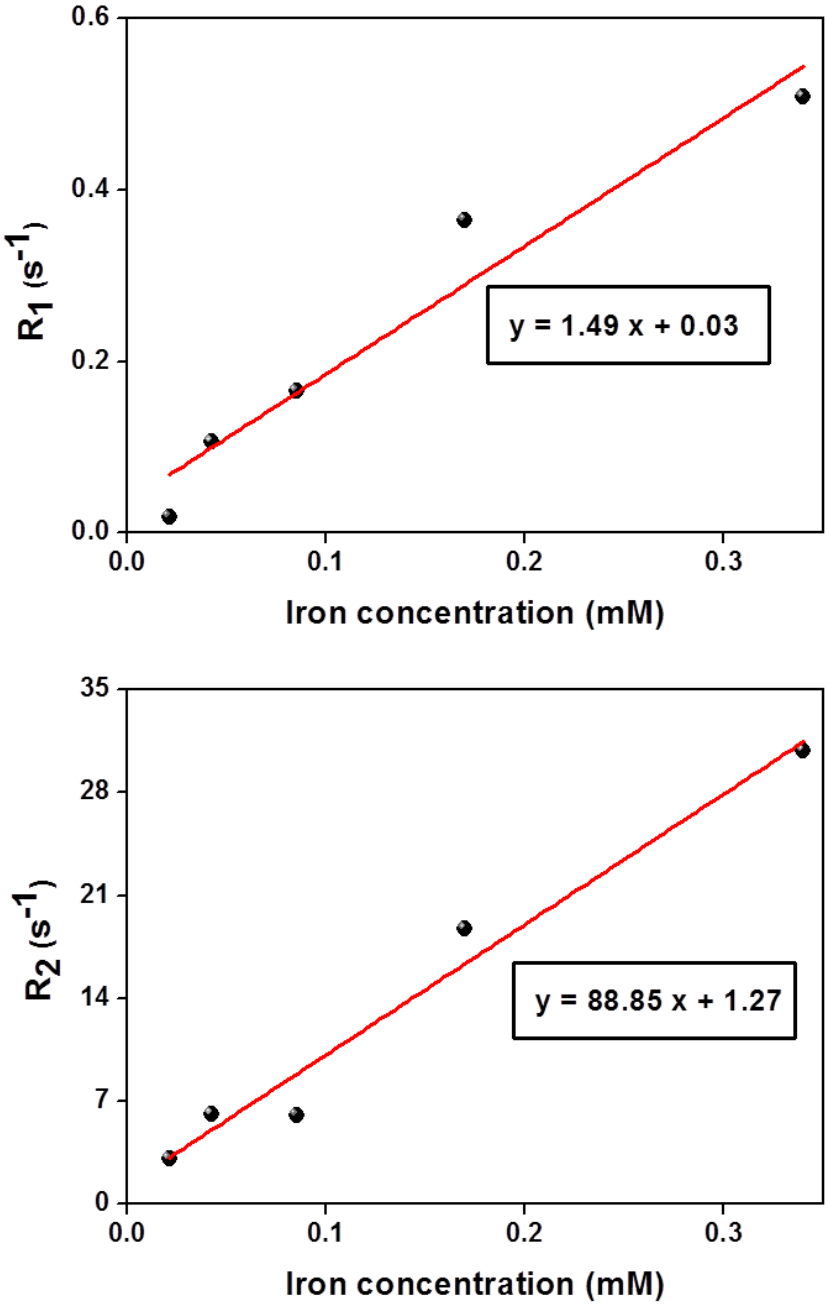

Fig. S5 Plots of R_1 ($1/T_1$) (top) and R_2 ($1/T_2$) (bottom) vs. Fe concentration for BNPs at 20 MHz and room temperature, and the corresponding linear regressions.

Table S1. Cell parameters and particle size of the nanostructured magnetic systems by full pattern profile refinement (Pawley method) - XRD analysis. The volume-weighted thickness (L_v), weighted pattern reliability factor (R_{wp}) and all other quantities in the table are given as defined by the TOPAS refinement program.[6]

Magnetite (SG: *F*d3m, *a* = 8.396 Å)
Sample FF
a = 8.3594(7) Å
D_{XRD} = 15.0(1)
L_v = 9.56(4)
R_{wp} = 3.817 %
Sample FF-APTES
a = 8.3595(5) Å
D_{XRD} = 15.3(1)
L_v = 9.75(6)
R_{wp} = 4.278 %
Sample BNPs
a = 8.3594(7) Å
D_{XRD} = 15.0(1)
L_v = 9.57(4)
R_{wp} = 3.821 %

References

1. B. Feng, R. Y. Hong, L. S. Wang, L. Guo, H. Z. Li, J. Ding, Y. Zheng and D. G. Wei, *Colloids and Surfaces A: Physicochemical and Engineering Aspects*, 2008, **328**, 52-59.
2. V. S. Zaitsev, D. S. Filimonov, I. A. Presnyakov, R. J. Gambino and B. Chu, *Journal of Colloid and Interface Science*, 1999, **212**, 49-57.
3. L. Guang-She, L. Li-Ping, R. L. Smith Jr and H. Inomata, *Journal of Molecular Structure*, 2001, **560**, 87-93.
4. S. Bruni, F. Cariati, M. Casu, A. Lai, A. Musinu, G. Piccaluga and S. Solinas, *Nanostructured Materials*, 1999, **11**, 573-586.
5. L. D. White and C. P. Tripp, *Journal of Colloid and Interface Science*, 2000, **232**, 400-407.
6. A. Coelho, *Journal of Applied Crystallography*, 2000, **33**, 899-908.

6 ARTIGO A SER SUBMETIDO À REVISTA *"COLLOIDS AND SURFACES B: BIOINTERFACES"*

RESEARCH ARTICLE

MUTIMODAL FLUORESCENT MAGNETIC NANOPROBES TO TARGET TRANSFERRIN RECEPTORS IN CANCER CELLS

Paulo E. Cabral Filho[1], Mariana P. Cabrera[1], Ana L. C. Cardoso[2], Otacílio A. Santana[1], Carlos F. G. C. Geraldes[3,4], Beate S. Santos[5], Maria C. Pedroso de Lima[2], Giovannia A. L. Pereira[6], Adriana Fontes[1*]

[1] Biophysics and Radiobiology Department, Federal University of Pernambuco, Recife, PE, Brazil.

[2] CNC- Center for Neuroscience and Cell Biology, University of Coimbra, Coimbra, Portugal.

[3] Department of Life Sciences, Faculty of Science and Technology, University of Coimbra, Coimbra, Portugal.

[4] Coimbra Chemistry Center, University of Coimbra, Coimbra, Portugal.

[5] Department of Pharmaceutical Sciences, Federal University of Pernambuco, Recife, PE, Brazil.

[6] Department of Fundamental Chemistry, Federal University of Pernambuco, Recife, PE, Brazil.

***Corresponding Author:** Adriana Fontes, Av. Prof. Moraes Rego, S/N. Departamento de Biofísica e Radiobiologia, CCB, UFPE, 50670-901, Recife, PE, Brazil - Phone: +55 81 21267818, e-mail: adriana.fontes.biofisica@gmail.com.

GRAPHICAL ABSTRACT

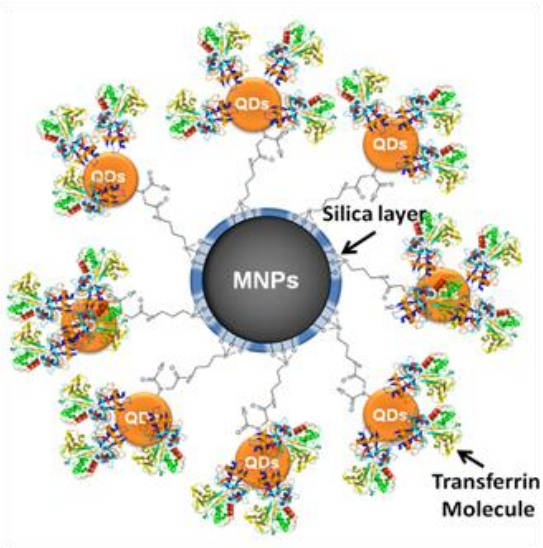

Abstract:

We developed a multimodal nanoprobe by conjugating optical-magnetic nanoparticles (BNPs) with the holo-human transferrin (Tf) to target the Tf receptor (TfR) in cancer cells. The BNPs-Tf were obtained by covalent coupling between iron oxide magnetic nanoparticles, functionalized with an amino silane agent, and hydrophilic carboxyl-coated CdTe quantum dots, which were further covalently conjugated to Tf. BNPs-Tf were characterized by emission spectroscopy and the bioconjugation efficiency was evaluated by fluorescence microplate assay (FMA). Moreover, the amount of Tf immobilized on BNPs was quantified by fluorescence, and the magnetic properties of these new systems were assessed by relaxometric measurements. The FMA results confirmed an efficient bioconjugation and the spectroscopy analyses indicated that practically all Tf (*ca.* 98%) was immobilized on BNPs. The multimodal nanoprobes also presented a bright fluorescence and an r_2 = 64 mM^{-1} s^{-1}, around 105% higher than for bare BNPs. Besides, the BNPs-Tf labeled, efficiently and specifically, the TfR in HeLa cells and presented a low cytotoxicity. Therefore, our BNPs-Tf showed to be promising multimodal nanoprobes, for fluorescence analyses and T_2-weighted images, with potential to be applied in, *in vitro* and *in vivo* studies, focusing the biology, diagnostic and therapeutics of cancer.

Keywords: bimodal nanoparticles, superparamagnetic, fluorescence, magnetic, transferrin, receptor.

1 INTRODUCTION

The design of multimodal nanoparticles, that simultaneously contain more than one functional property, is a recent research area and presents a high potential for biomedical applications [1], such as: (i) the improvement of the cancer biology comprehension, (ii) the development of early diagnosis methods, and (iii) the establishment of alternative, as well as, more effective types of therapies [2]. These new nanotools usually join, at least, the properties of two different techniques, being the most applied systems designed to combine the advantages of fluorescence analyses and magnetic resonance images (MRI) [3-5]. Fluorescence techniques provide a high specificity, by identification and quantification of biomolecules [6], while the resonance magnetic signal allows the acquisition of images with high anatomic details in deep biological tissues [7-9].

The specificity of fluorescence techniques is dependent on the use of optical probes, such as the quantum dots (QDs). These fluorescent semiconductor nanocrystals have been extensively applied in the biomedical area due to their unique properties, compromising: a narrow emission spectrum, a broad absorption band and a high resistance to photobleaching [10-14]. Furthermore, QDs present an active surface, allowing their conjugation with a variety of biomolecules [10, 12], drugs and other nanosystems, like as the superparamagnetic iron oxide nanoparticles – SPIONs [1, 15]. The magnetic properties of SPIONs, as well as their low toxicity, have made them a very used negative contrast agent in MRI [16, 17]. Moreover, SPIONs have also been applied for cell separation and for promoting therapy by hyperthermia [18].

The association of QDs and SPIONs, for obtaining bimodal nanoparticles (BNPs), is in focus and has been attracted the attention of researchers at different areas, in an attempt to overcome the challenges related to their design, which aim optimizing their complementary optical-magnetic properties, as well as bioconjugation processes for specific labeling, in order to generate versatile multimodal nanoprobes [1, 3, 19, 20].

The holo-human transferrin (Tf) is as single-chain β-globin glycoprotein, which binds to a cell surface receptor (TfR) that can be overexpressed in human carcinomas, including breast, ovary, cervical, and brain cancers [21-23]. Thus, the Tf has been widely applied as a cancer cell target for improving therapies, mainly those ones based on specific drug delivery nanosystems [21]. The TfR (CD71 receptor) promotes the cellular uptake of the ferric transferrin [24] by a clathrin-mediated endocytosis [25] and has been stated as one of the most fundamental receptors to the cell metabolism [21].

In this context, the aim of this work was the conjugation of BNPs to Tf, followed by application of these multimodal nanoprobes as TfR specific label in cancer cells. Here, HeLa cells (epithelial cervical carcinoma) were used as a model, because their TfRs were already extensively studied [22, 23, 26]. The BNPs were obtained by covalent coupling between superparamagnetic magnetite nanoparticles, functionalized with an amino silane agent, and hydrophilic carboxyl-coated CdTe QDs[15], which resulted in a nanosystem of *ca.* 17 nm diameter. The BNPs were then further covalently conjugated to Tf. An effective bioconjugation was confirmed by fluorescence microplate assay and the labeling specificity was corroborated by TfR saturation experiments. To our knowledge, this is the first work that prepared BNPs to target specifically the TfR and tested their toxicity against HeLa cells. The nanosystems showed a bright fluorescence and potential to be applied as contrast agents to T_2-weighted MRI. Thus, we believe that the BNPs-Tf are promising multimodal nanoprobes for developing *in vitro* and *in vivo* studies, related to the biology, diagnostic and therapeutic of cancer.

2 EXPERIMENTAL PROCEDURES

2.1 Bimodal Nanoparticles Synthesis and Conjugation with Transferrin

Bimodal nanoparticles (BNPs) and QDs were synthesized according to a work previously published by some of us [15]. Briefly, after the synthesis of superparamagnetic nanoparticles (MNPs), they were functionalized with (3-aminopropyl)triethoxysilane (APTES). Cadmium Telluride (CdTe) QDs were synthesized using the mercaptosuccinic acid (MSA) as functionalizing/stabilizing agent in a proportion of 5:1:6 (Cd:Te:MSA). Then, QDs (0.8 μM) and MNPs-APTES (0.1 μM) were conjugated by covalent binding using 1-ethyl-3-(3-dimethylaminopropyl)carbodiimide (EDC, at a final concentration of 4.4 $mg \cdot mL^{-1}$) and N-hydroxysulfosuccinimide sodium salt (Sulfo-NHS, at a final concentration of 5.5 $mg \cdot mL^{-1}$) to reach a proportion of *ca.* 8 QDs per MNPs.

After the BNPs preparation, they were conjugated with holo-transferrin human (Tf – Sigma-Aldrich), following a procedure, previously reported by some of us, with few adaptations [23]. In that work we applied the conjugates, in a proportion estimated as 2 Tf molecules per QD, to study and quantify the transferrin receptors (TfRs) in HeLa and glioblastoma cells (U87 and DBTRG). Thus, here, we choose to test the

proportions of 2 and 4 Tf molecules per QDs for the multimodal nanoparticles preparation (BNPs-Tf). For this, we used a super-strong neodymium magnet, also known as NdFeB, to concentrate the BNPs recently prepared in 3x, obtaining a final volume of 2 mL with a concentration of 0.1 μM, approximately. Then, BNPs were conjugated with 194 μL or 388 μL of Tf (1 $mg \cdot mL^{-1}$), without any further addition of the coupling agents (EDC and Sulfo-NHS), since QDs carboxylic groups were already actived in the bare BNPs preparation. As it was estimated that the ratio of QDs per MNPs was 8:1 [15], we assumed that the bimodal nanoparticle concentration was the same as the MNPs, which correspond to the core of the BNPs. Both BNPs-Tf systems, after preparation, remained for 2 h under stirring in a Mini Rotator Bio RS-24 (BioSan) and, then were reserved at 4 ºC until application.

2.2 Fluorescence Characterization of BNPs and BNPs-Tf

In order to evaluate the fluorescent properties before and after the conjugation, bare BNPs and BNPs-Tf were optically characterized by emission spectroscopy carried out in a spectrometer LS 55 (PerkinElmer) at λ_{exc} = 488 nm. For this, systems were washed by the NdFeB magnet and diluted at the proportion of 1:10 (v/v) in ultrapure water.

2.3 Bioconjugation Confirmation

The bioconjugation was evaluated by fluorescence microplate assay (FMA) [27], with some adaptations. This method is based on the presence or absence of fluorescence signals from samples placed in a fluorescence plate reader. For this, the systems, described as follows: *Control 1*: Tf; *Control 2*: bare BNPs; and the conjugates (BNPs-Tf) were placed in a polystyrene microplate (black 96-well Optiplate F HB microplates; PerkinElmer). All systems were added in quintuplicate and the microplate was incubated for 2 h in an incubator (water bath, humid chamber) at 37 °C. After incubation, the microplate was washed three times with ultrapure water (18.2 MΩ).

In this method, as bare BNPs do not have an affinity for polystyrene, they are removed after washing. The bare proteins are not removed, however, they do not present significative fluorescence under the conditions used in the experiments. Thus, only bioconjugates are able of showing a significantly detectable signal. For this reason, bare BNPs and proteins were used as controls and the BNPs-protein conjugates were the

systems tested. The intensity of the detected signal is proportional to the bioconjugation efficiency: as higher as the signal, more efficient is the bioconjugation.

Fluorescence measurements were performed using a WALLAC 1420 plate reader with the Victor^2 software (PerkinElmer). The excitation band pass filter used was the F405 (405 nm/5 nm) and the emission band pass filter was the F595 (595 nm/30 nm). The acquisition time was 1 second. The lamp was set to 20,000 and normal slits were used to excite the samples and collect the emission.

The relative fluorescence intensity (RF) of bioconjugates was calculated by using the following Equation 1:

$$RF(\%) = \frac{(\text{Bioconjugates FL} - \text{Control FL})}{\text{Control FL}} \text{ X } 100\% \qquad \text{Eq. 1}$$

where, "Bioconjugates FL" is the average fluorescence intensity of the BNPs–Tf conjugates and "Control FL" is the average of controls signal. According to Carvalho *et al*. [27], the bioconjugation is considered efficient when the systems show an RF higher than 100% compared to their controls. Using this methodology, we also analyzed the role of the Tf amount, applied in the experiments, in the bioconjugation process.

2.4 Transferrin Quantification

We used the autofluorescence of the holo-Tf to quantify the protein amount bounded to BNPs by emission spectroscopy. The experiments were performed in a spectrometer LS 55 (PerkinElmer) at λ_{exc} = 280 nm. The fluorescence was collected at 340 nm [28]. After the conjugation, we washed the BNPs-Tf using the NdFeB magnet and the supernatant was used to quantify the Tf amount that was not bound on the BNPs surface. For this, firstly we built a calibration curve by using known concentrations of Tf (81, 40.5, 20.2, 10.1, 5.0, 2.5 and 1.25 $\mu g \cdot mL^{-1}$). We choose to use Tf fluorescence properties to quantify the amount of biomolecules immobilized on the BNPs, because other protein quantification procedures, such as colorimetric assays, usually apply reagents that can interact with some components used to the BNPs preparation, resulting in unreliable data [29, 30].

2.5. Iron Concentration Measurements

The iron concentration of the colloidal systems was determined by Flame Atomic Absorption Spectrometry (FAAS) using an atomic absorption spectrometer (SpectrAA 220 IFS, Varian) equipped with an air-acetylene flame (air and acetylene flow rate: 13.5 and 2.0 $L \cdot min^{-1}$, respectively). For the analysis, the following conditions were used: iron hollow-cathode lamp as radiation source; wavelength: 372.0 nm; lamp current: 5.0 mA; slit width: 0.2 nm.

2.6. Nuclear Relaxation Times Measurements

The proton water transverse relaxation time (T_2) of bare BNPs and BNPs-Tf were measured in a Varian Unity Plus spectrometer at high magnetic fields (300 MHz, 7.05 T, 25 ^{o}C). Before T_2 analyses, the samples (bare BNPs and BNPs-Tf) were washed twice to remove any residual compounds came from the nanosystems preparation and, then, they were diluted 20x in ultrapure water. The systems presented a final pH of 6.0, approximately.

2.7. Cell Culture

HeLa cells (human epithelial cervical carcinoma) were obtained from the American Type Culture Collection (Manassas, VA, USA) and cultured in Dulbecco's modified Eagle's medium with high glucose (DMEM — Sigma-Aldrich) supplemented with 10% of fetal bovine serum (FBS - Gibco), 100 $mg \cdot mL^{-1}$ of streptomycin and 100 $units \cdot mL^{-1}$ of penicillin (Sigma-Aldrich) at 37 °C in a humidified atmosphere with 5% CO_2. When HeLa cells reached 90% confluence in the culture flask, they were detached with 0.25% of trypsin (Sigma-Aldrich) in Dissociation Buffer (Gibco).

2.8 Labeling HeLa cells with BNPs Conjugated to Transferrin

We used HeLa cells as a model, because they have the TfR extensively studied [22, 23]. For evaluating the specific labeling of TfR in these cells, firstly, we blocked the activated carboxylic groups of the BNPs-Tf system by using TRIS Base 0.1 mM in a proportion of 5:2 (BNPs-Tf:TRIS, v/v) for 2 h.

The cells were then seeded, and incubated for 24 h, in a 6-well plate (2.0×10^5 cells/well — Greiner Bio One Cellstar®) for flow cytometry studies and in a 1-well

plate (1.0×10^5 cells/well — Greiner Bio One Cellstar®) for fluorescence microscopy analysis. After the adhesion period, for both flow cytometry and microscopy analyses, cells were washed with phosphate buffered saline (PBS 1× – from now on named as PBS) and the following experimental conditions were assayed: (A) only cells (control); (B) BNPs-Tf (1:20 v/v ~ 6 nM) and (C) BNPs-Tf (1:10 v/v ~ 12 nM). After 40 min of incubation at 37 °C, under conditions A, B and C, cells were also washed with PBS before the analyses to remove any residual non-specific labeling on cell surfaces.

The percentage of labeled cells was determined by flow cytometry (Accuri™ C6 Flow Cytometer, Becton Dickinson). In these studies, HeLa cells, after incubation, were detached from the 6-well plate by using trypsin 0.25% in Dissociation Buffer followed by trypsin inactivation with DMEM, and then placed in suspension. The cell suspensions were further washed 3 times with PBS and pelleted by centrifugation at 1200 ×g, 30 s (MiniSpin — Eppendorf). Around 10,000 events were acquired for each experimental condition at 488 nm excitation. The emission was detected with the band pass filter 675/25 nm (FL4) and the collected data were processed by the Accuri™ C6 Software (Becton Dickinson).

Cells after incubation with the systems, as described above, were also observed under fluorescence microscopy (DMI 4000 Leica). In this analysis, it was used the excitation band pass (BP) filter at 560/40 and the emission BP filter at 645/75 nm (TX2 filter).

In order to confirm the specificity of the labeling, as well as the efficiency of the bioconjugation, cells were also incubated with an excess of free holo-transferrin human (at a final concentration of 5 $mg \cdot mL^{-1}$) for 30 min at 37 °C, aiming the TfRs saturation [23, 31]. After this, cells were also incubated with the BNPs-Tf at final concentrations of (D) 6 nM and (E) 12 nM, for 40 min, and then the systems were washed and analyzed by flow cytometry and fluorescence microscopy, at the same conditions presented before.

2.9 Cell Viability Assay

For the viability assay, cells were seeded into a 24-well plate (2.0×10^4 cells/well - Greiner Bio One Cellstar®) during 24 h for adherence. After this time, cells were washed and incubated with the systems to evaluate the viability for 24 h of incubation by using the resazurin assay [32]. For this, cells were incubated in triplicate with 5 different concentrations of QDs, bare MNPs-APTES and bare BNPs, as

summarized in Table 1. Furthermore, we also tested the cell viability against BNPs-Tf and the concentrations tested are also described in Table 1. In this case, the concentrations were choose according to the amount of BNPs-Tf necessary for obtaining a successful specific labeling of HeLa cells and also considering the concentrations with lower cytotoxic effect caused by bare BNPs. Moreover, the tested concentrations of bare QDs were higher than those for MNPs, because the BNPs are formed by 8 QDs to 1 MNP.

All samples were diluted with PBS. Thus, the negative control was consisted of DMEM plus PBS. After 24 h, cells were washed with PBS and then incubated with 400 µL of resazurin (3 $\mu g \cdot mL^{-1}$) for each well. After 45 min of resazurin incubation, 200 µL of the supernatant was transferred to a 96-well plate (Greiner Bio-One Cellstar®) and then absorption analyses were performed in a µQuant™ microplate spectrophotometer (BioTek) equipped with Gen5 2.06 software. The reading proceeded at two wavelengths (570 nm and 600 nm), which corresponding to the oxidized form of resazurin (600 nm) and to the reduced form, the resorufin (570 nm).

We used the resazurin assay because it has some advantages when compared to other cell viabilities assays, such as the MTT [3-(4,5-Dimethylthiazol-2-yl)-2,5-Diphenyltetrazolium Bromide], as following described: (1) cells keep alive and can be reused for other experiments, such as microscopy, if necessary and, (2) nanoparticles that remain inside the cells, or possibly adhered to the plates even after washing, are not detected in the absorbance readings, avoiding false results.

Cell viability was calculated according to the Equation 2, and reproduced by three independent experiments:

$$\text{Relative Cell Viability } (\%) = \frac{(A_{570\ nm} - A_{600\ nm})\ \text{of treated cells}}{(A_{570\ nm} - A_{600\ nm})\ \text{of control cells}} \times 100 \qquad \text{Eq. 2}$$

Table 1 – Concentrations of the systems tested in the cell viability assay by resazurin method.

Samples	MNPs-APTES (nM)	QDs (nM)	BNPs (nM)	BNPs-Tf (nM)
1	50	420	50	25
2	25	210	25	12.5
3	12.5	105	12.5	6.3
4	6.3	52	6.3	3.1
5	3.1	26	3.1	1.6

2.10 Statistical Analysis

The statistical analyses were performed using the software GraphPad Prism and the appropriated statistical method was evaluated for each analysis. For the viability assay we used one-way ANOVA since the data follow a normal distribution, and for the FMA was used the Wilcoxon test.

3 RESULTS

3.1 Optical Characterization

The first characterization of bare BNPs and BNPs-Tf suspensions were performed in glass cuvettes (Figure 1). After dilution in ultrapure water, in a proportion of 1:10 (BNPs/water or BNPs-Tf/water - v/v – Figure 1A), we observed a homogeneous suspension for both systems. Furthermore, by using a UV light (λ_{exc} = 365 nm – Figure 1B), it was possible to verify the bright fluorescence in the red region for both samples. When the same suspensions were submitted to the super-strong NdFeB magnet, it was observed the attraction of bare BNPs and BNPs-Tf by the external magnetic field (Figure 1C). Both systems were strongly attracted by the magnet and, after removing the NdFeB, the bare BNPs and BNPs-Tf were easily maintained in suspension again.

Moreover, it was also possible to infer that all QDs were bonded to MNPs, since their fluorescence was not observed in the supernatant (Figure 1C, left) after BNPs attraction by the NdFeB, as some of us have already demonstrated, by absorption electronic spectroscopy analysis, in previous study [15]. We use only one BNPs-Tf system (Figure 2C), as a representative sample, but both BNPs-Tf nanoparticles (388 μL and 194 μL of Tf) presented the same behavior that was observed for bare BNPs (Figure 1C, right).

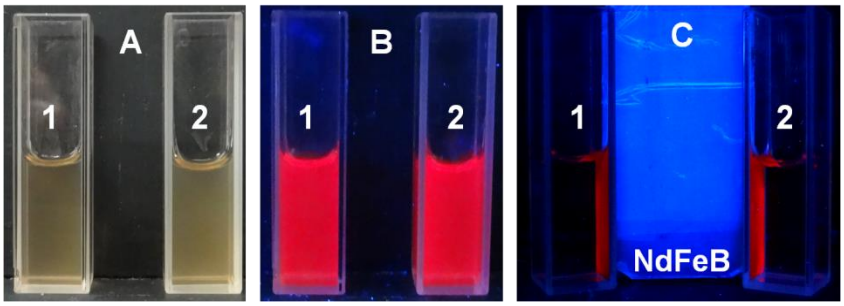

Figure 1 – Visual characterization of bare BNPs (1) and BNPs-Tf (2). In (A): images of the suspensions. In (B): suspensions under λ_{exc} = 365 nm. In (C): using a magnet NdFeB to attract bare BNPs and BNPs-Tf nanoparticles, also under λ_{exc} = 365 nm.

According to the emission spectroscopy analysis, bare BNPs and both BNPs-Tf systems (194 μL or 388 μL) showed a maximum intensity peak at *ca.* 638 nm, under λ_{exc} = 488 nm, as shown in Figure 2 (this wavelength was chosen, because it was the one applied for cell characterizations). These results suggest that the conjugation of BNPs to Tf practically did not change their optical properties when compared with bare BNPs. Furthermore, the full width at a half maximum (FWHM) for both systems was similar, *ca.* 48 nm.

Previously published works, applying different QDs types (such as organic CdSe or CdTe nanocrystals) to obtain BNPs, also using other procedures, demonstrated changes in the fluorescence profile (spectral shift and marked decrease of emission intensity), after conjugation with biomolecules, such as, antibodies or other proteins [4, 18, 33]. Therefore, our results demonstrated that the amount of Tf conjugated to BNPs was not sufficient for promoting considerable modifications in the emission spectrum profile and BNPs-Tf present a bright fluorescence as confirmed by Figure 1C.

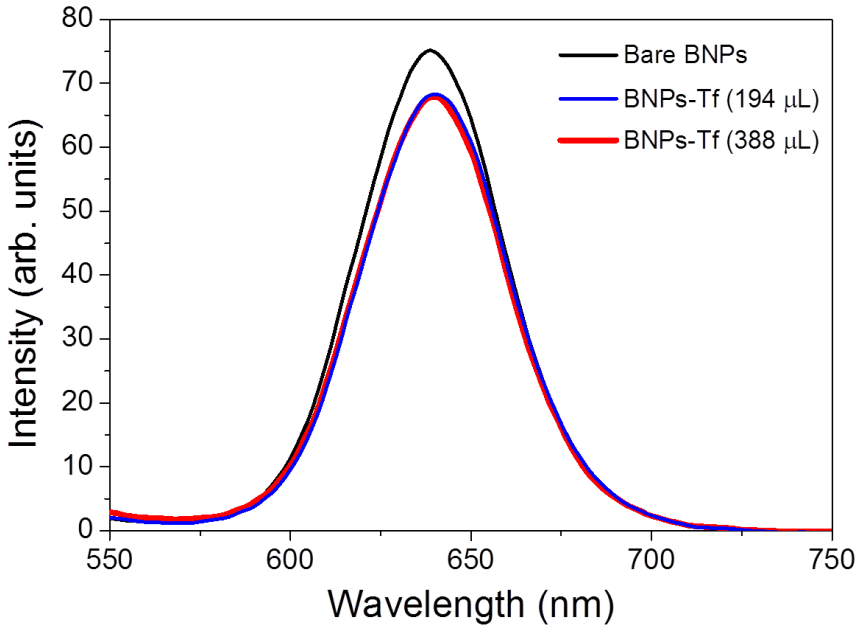

Figure 2 – Optical characterization of bare BNPs (full line) and BNPs-Tf (blue and red lines). We used λ_{exc} = 488 nm.

3.2 Bioconjugation Confirmation

Fluorescence microplate assay (FMA) results are presented in Figure 3 as the average of fluorescent signals of quintuplicate wells for controls and conjugates. After 4

days of the bioconjugation, BNPs-Tf (194 μL) presented an average signal of 3135 ± 961 arbitrary units, while BNPs-Tf (388 μL) showed a significant increasing in the detected photoluminescence, 18492 ± 843 arbitrary units, comparing to the controls signal of 241 ± 53 arbitrary units. These results, obtained in the microplate assay, correspond to relative fluorescence (RF) of 1202% and 6035%, respectively. According to Carvalho et al. [27], BNPs were successfully conjugated to both Tf amounts, since the RF values were higher than 100%. However, the system with the higher Tf amount presented a more efficient bioconjugation. Thus, we choose from now to use this system (with 388 μL of Tf) for further characterizations, as well as, for labeling the TfR in cancer cells.

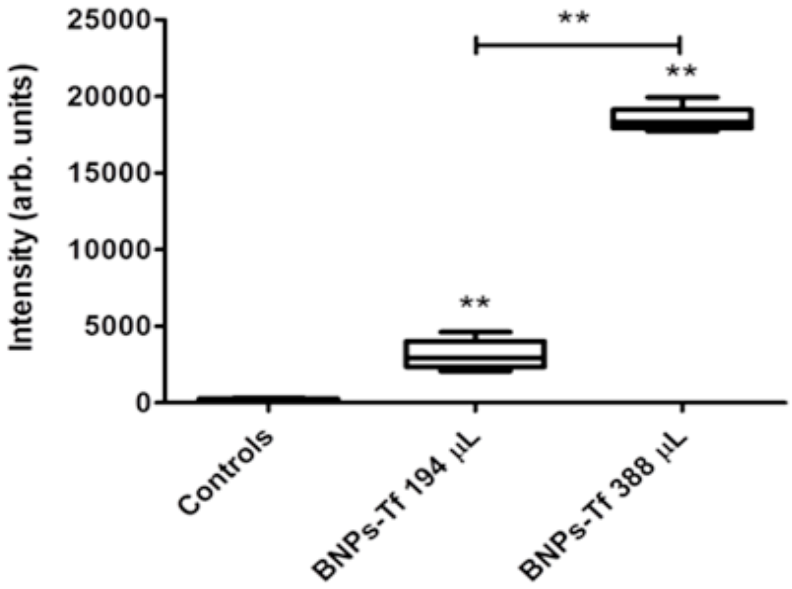

Figure 3 – FMA average signals for BNPs-Tf (194 μL and 388 μL) and their controls (only Tf and bare BNPs). Statistical analyses was performed by Wilcoxon test **p < 0.01.

3.3 Transferrin Quantification

We performed a calibration curve, as showed in Figure 4 (R^2 = 0.99065), and according to it, the Tf amount (detected in the supernatant) that remained not bound to BNPs after conjugation was 2.9 μg·mL^{-1} (0.04 μM). Therefore, since the final Tf concentration, applied to prepare the system BNPs-Tf with 388 μL Tf, was 162 μg·mL^{-1} (*ca.* 2.2 μM), the immobilization efficiency was better than 98%. Moreover, these results indicate that this system was consisted of *ca.* 4 Tf molecules per QD used for the BNPs-Tf preparation.

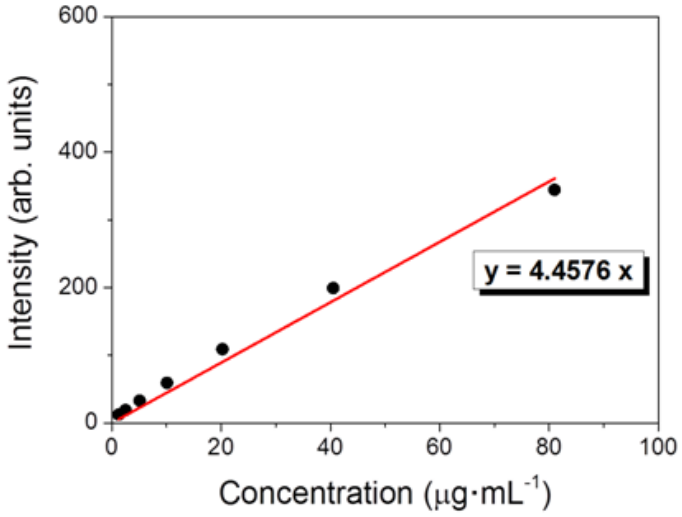

Figure 4 – Calibration curve for transferrin by using fluorescence spectroscopy, intensity vs. concentration.

3.4 Relaxometry

Relaxometric measurements were performed at 300 MHz (7.05 T) for bare BNPs and BNPs-Tf and are summarized in Table 2. The transverse relaxivity (r_2) values were obtained according to the Equation 3 [34, 35]:

$$\frac{1}{T_{2,obs}} = \frac{1}{T_{2,0}} + r_2[\mathrm{Fe}] \qquad \text{Eq. 3}$$

where, $T_{2,obs}$ is the transverse relaxation time measured experimentally in the presence of the magnetic nanomaterial, $T_{2,0}$ is the transverse relaxation time related to the diamagnetic water contribution in the absence of the contrast agent and [Fe] is the iron concentration (in mM). According to the FAAS measurements, we estimated the BNPs and BNPs-Tf original concentrations as approximately 4.0 mM.

We can observe in Table 2 the transverse relaxation rate (R_2) obtained experimentally for bare BNPs and BNPs-Tf. We also calculated the Fe amount in the samples, after dilutions (20x – see *Experimental Procedures section*), based on the concentrations determined by FAAS, in order to evaluate the transverse relaxivity (r_2) (Equation 3).

According to these results, the multimodal system presented a higher transversal relaxivity values (r_2 = 64.2 $mM^{-1}s^{-1}$) when compared to bare BNPs (r_2 = 31.3 $mM^{-1}s^{-1}$), that corresponds to a relative percentage 105% higher for the BNPs-Tf compared to bare BNPs. The sharp difference between r_2 values obtained for BNPs and BNPs-Tf can be attributed to some relevant factors. The first one is related to a higher stability of

BNPs-Tf, avoiding the fast particle precipitation, since these analyses were performed in a high magnetic field. Finally, the outer sphere diffusion process of bulk water molecules near to the magnetic core can be distinct for BNPs and BNPs-Tf, which can reflect directly on the relaxometric results. For all these reasons, additional experiments as well as theoretical analyses can be done in order to elucidate the relaxometric data for these nanosystems. In any case, our results also indicate that the BNPs-Tf as a potential probes for acquiring T_2-weighted MRI.

Table 2 - Transverse relaxivities (r_2), obtained from relaxometry measurements, for BNPs-Tf and bare BNPs (300 MHz, 298 K, 7.05 T).

Systems	R_2 (s^{-1})	r_2 ($s^{-1} \cdot mM^{-1}$)	*% increase in* r_2 [a]
BNPs	6.67	31.3	-
BNPs-Tf	13.24	64.2	105

[a]***The increase in the relaxivity of BNPs-Tf compared to bare BNPs***

3.5 Labeling HeLa Cells with BNPs-Tf

3.5.1 Flow Cytometry Analysis

According to flow cytometry, cells presented a specific labeling by BNPs-Tf as shown in Figure 5. In Figure 5A, control cells did not present considerable fluorescence in the FL4 filter. Figures 5B and 5C show representative histograms of cells incubated with BNPs-Tf, at 6 nM and 12 nM, presenting 72.3% and 87.8% of labeling, respectively. The labeled percentage for BNPs-Tf (12 nM) is in accordance with previously published works, which showed more than 85% of cells labeled, by using the TfR as specific target [22, 23].

On the other hand, in Figures 5D and 5E we can observe that no more than 2% of cells were labeled after the TfR saturation assay using free Tf in excess, indicating that the labeling by BNPs-Tf, showed in Figures 5B and 5C, was specific. In a previous report, published by some of us, QDs-Tf were applied to label specifically the TfR and *ca.* of 20% of HeLa cells was labeled after TfR saturation by free Tf in excess [23]. This difference in the labeling percentage is attributed to the size of nanosystems employed. Our BNPs have about 17 nm of diameter, while QDs present a size of only 3 nm, approximately. Thus, QDs are internalized non-specifically more easily by cancer cells than BNPs [36-38].

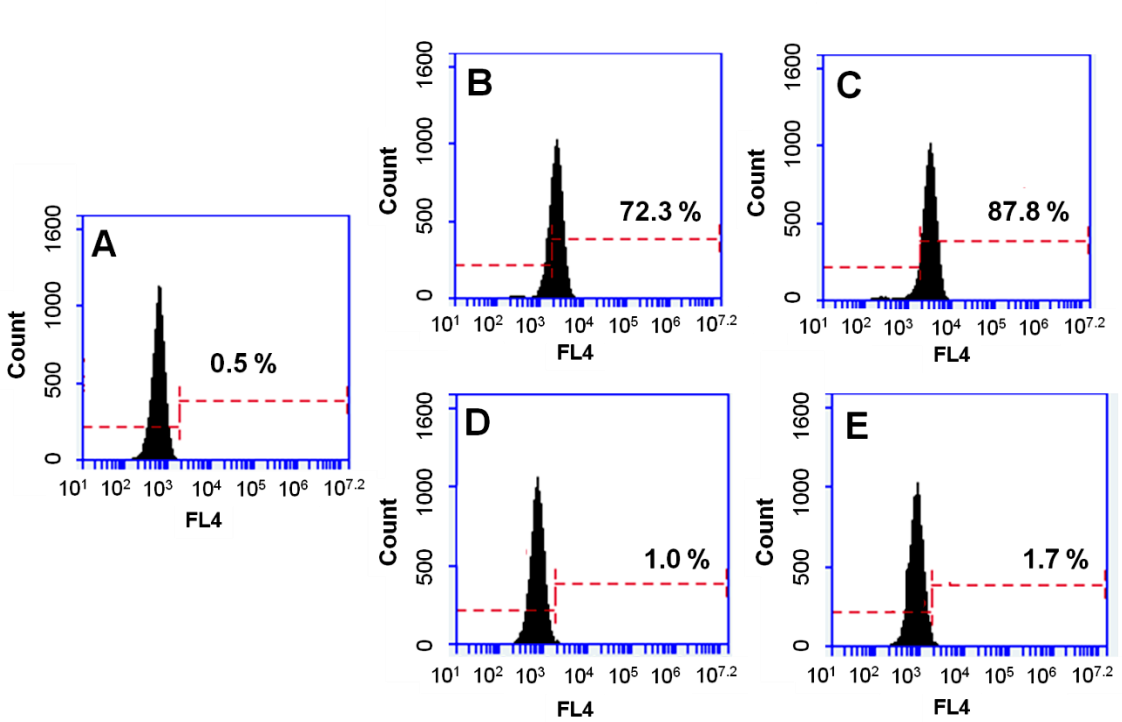

Figure 5 – Representative histogram profiles of cells incubated with BNPs-Tf. In (A) control cells, (B) cells incubated with BNPs-Tf (6 nM), (C) cells incubated with BNPs-Tf (12 nM), (D, E) cells incubated with BNPs-Tf (6 nM and 12 nM, respectively) after TfR saturation with excess of Tf. The events were acquired by using the filter FL4.

When we analyzed the dot plots of complexity (side scatter - SSC) *vs.* size (forward scatter - FSC), cells incubated with BNPs-Tf (12 nM) present more internal complexity than those saturated with Tf in excess (Figure 6). Using the signal average of the SSC parameter, cells labeled by BNPs-Tf presented a relative percentage of the complexity of about 231% (Figure 6A) higher, when compared to those ones incubated with the nanosystems after TfR saturation (Figure 6B).

We also believe that this internal complexity increasing is also related to the BNPs diameter (*ca.* 17 nm) [15], since a previous studies, published by some of us, using QDs-Tf, showed that the internal complexity was not change [23]. Moreover, it is important to mention that our multimodal system remained specifically labeling the TfRs on HeLa cells for at least 2 months.

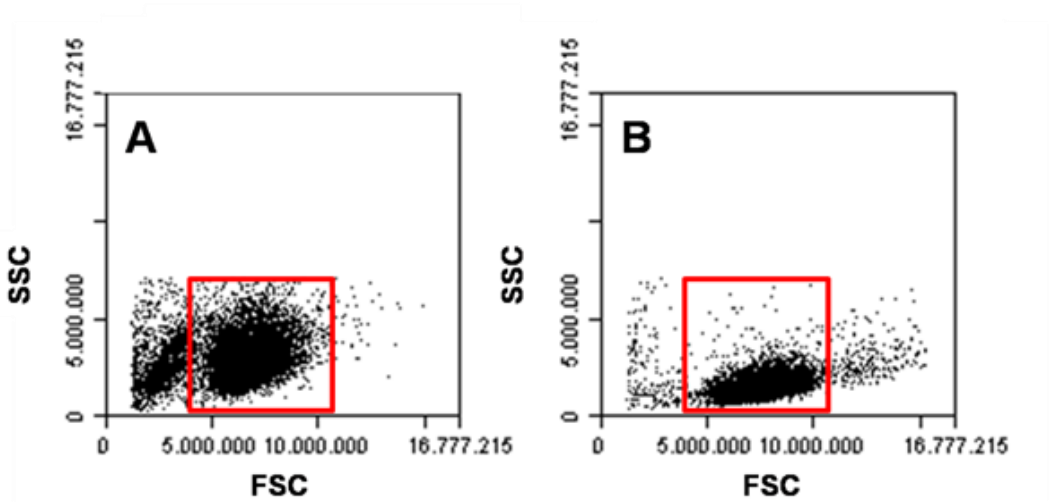

Figure 6 – Representative dot plots of cells: (A) incubated directly with BNPs-Tf and in (B) incubated with BNPs-Tf after TfR saturation.

3.5.2 Fluorescence Microscopy Analysis

As shown in Figure 7, efficient and specific labeling of the TfR was observed in HeLa cells incubated with BNPs-Tf (Figure 7A). Moreover, HeLa cells incubated with BNPs-Tf after TfR saturation by free Tf (Figure 7B), did not show considerable labeling, resulting in an image profile similar to the one obtained for control (in the absence of the multimodal system – data not shown). Our group presented in a previously published work, using QDs-Tf for specific TfR labeling, images with a similar profile that was observed here [23]. In both works the nanosystems conjugated to Tf were endocyted in vesicles (cells showed high fluorescence in endocytic vesicles), probably mediated by the clathrin pathway, as previously reported by Daniels et al. [24].

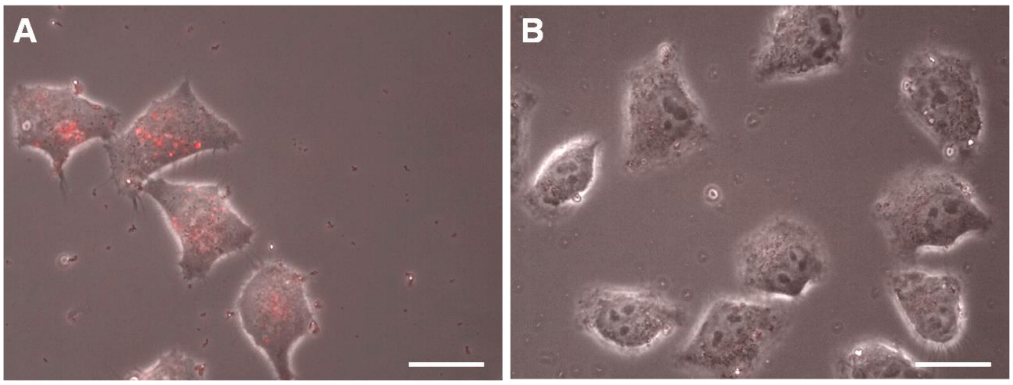

Figure 7 – HeLa cells incubated with BNPs-Tf: (A) phase contrast image merged with the fluorescence detected by the TX2 filter and (B) the same of (A) after TfR saturation. Scale bar = 25 μm.

Many works have used BNPs conjugated to antibodies or other proteins for fluorescence imaging studies [1, 39, 40]. In their works Chu et al. [40] conjugated CdTe QDs to epidermal growth factor (EGF) (QDs-EGF) and BNPs (obtained from CdTe QDs and magnetic polystyrene nanospheres by electrostatic interaction) were also conjugated with to EGF (BNPs-EGF). Both QDs-EGF and BNPs-EGF were used to label breast cancer cells (MDA-MB). These authors observed different labeling profile and suggested that BNPs-EGF systems were not endocyted by the receptor of EGF (EGRF) by cells MDA-MB while QDs-EGF were endocyted. In another work [39], also conjugated BNPs (obtained by CdTe decorated magnetite via dodecylamine as cross-linker) to EGF and applied for labeling Molt-4 cells (human leukemic cell – with high expression of EGRF) and K562 cells (myelogenous leukemia - without EGRF) by flow cytometry. According to the authors, BNPs-EGF conjugates were efficient in promoting the Molt-4 cells labeling. To our knowledge this is the first work that used BNPs conjugated to Tf for TfR specific labeling as a promising nanotool to study this receptor in cancer cells.

3.6 Cell Viability Assay

In order to evaluate biological toxicity of the BNPs-Tf and their constituents [bare BNPs, bare magnetic nanoparticles (MNPs) and bare QDs], an assay was performed for HeLa cells. As can be observed in Figure 8, bare MNPs do not cause significant effects in the cell viability, corroborating results previous published in the literature, which showed any cytotoxic effect for this type of nanoparticle [16, 17, 41]. Moreover, bare BNPs and bare QDs, at higher concentrations, promoted a decreasing in the cells viability, but both systems did not cause more than 50% of cells death. However, these systems in lower concentrations were not able to induce significant cytotoxic effect on HeLa cells.

In previous works, which accessed the cell viability using bare BNPs, the authors also found similar results as the presented by us, the increase of the concentration caused a discreet decrease of cells viability [18, 20, 39, 42]. As described above, bare BNPs in high concentrations (more than 12.5 nM) induce more toxic effect against HeLa cells. Probably this cytotoxic effect could have been caused due the carboxylic groups activated by the coupling agents used for BNPs preparation. These actived carboxylic groups of these nanosystems can be sufficient for promoting coupling with amine groups of the proteins present on the cell membranes, generating a

bright unspecific labeling [15]. These interactions, when BNPs are in high concentrations, can induce instability on cell membranes, leading to cell death.

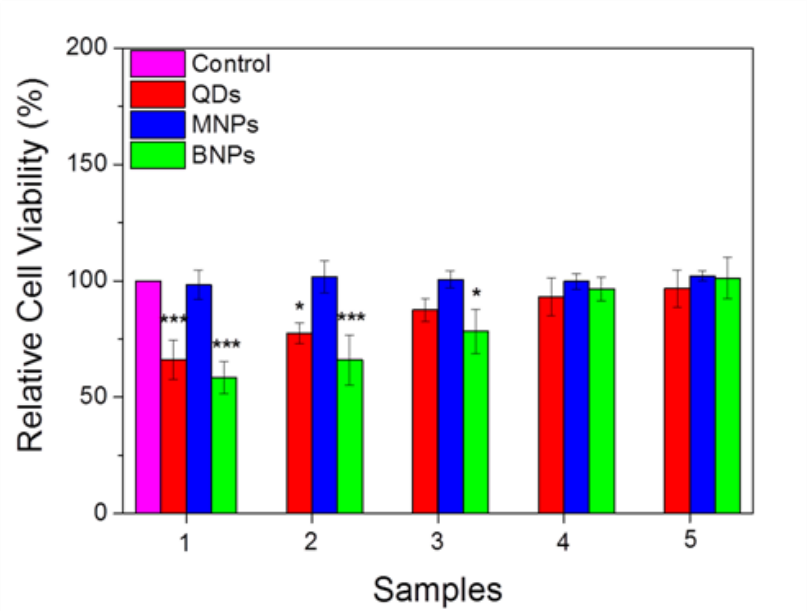

Figure 8 – Cell viability assay for bare BNPs, bare MNPs and bare QDs. Cell viability was assessed 24 h after incubation with the samples by the resazurin reduction method. Samples tested are better described in Table1 and the data are depicted as mean ± standard errors (S.E.) of three independent experiments. For statistical analysis we used the one way ANOVA with a pos test turkey ***$p < 0.001$ and * $p < 0.05$ and no symbol $p > 0.05$.

When we incubated the cells with BNPs-Tf about 25 nM was sufficient to cause a more evident effect on the cells viability, as shown in Figure 9, in contrast with the results obtained for bare BNPs, which showed that a lower concentration (12.5 nM) was already able to induce a discreet cytotoxic effect. In the last case (with BNPs-Tf), the high majority of the activated carboxylic groups from QDs already reacted with Tf. .Therefore, due to this, it was necessary a higher amount of BNPs-Tf to induce a more evident cytotoxic effect in HeLa cells (≥ 25 nM).

Both concentrations (6 and 12 nM) sufficient in promoting a specific labeling by the TfR using BNPs-Tf (Figure 6 and Figure 7) did not cause significant effect ($p > 0.05$) on the cell viability. To our knowledge this is the first work that conjugated BNPs to Tf and also evaluated their cytotoxicity effects by viability assays.

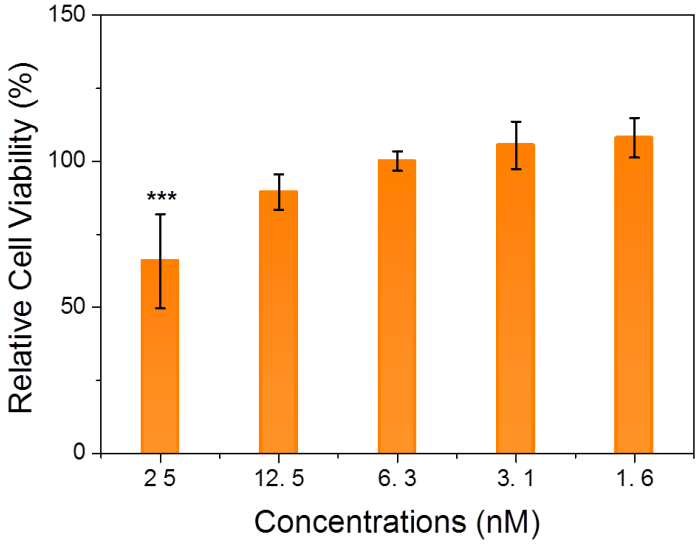

Figure 9 – Relative cell viability assay incubating BNPs-Tf with HeLa cells. Cell viability was assessed 24 h after incubation with the samples by the resazurin reduction method. The data are depicted as mean ± S.E. of three independent experiments. For statistical analysis we used the one way ANOVA with a pos test turkey of three independent experiments ***$p < 0.001$.

4 CONCLUSION

We obtained a multimodal nanosystem based on BNPs conjugated to Tf protein, which successfully labeled the TfR on HeLa cells with high specificity. The methodology applied allowed the immobilization, on BNPs, of more than 98% of the Tf offered in the conjugation process. The multimodal systems obtained in this work remained active for at least two months and labeling cells with high specificity.

The amount of multimodal systems need to label efficiently the TfRs was not sufficient to promote any toxic effect in HeLa cells, at least for 24 h. Moreover, the multimodal nanosystems present a bright fluorescence and a higher transversal relaxivity (r_2) compared to bare BNPs, showing to be potential probes for acquiring fluorescence and T_2-weighted MR images.

Thus, this work opens new possibilities for multimodal systems preparation also considering other biomolecules that have importance to the diagnosis of several diseases, as well as for cells' separation studies. Furthermore, the multimodal systems, developed by us, can be applied to improve the cancer cells biology comprehension *in vitro* and *in vivo*. Besides they can also help the diagnostic and therapeutic methods that exist for this disease, contributing with a more specific and earlier diagnostic of cancer

cells and to monitor the intracellular drug delivery systems and also following the therapies by hyperthermia.

Moreover, our multimodal nanoprobes can also be used for theranostic, allying the diagnostic effect, provided by the fluorescent-magnetic properties from these nanoparticles, with the potential in promoting hyperthermia (cell death by increasing temperature), through the magnetic features of these systems. Thus, multimodal probes are much more versatile when compared with isolated properties of the systems that constitute them.

DISCLOSURE

The authors confirm that there are no conflicts of interest in this work.

ACKNOWLEDGEMENTS

This work was supported by the Brazilian agencies: the Coordination for the Improvement of Higher Education Personnel (CAPES), through the Transnational Cooperation Program CAPES/FCT (331/13), the National Council for Scientific and Technological Development (CNPq), and the Foundation for Science and Technology of Pernambuco (FACEPE). This work is also linked to the National Institute of Photonics (INFo).

REFERENCES

[1] O. Chen, L. Riedemann, F. Etoc, H. Herrmann, M. Coppey, M. Barch, C.T. Farrar, J. Zhao, O.T. Bruns, H. Wei, Magneto-fluorescent core-shell supernanoparticles, Nature communications, 5 (2014).
[2] M.F. Kircher, U. Mahmood, R.S. King, R. Weissleder, L. Josephson, A Multimodal Nanoparticle for Preoperative Magnetic Resonance Imaging and Intraoperative Optical Brain Tumor Delineation, Cancer Research, 63 (2003) 8122-8125.
[3] C.Y. Ang, L. Giam, Z.M. Chan, A.W. Lin, H. Gu, E. Devlin, G.C. Papaefthymiou, S.T. Selvan, J.Y. Ying, Facile Synthesis of Fe2O3 Nanocrystals without Fe (CO) 5 Precursor and One-Pot Synthesis of Highly Fluorescent Fe2O3–CdSe Nanocomposites, Advanced Materials, 21 (2009) 869-873.
[4] P. Sun, H. Zhang, C. Liu, J. Fang, M. Wang, J. Chen, J. Zhang, C. Mao, S. Xu, Preparation and characterization of Fe3O4/CdTe magnetic/fluorescent nanocomposites and their applications in immuno-labeling and fluorescent imaging of cancer cells, Langmuir, 26 (2009) 1278-1284.
[5] H. Xu, Q. Li, L. Wang, Y. He, J. Shi, B. Tang, C. Fan, Nanoscale optical probes for cellular imaging, Chemical Society Reviews, 43 (2014) 2650-2661.
[6] B.N.G. Giepmans, S.R. Adams, M.H. Ellisman, R.Y. Tsien, The Fluorescent Toolbox for Assessing Protein Location and Function, Science, 312 (2006) 217-224.

[7] Geraldes, Laurent, Classification and basic properties of contrast agents for magnetic resonance imaging, Contrast Media & Molecular Imaging, 4 (2009) 1-23.
[8] A. Merbach, L. Helm, É. Tóth, The Chemistry of Contrast Agents in Medical Magnetic Resonance Imaging, in, John Wiley & Sons, Ltd, Chichester, UK, 2013.
[9] A.E. Merbach, É. Tóth, The chemistry of contrast agents in medical magnetic resonance imaging, Wiley Online Library, 2001.
[10] A. Fontes, R.B. Lira, M.A.B.L. Seabra, T.G. Silva, A.G.C. Neto, B.S. Santos, Quantum Dots in Biomedical Research, in: R. Hudak (Ed.) Biomedical Engineering - Technical Applications in Medicine, InTech, 2012.
[11] Santos, Farias, Fontes, Semiconductor Quantum Dots for Biological Applications, in: M. Henini (Ed.) Handbook of Self Assembled Semiconductor Nanostructures for Novel Devices in Photonics and Electronics, Elsevier, Amsterdam, 2008, pp. 773-798.
[12] B.S. Santos, P.M.A. Farias, F.D. Menezes, A.G. Brasil, A. Fontes, L. Romao, J.O. Amaral, V. Moura-Neto, D.P.L.A. Tenorio, C.L. Cesar, New highly fluorescent biolabels based on II–VI semiconductor hybrid organic–inorganic nanostructures for bioimaging, Applied Surface Science, 255 (2008) 790-792.
[13] P. Alivisatos, The use of nanocrystals in biological detection, Nat Biotech, 22 (2004) 47-52.
[14] M. Bruchez, M. Moronne, P. Gin, S. Weiss, A. Alivisatos, Semiconductor nanocrystals as fluorescent biological labels, Science., 281 (1998) 2013 - 2016.
[15] M.P. Cabrera, P.E.C. Filho, C.M.C.M. Silva, R.M. Oliveira, C.F.G.C. Geraldes, M.M.C.A. Castro, B.F.O. Costa, M.S.C. Henriques, J.A. Paixão, L.B.C. Jr, B.S. Santos, F. Hallwass, A. Fontesa, G.A.L. Pereira, Preparation and characterization of highly fluorescent superparamagnetic nanoparticles for biomedical applications, Journal of Materials Chemistry B, xx (2016) Artigo a ser submetido.
[16] M. Mahmoudi, S. Sant, B. Wang, S. Laurent, T. Sen, Superparamagnetic iron oxide nanoparticles (SPIONs): Development, surface modification and applications in chemotherapy, Advanced Drug Delivery Reviews, 63 (2011) 24-46.
[17] R. Weissleder, D.D. Stark, B.L. Engelstad, B.R. Bacon, C.C. Compton, D.L. White, P. Jacobs, J. Lewis, Superparamagnetic iron oxide: pharmacokinetics and toxicity, American Journal of Roentgenology, 152 (1989) 167-173.
[18] D. Cui, Y. Han, Z. Li, H. Song, K. Wang, R. He, B. Liu, H. Liu, C. Bao, P. Huang, Fluorescent magnetic nanoprobes for in vivo targeted imaging and hyperthermia therapy of prostate cancer, Nano Biomed Eng, 1 (2009) 94-112.
[19] L. Jie-Mei, X. Xiao-Liang, L. Ling, Y. Nai-Qiang, Z. Li-Xin, Preparation and Characterization of Bimodal Magnetofluorescent Nanoprobes for Biomedical Application, Chinese Physics Letters, 29 (2012) 097803.
[20] S.R. Ahmed, J. Dong, M. Yui, T. Kato, J. Lee, E.Y. Park, Quantum dots incorporated magnetic nanoparticles for imaging colon carcinoma cells, Journal of nanobiotechnology, 11 (2013) 28.
[21] H. Li, Z.M. Qian, Transferrin/transferrin receptor-mediated drug delivery, Medicinal research reviews, 22 (2002) 225-250.
[22] L.-Y. Guan, Y.-Q. Li, S. Lin, M.-Z. Zhang, J. Chen, Z.-Y. Ma, Y.-D. Zhao, Characterization of CdTe/CdSe quantum dots-transferrin fluorescent probes for cellular labeling, Analytica Chimica Acta, 741 (2012) 86-92.
[23] P.E. Cabral Filho, A.L.C. Cardoso, M.I.A. Pereira, A.P.M. Ramos, F. Hallwas, M.M.C.A. Castro, C.F.G.C. Geraldes, B.S. Santos, M.C. Pedroso de Lima, G.A.L. Pereira, A. Fontes, CdTe quantum dots as fluorescent probes to study transferrin receptors in glioblastoma cells, Biochimica et Biophysica Acta (BBA) - General Subjects, 1860 (2016) 28-35.

[24] T.R. Daniels, E. Bernabeu, J.A. Rodríguez, S. Patel, M. Kozman, D.A. Chiappetta, E. Holler, J.Y. Ljubimova, G. Helguera, M.L. Penichet, Transferrin receptors and the targeted delivery of therapeutic agents against cancer, Biochimica et biophysica acta, 1820 (2012) 291-317.
[25] W. Ding, L. Guo, Immobilized transferrin Fe(3)O(4)@SiO(2) nanoparticle with high doxorubicin loading for dual-targeted tumor drug delivery, International journal of nanomedicine, 8 (2013) 4631-4639.
[26] C. Schieber, A. Bestetti, J.P. Lim, A.D. Ryan, T.-L. Nguyen, R. Eldridge, A.R. White, P.A. Gleeson, P.S. Donnelly, S.J. Williams, P. Mulvaney, Conjugation of Transferrin to Azide-Modified CdSe/ZnS Core–Shell Quantum Dots using Cyclooctyne Click Chemistry, Angewandte Chemie International Edition, 51 (2012) 10523-10527.
[27] K.H. Carvalho, A.G. Brasi, E.C. Paulo Filho, D.P. Tenorio, A.C. de Siqueira, E.S. Leite, A. Fontes, B.S. Santos, Fluorescence plate reader for quantum dot-protein bioconjugation analysis, Journal of Nanoscience and Nanotechnology, 14 (2014) 3320-3327.
[28] S. Tang, R. MacColl, P.J. Parsons, Spectroscopic study of the interaction of aluminum ions with human transferrin, Journal of Inorganic Biochemistry, 60 (1995) 175-185.
[29] D.A. Zaia, C. Zaia, J. Lichtig, Determinação de proteínas totais via espectrofometria: vantagens e desvantagens dos métodos existentes, Química nova, 21 (1998) 787-793.
[30] P. Biotechnology, Pierce BCA Protein Assay Kit Instruction,, in: Thermo Fisher Scientific Inc. (Ed.), Illinois - USA, 2015.
[31] A.L.C. Cardoso, S. Simões, L.P. de Almeida, N. Plesnila, M.C. Pedroso de Lima, E. Wagner, C. Culmsee, Tf-lipoplexes for neuronal siRNA delivery: A promising system to mediate gene silencing in the CNS, Journal of Controlled Release, 132 (2008) 113-123.
[32] M.T. Calejo, A.M.S. Cardoso, A.-L. Kjøniksen, K. Zhu, C.M. Morais, S.A. Sande, A.L. Cardoso, M.C.P. de Lima, A. Jurado, B. Nyström, Temperature-responsive cationic block copolymers as nanocarriers for gene delivery, International Journal of Pharmaceutics, 448 (2013) 105-114.
[33] X. You, R. He, F. Gao, J. Shao, B. Pan, D. Cui, Hydrophilic high-luminescent magnetic nanocomposites, Nanotechnology, 18 (2007) 035701.
[34] F. Hajesmaeelzadeh, S. Shanehsazzadeh, C. Grüttner, F.J. Daha, M.A. Oghabian, Effect of coating thickness of iron oxide nanoparticles on their relaxivity in the MRI, Iranian Journal of Basic Medical Sciences, 19 (2016) 166-171.
[35] S. Laurent, D. Forge, M. Port, A. Roch, C. Robic, L. Vander Elst, R.N. Muller, Magnetic Iron Oxide Nanoparticles: Synthesis, Stabilization, Vectorization, Physicochemical Characterizations, and Biological Applications, Chemical Reviews, 108 (2008) 2064-2110.
[36] S. Zhang, J. Li, G. Lykotrafitis, G. Bao, S. Suresh, Size-Dependent Endocytosis of Nanoparticles, Advanced materials (Deerfield Beach, Fla.), 21 (2009) 419-424.
[37] K.-T. Yong, H. Ding, I. Roy, W.-C. Law, E.J. Bergey, A. Maitra, P.N. Prasad, Imaging Pancreatic Cancer Using Bioconjugated InP Quantum Dots, Acs Nano, 3 (2009) 502-510.
[38] D. Chen, G. Xu, B.A. Ali, K.-T. Yong, C. Zhou, X. Wang, J. Qu, P.N. Prasad, H. Niu, Uptake of transferrin-conjugated quantum dots in single living cells, Chin. Opt. Lett., 8 (2010) 940-943.

[39] A. Kale, S. Kale, P. Yadav, H. Gholap, R. Pasricha, J. Jog, B. Lefez, B. Hannoyer, P. Shastry, S. Ogale, Magnetite/CdTe magnetic–fluorescent composite nanosystem for magnetic separation and bio-imaging, Nanotechnology, 22 (2011) 225101.
[40] M. Chu, X. Song, D. Cheng, S. Liu, J. Zhu, Preparation of quantum dot-coated magnetic polystyrene nanospheres for cancer cell labelling and separation, Nanotechnology, 17 (2006) 3268.
[41] B. Lin, X. Yao, Y. Zhu, J. Shen, X. Yang, H. Jiang, X. Zhang, Multifunctional manganese-doped core-shell quantum dots for magnetic resonance and fluorescence imaging of cancer cells, New Journal of Chemistry, 37 (2013) 3076-3083.
[42] Q. Ma, Y. Nakane, Y. Mori, M. Hasegawa, Y. Yoshioka, T.M. Watanabe, K. Gonda, N. Ohuchi, T. Jin, Multilayered, core/shell nanoprobes based on magnetic ferric oxide particles and quantum dots for multimodality imaging of breast cancer tumors, Biomaterials, 33 (2012) 8486-8494.

7 CAPÍTULO DE LIVRO SUBMETIDO A "*ENCYCLOPEDIA OF NANOSCIENCE AND NANOTECHNOLOGY*"

ENN Encyclopedia of Nanoscience and Nanotechnology
www.aspbs.com/enn

Bimodal Nanostructured Materials Containing Quantum Dots for Optical and Magnetic Resonance Imaging

Goreti Pereira

Pharmaceutical Science Department, Federal University of Pernambuco, Recife, Pernambuco, Brazil; Biomedical Nanotechnology Research Group, Federal University of Pernambuco, Recife, Pernambuco, Brazil

Paulo E. Cabral Filho, Maria I. A. Pereira, Mariana P. Cabrera

Biomedical Nanotechnology Research Group, Federal University of Pernambuco, Recife, Pernambuco, Brazil; Biophysics and Radiobiology Department, Federal University of Pernambuco, Recife, Pernambuco, Brazil

Giovannia A. L. Pereira

Biomedical Nanotechnology Research Group, Federal University of Pernambuco, Recife, Pernambuco, Brazil; Fundamental Chemistry Department, Federal University of Pernambuco, Recife, Pernambuco, Brazil

Adriana Fontes

Biomedical Nanotechnology Research Group, Federal University of Pernambuco, Recife, Pernambuco, Brazil; Biophysics and Radiobiology Department, Federal University of Pernambuco, Recife, Pernambuco, Brazil

Beate S. Santos

Pharmaceutical Science Department, Federal University of Pernambuco, Recife, Pernambuco, Brazil; Biomedical Nanotechnology Research Group, Federal University of Pernambuco, Recife, Pernambuco, Brazil

CONTENTS

1. INTRODUCTION

Over the last years the interest in the development of bimodal probes, which could allow complementary

ISBN: x-xxxxx-xxx-x/$xx.00

Encyclopedia of Nanoscience and Nanotechnology
Edited by H. S. Nalwa
Volume xx: Pages (1–28)

diagnostic methods or that could be used as theranostic systems, has increased [1–3]. Since the majority of diseases that affect humans are multifactorial, the diagnostic techniques must be able to detect and distinguish the various mechanisms and/or phases of the disease. The association and simultaneous use of two or more diagnostic techniques will allow a more precise diagnostic, thus the utilization of two types of probes in one single particle can be very useful to reach this purpose [4–6]. In this chapter, we review the development of bimodal systems for optical and magnetic resonance images, specifically systems containing quantum dots (QDs).

Techniques based on fluorescence enabled not only the visualization, but also the biochemical analysis of several biological structures. Thus, advances in these techniques are the great interest in biomedical sciences, since these advances will allow a better understanding of the cellular functions and, consequently, the development of more efficient diagnostic and/or treatment approaches [7–9]. One of the principal advances in the microscopy-based techniques was the invention of fluorescence microscopy, which allowed the visualization in real-time images with chemical specificity and high sensibility [10, 11]. The use of fluorescent labels is important to evidence the desired structures of biomolecules. In this way, organic fluorophores are frequently used, although these dyes have some disadvantages such as fast photodegradation and high cytotoxicity [12, 13].

Scientific advances that aim to decrease the disadvantages associated with the currently used organic dyes has led to the emergence of a new class of fluorophores: quantum dots. QDs are semiconductor nanocrystals with dimensions of 1.5 to 10 nm that possess unique photophysical properties, due to the quantum confinement regime, such as great photostability, emission tunable according to the nanoparticle size, and an active surface, which allows their conjugation with other molecules [14, 15]. QDs have been widely used in bioanalytical assays, (1) for *in vitro* cells and tissues imaging, (2) for *in vivo* imaging of small animals, (3) for cancer and other diseases diagnosis, and (4) in biosensors [16–20].

Currently, the diagnostic imaging techniques available clinically are magnetic resonance image (MRI), X-ray computer tomography (also called CT), single photon emission tomography (SPECT), and positron emission tomography (PET), which can give images with resolution of a few millimeters. All these techniques have specific advantages and disadvantages, which can be related to spatial resolution, sensitivity, and/or the nature of the signal used for acquiring the images. MRI is one of the most powerful imaging diagnostic technique developed so far. It is non-invasive and produces images with anatomic detail able to draw inferences about the diagnosis of several diseases [6, 21]. When compared to the other clinical imaging techniques, MRI has several advantages, such as it does not use ionization radiation, images of normal and diseased tissues can be differentiable, and it presents a better spatial resolution (Fig. 1) [4, 5, 21].

In this context, the association of optical and magnetic resonance imaging techniques can offer a combination of imaging modalities more accurate for nanomedicine research and clinical applications. However, the development of multimodal imaging by association of optical and MRI probes is still considered a challenge, mainly since it depends on the design and fabrication of nanostructures that should have both properties in a unique and hybrid optimized nanoprobe. QDs have already been used in the development of bimodal probes for optical/PET, optical/CT and optical/MRI imaging [5, 6, 22–25].

In this chapter, we discuss not only the development of bimodal systems, for optical and magnetic resonance images, but also challenges and advances of their use in biomedical applications over the last 10 years. Aiming a better comprehension of the highlighted characteristics for the presented bimodal systems, first we present briefly QDs and MRI principles, followed by the development of bimodal nanostructures, which is divided into three parts according to the adopted preparation strategy, namely (1) QDs associated with iron-nanoparticles, (2) doped QDs, and (3) QDs associated to Gd^{3+} chelates.

2. BASIC PRINCIPLES OF QUANTUM DOTS AND MAGNETIC RESONANCE IMAGING

2.1. Quantum Dots

Nanotechnology has attracted the attention of many research groups and the nanomaterials have become fundamental elements to technology and science, due to their specific size-dependent properties. QDs dots are a class of these emerging nanomaterials and they are known to be powerful tool in several applications involving the production and use of fluorescence, such as in electroluminescent devices, photovoltaic cells, and more recently in biomedical application and also as probes for nanotheranostic and/or bimodal nanoparticles [14, 26–28].

QDs are semiconductor nanocrystals that have typical diameters ranging from 1.5 to 10 nm, and at this size range, they are under quantum confinement effect in three dimensions. As consequence of this effect, QDs have unique optical properties that are different from bulk semiconductors materials [17, 29]. The intrinsic fluorescence of the semiconductor materials arise due to electronic transitions from the valence band (VB) to the conduction band (CB) and their return to the fundamental state, promoting light emission [30]. The emission region depends on the energetic distance between CB and VB (band gap energy-E_g). In bulk semiconductors, the emission region is related to the material composition. As aforementioned, after light absorption by the semiconductor an electron (e^-) from the BV can be excited to the BC, resulting in a hole (h^+) in the BV. The electron–hole pair has a high attraction between them, due to the Coulomb forces during the small time of light absorption, and may become bounded together [31]. Therefore, the fluorescence is emitted when the e^- returns to its h^+. The e^-h^+ pair is called exciton and also can be considered a hydrogen-like species. Moreover, the distance between e^-h^+ pair is called exciton Bohr radius (a_B). When the semiconductor material has a small size, about a few nanometers, which is smaller than the Bohr radius, we can say that they are under quantum confinement regime [31, 32]. This was a brief explanation about the quantum confinement effect.

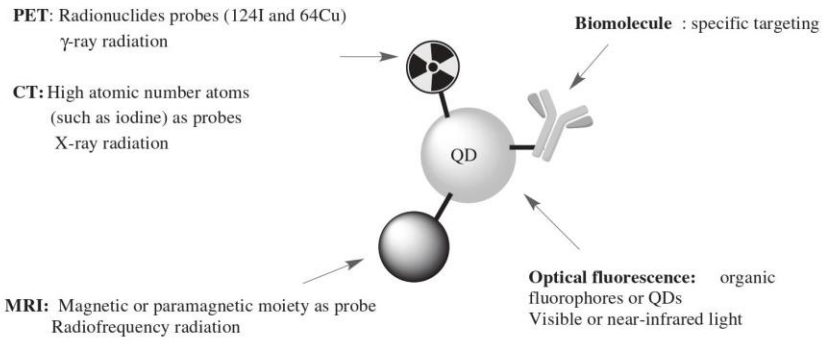

Figure 1. Characteristics of some diagnostic image techniques (PET, CT, MRI and optical fluorescence imaging). Adapted with permission from [4], R. Hachani, et al., *Nanoscale* 5, 11362 (2013). © 2013, Royal Society of Chemistry.

Thus, when the semiconductor materials are exclusively confined in three dimensions, they are called quantum dots. The cadmium selenide (CdSe) bulk, for example, has an exciton Bohr radius approximately $a_B = 5$ nm, thus we only have CdSe QDs if the a_B was less than 5 nm [17].

QDs with different sizes can present light emission from the ultraviolet (UV) to the infrared (IR), even if they have the same chemical composition. This is a consequence of the quantum confinement effect, that changes the E_g [15], which is higher as smaller is the QDs' size, as represented in Figure 2. In other words, after the absorption processes, the electrons return to VB and QDs' emission is proportional to their band gap. Thus, as energy is inversely proportional to the fluorescence wavelength, this means that the larger the QD, the smaller is the E_g and the more toward the red end of the spectrum is its corresponding fluorescence emission [31].

QDs used for biological applications are usually aqueous colloidal nanoparticles. Their nanocrystals structures are usually defined as a core/shell type (Fig. 3), where the core is responsible for fundamental optical properties of the nanoparticle, while the shell is used to improve their optical properties and reduce the chemical effects associated to the environment. The shell assures a physical separation of the core, and is usually composed by another semiconductor that presents an E_g higher than that of the core. Consequently, the optical properties of the nanoparticle become less sensitive to changes induced by medium, for example, the presence of oxidative species and the pH [14, 33].

For QDs' application in the life science, in which fluorescence in the visible/infrared region is usually required, both core and shell are commonly composed of elements from the II B and VI A groups of the Periodic Table (which correspond to groups 12 and 16 in the new International Union of Pure and Applied Chemistry (IUPAC) scheme). The importance of QDs for biophotonic applications is their use as fluorescent probes to replace organic dyes, since they present several advantages, such as [26, 34–39]:

- Photostability: QDs can be 100 times more photostable than organic fluorescent dyes, i.e., this allow the researchers to monitor long-term biological processes in real time.
- QDs' broad excitation (absorption) band: only one light source is necessary at the UV/blue region to excite several QDs, which have different emission colors.
- QDs' emission bands are symmetric and narrow with full width at half maxima (FWHM) usually smaller than

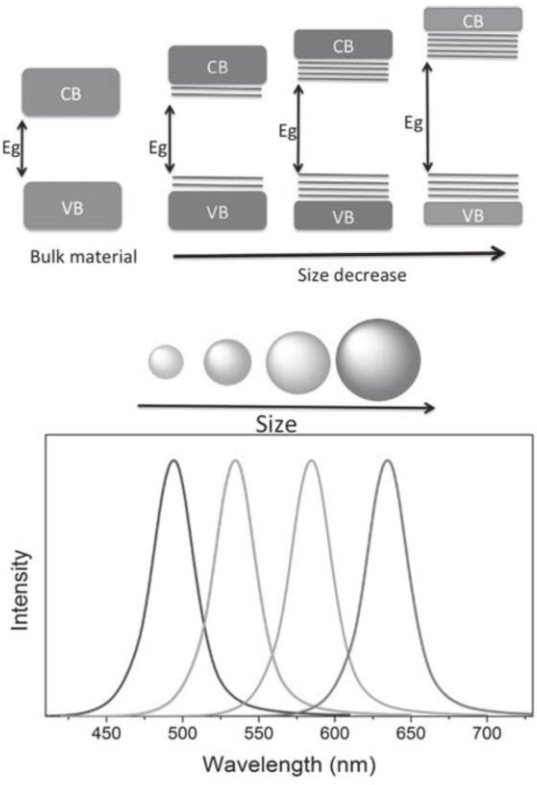

Figure 2. (A) Illustration of the quantum confinement effect with the size decrease that occurs in semiconductor materials of direct band. Energetic levels distribution of the bulk materials in the form of bands; CB = conduction band, VB = valence band, E_g = band gap. (B) Emission spectrum in function of the QD size with the same composition; the colored spheres represent the particle size.

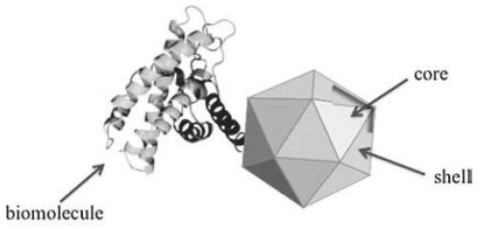

Figure 3. Schematic representation of a core–shell quantum dot functionalized and conjugated with a biomolecule.

50 nm, which can provide more colors in multi-staining methods avoiding cross-talking.

During the colloidal synthesis, the QDs are coated by either organic or inorganic compounds, which are called stabilizing or functionalizing agents [17, 40–43]. They keep the nanoparticles separated from each other preventing precipitation and agglomeration, resulting in stable QDs' suspensions [17, 31]. The main classes of organic molecules used, in aqueous media, as QDs' functionalizing/stabilizing agents are alkyl-thiol molecules, such as mercaptopropionic acid (MPA), mercaptoacetic acid (MAA) and mercaptosuccinic acid (MSA), dihydrolipoic acid (DHLA), cysteine (CYS), cysteamine (CYSAM) and different mercaptodithiols [44]. In organic synthesis, the QDs' functionalizing/stabilizing agents utilized possess long alkyl chains such as tri-n-octylphosphine oxide (TOPO) and hexadecylamine [45].

The QDs' active surfaces promoted by the functionalizing agents allow the QDs' interaction with biomolecules and/or other nanoparticles, enabling the QDs to be useful systems to site-specific biological applications or to develop multimodal image probes. The association/conjugation of QDs to biomolecules is also called bioconjugation [46]. The (bio)conjugation procedures can be carried out by adsorption or by covalent coupling to the systems. Nowadays, the main bioconjugation strategies in aqueous media are performed between carboxylic and amine groups using EDC (1-ethyl-3-(3-dimethylaminopropyl)carbodiimide) and sulfo-NHS (*N*-hidroxysulfosuccinimide), amine–amine using glutaraldehyde, disulfide bonds, and streptavidin-biotin interaction [14, 44, 47, 48]. QDs have been already associated with several biomolecules as fluorescent markers for biological applications [49–52].

Recently, the number of published works involving cell-specific labeling has increased. Some of these works, employing bioconjugated QDs, have been performed for a better comprehension of the antigen expression patterns on the cell surface [52], and also to study proteins or carbohydrates expressions to the comprehension of cell biology in some diseases, such as the cancer [53–55]. Cabral Filho et al. [54] conjugated aqueous CdTe QDs with transferrin (Tf) to study the expression of transferrin receptors (TfRs) in HeLa cells (human epithelial cervical carcinoma) and two glioblastoma cells lines, U87 cells (human primary glioblastoma), and DBRTG cells (human recurrent glioblastoma). The authors showed that HeLa and DBTRG cells present a large amount and a higher extent of TfRs internalization when compared to U87. Furthermore, using a TfR saturation assay, the authors concluded that DBRTG have a faster recycling of the TfR on the cell surface when compared to other two types. The results suggest that the TfR have an important role in cancer maintenance and in recurrent situations. Moreover, the studies about the molecular aspects of cancer cell biology can help in developing more effective therapeutic methods.

Furthermore, QDs conjugated to biomolecules have been used successfully to study the glycoconjugates on microbials cells, such as fungus [56] and bacteria [57]. These studies can help to optimize phototherapy protocols for microbial opportunistic infections. Tenório et al. [56] employed QDs conjugated with ConA (concanavalin A lectin) for understanding cells and biofilm-forming organisms of *Candida albicans*, a human opportunistic fugal pathogen. The authors showed that yeasts, hyphae cells, and biofilm structures were efficiently and specifically labeled indicating that glucose and manose are present in these structures. This work opens new possibilities to monitor glycoconjugates by fluorescence, which can help to improve phototherapy protocols for this kind of fungus.

However, QDs' conjugation with molecules or other nanoparticles to obtain bimodal nanoparticles is still considered a challenge, due to some remaining challenges, such as (1) the conjugation process cannot denature the molecule or cannot affect the nanoparticles' properties; (2) the binding of QDs with biomolecules or with other nanoparticles cannot dissociate during the application in biological systems, and (3) nonspecific interactions cannot occur between conjugated and biological systems [14]. For these reasons, many studies are being carried out to improve the conjugation procedures in an attempt to form bimodal nanostructured systems with high stability, versatility, and the ability to obtain images with high quality and specificity [58–61].

2.2. Magnetic Resonance Imaging (MRI)

MRI has become an indispensable tool in the clinical diagnostic area. This technique present several advantages compared with other clinical image techniques, such as high spatial resolution (0.2–0.3 mm), producing images with fine anatomic details, and it is a non-invasive technique, since it does not use ionizing radiation [62, 63]. The first demonstration that nuclear magnetic resonance (NMR) could be used to distinguish tumors and normal tissues was performed by Raymond [64]. This author showed that the nuclear magnetic relaxation times, T_1 and T_2, are distinct for normal and malignant tissues. After that, the MRI was first demonstrated in 1973 by Paul Lauterbur [65].

The NMR signal related to body water protons (^{1}H) is used to generate the MRI images. The reason for monitoring the ^{1}H water molecules is mainly due to the natural abundance of water in the live organisms and the high sensitivity of hydrogen protons to NMR. The sensibility of the ^{1}H atoms (present in the water molecules of the tissues at different concentration and mobility) to the magnetic field allows the detection of tumors and anomalies in the soft tissues of the body by the differentiation of the images of normal tissue and those which have some morphological or metabolic alterations [64–66]. In abnormal tissues, the values of intrinsic nuclear magnetic relaxation times (T_1 and T_2) change, consequently changing the images obtained.

Briefly, when the positively charged spinning nucleus of the hydrogen atom is in the presence of an external magnetic field (B_0), a spin alignment occurs, generating a resultant magnetization M_0, which is parallel and proportional to B_0. In equilibrium $M_0 = M_z$, where z is the longitudinal axis. To be able to measure M_0, it is necessary to apply a pulse of radio frequency oscillating in the Larmor frequency (or precession frequency) of the ^{1}H, in order to divert M_0 to the xy plane (transverse). Subsequently, the protons release the absorbed energy (at radio wave region) returning to the equilibrium state (the original alignment), a process that is known as relaxation. The relaxation process is modulated by two exponential time constants, T_1 and T_2, which depend on the physical and chemical properties of the tissues. The T_1, known as longitudinal or spin-lattice relaxation, reflects the relaxation due to the energy loss for the neighborhood, and T_2, known as transverse or spin–spin relaxation, is the relaxation due to the interactions between the spins (dipolar interactions). Generally, T_1 gives information about the recuperation velocity of the system's magnetization parallel to the static magnetic field after a perturbation is applied. And, T_2 is related to the quickness of coherence loses of the magnetization in the transverse plane to the static magnetic field and is smaller than T_1 [67]. In practice, this results in differences on the generated image for local chemically and/or morphologically different environments [21, 63, 68].

In order to enhance the quality of the generated images, contrast agents (CAs) are highly administrated in clinical procedures. These MRI CAs must contain paramagnetic or superparamagnetic ions. The most MRI CAs approved for clinical use are based on paramagnetic chelates containing a lanthanide ion, namely gadolinium (III), and iron oxide particles [69]. Usually, contrast agents are classified as T_1 or T_2 MRI CAs, depending on whether they affect mainly the longitudinal (T_1) or the transverse (T_2) relaxation times of the water protons, correspondently. Contrast agents containing gadolinium and manganese ions are commonly T_1 contrast agents, while iron oxides particles are T_2 contrast agents [67].

The Gd^{3+} ion has specific physical properties that are suitable for reducing mainly the longitudinal (T_1) proton relaxation times of surrounding molecules, specifically water molecules protons. Since the Gd^{3+} ion undergoes a rapid hydrolysis at physiological pH, producing insoluble $Gd(OH)_3$ and accumulates in bones and liver, a high thermodynamic and kinetic stability of the complexes used as MRI CAs are required, and these properties are fundamental for their use *in vivo*. Iron oxide particles possess several properties that make them good candidates to be used as MRI contrast agents, and their low toxicity makes them attractive alternatives to gadolinium-based contrast agents [70].

The efficiency of the MRI CAs is measured in terms of the relaxivity (r_i, in $s^{-1} \cdot mM^{-1}$, $i = 1,2$) that indicates their ability to decrease the relaxation times of the water protons per unit (mM) concentration of the paramagnetic ion. Higher values of r_1 and r_2 correspond respectively to smaller T_1 and T_2 values. Longitudinal and transverse relaxivities (r_1 and r_2, respectively) are generally different, and they depend on the magnetic field strength [70]. Relaxivity can be defined as the increase in the water protons relaxation rates provoked by 1 $mmol \cdot L^{-1}$ of the para- or superparamagnetic ion [71]. The relaxivity can be obtained by Eq. (1):

$$r_{1,2} = \frac{R_{1,2}^{obs} - R_{1,2}^{dia}}{C} \quad (1)$$

where $R_{1,2}^{obs}$ is the longitudinal or transverse relaxation rate ($1/T_{1,2}$) of the water protons observed in the presence of the para- or superparamagnetic ions, $R_{1,2}^{dia}$ is the diamagnetic longitudinal or transverse relaxation rate ($1/T_{1,2}$) of the water protons (in the absence of the para- or superparamagnetic ions), and C is the concentration of the para- or superparamagnetic ions [72]. Usually, water protons' longitudinal relaxation time are around 2500 ms, and its transverse relaxation times around 3000 ms.

The enhancement of the contrast is obtained when one tissue has either a higher affinity for the CAs or a higher vascularity than another one. Diseased tissues, such as tumors, are metabolically different compared with healthy tissues, and they have a much higher uptake of the contrast agents, resulting in a higher contrast in MRI images [73].

Despite its high spatial resolution (0.2–0.3 mm), the investigation of molecular events at the cellular level using MRI is limited, because it requires a relatively large local concentration of CAs to achieve an observable contrast enhancement. Considering the molecular structures that usually are used as CA, this is not an easy task. Recently, one of the approaches to overcome this limitation is the use of nanoparticulate systems as MRI contrast agents, which could be able to increase the local concentration of paramagnetic or superparamagnetic ions to each target site [74–76]. Several nanosystems have been developed as CA for MRI such as polymeric nanoparticles [77–79], micelles [80, 81], carbon nanotubes [82–84], liposomes [85, 86], dendrimers [87, 88], proteins [89, 90] and gold nanoparticles [91, 92]. Their r_1 values can be at least 100 times higher per unit CA than those values found to molecular clinical approved MRI CA, such as $[Gd(DTPA)]^-$. The r_2/r_1 ratio is dependent on the particles size, water content, and porosity and can give us the classification of the CAs. Depending on the r_2/r_1 ratios and magnetic field used, they can thus be useful as CAs for T_2-weighting (negative contrast) and/or T_1-weighting (positive contrast) imaging [93]. A contrast agent enhances the positive contrast (T_1) when the $r2/r1$ is around 1–2, and negative CAs usually have r_2/r_1 ratios higher than 10 [94].

The work of Turner et al. [79] is one example of the improvement of the relaxometric properties by preparing nanostructured CAs. They prepared a micellar nanoparticle by aqueous assembly of a diblock copolymer and conjugated them to a Gd-DTPA complex derivative. The nanoparticle prepared presented a r_1 value of 21.2 $mM^{-1}s^{-1}$ (at 0.47 T and 25 °C), which shows an improvement when compared to the Gd-DTPA complex (r_1 = 4.3 $mM^{-1}s^{-1}$ at 0.47 T and 25 °C).

Covalent functionalization of carbon nanotubes with DTPA chelates followed by complexation with Gd^{3+}, originated CAs nanostructured with an improvement in r_1 value by a factor of two, when compared with the DTPA-Gd^{3+} complexes [84].

Other example is the report of Ferreira et al. [92], where they attached DOTA (1,4,7,10-tetraazacyclododecane-1,4,7,10-tetraacetic acid) derivatives complexed with gadolinium to gold nanoparticles, and they observed an enhancement in the r_1 value (at 0.7 T) of at least three times for the nanoparticle system when compared to the bare chelates.

Furthermore, nanoparticles can be important for the development of specific contrast agents for MRI. Several nanoparticles have a functionalized surface that allows the conjugation to biomolecules, conveying the CA to a specific target, which will be fundamental to monitoring cellular events *in vivo* [95].

3. BIMODAL NANOSTRUCTURED PARTICLES

The development of bimodal nanostructures, containing QDs for optical and magnetic resonance images, relies on the design and further preparation of nanomaterials that will present both technique properties. To prepare new particles as potential bimodal nanoprobes for biological applications, some criteria must be considered. The bimodal probes must have [96]:

- High relaxivity and quantum yield;
- Appropriate size for the application
- A simple and cheap preparation method
- Low toxicity
- Kinetic and thermodynamic stability, to avoid inaccurate images and/or toxicity

One of the QDs advantages is their chemically active surface, allowing the conjugation with a variety of molecules and/or other particles, which can originate new multimodal nanostructured particles. The most common approaches used to prepare bimodal nanostructures containing QDs for optical and MR images are their association with iron-oxide based nanoparticles by doping QDs with paramagnetic ions and by their association with paramagnetic chelates. The interest in bimodal nanoparticles for optical and magnetic resonance imaging containing QDs aroused attention throughout the last 10 years. In the next sections, we will present a review of the development of materials aimed at bimodal properties, giving special attention to the maintenance of optical/relaxometric or magnetic properties and their application in biological systems.

3.1. Quantum Dots–Iron Oxide Nanoparticles

QDs associated with magnetic nanoparticles (MNPs) have generated great interest as a new class of materials, because this association can provide a combination of optical and magnetic properties in a single material, enabling simultaneous biolabeling/imaging, cells sorting/separation and therapy/diagnostic (nanotheranostic particles) [97, 98]. There are many examples of multimodal imaging agents containing MNPs, the superparamagnetic iron oxide nanoparticles (SPIONs) being the most used, since the US Food and Drug Administration approved them as contrast agents for MR [I.99].

Bulk iron oxide is classified as a ferromagnetic material, because it presents a permanent magnetization, even without an external magnetic field [100, 101]. Decreasing particles' size from macroscopic to nanoscale, their physical and chemical properties are changed. When iron oxide particles are reduced to a few nanometers (~1–20 nm), each particle behaves as a magnetic single-domain, so their magnetic properties are considerably altered, due to quantum size effects and surface area increase, becoming superparamagnetic [71, 97, 100]. SPIONs are in a uniform magnetization state, which means that after removal of the external magnetic field they lose their magnetization, making them dispersed and diminishing their tendency to aggregate [98].

SPIONs possess an iron oxide core, which provides their magnetic properties, such as the superparamagnetism. The more common iron oxide cores are the magnetite crystalline phase (Fe_3O_4) and its fully oxidized form, the maghemite crystalline form (γ-Fe_2O_3). However, the most used iron oxide core to produce bimodal nanoparticles is the magnetite type, because it has better ferromagnetic response presenting a saturation magnetization (*Ms*) about 92–100 emu $\cdot$ g^{-1} at 300 K, while the maghemite form presents a *Ms* about 60–80 emu $\cdot$ g^{-1} at 300 K [101]. The core is, usually capped with a biocompatible polymer, which shields the core from the surrounding environment and allows the nanoparticles' functionalization, enabling the attachment of other particles or molecules [102].

There are several synthetic methodologies for the SPIONs preparation, such as coprecipitation, microemulsion, hydrothermal processes, electrochemical deposition, sonochemical reactions, thermal decompositions, gas phase depositions and sol–gel processes. The most used methodology is coprecipitation since it is a simple and less expensive method. In this methodology, iron salts in both oxidative stats (ferric and ferrous ions in 2:1 molar ratio) are added to an alkali solution, under inert atmosphere, and the SPIONs are obtained by precipitation [97, 102, 103].

Today, iron-based MNPs are attracting much attention from several research groups, since they have found application in many fields, such as in the material and life sciences. MNPs have been used for *in vivo* biomedical applications, such as contrast agents for MRI, therapeutic agents for hyperthermia, drug carriers, and in radionuclide therapy [104–108].

For biological applications, some characteristics need to be considered: (1) the probe needs to be hydrophilic and stable in water at physiological pH, (2) it should have a narrow size distribution, and (3) it must have a surface coated with biocompatible polymers and a chemical active surface for conjugation with other molecules [98, 102, 109].

Especially for MRI applications, the probes used produce an image contrast enhancement. Although SPIONs can affect the longitudinal relaxation time (T_1), they affect primarily the transverse relaxation time (T_2) of the water protons. Usually, SPIONs have greater transverse relaxivity (r_2) than longitudinal relaxivity (r_1), producing hypointense (dark) signal in MRI [67, 70, 110].

Magnetic properties of SPIONs arise from the presence of Fe^{2+} and Fe^{3+} ions and depend on several factors, such as size, composition, shape, and crystallinity. The magnetic characterization is usually performed by saturation

magnetization (*Ms*) measurements, which indicates the magnetization magnitude of the material when submitted to an external magnetic field. The *Ms* value indicates the higher magnetization of the material, meaning that all the single domains are aligned with the field. However, the efficiency of CAs for MRI is generally discussed based on the materials relaxivity values (r_1 and/or r_2). Many researchers working with SPIONs do not present the relaxivity values and only measure the *Ms* of the material. A direct correlation between saturation magnetization and relaxivity does not exist, although a higher *Ms* will increase the local magnetic field, affecting the surrounding protons and enhancing the MRI signal [111, 112].

Since *Ms* and relaxivity are related, the same factors that affect the magnetization will also affect their ability to reduce T_2. Namely, this ability increases with their size, since their magnetic properties are attenuated in the surface, a smaller ratio between the atoms near the surface and ones in the core will improve their T_2 reduction capacity. The surface coating of the nanoparticles can also affect their CA efficiency, and it has been observed that T_2 contrast decreases with increasing the coating thickness [67, 111, 113, 114].

Several reports demonstrated the association of QDs and SPIONs aimed at the generation of bimodal nanoparticles. In an attempt to overcome the challenges of the bimodal nanoparticles' production using SPIONs and QDs, most works have been concerned with the optimization of the binding process between these nanoparticles. These studies include methodologies to insert QDs and SPIONs in silica spheres [115, 116], micelles [117] and polymer nanospheres [118], mediated by cross-linkers [119, 120] or electrostatic interaction [99, 121, 122].

In this section, we focus our discussion on the different bimodal nanoparticles reported in the literature for biological applications, composed by QDs and SPIONs, which contain their optical and magnetic properties. For better comparison between the bimodal systems developed, we organized them by their synthesis strategy.

3.1.1. Association of QDs and SPIONs by Covalent Binding

One approach to associate QDs and SPIONs is to bind covalently the two nanoparticles using conjugation strategies and cross-linkers (Fig. 4) [119, 120, 122–124].

To our knowledge, the first work describing the formation of a bimodal system by covalently associating cadmium selenide/zinc sulfide (CdSe/ZnS) QDs and SPIONs (γ-Fe_2O_3) was reported by Wang et al. [125], using thiol groups. Since then, other groups have prepared bimodal nanoparticles using this methodology.

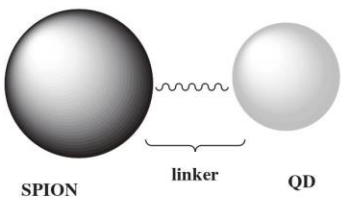

Figure 4. Schematic representation of the covalent association between QDs and SPIONs.

The same approach to bind cadmium telluride (CdTe) QDs to Fe_3O_4 was adopted by Sun et al. [126], where thioglycolic acid (TGA)-stabilized CdTe QDs were linked to the surface of silica (SiO_2)-coated SPIONs. The nanocomposites prepared presented an emission similar to the precursors QDs, and an *Ms* of 2.26 emu $\cdot$ g^{-1}, which is smaller than the *Ms* of bare Fe_3O_4 nanoparticles (49.97 emu $\cdot$ g^{-1}). Then Fe_3O_4@SiO_2-CdTe magnetic/fluorescent nanocomposites were conjugated to the anti-CEACAM8 antibody, which recognized the CEACAM8 receptor on the HeLa (adenocarcinoma cervical human) cell membrane, using *N*-hydroxysuccinimide (NHS) as a cross-linker. The bimodal nanoparticles-anti-CEACAM8 were successfully employed for immune-labeling and fluorescent imaging of HeLa cells.

Kale et al. [119] prepared bimodal nanoparticles by controlled synthesis from CdTe QDs decorated with magnetite nanoparticles using dodecyl amine (DDA) as a linker. CdTe QDs functionalized with mercaptopropionic acid (MPA) were prepared in the presence of the Fe_3O_4 core functionalized with DDA. The bimodal nanoparticles presented a maximum emission at 531 nm with a fluorescence quantum yield (QY) of 18%, in water. The magnetite decorated with CdTe retained the superparamagnetic property of the core, presenting an *Ms* of 44 emu $\cdot$ g^{-1}. The bimodal nanoparticles were conjugated with anti-EGFR antibody and used to specific separation and imaging of positive T leukemic cells (Molt-4), utilizing a mixed cell suspension of Molt-4 and myelogenous leukemia (K562) cells. This specific separation was possible since the EGFR is highly expressed on Molt-4 cells, whereas K562 cells lack this receptor. The results showed that these bimodal nanoparticles exhibited an excellent potential for the magnetic separation and for acquiring fluorescent images of positive leukemic cells (Molt-4).

Koktysh et al. [99] demonstrated the preparation of bimodal nanoparticles by covalent binding of glutathione-coated visible CdTe/CdS (600 nm) or near-infrared (NIR) light-emitting CdHgTe/CdS QDs (800 nm) to Fe_3O_4 nanoparticles functionalized by dextran, which is a biocompatible stabilizing agent commonly used to increase the CAs retention on the blood circulation. According to TEM images, the bimodal nanoparticles showed an average size of around 7.8 nm. Furthermore, inductively coupled plasma (ICP) and energy-dispersive X-ray spectroscopy (EDS) confirming the presence of Fe > 80% and Cd > 13% for both techniques, and the optical characterization showed no changes in the emission spectrum profile. The authors reported that none toxicity of the particles was observed in mice. The *ex vivo* images showed that the particles were accumulated in the lungs and subsequently in the draining lymph nodes. At the end, the authors stated that the bimodal nanoparticles are a combined system that could be used for simultaneous optical and MR images; however, the authors did not present magnetic properties of the systems or magnetic resonance images.

3.1.2. Coating QDs and SPIONs with Silica Layers

Another approach for the synthesis of bimodal nanoparticles is the encapsulation of QDs and magnetic nanoparticles in an outer shell of silica (Fig. 5) [127–133].

Salgueiriño-Maceira et al. [134] incorporated Fe_3O_4/γ-Fe_2O_3 nanoparticles coated with silica and CdTe QDs in an outer shell of silica. The bimodal particles presented a diameter around 220 nm an *Ms* of 1.34 emu $\cdot$ g^{-1} at room temperature and showed efficient fluorescence. The same approach was used by Li et al. [131], avoiding the direct interaction of QDs and MNPs, improving the optical and magnetic response of the bimodal nanosystem. They prepared magnetic-fluorescent dual-functional nanoparticles with a mean size of 60 nm, *Ms* of 3.2 emu $\cdot$ g^{-1} and an emission maximum at 618 nm. In both works the authors presented the bimodal nanoparticle, with a silica shell, as a new bimodal tool for biological application. Further, in 2009 the same research group [135] also used the reverse microemulsion approach to prepare bimodal nanoparticles in order to label specifically prostate cancer cells. The bimodal nanoparticles (with 50 nm of mean diameter and an *Ms* = 3.24 emu $\cdot$ g^{-1}) were functionalized by 3-aminopropyltrietoxysilan (APS) and conjugated to single chain variable fragment antibody (scFv) of human γ-seminoprotein-specific, using glutaraldehyde as coupling agent. The specific bimodal nanostructures were applied in human embryonic kidney cells (HEK293) as a negative control and human prostate cancer cells (LNCaP) as a positive test, since LNCaP cells have an overexpression of γ-seminoprotein. Both cells were analyzed by fluorescence microscopy. Furthermore, the authors also injected LNCaP cells subcutaneously into female nude mice, and then the animals were analyzed by MR and fluorescence images. The results showed that bimodal nanoparticles-scFv did not label HEK293 cells, while LNCaP cells were labeled both on the membrane and also inside the cells. Moreover, the bimodal nanoparticles did not present apparent toxicity. In mice after 6 h, bimodal nanoparticles-scFv were concentrated in the tumor tissues and in other organs, such as the liver, lung, heart, and kidney. However, after 24 h, most of the nanoparticles disappeared from the organs of mice and were mainly observed in local tumor tissues, both by fluorescence imaging as MRI. The authors also explored the hyperthermia using bimodal nanoparticles-scFv and found that the number of LNCaP cells destroyed was proportional to the concentration of the nanoprobes in the medium.

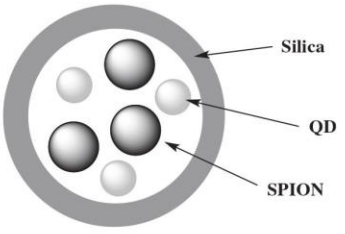

Figure 5. Schematic representation of QDs and SPIONs encapsulated in an outer silica shell.

In other works of the same group [116], they used the amino-modified bimodal nanoparticles (Fe_3O_4–CdTe@SiO_2) to label mesenchymal stem cells (MSCs) in gastric cancer, *in vitro* and *in vivo*. *In vitro* studies showed that the fluorescent and magnetic resonance signals of the labeled cells, with the bimodal nanoparticles, were stable for up to 14 days. Then the *in vivo* studies were performed by the intravenous injection of the MSC labeled with bimodal nanoparticles in nude mice containing gastric cancer. Bimodal nanoparticles distributions in the whole body were monitored for a period of 14 days after injection by using *in vivo* image system (IVIS) and MRI. It was observed that the fluorescent and MR signals in the tumor tissue increased gradually from day 7 to 14 post-injection. The hyperthermia therapy study showed that only amino-modified bimodal nanoparticles presented tumor shrinkage while bimodal nanoparticles did not show evident alteration.

Ma et al. [136] synthesized bimodal nanoparticles from two color emission CdSeTe/CdS hydrophobic QDs (λ = 600 nm and λ = 780 nm) and Fe_3O_4 nanoparticles. To obtain the bimodal nanoparticles, authors grew a silica layer in a Fe_3O_4 MNP core, forming a MNP bead. Then they added the QDs and tetraethyl orthosilicate (TEOS) to form a thin shell of QDs/silica around the MNP beads. Bimodal nanoparticles have an average size of about 150 nm and maxima emission at λ = 600 and λ = 750 nm. The authors referred that these bimodal nanoparticles acted predominately in T_2-weighted images, because the nanoparticles presented relaxivity values for r_1 and r_2 about 13 and 1914 mg $\cdot$ L^{-1} $\cdot$ s^{-1}, respectively. For specific labeling, they conjugated the bimodal nanoparticles to anti-HER2 (human epidermal growth receptor 2 antibody) antibody using EDC. To confirm the ability of the bimodal nanoparticles functionalized with anti-HER2 antibody to label specific target, the authors performed *in vivo* and *in vitro* tumor imaging. Breast cancer tumors were induced on nude mice by transplantation of green fluorescent protein (GFP) human breast cancer cells (KPL-4 cells). The specific binding *in vitro* was confirmed by fluorescence microscopy and fluorescence cell sorting analysis and for *in vivo* images, they used near-infrared fluorescence (NIR-fluorescence) and MR imaging. The authors presented an efficient method to produce bimodal nanoparticles that can be used for biomedical applications and as diagnostic methods of several diseases.

Chen et al. [133] also prepared magneto-fluorescent nanoparticles, mixing hydrophobic CdSe/CdS QDs and Fe_3O_4 SPIONs, and transferred them to aqueous solution using the surfactant dodecyltrimethylammonium bromide (DTAB). Briefly, the authors synthesized the bimodal nanoparticles in four steps: (1) micelle formation in chloroform by using DTAB as a surfactant with a random magnetic core, (2) a supercrystalline magnetic core formation by using poly(vinylpyrrolidone)/ethylene glycol (PVP/EG) under heating at ~80 °C and stirring, (3) silica shell growth using TEOS, and (4) finally the silica-bimodal nanoparticles were coated by polyethylene glycol (PEG). In this work, the authors demonstrated that after coating with PEG, silica-coated-bimodal nanoparticles showed an efficient bimodal image probe for *in vivo* multiphoton (MP) and MRI, with a size of 120 nm, an *Ms* of 15.2 emu $\cdot$ g^{-1} (at room temperature), and a QY of 12% in water. Intravital multiphoton

microscopy images were obtained through a cranial window in model C_3H mice after injection of murine cancer cells stage IV (MCaIV). Figure 6 shows the intravital MP images, where in Figure 6(A) shows MP image before injection of bimodal nanoparticle, Figure 6(B) after 4 h of injection, and Figure 6(C) after 24 h of injection. MRI (Fig. 7) was obtained in a 9.4 T magnet, before (Fig. 7(A)) and after 24 h (Fig. 7(B)) of the bimodal nanoparticles injection.

3.1.3. Incorporation of QDs and SPIONs in Polymer Beads

Another approach for the preparation of bimodal nanoparticles containing QDs and SPIONs is the incorporation of these nanoparticles in polymer beads (Fig. 8) [118, 137–142].

Although there are many reports using this methodology to prepare bimodal nanoparticles, to our knowledge only one research group applies them in biological studies. Song et al. [118] synthesized bimodal nanoparticles by an organic route, using an hydrazine-treated poly-(styrene/acrylamide) copolymer nanosphere. The bimodal nanoparticles were constituted of CdSe/ZnS QDs and the Fe_2O_3. The bimodal nanospheres were conjugated to avidin that was associated to a biotynilated goat anti-mouse IgG (Fc specific polyclonal antibody), and then, mouse anti-human anti-CD3 monoclonal antibody (mAb) or mouse anti-human anti-PSMA mAb, respectively. The authors demonstrated the potential of the bimodal system conjugated to the antibody for the detection and isolation of cancer cells. They used two complex samples containing Jurkat T cells (human peripheral blood leukemia T cells) and red blood cells (RBCs) and another containing LNCaP and RBCs as a control. The Jurkat T cells were bound to anti-CD3 mAb-coupled bimodal nanoparticles, and the LNCaP cells were bound to anti-human anti-PSMA mAb-coupled bimodal nanoparticles and separated using an external magnetic field. They reported that the conjugated nanoparticles were able to detect and extract two different types of tumor cells (leukemia cells and prostate cancer cells) from a complex sample. Therefore, the authors presented a simple and sensitive approach for detection and isolation of multiple cancer cells at early stages, *in vitro*.

3.1.4. Association of QDs to SPIONs by Electrostatic Interactions

The electrostatic interactions based on oppositely charged materials attraction was employed by some authors [122, 132, 143–145] to prepare magnetic-luminescent nanocomposites (Fig. 9).

Ahmed et al. [121] synthesized bimodal nanoparticles associating Fe_3O_4 and green CdTe QDs by electrostatic interaction. The bimodal nanoparticles were obtained with a mean size of 50 nm and an *Ms* of 65 emu $\cdot$ g^{-1}. The bimodal systems were incubated with human embryonic kidney cells (HEK293) and human epithelial colon cell line (LS174TK), after conjugation to antigen-binding fragment (Fab) region of hCC49 antibodies also by electrostatic interaction. The conjugated nanoparticles were specifically attached around the nucleus of LS174T cancer cells, while HEK293 cells presented no labeling around the nucleus.

Using the interaction of the metal coordination bonding to DNA, Lee and collaborators [146, 147] developed a new strategy for the preparation of bimodal nanoprobes. These authors linked QDs conjugated with platinum to magnetic nanoparticles (MNPs) functionalized with guanines (Fig. 10(A)), using the coordination bonding of Pt with the guanines. They used two QDs with different emission maximum (605 and 800 nm) and the association with the MNPs has not changed their emission properties. The bimodal nanoparticles prepared presented an average size of 50 nm (determined by DLS) and they were tested with HeLa cells. Fluorescence microscopy showed that the HeLa cells internalized these particles, and the nanoparticles were mainly located next to the nuclei (Figs. 10(B and C)). The magnetization curve showed that the magnetism of the MNPs was maintained after conjugation with the QDs. *In vitro* magnetic resonance images of HeLa cells incubated with QDs-MNPs conjugates showed the preservation of the magnetic properties of the bimodal systems (Fig. 10(D)).

3.1.5. Final Considerations About QDs–Iron Nanoparticles

Most authors cited in this section reported a decrease in the saturation magnetization (*Ms*) of the bimodal nanoparticles, when compared to the bare magnetic nanoparticles (Table 1). Table 1 also shows data from several research groups that employed different methodologies to associate QDs and SPIONs. They did not necessarily apply these systems; however we presented them as potential bimodal probes for biological applications.

3.2. Doped Quantum Dots

At the nanoscale range, the QDs structural stability, the electronic and photophysical properties can be changed by

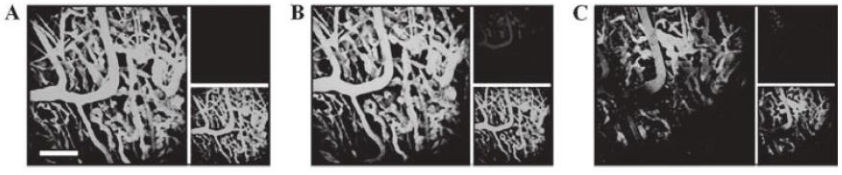

Figure 6. Intravital MP microscopy images of the cranial window. In (A) before injection, (B) 4 h after injection and (C) 24 h after injection of bimodal nanoparticles. Images from red and green channels are shown in small panels (top: red channel, bottom: green channel). Green emission signals was generated from fluorescein isothiocyanate–dextran (FITC–dextran) a blood vessel tracer and the red emission are generated by bimodal nanoparticles. Scale bar = 150 mm. Adapted with permission from [133], O. Chen, et al., *Nature Comm.* 5 (2014). © 2014, Nature Publishing Group.

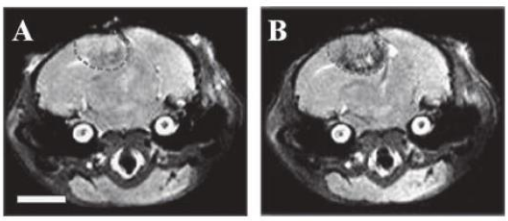

Figure 7. *In vivo* T_2-weighted MRI. In (A) before bimodal nanoparticles injection, and in (B) 24 h after bimodal nanoparticles injection. After 24 h post injection image (B) show clear tumor visualization (inside the red dashed line). Scale bar = 3 mm. Adapted with permission from [133], O. Chen, et al., *Nature Comm.* 5 (2014). © 2014, Nature Publishing Group.

any perturbation in the crystalline lattice. Thus, the incorporation of dopant ions in QDs can bring new properties that could lead to new advances for several applications. The control over size and shape in colloidal synthesis, developed so far, allowed the incorporation of transition metal ions in semiconductor QDs. In an effective doping procedure, the dopant ions will replace some atoms on the host crystal structure in the QD matrix [149–151]. However, nanocrystals try to purify themselves, and during their growth process, they tend to anneal out the dopants, since the impurities incorporation requires much more energy [152, 153].

As aforementioned, in non-doped QDs, an electron from the VB upon absorption of light goes to the CB, and its return to the fundamental state promotes the emission of a photon of wavelength related to the QDs' bang gap energy. The presence of impurities or high concentration of surface defects will increase the nonradiative decay pathways in a random way, which will decrease or quench the photoluminescence and change the expected spectral profile. The incorporation of dopants in QDs will create new defined electronic states inside the band gap region (between the VB and CB) (Fig. 11). Thus, it will decrease the energy separation between the CB and the VB, leading to adjustments in the relaxation pathways to the fundamental state, originating new luminescence properties. In other words, the doped QDs' emission will be red-shifted when compared to the non-doped QDs and the bandwidth will increase. Hence, QDs' optical and electronic properties can be tuned by controlling the dopant's type and concentration [150, 151, 154].

In the last years, there have been several reports on the preparation of doped QDs, using several transition metals and lanthanides ions, such as Mn, Co, Cu, Fe, Eu, and Yb, showing promising applications in biological imaging [155], MRI [6], solar cells [156, 157], light-emitting

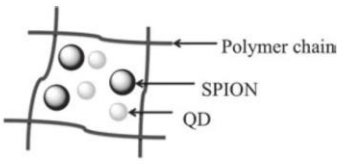

Figure 8. Schematic representation of the incorporation of QDs and SPIONs in polymer beads.

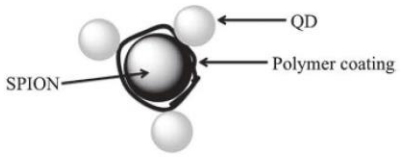

Figure 9. Schematic representation of QDs and SPION associated by electrostatic interactions.

devices (LEDs) [158, 159], biosensors [160, 161], and photocatalysis [162]. In this section we will focus our attention only on doped QDs developed simultaneously for optical and magnetic resonance imaging reported in the literature, which present optical and relaxometric studies.

For MRI proposes, QDs have been doped with Mn^{2+}, Gd^{3+}, and Fe^{2+}. Paramagnetic metal ions, with a large spin number, are often chosen as CA for MRI, since they have physical properties that are able to decrease the nuclear relaxation times of specific isotopes on the surrounding environment. The paramagnetic lanthanide ion most used is gadolinium, since it has seven unpaired electrons. Another metal ion widely used is manganese, which has five unpaired electron in its bivalent state. These ions, when used as CA, shorten the longitudinal relaxation time (T_1) of water protons, enhancing the T_1-weighted MR images [163, 164], while iron shortens the transverse relaxation time (T_2) of water protons, enhancing the T_2-weighted MR images. Therefore in this section we will discuss first the Mn^{2+} doped QDs, followed by Gd^{3+} and Fe^{2+} doped QDs.

3.2.1. Manganese-Doped QDs

The first QD doped with manganese was reported by Bhargava et al. [165], and the optical properties of ZnS:Mn were studied by these authors. These authors reported that incorporation of Mn^{2+} in QDs changed their optical properties, shifting the emission to the yellow emission region, which was being associated with the Mn^{2+} ions intrinsic electronic transitions. This means that after excitation of zinc sulfide (ZnS) QDs, a subsequent transfer of electron and hole into the electronic level of the Mn^{2+} occurs, leading to the characteristic emission of Mn^{2+}. Since then, several reports on the preparation of manganese doped QDs have appeared [151, 166–169].

Several authors reported the synthesis and the potential of QDs doped with manganese as bimodal markers for optical and MRI [155, 170, 171]. However, Wang et al. [172] were the first to present, simultaneously, the optical properties together with relaxivity measurements for these materials. These authors prepared core/shell QDs of CdSe/ZnS doped with manganese (CdSe/ZnS:Mn) by an organometallic route, with an average size of 4.7 nm (estimated by TEM). They achieved a dopant maximum of 6.2% (determined by elemental analysis), and they verified by electronic paramagnetic resonance (EPR) studies that the Mn^{2+} was incorporated into the shell. The nanoparticles, containing different amounts of Mn^{2+}, showed an emission centered from 570 to 650 nm. In organic solvents, these QDs presented a fluorescence quantum yield (QY) of 60%, but in water (after being coated with an amphiphilic polymer) the

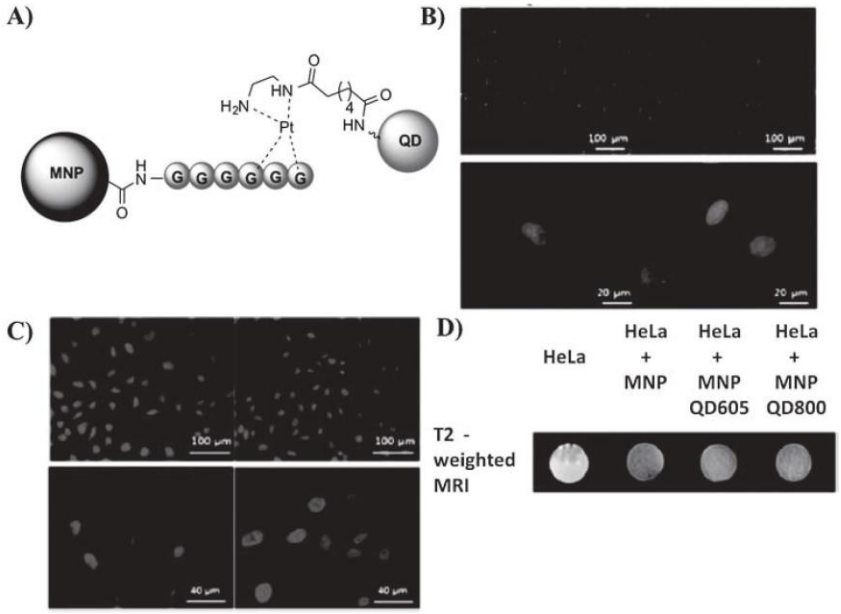

Figure 10. (A) Schematic representation of the bimodal system (MNP-QD) prepared by Lee et al. Fluorescence microscopy images of MNP-QD systems incubated with HeLa cells (B) with emission at 605 nm and (C) at 800 nm. (D) MRI results of HeLa cells incubated with MNP, MNP-QD with emission at 605 nm and 800 nm. Adapted with permission from [147], J. Lee, et al., *Analyst.* 140, 2864 (2015). © 2015, Royal Society of Chemistry.

QY decreased to 21%. The CdSe/ZnS:Mn also showed high longitudinal relaxivity value (r_1), being 18 mM^{-1} s^{-1} (at 7 T and room temperature) for the QD with 6.2% of Mn^{2+}. These authors have performed both optical and MR images incubating the water-dispersed nanoparticles (0.408 mM) with macrophages. They observed spots of luminescence in the cytoplasm of the cells by confocal microscopy, and a contrast enhancement of the incubated cells, compared with the unlabeled ones, by MRI. This means that the quantity of Mn^{2+} incorporated in the QDs was reasonable to produce images in both modalities, and the bimodal nanoparticle is suitable to be used in both optical and MR imaging.

ZnS QDs doped with manganese were prepared as a dual-imaging contrast agent, for optical and MR images, by Gaceur et al. [173]. These nanoparticles presented a 10% concentration of Mn^{2+} (estimated by X-ray Diffraction, XRD) with a diameter about 1.5 nm (determined by TEM). The ZnS:Mn showed a blue-green emission, with a broad band centered at 466 nm with a shoulder at 507 nm. As opposed to previous studies [165], in this report no emission arising from the Mn^{2+} electronic level (580–600 nm) was observed. These authors attributed this fact to concentration quenching, i.e., the number of Mn^{2+}–Mn^{2+} pairs increased when the Mn^{2+} concentration was high, which resulted in an

Table 1. SPIONs saturation magnetization values before and after conjugation to QDs.

Synthetic strategy	Bimodal nanoparticle composition	Size (nm)	*Ms* of bare SPIONs (emu · g^{-1})[a]	*Ms* of bimodal nanoparticles (emu · g^{-1})[a]	Reference
Cross-linking	Fe_3O_4@SiO_2-CdSe/ZnS	25	67.7	2.38	[124]
	Fe_3O_4@SiO_2-CdTe	30	40.97	2.26	[126]
	SPION-CdS	100	55	9.5	[120]
	Fe_3O_4-CdTe/CdS	11	62	44	[119]
Silica coating	(Fe_3O_4/γ-Fe_2O_3@SiO_2-CdTe)@SiO_2	220	54	1.43	[134]
	(Fe_3O_4-CdTe)@SiO_2	50	54	3.21	[130]
	Fe_3O_4@SiO_2-CdSe/ZnS@SiO_2	60	45.2	3.2	[131]
	(γ-Fe_2O_3-CdSe)@SiO_2	11	26[b]	0.4[b]	[148]
	(Fe_3O_4-CdSe/CdS)@ SiO_2	100	63.7	15.2	[133]
Polymer coating	(Fe_3O_4-CdTe)chitosan	65	77	11	[139]
Electrostatic interactions	Fe_3O_4@SiO_2-CdSe	~100	68	11.7	[132]
	Fe_3O_4@SiO_2_ CdTeS	100	38.26	9.09	[144]
	CdTe–Fe_3O_4	50	71	65	[121]

Notes: [a] at room temperature–300 K. [b] at 15 K.

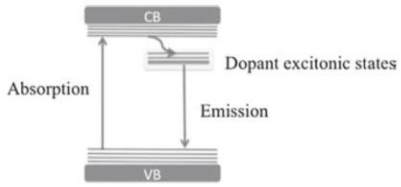

Figure 11. Scheme illustrating the creation of electronic states inside the band gag region, due to the incorporations of dopants in QDs and its decay pathways.

increase in the non-radiative decays from the excited states being observed. Relaxometric studies gave a value of r_1 of 20 mM^{-1} s^{-1} (at 3 T and 25 °C). These nanoparticles were used in an intracellular uptake study using Chinese hamster ovarian (CHO) cells, and it was observed by confocal microscopy that after 24 h of exposure, the QDs were internalized and were dispersed in the cytosol. Cytotoxic studies showed that these QDs did not hinder the cell viability and proliferation (at concentration of 0.05 mM of Mn^{2+}).

Jing et al. [174] prepared core/shell CdTe/ZnS QDs doped with manganese ions using colloidal aqueous synthesis. These nanoparticles presented a diameter of 4.3 nm (estimated by TEM) and different dopant levels were used (4.7–9.7%, determined by inductively coupled plasma optical emission spectrometry (ICP-OES)). EPR studies confirmed that the dopant ions are in the surface region distributed within the ZnS shell. Fluorescence studies showed that CdTe/ZnS:Mn emitted at 650 nm, and their QY decrease with increasing the dopant proportion. This QY decrease may be explained by the presence of some manganese ions in the core/shell interface. The QDs with 4.7, 7.5, and 9.7% of Mn^{2+} presented ionic longitudinal relaxivity values of 10.7, 6.5, and 5.4 $mM^{-1}s^{-1}$ (per Mn^{2+}, at 3 T and room temperature). These results showed that ionic relaxivity values decrease with increasing Mn^{2+}.

Lin et al. [175] prepared cadmium-free QDs with paramagnetic properties. These authors synthesized an I–III–VI ternary core, copper indium disulfide ($CuInS_2$), capped with manganese-doped ZnS, by colloidal organic synthesis. ICP confirmed that they were able to incorporate 0.2 to 2.3% of Mn^{2+}, by EPR was confirmed that the Mn^{2+} was present in the ZnS shell, and by TEM was observed that these nanoparticles have a diameter of 4 nm. These QDs emitted around 600 nm and their QY in organic solvent was 52%, but when transferred to an aqueous phase the QY decreased to 18%. Relaxivity measurements presented values between 5.1 and 7.2 mM^{-1} s^{-1} (3 T at room temperature), depending on the quantity of Mn^{2+}. In order to show that these QDs can be used as dual-modality probes, they incubated the $CuInS_2$/ZnS:Mn with human pancreatic cancer cells (BXPC-3 cells line). The red emission observed in confocal microscopy indicated that BXPC-3 cells internalized these QDs. In cells lysates it was possible to observe that the internalized QDs produced MRI contrast enhancement in a T_1-weighted image.

Manganese doped zinc selenide (ZnSe:Mn) QDs for dual-modal imaging were prepared by Sharma et al. [176], in organic medium and varying Mn^{2+} concentration. These nanoparticles had an average size of 6.5 nm (observed by TEM) and ICP confirmed they had incorporated 1.1 to 5.9% of Mn^{2+}. As others before, these authors also observed that by increasing Mn^{2+} concentration, the emission intensity first increases (these QDs reached a maximum at Mn^{2+}concentration of 3.2%), starting to decrease after. However, the emission peak position stayed at 585 nm independent of the dopant concentration. The QY for these QDs, in water, was determined to be 18%, after a ligand exchange, using the MPA as functionalizing/stabilizing agents. The potential application of the ZnSe:Mn for MRI was investigated, and these nanoparticles presented a relaxivity value of 2.95 $mM^{-1}s^{-1}$ (at 3 T and 25 °C).

Zhang et al. [177] prepared Mn^{2+} doped CdTe QDs in aqueous solution, obtaining QDs with a size of around 3.7 nm (estimated by TEM) and a Mn^{2+} level of 2.8% (by atomic absorption spectroscopy). Fluorescence studies, in water, showed that the QY of CdTe:Mn (48%) increases when compared to CdTe (23%), and decreases with further increase of Mn^{2+} concentration. The emission wavelength can be tuned with the Mn^{2+} amount, and the doped QDs emission peak was red-shifted, relatively to non-doped QDs, emitting at 545 nm. The longitudinal relaxivity of these CdTe:Mn value was 4.29 $mM^{-1}s^{-1}$ (measured at 7 T and room temperature).

Although several groups reported the potential of manganese-doped QDs for optical and MR imaging, only Ding et al. [178] presented experiments of fluorescence and MR imaging *in vivo* for passive tumor targeting. They prepared $CuInS_2$/ZnS:Mn nanoparticles with a diameter of 3.6 nm (determined by TEM) and emissions around 620 nm. The QDs containing a Mn^{2+} concentration of 1.4% (by ICP-OES), presented the higher QY, and a relaxivity of 5.84 $Mm^{-1}s^{-1}$ (at 1.5 T and 37 °C). For the *in vivo* studies, first the cytotoxicity of PEGylated QDs on the proliferation of HeLa cells was evaluated, and it was observed that these QDs presented no toxicity for the concentration below of 9 mM. Nude mice, subcutaneously transplanted with human colon cancer (LS180) tumor cells at the leg, was injected intravenously with the PEGylated $CuInS_2$/ZnS:Mn. By optical images, it was observed that the fluorescence signal appears 10 min after the injection and reaches its maximum around 6 h post-injection. For the MRI studies, the nude mice were implanted with a tumor and injected intravenously with the same dosage level of nanoparticles. T_1-weighted MR images showed that the contrast reaches its maximum at 8 h post-injection, companying the decrease of the T_1 value. The biodistribution of the QD-injected studies showed that the strongest fluorescent signal was found in the liver, followed by stomach, kidney, tumor, and spleen. But in the heart and lungs no optical signal was observed.

3.2.2. Gadolinium-Doped QDs

The first example of gadolinium-doped QDs as multimodal agents for optical and MR images was reported by Li and Yeh [179]. These authors prepared CdSe:Gd capped with TOPO, with a diameter of 6.3 nm (estimated from TEM) and a dopant level of 0.061% (from ICP). These QDs have an emission maximum at 600 nm, and it was observed that by increasing the dopant amount, a decrease in the QY was observed. Exchanging the stabilizer from TOPO to the water-soluble MPA stabilizing agents leads to a decrease in

the QY from 4.6 to 0.2% (relative to rhodamine). The longitudinal and transverse relaxivities were measured at 3 T, and these CdSe:Gd presented a $r_1 = 76.7\ mM^{-1}s^{-1}$ and a $r_2 = 54.3\ mM^{-1}s^{-1}$. Since the r_2/r_1 value was 0.7 (close to 1) these QDs could act as a positive contrast agents, for T_1-weighted images.

Liu et al. [96] prepared zinc oxide (ZnO) QDs doped with Gd^{3+} in ethanol, with a Gd/Zn rate of 8% (determined by inductively coupled plasma mass spectrometry, ICP-MS). The ZnO:Gd presented a size of 4 nm (estimated by TEM) and an emission maximum around 550 nm. The incorporation of Gd^{3+} (8%) increased the fluorescence QY (from 13.5 to 34%, in ethanol relatively to rhodamine), but further incorporation of Gd^{3+} led to a decrease in the QY. A surface modification using *N*-(2-aminoethyl)aminopropyltrimethoxysilane (AEAPS) was performed in order to disperse the QDs in aqueous medium and to use them in biological systems. The ZnO:Gd cytotoxicity was studied in HeLa cells showed a low toxicity, with 1 mM of QDs during 24 h. The longitudinal relaxivity was determined at 1.5 T showing a value of $r_1 = 16\ mM^{-1}s^{-1}$. The ZnO:Gd were incubated with HeLa cells and a yellow emission, due to the presence of QDs, was observed in confocal microscopy. Cell pellets of HeLa cells with and without QDs were used in T_1-weighted MR imaging, proving that the cells treated with QDs showed brighter images than the others.

Quaternary QDs of zinc copper indium sulfide (ZnCuInS) were doped with Gd^{3+} and capped with ZnS by Guo et al. [180]. These authors prepared ZnCuInS:Gd with an amount of Gd^{3+} from 7.9 to 14.3% (determined by ICP-MS), and passivated them with a shell of ZnS in order to enhance their fluorescence. These ZnCuInS:Gd/ZnS presented a size around 4.3 nm (determined by TEM) and an emission centered between 550 nm to 725 nm depending on the Zn/Cu ratio, with increasing the amount of Zn a blue-shift was observed. Also a slight decrease in QY was observed with the incorporation of Gd^{3+}. For biological applications, the doped QDs were coated with bovine serum albumin (BSA), forming nanohybrids with a hydrodynamic diameter around 70 nm. Relaxivity studies of ZnCuInS:Gd/ZnS@BSA showed that these systems presented stronger T_1 effect, with r_1 values of 11.53, 13.65, and 15.78 $mM^{-1}s^{-1}$ (7 T) for the systems with 7.9, 10.6, and 14.3% of Gd^{3+}, correspondingly.

For the *in vitro* studies, the ZnCuInS:Gd/ZnS were incubated with HeLa cells, a fluorescence signal was observed inside the cells except for the nucleus region, and the MR signal was enhanced in the cells containing these systems for 6 h, showing that these QDs were uptaken by the cells. The toxicity studies of ZnCuInS:Gd/ZnS@BSA in HeLa cells showed no apparent loss of the cell viability, after incubation with QDs with a concentration of 500 $\mu g\ mL^{-1}$ for 24 h. The ZnCuInS:Gd/ZnS@BSA nanohybrids were also used in *in vivo* imaging, injecting them intravenously into BALB/c mice at a dosage of 0.05 mmol Gd/kg. By fluorescence imaging it was observed that these systems accumulated in the liver 30 min after injection, and using a MRI scanner (7 T) an enhancement in T_1-weighted MR images was observed 1 h post-injection. At 6 h after injection, the mice were sacrificed and it was observed that the majority of the nanohybrids remained in the liver and the spleen. No fluorescence in the kidneys was observed, which can mean that particles with this size do not undergo renal clearance. To evaluate the toxicity of these nanohybrids in major organs (such as heart, liver, spleen, lungs, and kidneys), H&E (hematoxylin and eosin) staining examination was performed. The organs were collected at 2 and 14 days after the injection, and the results revealed no organ abnormality or lesions in mice administrated with ZnCuInS:Gd/ZnS@BSA, indicating a good biocompatibility of these systems [180].

Zhang et al. [181] prepared CdTe:Gd in aqueous suspension with an amount of 2.03% (determined by ICP) of dopant and a size around 3 nm (determined by TEM). These QDs have a maximum emission peak in 640 nm with a QY of 38% in water (relatively to rhodamine), which decreases when the amount of Gd^{3+} increases. Paramagnetic studies demonstrated a longitudinal relaxation rate (r_1) value of 3.27 $mM^{-1}s^{-1}$ (3 T). For targeting cancer cells, the CdTe:Gd QDs were conjugated with folic acid (FA) using the EDC/NHS coupling strategy. For the *in vitro* studies, the conjugates were incubated with HepG2 cells (human liver cancer cells) and a red fluorescence was observed, showing that the CdTe:Gd-FA successfully labeled the cells, compared to CdTe-Gd that could not label the cells. Using MTT (methyl thiazolyl tetrazolium) assay, the cytotoxicity of CdTe:Gd-FA in HepG2 cells was evaluated, showing that, after 24 h, more than 80% of the cells remained viable with a conjugate concentration of 0.5 $mg \cdot mL^{-1}$. For the *in vivo* studies, BALB/c nude mice were injected with HepG2 cells into their right axillar, and then CdTe:Gd-FA were injected in their eye veins. Fluorescence and MR images were recorded, and an enhancement in the fluorescence and the MR signals were observed in the tumor site.

Gd-doped CuInS caped with ZnS (Gd:CuInS/ZnS) were prepared by Yang et al. [182] as bimodal QDs. These particles presented a size around 3.0 nm (determined by TEM), a 3.05% Gd:CuInS (calculated by EDS) and an emission maximum around 670 nm. For the magnetic properties studies and further applications, the hydrophobic QDs obtained were encapsulated with the PEG and transferred to aqueous phase. Gd:CuInS/ZnS@PEG bimodal systems presented a r_1 value of 9.41 s^{-1} per mM of Gd^{3+} (at 1.5 T), suggesting that these particles can be used as T_1 contrast agents. MTT studies with U87MG cells (glioblastoma astrocytoma) showed that Gd:CuInS/ZnS@PEG presented low cytotoxicity against these cells. *In vivo* studies were performed to detect U87-expression in tumors by fluorescence imaging, and the fluorescence signal due to the presence of these bimodal nanoparticles were detected in tumor and liver 4 h post-injection (Fig. 12(A)). T_1-weighted MR images were obtained, after injecting a dosage of 0.05 mmol Gd/Kg body weight of nude mice, which showed a enhancement in the MRI signal in the tumor site 4 h post-injection (Fig. 12(B)). H&E staining study of several major organs, allowed the study of the *in vivo* toxicity of the Gd:CuInS/ZnS@PEG nanoparticles, and no necrosis and inflammation in the tissue of several organs was observed 7 days after injection.

3.2.3. Iron-Doped QDs

As far as we know, up to the present moment in the literature exists only one report of iron-doped QDs for optical and MR imaging that presents its emission and relaxivity

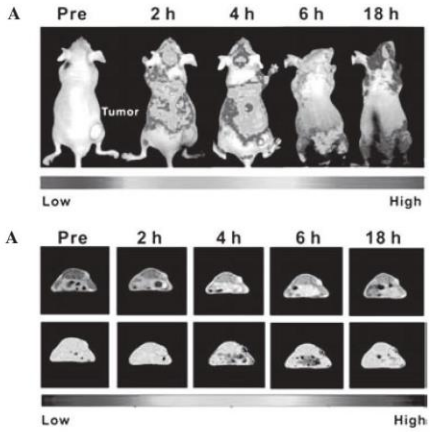

Figure 12. *In vivo* (A) fluorescence images and (B) T_1-weighted MRI of mice bearing U87 tumor cells. Adapted with permission from [182], W. Yang, et al., *ACS Appl. Mater. Interfaces* 7, 18759 (2015). © 2015, American Chemical Society.

properties for these QDs. Saha and collaborators [183] prepared CdTe:Fe QDs for magnetic and vis-NIR imaging. These QDs have been synthesized by an aqueous hydrothermal technique, using Teflon®-lined autoclaves. This methodology allows the utilization of high temperatures in aqueous media, which accelerates the nanocrystal growth rate. The CdTe:Fe presented an emission between 530 and 738 nm, depending on the reaction time. The nanocrystals were obtained with a diameter around 4.9 nm (determined by TEM) and 5.6% of iron (determined by ICP) in their composition. As have been seen for other dopants (such as Mn^{2+} and Gd^{3+}), an increase in dopant concentration leads to a decrease in fluorescence intensity. By X-ray photoelectron spectroscopy (XPS), these authors verified that the major quantity of Fe^{2+} was found in the core, decreasing toward the border. The transverse relaxivity (r_2) for CdTe:Fe was determined to be 3.6 $mM^{-1}s^{-1}$ (in 4.7 T at room temperature). As a proof of concept, these QDs were incubated with murine macrophages cell line (J774) cells, in water for 6 h with a concentration of 0.37 mM of Fe^{2+}, and the results showed optical images with high emission intensity and T_2-weighted MR images. This demonstrated that these QDs had the capability to produce both optical and MR images.

3.2.4. Final Considerations About Doped QDs

Doped quantum dots have attracted much attention, but the control of the doping efficiency is still a challenge. Doping efficiency depends of various aspects such as the size difference between the host and the dopant cations, and the precursor source (which can control the ligand-metal bond strength) [151]. Although some advantages have also been linked to the use of doped QDs [181]:

- Integration of two capabilities in a single nanoparticle, such as bimodal imaging agent.
- Smaller size, when compared with other dual-modal imaging agents, such as QDs-iron oxide or paramagnetic coating of Gd^{3+} chelates.
- The loss in the fluorescence properties can be avoided; it depends on the dopant amount.
- These nanoparticles can be prepared in a one-pot strategy, reducing the cost, the reaction steps and the waste of reagents.

From the presented examples, we can notice that the incorporation of certain ions (such as manganese, gadolinium, and iron) in QDs is a possible methodology to produce bimodal nanoparticles for optical and MR imaging (Table 2). Although, it seems consensual that the main drawback for these systems is that the introduction of a high quantity of dopant in the nanocrystal (without changing the nanoparticle crystalline lattice) is not easy, and it leads to fluorescence quenching. Consequently, the improvement of MRI properties will cause the degradation of the optical properties. Thus, other methods for the incorporation of paramagnetic ions in QDs, which will not modify their emission efficiency and produce small nanostructures, are still desirable.

3.3. Quantum Dots Associated with Gd^{3+} Chelates

As has been previously mentioned, among the CAs, paramagnetic chelates containing Gd^{3+} ions are widely used. Gadolinium has physical properties that make it a good candidate to be used as CA. It possesses seven unpaired electrons (highest spin density) and relatively long electronic relaxation times, reducing the longitudinal (T_1) proton relaxation times [184, 185]. Gd^{3+} cannot be used freely in human body, since at physiological pH it suffer hydrolysis and produces insoluble $Gd(OH)_3$, which accumulates in the bones and liver. Thus, it has been a great interest in the development of highly stable Gd^{3+} complexes, to be used as CA for MRI [21, 186]. Gd^{3+} chelates must present several properties, such as water solubility, chemical stability, high aqueous relaxivity, and low toxicity *in vivo* and be relatively rapidly cleared from the circulation after their application for diagnosis procedure [73, 94, 187]. From the beginning of the 1980s, the majority of CAs used clinically in MRI have chelates Gd^{3+} as their active component, since CAs based on chelates ensures great security for human use, less toxicity than the free gadolinium ions, and different biodistribution [188].

Gd^{3+} complex-based MRI CAs are mainly classified into two groups: linear and macrocyclic chelates, the latter being more stable than the linear ones (Fig. 13). Currently, among the macrocyclic CAs gadolinium-based for MRI most used clinically are Dotarem® [gadoterate, Gd-DOTA (tetraazacyclododecane tetraacetic acid)], Prohance® [gadoteridol, Gd(HP-DO3A)], and Gadovist® (Gd-BT-DO3A). And those with linear structure are: Magnevist® (gadopentetate dimeglumine, Gd-DTPA (diethylene triamine pentaacetic acid), Omniscan® (gadodiamide, Gd(DTPA-BMA)), OptiMARK (Gd-DTPA-BMEA), Multihance® (Gd-BOPTA), and Eovist® or Primovist® [Gd(EOB-DTPA)] [189]. These CAs affect specially the longitudinal relaxation time (T_1), providing bright contrast, which facilitates diagnosis of diseases, besides being well tolerated when administered in patients [190].

In order to increase the relaxivity, paramagnetic chelates have been bounded to larger structures, such as

Table 2. Dopant amount (%), size (nm), emission wavelength (nm), relaxivity ($mM^{-1}s^{-1}$) of the doped QDs discussed in this chapter.

Dopant	QD	Dopant amount (%)	Size (nm)	λ_{em} (nm)	r_1 ($mM^{-1}s^{-1}$)[a]	Ref.
Mn^{2+}	CdSe/ZnS	6.2	4.7	650	18[b]	[172]
	ZnS	10	1.5	466, 507(sh)[c]	20[d]	[173]
	CdTe/ZnS	4.7–9.7	4.3	650	10.7–5.4[d]	[174]
	$CuInS_2$/ZnS	2.3	4.0	600	7.2[d]	[175]
	CdTe	2.8	3.7	545	4.29[b]	[177]
	$CuInS_2$/ZnS	1.4	3.6	620	5.84[e, f]	[178]
Gd^{3+}	CdSe	0.061	6.3	600	76.7[d]	[179]
	ZnO	8	4	550	16[c]	[96]
	ZnCuInS/ ZnS@BSA	7.9–14.3	70	700	11.53–15.78[b]	[180]
	CdTe	2.03	3	640	3.27[d]	[181]
	CuInS/ZnS @PEG	3.05	3	670	9.41[e]	[182]
Fe^{2+}	CdTe	5.6	4.9	530–738	$r_2 = 3.6$[g]	[183]

Notes: [a] room temperature, [b] 7 T, [c] shoulder, [d] 3 T, [e] 1.5 T, [f] 37 °C and [g] 4.7 T.

biomolecules [191] and gold nanoparticles [92, 192] and have also been used to coating silica and lipid-nanostructures (nanospheres, micelles, and liposomes) [193].

A recent study by Zhou and Lu [194] showed that the relaxivity of encapsulated Gd^{3+} chelates is lower than that of the corresponding small molecular complex, due to a permeability barrier imposed by the vesicle membrane, making difficult the exchange between bulk water and the water complexed to encaged Gd^{3+}. However, if the chelates are linked to the nanostructures' surface, it can increase their relaxivity, since bulk water could easily access the Gd^{3+} chelates. Moreover, a nanocarrier containing both core-encapsulated and surface-conjugated Gd^{3+} chelates presents a better relaxivity [195]. This fact is due to a higher Gd^{3+} concentration per unit of liposomal particle. Most contrast agents based on Gd^{3+} chelates act by increasing the longitudinal relaxivity r_1, but can also provide enhancement in transverse relaxivity r_2 [196].

As previously mentioned in the QDs section, they have a chemically active surface that can be easily modified and that makes it possible to conjugate them with a variety of organic and inorganic particles, such as, peptides, antibodies, DNA, drugs, and magnetic materials, as well as to make them water-dispersed and biocompatible in biological fluids [14]. The main motivation for the preparation of QDs-Gd^{3+} chelates is that with this combination it will be possible to produce nanoparticles with a high concentration of Gd^{3+} ions, which can increase the relaxivity per particle and decrease the dosage needed for MRI contrast [21, 197]. Thus, several approaches to develop bimodal nanoparticles for optical and MR imaging involving the association of Gd^{3+} chelates to QDs have been reported [198–202]. In this

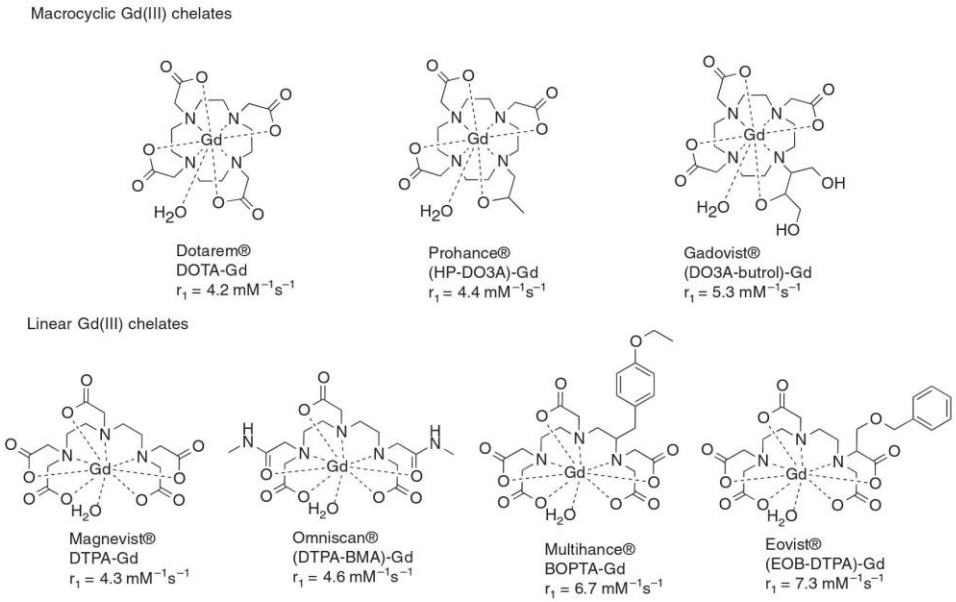

Figure 13. Chemical structure of the principals ACs based- gadolinium paramagnetic with its relaxivity values at 1.5 T189.

section, we divided them in three categories: coating QDs with molecules containing Gd^{3+} chelates, encapsulation of free QDs together with chelates in nanostructures, and direct conjugation of the chelates with the QDs' surface.

3.3.1. Coating of Quantum Dots with Molecules Containing Gd^{3+} Chelates

Lipids and other amphiphilic compounds have been used as building blocks for the preparation of bimodal nanoparticles for optical images and MRI. These amphiphilic structures possess both hydrophobic and hydrophilic sites and the unfavorable contact between the non-polar part and the water leads to a self-organization in aggregates. When in the presence of hydrophobic QDs, the hydrophobic chain of the amphiphiles can interact with QDs' stabilization agents, coating QDs one by one as represented in Figure 14 [193].

Lipid-based particles can carry several Gd^{3+} chelates exhibiting a higher relaxivity per particle [199]. An example of this approach is the work of Mulder et al. [198]. They synthesized CdSe/ZnS core/shell QDs, emitting fluorescence around 560 nm in chloroform. In order to make these QDs water-dispersed and biocompatible, they were coated with a mixture of PEGylated [PEG-DSPE: 1,2-Distearoyl-*sn*-glycero-3-phosphoethanolamine-*N*-(methoxy(poly-ethyleneglycol))-2000] and paramagnetic [Gd-DTPA-BSA:Gd-DTPA-bis(stearylamide)] lipids (p-QDs). These authors suggested that a lipid monolayer coating the QD could be obtained using a huge amount of PEGylated lipids in the formulation. This bimodal nanoprobe presented a high r_1 of 12 $mM^{-1}s^{-1}$ per ions (at 1.41 T), which is higher than for the Gd-DTPA alone, and 2000 $mM^{-1}s^{-1}$ per QDs (also at 1.41 T). These p-QDs were conjugated covalently with the cyclic peptide RGD (arginine-glycine-aspartic acid), via a maleimide-functionalized PEGylated lipid (PEG-DSPE-Mal), in order to prepare a specific probe for angiogenic blood vessels. The p-QDs-RGD was incubated with human umbilical vein endothelial cells (HUVECs) for *in vitro* assays. Fluorescence microscopy images showed that the p-QDs-RGD were internalized by the cells and accumulated at a perinuclear location. Cells incubated with p-QDs also presented a minor fluorescence signal, indicating that a non-specific cellular internalization also occurred. Cell pellet of the cells incubated with p-QDs-RGD presented a brighter T_1-weighted image than the ones incubated with p-QDs. The results suggested that these systems could be attractive contrast agents to early screening and for following the effect of anti-angiogenesis therapy.

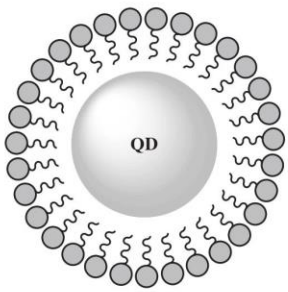

Figure 14. Schematic representation of a QD coated by lipids.

In other work the same group [203] used the p-QDs-RGD intravenously injected for further *in vivo* studies of ongoing tumor angiogenesis in mice. This single molecular imaging contrast agent (p-QDs-RGD) allowed parallel detection by both optical [intravital microscopy (IVM) and optical imaging] and magnetic (MRI) techniques. The IVM allowed the detection of microvessels in tumor-bearing mice at cellular resolution and the observation of their typical tortuous morphology (Fig. 15). By fluorescence microscopy, 5 to 10 min post-injection, the authors also observed endothelial cells labeled by bimodal nanoparticle in the tumor blood vessels (Fig. 15). None fluorescence emission was found in the blood vessels from distant normal tissues. MRI *in vivo* was also performed providing an anatomical resolution of the entire tumor and the p-QDs-RGD was also injected in real time inside the MR image scanner, to be able to compare the pre- and post-injection images. MRI, taken 45 min after the injection, showed an enhancement in T_1-weighted images, observed in the tumor periphery (the regions where the angiogenic activity was higher (Fig. 15). Biodistribution studies showed that the p-QDs-RGDs accumulated in the liver and spleen.

In other work, the Mulder's group published a paper about the application of recombinant human annexin A5 conjugated to bimodal nanoparticles in apoptotic cells using a similar p-QDs coated by paramagnetic lipids [205]. The maleimide group of Mal-PEG-DSPE, present in the p-QDs' coating, was covalently conjugated to the cysteine of the recombinant human annexin-A5. The ionic relaxivities of this nanomicelles were equivalent to those found in p-QDs-RGDs [198], being 12.4 (r_1) and 18.0 $mM^{-1}s^{-1}$ (r_2), whereas the relaxivity per particles was at least 150 times higher than ionic relaxivity. They demonstrated the specificity of annexin A5-p-QDs to detect apoptotic events *in vitro* by fluorescence microscopy and MRI in Jurkat cells (T-lymphoma cell line).

The annexin A5 is a molecular bioprobe to target the phosphatidylserine (PS) exposed on the cell surface, which is an amino-phospholipid present in the membrane of apoptotic cells, triggering phagocytosis. For this, PS has been

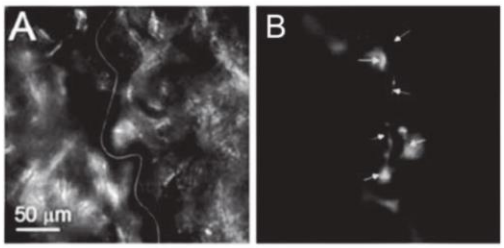

Figure 15. Images of tumor blood vessels were specifically labeled by RGD-labeled paramagnetic quantum dots (p-QDs-RGD) using parallel detection of IVM (A) and fluorescence microscopy (B). (A) Bright field image showing typical tortuous morphology of the angiogenic blood vessels (indicated by the yellow lines). (B) Fluorescence image showing endothelial cells labeled by contrast agent (p-QDs-RGD) (indicated by yellow arrows). Adapted with permission from [204], W. J. Mulder, et al., *Angiogenesis* 12, 17 (2009). © 2009, Springer.

considered one of the most explored targets of programmed cell death (PCD) [206].

To study PCD in apoptotic cells with the annexin A5, Jurkat cells were incubated with anti-Fas (CD95 human monoclonal antibody) for 15 min to induce an increase of apoptotic events. When apoptotic cells were incubated with A5-p-QDs, a high brightness image was observed by fluorescent microscopy. On the other hand, when the cells were not stimulated with anti-Fas, less bright images were observed. In relation to T_1-weighted images, a strong signal of the apoptotic cells incubated with A5-p-QDs was revealed. However, cells that were not treated with anti-Fas also presented some signal, because they undergo naturally apoptosis even in the culture without stimuli, in about 5% to 10% of the cells [205]. Therefore, in other studies involving annexin A5 with radioactive compounds, a tumor decrease was observed due to the increase of the cellular uptake after radiotherapy, indicating therapy efficiency caused by radiation-induced apoptosis [207]. Thus, fluorescence and MRI images with annexin A5 can allow the evaluation of the cancer development and treatment by detecting apoptosis using A5-p-QDs. According to these authors, the A5-p-QDs nanoparticles can be applied for acquiring *in vivo* and *in vitro* apoptosis images, being bimodal nanoparticles with potential use in MRI and intravital microscopy [205].

A different approach, using silica as the capping agent, was reported by Yang et al. [208]. These authors synthesized core/shell QDs of cadmium sulfide: manganese/zinc sulfide (CdS:Mn/ZnS) by a reverse-micelle method and to make them water-dispersed and biocompatible, coated then with a silica layer, by injecting the following components in the QDs micellar solution: tetraethyl orthosilicate (TEOS), 3-(aminopropyl)-triethoxysilane (APTES), and 3-(trihydroxysilyl)-propylmethylphosphonate (THPMP). The CdS:Mn/ZnS/Si were associated with a paramagnetic chelate using a silane-coupling agent [*N*-(trimethoxysilylpropyl)-ethylenediamine triacetic acid trisodium salt, TSPETE], acting also as a chelating agent for Gd^{3+}. TEM images of the final systems showed the presence of nanoparticles with a diameter of about 7 to 10 nm, containing an electron-dense core of 3 nm. Their emission spectrum presented a maximum at 590 nm, corresponding to the yellow emission of Mn^{2+}. XPS was used to confirm the presence of Gd^{3+} in the nanoparticle surface, and the number of Gd^{3+} ions per particle was determined by ICP, which provided a value of around 107 Gd^{3+} ions per particle. Relaxometric studies at 4.7 T provided a longitudinal relaxivity (r_1) of 20.5 $mM^{-1}s^{-1}$ and a transverse relaxivity (r_2) of 151 $mM^{-1}s^{-1}$, which indicate that these particles may be used as both T_1 and T_2 contrast agents.

Koole et al. [199] prepared bimodal agents by coating QDs with silica and an additional lipid dense monolayer. QDs of CdSe/CdS/ZnS were prepared with a diameter of 7.7 nm (determined by TEM). These QDs were incorporated in silica particles using TEOS, rendering particles of 31 nm. In a next step, the silica capping QDs (QD-Si) were coated with octadecanol to make them hydrophobic, after which they were covered with PEGylated, maleimide-PEGylated, and paramagnetic lipids (containing Gd-DTPA), using the same approach described in their previous work [198]. The average size for these particles (QD-Si-pLip) was 58 nm determined by dynamic light scattering (DLS). From photophysical studies, it was observed that the successive coatings did not affect the absorption and emission spectra, and the nanoparticles' emission maximum remained at 630 nm. Longitudinal relaxivity (r_1) of the QD-Si-pLip was determined as 14.4 $mM^{-1}s^{-1}$ (at 6.3 T) and by ICP it was found that each nanoparticle contains 2500 Gd^{3+} ions. As a proof of concept, tests *in vitro* were performed with serum-activated of human umbilical vein endothelial cells (HUVEC). Using the same methodology as before [198], the RGD peptide was conjugated with the nanoparticle, and the QD-Si-pLip-RGD obtained was incubated with the cells for 7 h at 37 °C. By fluorescence microscopy it was observed that HUVEC cells were specifically labeled by QD-Si-pLip-RGDs. The nanoparticles were internalized, and they also accumulated in a perinuclear location of these cells. T_1-weighted images of cells pellets showed an enhancement in signal intensity coming from the cells incubated with QD-Si-pLip-RGDs when compared with the ones incubated with QD-Si-pLips, confirming the specific uptake by HUVEC cells.

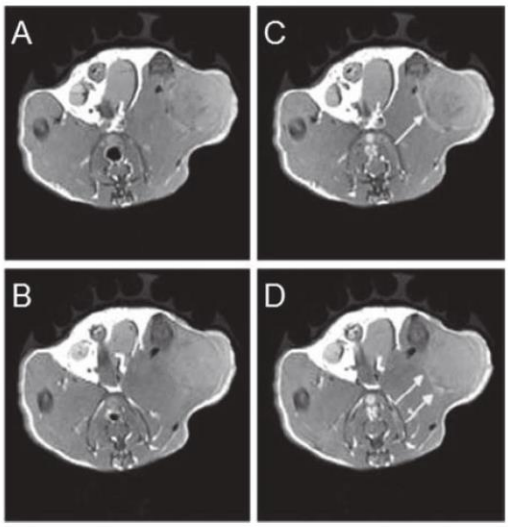

Figure 16. Images by MRI of two slices from the tumor of the mice that was infused with p-QDs-RGD. [A, B] T_1-weighted images before the injection of the contrast agent and [C, D] after the injection, where it was observed bright regions in the peripheral part of the tumor (indicated by yellow arrows). Adapted with permission from [204], W. J. Mulder, et al., *Angiogenesis* 12, 17 (2009). © 2009, Springer.

Ternary semiconductors QDs of $CuInS_2$ coated with ZnS were prepared by an organometallic synthesis [209]. In order to make these QDs water-dispersed, they were capped with an amphiphilic polymer PMO [poly(maleic anhydride-alt-1-octadecene)] by self-assembly of the polymer around the QDs. In water, the maleic anhydride residues presented in the PMO were hydrolyzed forming two carboxylate groups. This way, the capping step makes the QDs hydrophilic and allows further conjugations with the reactive carboxylic groups. These QDs-PMO-COOH particles were reacted

with ethylenediamine, using a standard EDC/NHS procedure, to introduce amine groups in the surface, giving QDs-PMO-NH_2. Gd-DTPA was conjugated with QDs-PMO-NH_2 using the EDC/NHS methodology, associating optical and paramagnetic properties in the same nanoparticle (QD-PMO-Gd). Finally, these authors conjugated a target ligand to the nanoparticle, the folic acid (FA), creating the complex system QD-PMO-Gd-FA. The fluorescence studies showed that the successive coatings and conjugations did not affect significantly the emission, which presented a maximum at 574 nm for QDs-PMO-Gd-FA. Longitudinal relaxation times were measured for these particles, and it obtained a $r_1 = 3.72\ mM^{-1}s^{-1}$ at 7 T. Results from MTT assays with HeLa, MCF-7 (breast cancer of Michigan Cancer Foundation-7) and HepG2 cells, showed no significant cytotoxicity. Incubation of QD-PMO-Gd-FA with HeLa, for 1 h, originated a red fluorescence inside the cells, in the cytoplasm region, which were observed by confocal microscopy. For MCF-7 and HepG2 cells, after incubation in the same conditions, only images with punctuated fluorescence were observed. The authors attributed these results to the fact that both MCF-7 and HepG2 cells present few folate receptors on their membrane, thus they cannot internalize high amounts of QD-PMO-Gd-FA, while HeLa cells possess many folate receptors.

3.3.2. Encapsulation of QDs and Gd^{3+} Chelates

Another approach used to associate Gd^{3+} chelates and QDs is the encapsulation of these two components in polymers or liposomes. In this type of methodology, the QDs are free inside polymeric/lipidic micelles, and the chelates can be inside or on the surface of the nanocomposite. Just one particle can have multiple QDs and Gd^{3+} chelates (Fig. 17) [200, 210].

Tan and Zhang [210] encapsulated QDs and the Gd^{3+} chelate Gd-DTPA in the biopolymer chitosan to produce fluorescent and paramagnetic labels. To prepare this system, the negatively charged CdSe/ZnS QDs (stabilized with 3-mercaptopropionic acid) and Gd-DTPA were dispersed in an acidic solution containing chitosan. Chitosan is a polymer that possesses amino groups, which will be protonated in an acid medium, being positively charged. Thus, it can interact electrostatically with the QDs and the chelates, encapsulating them. These systems presented a size of around 50 nm (determined by TEM and DLS), and it was found that the chitosan-encapsulated system contain 34% of QD and 6% of Gd-DTPA, in mass. The encapsulation of the QDs does not change their fluorescence properties; the emission maximum remained around 565 nm. The relaxometric studies showed that the chitosan bimodal nanobeads presented smaller longitudinal relaxation ($r_1 \approx 33\ mM^{-1}s^{-1}$, 7 T) than the Gd-DTPA chelates ($r_1 \approx 38\ mM^{-1}s^{-1}$, 7 T), although these authors stated that the difference is not statistically significant.

Liu et al. [200] encapsulated QDs in polymers, followed by their conjugation with a Gd-DOTA derivative. Hydrophobic CdTe/ZnS QDs were encapsulated into two polymers, in the amine-terminated m-PEG-phospholipid and in the amine-modified Pluronic F127. The average sizes obtained by TEM were 10.8 nm for PEG-QD and 22.1 nm for F127-QD. The optical studies showed a red shift, about 20–40 nm, in the emission spectra for the encapsulated QDs, when compared with non-encapsulated ones. In order to obtain nanoprobes that could be used also in MRI, they conjugated the encapsulated systems with the chelating agent DOTA, followed by addition of $GdCl_3$. The relaxivity measurement provided a value of $r_1 = 4.38$ and $8.17\ mM^{-1}s^{-1}$ (4.7 T), for PEG-QD-Gd and F127-QD-Gd, respectively. These authors also performed *in vitro* studies, incubating the PEG-QD-Gd and F127-QD-Gd with macrophage cells for 2 h. By confocal microscopy it was possible to observe the accumulation of the nanoparticles inside the cells without apparent damage to the cells. Cell viability studies were done, and the results suggested that the cells treated with PEG-QD-Gd presented lower cell viability that the ones treated with F127-QD-Gd.

3.3.3. Direct Conjugation of Quantum Dots to Gd^{3+} Chelates

Bimodal imaging probes by covalent attachment of a Gd^{3+} chelate to the QDs' surface was used by Stasiuk et al. [211]. They linked covalently Gd^{3+} chelates to indium phosphide/zinc sulfide (InP/ZnS) QDs' surface by a stabilizer exchange (Fig. 18). The Gd^{3+} chelate was prepared by reacting a 1,4,7-triazacyclononane derivative (TACN) and lipoic acid. By magnetic susceptibility measurements and UV-visible spectroscopy, these authors confirmed the attachment of around 80 Gd^{3+} complexes. The attachment of the chelates to QDs increased nanoparticles hydrodynamic diameter from 6.9 to 8.6 nm, measured by DLS. The photophysical studies showed that the linkage of the Gd^{3+} complexes to the QDs did not affect their luminescence,

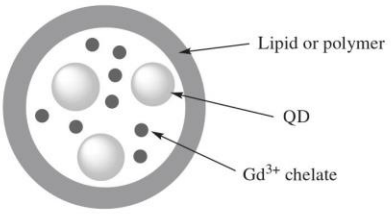

Figure 17. Schematic representation of QDs and Gd^{3+} chelates encapsulated inside polymeric/lipidic micelles.

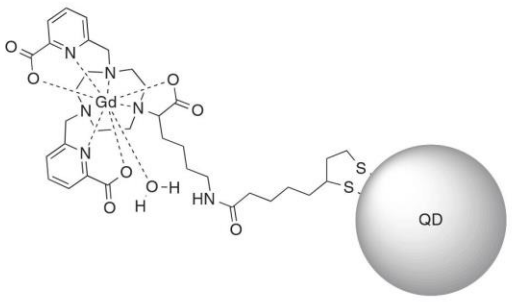

Figure 18. Schematic structure of the bimodal system prepared by Stasiuk et al. Adapted with permission from [212], G. J. Stasiuk, et al., *ACS Nano.* 5, 8193 (2011). © 2011, ACS Publications.

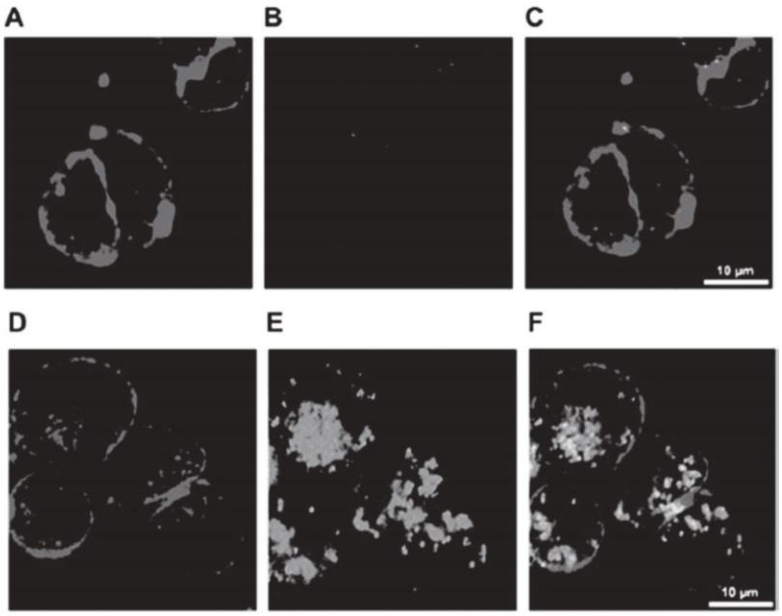

Figure 19. Optical images of CHO cells. The cell were incubated with (A, D) concanavalin A rhodamine (in red); (B) Gd-QDs (in green); (E) QDs-Gd-MCa (in green). In C: merged image of A and B. In F: merged image of D and E. [Adapted with permission from [211], G. J. Stasiuk, et al., *ACS Nano* 5, 8193 (2011). © 2011, American Chemical Society.

maintaining their emission peak around 620 nm, although with a slight decrease in the QY, from 8.5 to 6.1% in water. Relaxivity measurements gave values of $r_1 = 13$ $mM^{-1}s^{-1}$ per Gd^{3+} ion (0.81 T, 25 °C) and 900 $mM^{-1}s^{-1}$ per bimodal particle (0.81 T, 25 °C).

For monitoring biological events the nanoparticles needed to be internalized by cells. For this reason, these authors conjugated a cell penetrating peptide (maurocalcine, MCa) and the Gd^{3+} chelates to the QDs, obtaining a probe with 30–40 Gd^{3+} complexes (QDs-Gd-MCa) [211]. The final systems were incubated with Chinese hamster ovarian cells (CHO cell) during 2 h, which were evaluated by confocal microscopy (Fig. 19). The appearance of punctuate dots inside cells incubated with the QDs-Gd-MCa was observed, suggesting that these systems were trapped in endosomes showing that they were uptaken by cells through an endocytosis-mediated mechanism. To delimitate the cells, they authors stained the cell plasma membrane with rhodamine-conjugated concanavalin A. MRI studies showed that QDs-Gd-MCa (injected in rats) led to a distinct signal, 15 min after injection. And when compared with Dotarem®, this dual-probe had an higher tissue retention time; the signal intensity was still measurable after 4 h (Fig. 20) [211].

Theoretically, restrictions of internal rotations of the complex (bond to QDs) will accelerate the water exchange of the water coordinated to Gd^{3+} and the surrounding bulk water molecules, increasing the relaxivity value. Thus, in order to optimize the relaxivity of Gd^{3+} chelates linked to InP/ZnS, these same authors prepared three ligands with different linkers (Fig. 21) [212]. They used linkers with different flexibility: lipoic acid (L1), which has a dithiol promoting a strong bond with the QDs' surface; mercaptopropionic acid (L2), which probably will reduce the mobility of the complex due to its shorter aliphatic chain; and mercaptobenzoic acid (L3), which has a rigid π-conjugated system that could reduce the internal rotation of the complex. The

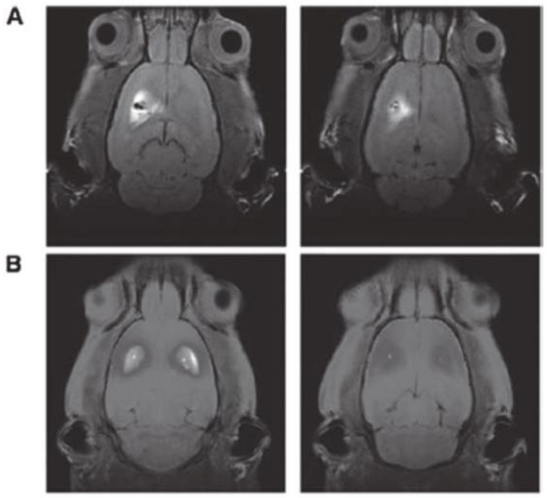

Figure 20. T_1-weighted MRI images of rat brain incubated with (A) QDs-Gd-MCa and (B) with Dotarem®, after 15 min (left) and after 4 h (right). The images were obtained at 7 T. Adapted with permission from [211], G. J. Stasiuk, et al., *ACS Nano.* 5, 8193 (2011). © 2011, American Chemical Society.

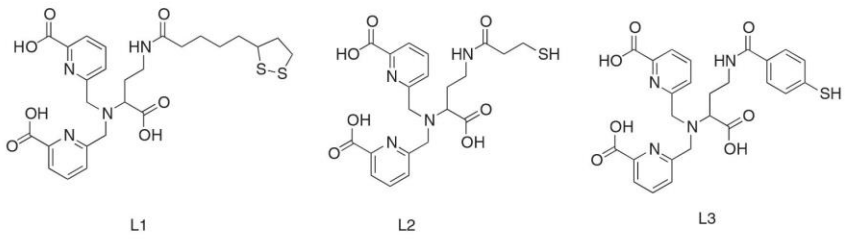

Figure 21. Schematic representation of the ligands prepared by Stasiuk et al. Adapted with permission from [212], G. J. Stasiuk, et al., *ACS Nano.* 5, 8193 (2011). © 2011, ACS Publications.

QDs and the QDs-Gd^{3+} chelates were prepared using the same methodology as before [211], and it was observed that the number of complexes bonded to QDs depend on the linker, affording 115, 66, and 80 complexes per QD for QD-L1, QD-L2 and QD-L3 respectively. As observed in their previous work, no change was observed in the emission spectrum, when compared with InP/ZnS QDs. The relaxivity measurements provided values of r_1 of 21, 9, and 31.5 $mM^{-1}s^{-1}$ per Gd^{3+} ion (at 0.81 T and 25 °C) for QD-L1, QD-L2 and QD-L3 respectively. The r_1 values per QD of 2406, 585 and 2523 $mM^{-1}s^{-1}$ (at 0.81 T and 25 °C) for QD-L1, QD-L2 and QD-L3 correspondingly. QD-L3 showed the higher relaxivity, per Gd^{3+} ion and per QD, indicating that the rigidity of the linkage between the complex and the QD is higher for the benzoyl linker, decreasing more effectively the internal rotation and increasing the exchange of the coordinated water molecules, giving a higher relaxivity.

Other important factor that should be taking in attention, when applying these probes in biological systems, is that cell-internalization could affect the probe properties. This issue was studied by Starmans, et al. [213], and they observed that the internalized p-QDs-RGD and p-QDs showed lower longitudinal relaxivity, when compared with the same systems in solution. This may be explained by the fact that the internalization was mediated by endocytosis, entrapping the Gd-based CA into endosomes.

In 2015, Xing and co-authors [214] developed a paramagnetic-fluorescent nanoprobe based on CdSe QDs coated with DTPA-Gd, coupled to BSA and labeled with anti-Glut1 polyclonal antibody (^{Gd}DTPA·BSA@QDs-PcAb) for targeting colorectal cancer *in vivo* by MRI (diagnosis) and *in vitro* tissue "biopsy-imaging." BSA was an important multivalent ligand for water-solubilization hydrophobic QDs and allowed the conjugation of DTPA to BSA (confirmed by FTIR analysis) and anti-Glut1. The nanoprobes presented diameters of around 35 nm by TEM and the emission maximum at 680 nm, which was maintained for 7 days of storage.

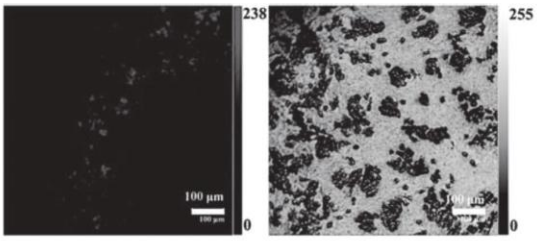

Figure 22. Confocal microscopy images of BXPC-3 cells incubated with Fe_3O_4/CIS@SiO_2 (DTPA-Gd)-RGD, when irradiated at 488 nm (A) and bright field (B). Adapted with permission from [215], J. Shen, et al., *J. Mater. Chem. B* 3, 2873 (2015). © 2015, Royal Society of Chemistry.

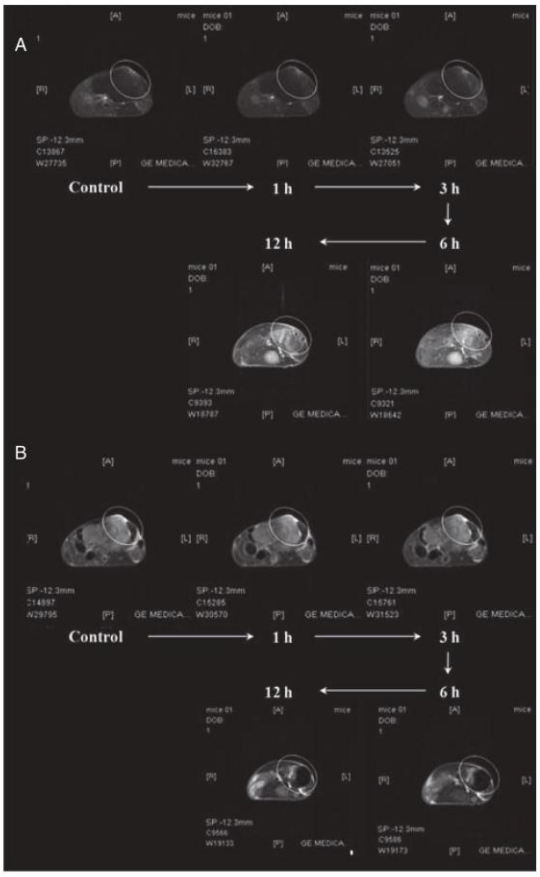

Figure 23. *In vivo* T_1-(A) and T_2-weighted (B) MR images of pancreatic adenocarcinoma obtained before injection, 1 h, 3 h, 6 h and 12 h post-injection with Fe_3O_4/CIS@SiO_2 (DTPA-Gd)-RGD. Adapted with permission from [215], J. Shen, et al., *J. Mater. Chem. B* 3, 2873 (2015). © 2015, Royal Society of Chemistry.

Table 3. Size (nm), emission wavelength (nm), and relaxivity ($mM^{-1}s^{-1}$) of the QDs associated with Gd^{3+} chelates discussed in this chapter.

Association method	Ligand	Size (nm)	λ_{em} (nm)	r_1 ($mM^{-1}s^{-1}$)[a]	Reference
Coating					
Lipids and RGD	DTPA	–	560	12[b]	[198]
Lipids and annexin	DTPA	–	560	12.4[b]	[205]
Silica	TSPETE	7–10	590	20.5[c]	[208]
Silica and lipids	DTPA	58	630	14.4[d]	[199]
Polymer	DTPA	–	574	3.72[e]	[209]
Encapsulation					
Chitosan	DTPA	50	565	33[e]	[210]
Polymers	DOTA	10.8–22-1	630	4.4–8.2[c]	[200]
Conjugation					
Disulfide bond	TACN	8.6	620	13[f]	[211]
Adsorption	DTPA	35	680	16.561[b]	[214]
Amide bond	DTPA	45	650	1.56[g]	[215]

Notes: [a] Room temperature, [b] 1.41 T, [c] 4.7 T, [d] 6.3 T, [e] 7 T, [f] 0.81 T, [g] 3 T.

The NMR analysis, confirmed high relaxivity of 16.561 (r_1) and 27.702 (r_2) $mM^{-1}s^{-1}$ per Gd^{3+} ion (at 1.4 T, 37 °C). The MTT studies showed that no significant cytotoxicity was found in 3T3 cells incubated with the bimodal nanoprobes, indicating good biocompatibility. Human colonic cancer cells (HCT116) were incubated with ^{Gd}DTPA · BSA@QDs-PcAb and the authors observed intense red fluorescence by confocal laser scanning microscopy, indicating specific binding of Glut1-targeted nanoprobes to these cancer cells. ^{Gd}DTPA · BSA@QDs-PcAb were also used as CAs for detection of tumor accumulation *in vivo* by MRI, and they showed a contrast enhancement in T_1-weighted images.

Shen et al. [215] reported multifunctional nanocomposites with (DTPA-Gd) conjugated to the surface of nanoparticles composed by superparamagnetic Fe_3O_4NPs and $CuInS_2$ (CIS) QDs coated by a silica shell (Fe_3O_4/CIS@SiO_2). Silica coating protects the Fe_3O_4 and CIS from the environment, and in addition promotes biocompatibilization (as confirmed by MTT assay on human pancreatic cancer cell line, BXPC-3 cells), essential for *in vivo* applications. This silica coating was accomplished using a mixture of tetraethyl orthosilicate (TEOS) and (3-aminopropyl) triethoxysilane (APS), resulting in an aminated surface, which allowed conjugation with Gd-DTPA complex and RGD peptides via EDC/NHS strategy, obtaining the multimodal composites Fe_3O_4/CIS@SiO_2(DTPA-Gd)-RGD. The multimodal nanocomposites presented an emission maximum at 650 nm, with a red shift in their emission spectra when compared to the QDs. These nanoprobes presented a diameter of around 45 nm, determined by TEM before and after functionalization with DTPA-Gd and RGD. This integrated nanoprobe is a platform for *in vivo* tri-mode imaging, for fluorescent imaging and for T_1- weighted positive ($r_1 = 1.56$ $mM^{-1}s^{-1}$, at 3 T) and T_2-weighted negative ($r_2 = 23.22$ $mM^{-1}s^{-1}$, at 3 T) MR imaging, improving the accuracy of the diagnosis. By confocal microscopy, it was observed that the NPs were readily internalized into BXPC-3 cells, in *in vitro* assays (Fig. 22). In relation to *in vivo* assays, the uptake of these NPs by pancreatic adenocarcinoma cell was slower compared to internalization in the *in vitro* assay. A brighter and darker enhancement effect in T_1 and T_2-weighted MRI, 6 h post-injection with improvement after 12 h, was observed (Fig. 23). The authors stated the advantage of the association of the Gd and Fe to imaging simultaneously to assist in clinical surgery.

3.4. Final Considerations About the Association of QDs and Gadolinium Chelates

In this section we presented several strategies to associate QDs to Gd^{3+} chelates that could be used for dual-imaging purposes (Table 3). Although, these bimodal probes presented good fluorescence properties and high relaxivity, some of them lack an easy preparation procedure and have multiple steps. Furthermore, the longitudinal relaxometric performance due to the presence of Gd^{3+} chelates is probably favored by changes in the water proton exchange rate between the coordinated water molecule and the bulk water (Table 3). Thus, it seems that the direct attachment of the chelate to the QD surface is a synthetic strategy with the potential to prepare efficient bimodal probes. However, the dissociation of the Gd^{3+} ions from the nanoparticle, when applied *in vivo*, is a serious concern, since it can lead to inaccurate images and the formation of $Gd(OH)_3$ is harmful to living organisms. Thus, before the *in vivo* applications, the stability toward transmetallation and leaching of the Gd^{3+} ions presented in the bimodal systems should be well studied [6, 73, 216].

4. CONCLUSION

Bimodal nanoparticles based on QDs, for optical and magnetic resonance images, have attracted much interest. In this chapter, different approaches for the development of these bimodal nanostructures were presented, such as the association of QDs to iron oxide nanoparticles, QDs' doping with paramagnetic ions, and the association of QDs and gadolinium chelates. Although many bimodal systems have been prepared, there still exists a lack in the study of these particles *in vivo*, in order to know their stability and toxicity. In the case of QD-iron oxide nanoparticles, relaxometric studies are also needed to allow comparing with other contrast agents. Thus, further development of nanoparticles for optical and MR imaging with improvement of their

properties and stability, and with flexible and simple synthetic strategies, which could allow the size and composition manipulation, and the conjugation to biomolecules for specific cellular targeting, are still required.

ACKNOWLEDGEMENTS

The authors are grateful for the discussion with the research group Nanotecnologia Biomédica/UFPE members, to Fundação de Amparo a Ciência e Tecnologia do Estado de Pernambuco (FACEPE), to Conselho Nacional de Desenvolvimento Científico e Tecnológico (CNPq), to Coordenação de Aperfeiçoamento de Pessoal de Nível Superior (CAPES), to Academia Brasileira de Ciências, to Instituto Nacional de Ciência e Tecnologia de Fotônica (INCT-INFo), and to the Universidade Federal de Pernambuco (UFPE).

GLOSSARY

Bimodal probes Bimodal probes associate two types of probes in one single system, allowing the simultaneous use of two or more diagnostic techniques. These bimodal systems aim to sum the advantages of both techniques and suppress the limitations of each one, becoming potential and innovative probes for biological investigation.

Bioconjugation A strategy to conjugate, non-covalent (by electrostatic interaction) or covalently (via coupling agents), particles and biomolecules such as amino acids, proteins, antibodies, or DNA sequences.

Contrast agents (CAs) Molecules or particles used to enhance the quality of the images generated by magnetic resonance. The MRI CAs approved for clinical use are based on paramagnetic chelates containing a lanthanide ion, namely gadolinium (III), and iron oxide particles.

Doped QDs QDs containing dopant ions in their crystalline lattice, which change their electronic and photophysical properties. An effective doping procedure requires the replacement of some atoms of the host QD's crystal structure by adequate ions, creating new defined electronic states inside the band gap region.

Fluorescence A rapid process of light emission (10^{-9} to 10^{-7} seconds) by a substance/particle when decaying from the electronic excited state, after absorption of light.

Functionalization Surface particle modification with functional groups, such as amine, carboxyl, or thiol groups, in order to make them able to bind to organic molecules.

Gadolinium chelates Coordination compounds containing gadolinium as metal ion and organic molecules as ligands. The gadolinium chelates are clinically used as MRI CAs, since they avoid the free gadolinium and consequently its toxicity.

Magnetic resonance imaging (MRI Diagnostic image technique based on the nuclear magnetic resonance (NMR) phenomenon. This technique is non-invasive, has a high spatial resolution (0.2–0.3 mm) giving images with anatomical details, and does not use ionizing radiation. MRI is a very efficient technique to reveal differences in the water constitution of the different body tissues, revealing the existence of anomalies in the soft tissues of the body.

Non-specific labeling/marker Cell labeling promoted by a direct interaction with chemical structures, without a specific target.

Optical imaging Technique that relies on the acquisition of images by using light excitation (ultraviolet, visible, or infrared regions of the electromagnetic spectrum). This technique uses fluorescent labels (frequently organic fluorophores) to evidence the desired structures or biomolecules.

Quantum dots (QDs) Fluorescent semiconductor nanocrystals quantum-confined in three dimensions, with a size of 1.5 to 10 nm. QDs have unique photophysical properties, such as photostability, fluorescence tuned with their size, and a chemically active surface. Due to their optical properties, they have been studied as probes in biomedical sciences and in electronic devices.

Quantum yield (QY) Parameter used to determine the efficiency of the fluorescence process. It is defined by the ratio between the number of emitted photons and the number of absorbed photons per time unit.

Relaxation times The relaxation process is modulated by two exponential time constants, T_1 and T_2, which depend on the physical and chemical properties of the environment. In practice, it results in differences on the generated image for local chemically and/or morphologically different tissues.

Relaxivity (r_i, $i = 1,2$) Parameter used to determine of the contrast agent efficiency, and it is given in s^{-1} by mM of paramagnetic ion. This parameter indicates the CAs ability to decrease the relaxation times of the water molecules protons that are located near the paramagnetic system.

Saturation magnetization (Ms) The *Ms* value indicates the higher magnetization of the material, beyond this value no further increase in magnetization occurs, meaning that all the single domains are aligned with the field.

Specific labeling/marker Cells labeling mediated by antibodies or other biomolecules, which provide a specific direction to target.

Superparamagnetic iron oxide nanoparticles Nanoparticles composed by an iron oxide core and in an uniform magnetization state, which means that after removal of the external magnetic field they lose their magnetization.

T_1 The longitudinal or spin-lattice relaxation. Reflects the relaxation due to the energy loss for the neighborhood and gives information about the recuperation velocity of the system's magnetization parallel to the static magnetic field after a perturbation is applied.

T_2 The transverse or spin-spin relaxation. The relaxation due to the interactions between the spins (dipolar interactions) and related to the quickness of coherence losses of the magnetization in the plane transverse to the static magnetic field.

REFERENCES

1. Y.-P. Ho and K. W. Leong, Quantum dot-based theranostics. *Nanoscale* 2, 60 (2010).
2. S. P. Singh, Multifunctional magnetic quantum dots for cancer theranostics. *J. Biomed. Nanotechnol.* 7, 95 (2011).
3. F. Lux, L. Sancey, A. Bianchi, Y. Crémillieux, S. Roux, and O. Tillement, Gadolinium-based nanoparticles for theranostic MRI-radiosensitization. *Nanomedicine* 10, 1801 (2015).

4. R. Hachani, M. Lowdell, M. Birchall, and N. N. T. K. Thanh, Tracking stem cells in tissue-engineered organs using magnetic nanoparticles. *Nanoscale* 5, 11362 (2013).
5. D. P. Cormode, B. L. Sanchez-Gaytan, A. J. Mieszawska, Z. A. Fayad, and W. J. M. Mulder, Inorganic nanocrystals as contrast agents in MRI: Synthesis, coating and introduction of multifunctionality. *NMR in Biomed.* 26, 766 (2013).
6. L. Jing, K. Ding, S. V. Kershaw, I. M. Kempson, A. L. Rogach, and M. Gao, Magnetically engineered semiconductor quantum dots as multimodal imaging probes. *Adv. Mat.* 26, 6367 (2014).
7. H. Xu, Q. Li, L. Wang, Y. He, J. Shi, B. Tang, and C. Fan, Nanoscale optical probes for cellular imaging. *Chem. Soc. Rev.* 43, 2650 (2014).
8. K. M. Dean and A. E. Palmer, Advances in fluorescence labeling strategies for dynamic cellular imaging. *Nat. Chem. Biol.* 10, 512 (2014).
9. Z. Guo, S. Park, J. Yoon, and I. Shin, Recent progress in the development of near-infrared fluorescent probes for bioimaging applications. *Chem. Soc. Rev.* 43, 16 (2014).
10. P. W. Winter and H. Shroff, Faster fluorescence microscopy: Advances in high speed biological imaging. *Curr. Opin. Chem. Biol.* 20, 46 (2014).
11. A. J. Meixner, The nobel prize in chemistry 2014 for the development of super-resolved fluorescence microscopy. *Anal. Bioanal. Chem.* 407, 1797 (2015).
12. B. N. G. Giepmans, S. R. Adams, M. H. Ellisman, and R. Y. Tsien, The fluorescent toolbox for assessing protein location and function. *Science* 312, 217 (2006).
13. U. Resch-Genger, M. Grabolle, S. Cavaliere-Jaricot, R. Nitschke, and T. Nann, Quantum dots versus organic dyes as fluorescent labels. *Nat. Meth.* 5, 763 (2008).
14. A. Fontes, R. B. D. Lira, M. A. B. L. Seabra, T. G. D. Silva, A. G. D. C. Neto, and B. S. Santos, "Biomedical Engineering—Technical Applications in Medicine" (R. Hudak, Ed.), InTech. 2012.
15. C. L. Cesar, "Quantum Dots: Applications in Biology," pp. 3–9. Springer, 2014.
16. S. K. Vashist, R. Tewari, R. P. Bajpai, L. M. Bharadwaj, and R. Raiteri, Review of quantum dot technologies for cancer detection and treatment. *AZojono J. Nanotechnology Online* 2, 1 (2006).
17. B. S. Santos, P. M. A. Farias, and A. Fontes, "Handbook of Self Assembled Semiconductor Nanostructures for Novel Devices in Photonics and Electronics" (M. Henini, Ed.). pp. 773–798. Elsevier, Amsterdam, 2008.
18. Y. Wang and L. Chen, Quantum dots, lighting up the research and development of nanomedicine. *Nanomed. Nanotechnol. Biol. Med.* 7, 385 (2011).
19. L.-W. Wang, C.-W. Peng, C. Chen, and Y. Li, Quantum dots-based tissue and *in vivo* imaging in breast cancer researches: Current status and future perspectives. *Breast Cancer Res. Treat* 151, 7 (2015).
20. K. D. Wegner and N. Hildebrandt, Quantum dots: Bright and versatile *in vitro* and *in vivo* fluorescence imaging biosensors. *Chem. Soc. Rev.* (2015).
21. G. A. Pereira and C. F. G. C. Geraldes, Design and optimization of gadolinium based contrast agents for magnetic resonance imaging. *Ann. Magn. Reson.* 6, 1 (2007).
22. W. Cai, K. Chen, Z.-B. Li, S. S. Gambhir, and X. Chen, Dual-function probe for PET and near-infrared fluorescence imaging of tumor vasculature. *J. Nucl. Med.* 48, 1862 (2007).
23. K. Chen, Z.-B. Li, H. Wang, W. Cai, and X. Chen, Dual-modality optical and positron emission tomography imaging of vascular endothelial growth factor receptor on tumor vasculature using quantum dots. *Eur. J. Nucl. Med. Mol. Imaging* 35, 2235 (2008).
24. C. Tu, X. Ma, A. House, S. M. Kauzlarich, and A. Y. Louie, PET imaging and biodistribution of silicon quantum dots in mice. *ACS Med. Chem. Lett.* 2, 285 (2011).
25. W. Guo, X. Sun, O. Jacobson, X. Yan, K. Min, A. Srivatsan, G. Niu, D. O. Kiesewetter, J. Chang, and X. Chen, Intrinsically radioactive [64Cu]CuInS/ZnS quantum dots for PET and optical imaging: Improved radiochemical stability and controllable cerenkov luminescence. *ACS Nano.* 9, 488 (2015).
26. I. L. Medintz, H. T. Uyeda, E. R. Goldman, and H. Mattoussi, Quantum dot bioconjugates for imaging, labelling and sensing. *Nat. Mater.* 4, 435 (2005).
27. X. Michalet, F. F. Pinaud, L. A. Bentolila, J. M. Tsay, S. Doose, J. J. Li, G. Sundaresan, A. M. Wu, S. S. Gambhir, and S. Weiss, Quantum dots for live cells, *in vivo* imaging, and diagnostics. *Science* 307, 538 (2005).
28. L. Shao, Y. Gao, and F. Yan, Semiconductor quantum dots for biomedicial applications. *Sensors* 11, 11736 (2011).
29. X. Michalet, L. A. Bentolila, and S. Weiss, Eds., "Molecular Imaging: Physics and Bioapplications of Quantum Dots" 2008.
30. A. M. Smith, X. Gao, and S. Nie, Quantum dot nanocrystals for *in vivo* molecular and cellular imaging. *Photochem. Photobiol.* 80, 377, (2004).
31. L. E. Brus, Electron–electron and electron–hole interactions in small semiconductor crystallites: The size dependence of the lowest excited electronic state. *J. Chem. Phys.* 80, 6 (1984).
32. P. Petroff, "Single Quantum Dots," Vol. 90, pp. 1–24, Springer Berlin, Heidelberg, 2003.
33. B. O. Dabbousi, J. Rodriguez-Viejo, F. V. Mikulec, J. R. Heine, H. Mattoussi, R. Ober, K. F. Jensen, and M. G. Bawendi, (CdSe)ZnS core–shell quantum dots: Synthesis and characterization of a size series of highly luminescent nanocrystallites. *J. Phys. Chem. B* 101, 9463 (1997).
34. Y. Xiao, S. P. Forry, X. Gao, R. D. Holbrook, W. G. Telford, and A. Tona, Research dynamics and mechanisms of quantum dot nanoparticle cellular uptake. *J. Nanobiotechnology* 8 (2010).
35. X. Wu, H. Liu, J. Liu, K. N. Haley, J. A. Treadway, J. P. Larson, N. Ge, F. Peale, and M. P. Bruchez, Immunofluorescent labeling of cancer marker Her2 and other cellular targets with semiconductor quantum dots. *Nat. Biotech.* 21, 41 (2003).
36. P. Alivisatos, The use of nanocrystals in biological detection. *Nat. Biotech.* 22, 47 (2004).
37. T. Jamieson, R. Bakhshi, D. Petrova, R. Pocock, M. Imani, and A. M. Seifalian, Biological applications of quantum dots. *Biomaterials* 28, 4717 (2007).
38. A. Sukhanova and I. Nabiev, Fluorescent nanocrystal quantum dots as medical diagnostic tools. *Expert. Opin Med. Diagn.* 2, 429 (2008).
39. M. A. Walling, J. A. Novak, and J. R. Shepard, Quantum dots for live cell and *in vivo* imaging. *Int. J. Mol. Sci.* 10, 441 (2009).
40. W. C. W. Chan, D. J. Maxwell, X. Gao, R. E. Bailey, M. Han, and S. Nie, Luminescent quantum dots for multiplexed biological detection and imaging. *Curr. Opin Biotechnol.* 13, 40 (2002).
41. O. I. Mićić and A. J. Nozik, "Nanostructured Materials and Nanotechnology," (H. S. Nalwa, Ed.). pp. 183–205. Academic Press, San Diego, 2002.
42. F. D. Menezes, A. G. Brasil Jr., W. L. Moreira, L. C. Barbosa, C. L. Cesar, R. D. C. Ferreira, P. M. A. de Farias, and B. S. Santos, CdTe/CdS core shell quantum dots for photonic applications. *Microelectr. J.* 36, 989 (2005).
43. C. Carrillo-Carrion, S. Cardenas, B. M. Simonet, and M. Valcarcel, Quantum dots luminescence enhancement due to illumination with UV/Vis light. *Chem Comm.* 5214 (2009).
44. E. R. Goldman, G. P. Anderson, P. T. Tran, H. Mattoussi, P. T. Charles, and J. M. Mauro, Conjugation of luminescent quantum dots with antibodies using an engineered adaptor protein to provide new reagents for fluoroimmunoassays. *Anal. Chem.* 74, 841 (2002).
45. X. Gao, L. Yang, J. A. Petros, F. F. Marshall, J. W. Simons, and S. Nie, *In vivo* molecular and cellular imaging with quantum dots. *Curr. Opin. Biotechnol.* 16, 63 (2005).
46. K. H. G. Carvalho, A. G. Brasil Jr., P. E. Cabral Filho, D. P. L. A. Tenorio, A. C. A. de Siqueira, E. S. Leite, A. Fontes, and B. S.

Santos, Fluorescence plate reader for quantum dot-protein bioconjugation analysis. *J. Nanosci. Nanotechnol.* 14, 3320 (2014).
47. G. T. Hermanson, "Bioconjugate Techniques" (G. T. Hermanson, Ed.), pp. 169–212, Academic Press, New York, 2008.
48. G. T. Hermanson, "Bioconjugate Techniques" (G. T. Hermanson, Ed.), pp. 213–233, Academic Press, New York, 2008.
49. C. G. Andrade, P. E. Cabral Filho, D. P. L. Tenório, B. S. Santos, E. I. C. Beltrão, A. Fontes, and L. B. Carvalho Jr., Evaluation of glycophenotype in breast cancer by quantum dot-lectin histochemistry. *Int. J. Nanomedicine.* 8, 4623 (2013).
50. A. Fontes and B. S. Santos, "Quantum Dots: Applications in Biology" Springer, 2014.
51. D. P. L. A. Tenório, C. G. Andrade, P. E. Cabral Filho, C. P. Sabino, I. T. Kato, L. B. Carvalho Jr., S. Alves Jr, M. S. Ribeiro, A. Fontes, and B. S. Santos, CdTe quantum dots conjugated to concanavalin A as potential fluorescent molecular probes for saccharides detection in Candida albicans. *J. Photochem. Photobiol. B Biol.* 142, 237 (2015).
52. P. E. Cabral Filho, M. I. A. Pereira, H. P. Fernandes, A. A. de Thomaz, C. L. Cesar, B. S. Santos, M. L. Barjas-Castro, and A. Fontes, Blood group antigen studies using CdTe quantum dots and flow cytometry. *Int. J. Nanomedicine* 10, 4393 (2015).
53. M.-Z. Zhang, R.-N. Yu, J. Chen, Z.-Y. Ma, and Y.-D. Zhao, Targeted quantum dots fluorescence probes functionalized with aptamer and peptide for transferrin receptor on tumor cells. *Nanotechnology* 23, 485104 (2012).
54. P. E. Cabral Filho, A. L. C. Cardoso, M. I. A. Pereira, A. P. M. Ramos, F. Hallwas, M. M. C. A. Castro, C. F. G. C. Geraldes, B. S. Santos, M. C. Pedroso de Lima, G. A. L. Pereira, and A. Fontes, CdTe quantum dots as fluorescent probes to study transferrin receptors in glioblastoma cells. *Biochimica et Biophysica Acta (BBA)-General Subjects* 1860, 28 (2016).
55. C. G. Andrade, P. E. Cabral Filho, D. P. L. Tenório, B. S. Santos, E. I. C. Beltrão, A. Fontes, and L. B. Carvalho, Evaluation of glycophenotype in breast cancer by quantum dot-lectin histochemistry. *Int. J. Nanomedicine.* 8, 4623 (2013).
56. D. P. L. A. Tenório, C. G. Andrade, P. E. Cabral Filho, C. P. Sabino, I. T. Kato, L. B. Carvalho Jr., S. Alves Jr., M. S. Ribeiro, A. Fontes, and B. S. Santos, CdTe quantum dots conjugated to concanavalin A as potential fluorescent molecular probes for saccharides detection in Candida albicans. *Journal of Photochemistry and Photobiology B: Biology* 142, 237 (2015).
57. V. Biju, T. Itoh, and M. Ishikawa, Delivering quantum dots to cells: Bioconjugated quantum dots for targeted and nonspecific extracellular and intracellular imaging. *Chem. Soc. Rev.* 39, 3031 (2010).
58. K. Klepárník, V. Datinská, I. Voráčová, and M. Lišková, "Quantum Dots: Applications in Biology," (A. Fontes and B. S. Santos, Eds.). Vol. 1199, pp. 33–54. Springer, New York, 2014.
59. K. Brazhnik, I. Nabiev, and A. Sukhanova, "Quantum Dots: Applications in Biology," (A. Fontes and B. S. Santos, Eds.), Vol. 1199, pp. 55–66. Springer, New York, 2014.
60. D. East, M. Todd, and I. Bruce, "Quantum Dots: Applications in Biology," (A. Fontes and B. S. Santos, Eds.), Vol. 1199, pp. 67–83. Springer, New York, 2014.
61. A. G. Brasil Jr., K. H. G. Carvalho, E. S. Leite, A. Fontes, and B. S. Santos, Quantum Dots: Applications in Biology, (A. Fontes and B. S. Santos, Eds.), Vol. 1199, pp. 103–110, Springer, New York, 2014.
62. L. Landini, V. Positano, and M. Santarelli, Advanced image processing in magnetic resonance imaging. *Taylor and Francis Group* (2005).
63. R. B. Buxton, "Introduction to Functional Magnetic Resonance Imaging: Principles and Techniques," pp. 67–84, Cambridge University Press, 2009.
64. R. Damadian, Tumor detection by nuclear magnetic resonance. *Science* 171, 1151 (1971).
65. P. C. Lauterbur, Image formation by induced local interactions: Examples employing nuclear magnetic resonance. *Nature* 242, 190 (1973).
66. A. Merbach, L. Helm, and É. Tóth, Eds., "The Chemistry of Contrast Agents in Medical Magnetic Resonance Imaging," John Wiley & Sons, Ltd, Chichester, UK, 2013.
67. T. Lam, P. Pouliot, P. K. Avti, F. Lesage, and A. K. Kakkar, Superparamagnetic iron oxide based nanoprobes for imaging and theranostics. *Adv. Colloid Interface Sci.* 199–200, 95 (2013).
68. R. R. Edelman and S. Warach, Magnetic resonance imaging. *N. Engl. J. Med.* 328, 708 (1993).
69. G.-P. Yan, L. Robinson, and P. Hogg, Magnetic resonance imaging contrast agents: Overview and perspectives. *Radiography* 13, e5 (2007).
70. J. S. Weinstein, C. G. Varallyay, E. Dosa, S. Gahramanov, B. Hamilton, W. D. Rooney, L. L. Muldoon, and E. A. Neuwelt, Superparamagnetic iron oxide nanoparticles: Diagnostic magnetic resonance imaging and potential therapeutic applications in neurooncology and central nervous system inflammatory pathologies, a review. *J. Cereb. Blood Flow Metab.* 30, 15 (2010).
71. S. Laurent, D. Forge, M. Port, A. Roch, C. Robic, L. Vander Elst, and R. N. Muller, Magnetic iron oxide nanoparticles: Synthesis, stabilization, vectorization, physicochemical characterizations, and biological applications. *Chem. Rev.* 108, 2064 (2008).
72. C. Henoumont, S. Laurent, and L. Vander Elst, How to perform accurate and reliable measurements of longitudinal and transverse relaxation times of MRI contrast media in aqueous solutions. *Contrast Media Mol. Imaging* 4, 312 (2009).
73. C. F. G. C. Geraldes and S. Laurent, Classification and basic properties of contrast agents for magnetic resonance imaging. *Contrast Media Mol. Imaging* 4, 1 (2009).
74. H. B. Na, I. C. Song, and T. Hyeon, Inorganic nanoparticles for MRI contrast agents. *Adv. Mat.* 21, 2133 (2009).
75. S. H. Lee, B. H. Kim, H. B. Na, and T. Hyeon, Paramagnetic inorganic nanoparticles as T_1 MRI contrast agents. *Wiley Interdiscip Rev. Nanomed. Nanobiotechnol.* 6, 196 (2014).
76. M. A. Bruckman, X. Yu, and N. F. Steinmetz, Engineering Gd-loaded nanoparticles to enhance MRI sensitivity via T 1 shortening. *Nanotechnology* 24, 462001 (2013).
77. F. Mouffouk, T. Simão, D. F. Dornelles, A. D. Lopes, P. Sau, J. Martins, K. M. Abu-Salah, S. A. Alrokayan, A. M. Rosa da Costa, and N. R. dos Santos, Self-assembled polymeric nanoparticles as new, smart contrast agents for cancer early detection using magnetic resonance imaging. *Int. J. Nanomedicine.* 10, 63 (2015).
78. R. Srikar, A. Upendran, and R. Kannan, Polymeric nanoparticles for molecular imaging. *Wiley Interdiscip Rev Nanomed Nanobiotechnol.* 6, 245 (2014).
79. J. L. Turner, D. Pan, R. Plummer, Z. Chen, A. K. Whittaker, and K. L. Wooley, Synthesis of gadolinium-labeled shell-crosslinked nanoparticles for magnetic resonance imaging applications. *Adv. Funct. Materials* 15, 1248 (2005).
80. E. Chung, F. Pineda, K. Nord, and L. S. Karczmar, Fibrin-targeting, peptide amphiphile micelles as contrast agents for molecular MRI. *J. Cell. Sci. Ther.* 5, 2 (2014).
81. K. B. Vargo, A. A. Zaki, R. Warden-Rothman, A. Tsourkas, and D. A. Hammer, Superparamagnetic iron oxide nanoparticle micelles stabilized by recombinant oleosin for targeted magnetic resonance imaging. *Small* n/a–n/a (2014).
82. B. Sitharaman, K. R. Kissell, K. B. Hartman, L. A. Tran, A. Baikalov, I. Rusakova, Y. Sun, H. A. Khant, S. J. Ludtke, W. Chiu, S. Laus, E. Toth, L. Helm, A. E. Merbach, and L. J. Wilson, Superparamagnetic gadonanotubes are high-performance MRI contrast agents. *Chem. Comm.* 3915 (2005).
83. N. KuŸnik, M. M. Tomczyk, S. Boncel, A. P. Herman, K. K. K. Koziol, and M. Kempka, Fe3+ ions anchored to Fe@O-MWCNTs as double impact T_2 MRI contrast agents. *Mater Lett.* 136, 34 (2014).

84. I. Marangon, C. Ménard-Moyon, J. Kolosnjaj-Tabi, M. L. Béoutis, L. Lartigue, D. Alloyeau, E. Pach, B. Ballesteros, G. Autret, T. Ninjbadgar, D. F. Brougham, A. Bianco, and F. Gazeau, Covalent functionalization of multi-walled carbon nanotubes with a gadolinium chelate for efficient T_1-weighted magnetic resonance imaging. *Adv. Funct. Mater.* 24, 7173 (2014).
85. L. Zhang, H. Zhou, O. Belzile, P. Thorpe, and D. Zhao, Phosphatidylserine-targeted bimodal liposomal nanoparticles for *in vivo* imaging of breast cancer in mice. *J. Control Release* 183, 114 (2014).
86. G. Mulas, G. Ferrauto, W. Dastrù, R. Anedda, S. Aime, and E. Terreno, Insights on the relaxation of liposomes encapsulating paramagnetic Ln-based complexes. *Magn. Reson. Med.* n/a (2014).
87. H. Kobayashi and M. W. Brechbiel, Nano-sized MRI contrast agents with dendrimer cores. *Adv. Drug. Deliv. Rev.* 57, 2271 (2005).
88. J. Zhu, E. M. Gale, I. Atanasova, T. A. Rietz, and P. Caravan, Hexameric MnII dendrimer as MRI contrast agent. *Chem. Eur. J.* 20, 14507 (2014).
89. B. B. Bartelle, M. D. Mana, G. A. Suero-Abreu, J. J. Rodriguez, and D. H. Turnbull, Engineering an effective Mn-binding MRI reporter protein by subcellular targeting. *Magn. Reson. Med.* n/a (2014).
90. L. I. Liron, I. K. Elena, A. B. Anna, M. S. Alexander, R. Ina, K. Jörg, P. Lorena, and L. Jean-Paul, Towards hybrid biocompatible magnetic rHuman serum albumin-based nanoparticles: Use of ultra-small (CeL n) 3/4 + cation-doped maghemite nanoparticles as functional shell. *Nanotechnology* 26, 045601 (2015).
91. C. Zeng, X. Shi, B. Wu, D. Zhang, and W. Zhang, Colloids containing gadolinium-capped gold nanoparticles as high relaxivity dual-modality contrast agents for CT and MRI. *Colloids Surf. B* 123, 130 (2014).
92. M. F. Ferreira, J. Goncalves, B. Mousavi, M. I. M. Prata, S. P. J. Rodrigues, D. Calle, P. Lopez-Larrubia, S. Cerdan, T. B. Rodrigues, P. M. Ferreira, L. Helm, J. A. Martins, and C. F. G. C. Geraldes, Gold nanoparticles functionalised with fast water exchanging Gd3 + chelates: Linker effects on the relaxivity. *Dalton Trans.* (2015).
93. Y. Gossuin, P. Gillis, A. Hocq, Q. L. Vuong, and A. Roch, Magnetic resonance relaxation properties of superparamagnetic particles. *Wiley Interdiscip Rev. Nanomed. Nanobiotechnol.* 1, 299 (2009).
94. P. Caravan, J. J. Ellison, T. J. McMurry, and R. B. Lauffer, Gadolinium (III) chelates as MRI contrast agents: Structure, dynamics, and applications. *Chem. Rev.* 99, 2293 (1999).
95. R. López-Cebral, M. Martín-Pastor, B. Seijo, and A. Sanchez, Progress in the characterization of bio-functionalized nanoparticles using NMR methods and their applications as MRI contrast agents. *Prog. Nucl. Magn. Reson. Spectrosc.* 79, 1 (2014).
96. Y. Liu, K. Ai, Q. Yuan, and L. Lu, Fluorescence-enhanced gadolinium-doped zinc oxide quantum dots for magnetic resonance and fluorescence imaging. *Biomaterials* 32, 1185 (2011).
97. J. Yang, J. Gunn, S. R. Dave, M. Zhang, Y. A. Wang, and X. Gao, Ultrasensitive detection and molecular imaging with magnetic nanoparticles. *Analyst* 133, 154 (2008).
98. P. B. Santhosh and N. P. Ulrih, Multifunctional superparamagnetic iron oxide nanoparticles: Promising tools in cancer theranostics. *Cancer Lett.* 336, 8 (2013).
99. D. Koktysh, V. Bright, and W. Pham, Fluorescent magnetic hybrid nanoprobe for multimodal bioimaging. *Nanotechnology* 22, 275606 (2011).
100. A. K. Gupta and M. Gupta, Synthesis and surface engineering of iron oxide nanoparticles for biomedical applications. *Biomaterials* 26, 3995 (2005).
101. A. S. Teja and P.-Y. Koh, Synthesis, properties, and applications of magnetic iron oxide nanoparticles. *Prog. Cryst. Growth Charact. Mater.* 55, 22 (2009).
102. M. Mahmoudi, S. Sant, B. Wang, S. Laurent, and T. Sen, Superparamagnetic iron oxide nanoparticles (SPIONs): Development, surface modification and applications in chemotherapy. *Adv. Drug. Deliv. Rev.* 63, 24 (2011).
103. A. K. Gupta, R. R. Naregalkar, V. D. Vaidya, and M. Gupta, Recent advances on surface engineering of magnetic iron oxide nanoparticles and their biomedical applications. *Nanomedicine* 2, 23 (2007).
104. A. Ito, M. Shinkai, H. Honda, and T. Kobayashi, Medical application of functionalized magnetic nanoparticles. *J. Biosci. Bioeng.* 100, 1 (2005).
105. R. Jurgons, C. Seliger, A. Hilpert, L. Trahms, S. Odenbach, and C. Alexiou, Drug loaded magnetic nanoparticles for cancer therapy. *J. Phys. Condens. Matter.* 18, S2893 (2006).
106. R. Weissleder, Molecular imaging in cancer. *Science* 312, 1168 (2006).
107. R. A. Frimpong and J. Z. Hilt, Magnetic nanoparticles in biomedicine: Synthesis, functionalization and applications. *Nanomedicine* 5, 1401 (2010).
108. L. H. Reddy, J. L. Arias, J. Nicolas, and P. Couvreur, Magnetic nanoparticles: Design and characterization, toxicity and biocompatibility, pharmaceutical and biomedical applications. *Chem. Rev.* 112, 5818 (2012).
109. Q. A. Pankhurst, J. Connolly, S. Jones, and J. Dobson, Applications of magnetic nanoparticles in biomedicine. *J. Phys. D: Appl. Phys.* 36, R167 (2003).
110. D. Jańczewski, Y. Zhang, G. K. Das, D. K. Yi, P. Padmanabhan, K. K. Bhakoo, T. T. Y. Tan, and S. T. Selvan, Bimodal magnetic–fluorescent probes for bioimaging. *Microsc ResTech.* 74, 563 (2011).
111. Z. R. Stephen, F. M. Kievit, and M. Zhang, Magnetite nanoparticles for medical MR imaging. *Mater. Today* 14, 330 (2011).
112. H. Jaganathan and A. Ivanisevic, "Nanobiomaterials Handbook," (B. Sitharaman Ed.), pp. 1–17, CRC Press, 2011.
113. A.-H. Lu, E. L. Salabas, and F. Schüth, Magnetic nanoparticles: Synthesis, protection, functionalization, and application. *Angew. Chem. Int. Ed.* 46, 1222 (2007).
114. S. L. C. Pinho, G. A. Pereira, P. Voisin, J. Kassem, V. Bouchaud, L. Etienne, J. A. Peters, L. Carlos, S. Mornet, C. F. G. C. Geraldes, J. Rocha, and M.-H. Delville, Fine tuning of the relaxometry of ã-Fe_2O_3@SiO_2 Nanoparticles by tweaking the silica coating thickness. *ACS Nano* 4, 5339 (2010).
115. N. Insin, J. B. Tracy, H. Lee, J. P. Zimmer, R. M. Westervelt, and M. G. Bawendi, Incorporation of iron oxide nanoparticles and quantum dots into silica microspheres. *ACS Nano* 2, 197 (2008).
116. J. Ruan, J. Ji, H. Song, Q. Qian, K. Wang, C. Wang, and D. Cui, Fluorescent magnetic nanoparticle-labeled mesenchymal stem cells for targeted imaging and hyperthermia therapy of in vivo gastric cancer. *Nanoscale Res. Lett.* 7, 1 (2012).
117. G. Ruan, G. Vieira, T. Henighan, A. Chen, D. Thakur, R. Sooryakumar, and J. O. Winter, Simultaneous magnetic manipulation and fluorescent tracking of multiple individual hybrid nanostructures. *Nano Lett.* 10, 2220 (2010).
118. E.-Q. Song, J. Hu, C.-Y. Wen, Z.-Q. Tian, X. Yu, Z.-L. Zhang, Y.-B. Shi, and D.-W. Pang, Fluorescent-magnetic-biotargeting multifunctional nanobioprobes for detecting and isolating multiple types of tumor cells. *ACS Nano* 5, 761 (2011).
119. A. Kale, S. Kale, P. Yadav, H. Gholap, R. Pasricha, J. Jog, B. Lefez, B. Hannoyer, P. Shastry, and S. Ogale, Magnetite/CdTe magnetic–fluorescent composite nanosystem for magnetic separation and bio-imaging. *Nanotechnology* 22, 225101 (2011).
120. D. Thakur, S. Deng, T. Baldet, and J. O. Winter, pH sensitive CdS–iron oxide fluorescent–magnetic nanocomposites. *Nanotechnology* 20, 485601 (2009).
121. S. R. Ahmed, J. Dong, M. Yui, T. Kato, J. Lee, and E. Y. Park, Quantum dots incorporated magnetic nanoparticles for imaging colon carcinoma cells. *J. Nanobiotechnology* 11, 28 (2013).

122. X. You, R. He, F. Gao, J. Shao, B. Pan, and D. Cui, Hydrophilic high-luminescent magnetic nanocomposites. *Nanotechnology* 18, 035701 (2007).
123. D. Wang, J. He, N. Rosenzweig, and Z. Rosenzweig, Superparamagnetic Fe_2O_3 beads-CdSe/ZnS quantum dots core–shell nanocomposite particles for cell separation. *Nano Lett.* 4, 409 (2004).
124. Y. Zhang, S.-N. Wang, S. Ma, J.-J. Guan, D. Li, X.-D. Zhang, and Z.-D. Zhang, Self-assembly multifunctional nanocomposites with Fe_3O_4 magnetic core and CdSe/ZnS quantum dots shell. *J. Biomed. Mater. Res. A* 85A, 840 (2008).
125. D. Wang, J. He, N. Rosenzweig, and Z. Rosenzweig, Superparamagnetic Fe_2O_3 beads-CdSe/ZnS quantum dots core–shell nanocomposite particles for cell separation. *Nano Lett.* 4, 409 (2004).
126. P. Sun, H. Zhang, C. Liu, J. Fang, M. Wang, J. Chen, J. Zhang, C. Mao, and S. Xu, Preparation and characterization of Fe_2O_3/CdTe magnetic/fluorescent nanocomposites and their applications in immuno-labeling and fluorescent imaging of cancer cells. *Langmuir* 26, 1278 (2009).
127. D. K. Yi, S. T. Selvan, S. S. Lee, G. C. Papaefthymiou, D. Kundaliya, and J. Y. Ying, Silica-coated nanocomposites of magnetic nanoparticles and quantum dots. *J. Am. Chem. Soc.* 127, 4990 (2005).
128. Q. Wang, Y. Liu, C. Lin, and H. Yan, Layer-by-layer growth of superparamagnetic, fluorescent barcode nanospheres. *Nanotechnology* 18, 405604 (2007).
129. S. T. Selvan, P. K. Patra, C. Y. Ang, and J. Y. Ying, Synthesis of silica-coated semiconductor and magnetic quantum dots and their use in the imaging of live cells. *Angew. Chem. Int. Ed.* 46, 2448 (2007).
130. R. He, X. You, J. Shao, F. Gao, B. Pan, and D. Cui, Core/shell fluorescent magnetic silica-coated composite nanoparticles for bioconjugation. *Nanotechnology* 18, 315601 (2007).
131. L. Li, E. S. G. Choo, Z. Liu, J. Ding, and J. Xue, Double-layer silica core–shell nanospheres with superparamagnetic and fluorescent functionalities. *Chem. Phys. Lett.* 461, 114 (2008).
132. B. Liu, W. Xie, D. Wang, W. Huang, M. Yu, and A. Yao, Preparation and characterization of magnetic luminescent nanocomposite particles. *Mater. Lett.* 62, 3014 (2008).
133. O. Chen, L. Riedemann, F. Etoc, H. Herrmann, M. Coppey, M. Barch, C. T. Farrar, J. Zhao, O. T. Bruns, and H. Wei, Magneto-fluorescent core–shell supernanoparticles. *Nature Comm.* 5 (2014).
134. V. Salgueiriño-Maceira, M. A. Correa-Duarte, M. Spasova, L. M. Liz-Marzán, and M. Farle, Composite silica spheres with magnetic and luminescent functionalities. *Adv. Funct. Mater.* 16, 509 (2006).
135. D. Cui, Y. Han, Z. Li, H. Song, K. Wang, R. He, B. Liu, H. Liu, C. Bao, and P. Huang, Fluorescent magnetic nanoprobes for *in vivo* targeted imaging and hyperthermia therapy of prostate cancer. *Nano Biomed. Eng.* 1, 94 (2009).
136. Q. Ma, Y. Nakane, Y. Mori, M. Hasegawa, Y. Yoshioka, T. M. Watanabe, K. Gonda, N. Ohuchi, and T. Jin, Multilayered, core/shell nanoprobes based on magnetic ferric oxide particles and quantum dots for multimodality imaging of breast cancer tumors. *Biomaterials* 33, 8486 (2012).
137. G.-P. Wang, E.-Q. Song, H.-Y. Xie, Z.-L. Zhang, Z.-Q. Tian, C. Zuo, D.-W. Pang, D.-C. Wu, and Y.-B. Shi, Biofunctionalization of fluorescent-magnetic-bifunctional nanospheres and their applications. *Chem. Comm.* 4276 (2005).
138. T. R. Sathe, A. Agrawal, and S. Nie, Mesoporous silica beads embedded with semiconductor quantum dots and iron oxide nanocrystals: Dual-function microcarriers for optical encoding and magnetic separation. *Anal. Chem.* 78, 5627 (2006).
139. L. Li, D. Chen, Y. Zhang, Z. Deng, X. Ren, X. Meng, F. Tang, J. Ren, and L. Zhang, Magnetic and fluorescent multifunctional chitosan nanoparticles as a smart drug delivery system. *Nanotechnology* 18, 405102 (2007).
140. C. Tu, Y. Yang, and M. Gao, Preparations of bifunctional polymeric beads simultaneously incorporated with fluorescent quantum dots and magnetic nanocrystals. *Nanotechnology* 19, 105601 (2008).
141. Y. F. Tan, P. Chandrasekharan, D. Maity, C. X. Yong, K.-H. Chuang, Y. Zhao, S. Wang, J. Ding, and S.-S. Feng, Multimodal tumor imaging by iron oxides and quantum dots formulated in poly(lactic acid)-D-alpha-tocopheryl polyethylene glycol 1000 succinate nanoparticles. *Biomaterials* 32, 2969 (2011).
142. Y.-H. Li, T. Song, J.-Q. Liu, S.-J. Zhu, and J. Chang, An efficient method for preparing high-performance multifunctional polymer beads simultaneously incorporated with magnetic nanoparticles and quantum dots. *J. Mater. Chem.* 21, 12520 (2011).
143. X. Hong, J. Li, M. Wang, J. Xu, W. Guo, J. Li, Y. Bai, and T. Li, Fabrication of magnetic luminescent nanocomposites by a layer-by-layer self-assembly approach. *Chem. Mater.* 16, 4022 (2004).
144. L. Jie-Mei, X. Xiao-Liang, L. Ling, Y. Nai-Qiang, and Z. Li-Xin, Preparation and characterization of bimodal magnetofluorescent nanoprobes for biomedical application. *Chin. Phys. Lett.* 29, 097803 (2012).
145. H.-M. Fan, M. Olivo, B. Shuter, J.-B. Yi, R. Bhuvaneswari, H.-R. Tan, G.-C. Xing, C.-T. Ng, L. Liu, S. S. Lucky, B.-H. Bay, and J. Ding, Quantum dot capped magnetite nanorings as high performance nanoprobe for multiphoton fluorescence and magnetic resonance imaging. *J. Am. Chem. Soc.* 132, 14803 (2010).
146. J. Lee, H. Kim, T. Sim, and R. Song, A new quantum dot-platinum conjugate for self-assembled nanoconjugates by coordination bonding mediated recognition. *Chem. Comm.* 49, 6182 (2013).
147. J. Lee, G. Hwang, Y. S. Hong, and T. Sim, One step synthesis of quantum dot-magnetic nanoparticle heterodimers for dual modal imaging applications. *Analyst.* 140, 2864 (2015).
148. P.-C. Lin, T.-W. Chiou, and H.-J. Harn, "Evidence-Based Anticancer Materia Medica," (W. C. S. Cho, Ed.), pp. 131–153, Springer Netherlands, 2011.
149. S. C. Erwin, L. Zu, M. I. Haftel, A. L. Efros, T. A. Kennedy, and D. J. Norris, Doping semiconductor nanocrystals. *Nature* 436, 91 (2005).
150. R. Beaulac, S. T. Ochsenbein, and D. R. Gamelin, "Nanocrystal Quantum Dots," (V. I. Klimov, Ed.). Taylor and Francis, Boca Raton, 2010.
151. R. Buonsanti and D. J. Milliron, Chemistry of doped colloidal nanocrystals. *Chem. Mater.* 25, 1305 (2013).
152. G. M. Dalpian and J. R. Chelikowsky, Self-purification in semiconductor nanocrystals. *Phys. Rev. Lett.* 96, 226802 (2006).
153. D. J. Norris, A. L. Efros, and S. C. Erwin, Doped nanocrystals. *Science* 319, 1776 (2008).
154. D. Mocatta, G. Cohen, J. Schattner, O. Millo, E. Rabani, and U. Banin, Heavily doped semiconductor nanocrystal quantum dots. *Science* 332, 77 (2011).
155. P. Wu and X.-P. Yan, Doped quantum dots for chemo/biosensing and bioimaging. *Chem. Soc. Rev.* 42, 5489 (2013).
156. P. K. Santra and P. V. Kamat, Mn-doped quantum dot sensitized solar cells: A strategy to boost efficiency over 5%. *J. Am. Chem. Soc.* 134, 2508 (2012).
157. Z. Huang, X. Zou, and H. Zhou, A strategy to achieve superior photocurrent by Cu-doped quantum dot sensitized solar cells. *Mater. Lett.* 95, 139 (2013).
158. S. K. Panda, S. G. Hickey, H. V. Demir, and A. Eychmüller, Bright white-light emitting manganese and copper co-doped ZnSe quantum dots. *Angew. Chem. Int. Ed.* 123, 4524 (2011).
159. N. Pradhan and D. D. Sarma, Advances in light-emitting doped semiconductor nanocrystals. *J. Phys. Chem. Lett.* 2, 2818 (2011).
160. M. Geszke-Moritz, G. Clavier, J. Lulek, and R. Schneider, Copper- or manganese-doped ZnS quantum dots as fluorescent probes for detecting folic acid in aqueous media. *J. Lumin.* 132, 987 (2012).
161. P. Wu, L.-N. Miao, H.-F. Wang, X.-G. Shao, and X.-P. Yan, A Multidimensional sensing device for the discrimination of proteins

based on manganese-doped ZnS quantum dots. *Angew. Chem. Int. Ed.* 50, 8118 (2011).
162. H. R. Rajabi, O. Khani, M. Shamsipur, and V. Vatanpour, High-performance pure and Fe^{3+}-ion doped ZnS quantum dots as green nanophotocatalysts for the removal of malachite green under UV-light irradiation. *J. Hazard. Mater.* 250–251, 370 (2013).
163. M. H. Mendonça-Dias, E. Gaggelli, and P. C. Lauterbur, Paramagnetic contrast agents in nuclear magnetic resonance medical imaging. *Semin. Nucl. Med.* 13, 364 (1983).
164. D. Pan, A. H. Schmieder, S. A. Wickline, and G. M. Lanza, Manganese-based MRI contrast agents: Past, present, and future. *Tetrahedron* 67, 8431 (2011).
165. R. N. Bhargava, D. Gallagher, X. Hong, and A. Nurmikko, Optical properties of manganese-doped nanocrystals of ZnS. *Phys. Rev. Lett.* 72, 416 (1994).
166. R. Beaulac, P. I. Archer, S. T. Ochsenbein, and D. R. Gamelin, Mn^{2+}-doped CdSe quantum dots: New inorganic materials for spin-electronics and spin-photonics. *Adv. Funct. Mater.* 18, 3873 (2008).
167. K.-T. Yong, Mn-doped near-infrared quantum dots as multimodal targeted probes for pancreatic cancer imaging. *Nanotechnology* 20, 015102 (2009).
168. G. Sitbon, S. Bouccara, M. Tasso, A. Francois, L. Bezdetnaya, F. Marchal, M. Beaumont, and T. Pons, Multimodal Mn-doped I–III–VI quantum dots for near infrared fluorescence and magnetic resonance imaging: From synthesis to *in vivo* application. *Nanoscale* 6, 9264 (2014).
169. T. Jahanbin, M. Gaceur, H. Gros-Dagnac, S. Benderbous, and S. Merah, High potential of Mn-doped ZnS nanoparticles with different dopant concentrations as novel MRI contrast agents: Synthesis and *in vitro* relaxivity studies. *J. Nanopart. Res.* 17, 1 (2015).
170. S. Santra, H. Yang, P. H. Holloway, J. T. Stanley, and R. A. Mericle, Synthesis of water-dispersible fluorescent, radio-opaque, and paramagnetic CdS:Mn/ZnS quantum dots: A multifunctional probe for bioimaging. *J. Am. Chem. Soc.* 127, 1656 (2005).
171. H. Yang, S. Santra, and P. H. Holloway, Syntheses and applications of Mn-doped II–VI semiconductor nanocrystals. *J. Nanosc. Nanotech.* 5, 1364 (2005).
172. S. Wang, B. R. Jarrett, S. M. Kauzlarich, and A. Y. Louie, Core/shell quantum dots with high relaxivity and photoluminescence for multimodality imaging. *J. Am. Chem. Soc.* 129, 3848 (2007).
173. M. Gaceur, M. Giraud, M. Hemadi, S. Nowak, N. Menguy, J. P. Quisefit, K. David, T. Jahanbin, S. Benderbous, M. Boissière, and S. Ammar, Polyol-synthesized Zn0.9Mn0.1S nanoparticles as potential luminescent and magnetic bimodal imaging probes: Synthesis, characterization, and toxicity study. *J. Nanopart. Res.* 14, 1 (2012).
174. L. Jing, K. Ding, S. Kalytchuk, Y. Wang, R. Qiao, S. V. Kershaw, A. L. Rogach, and M. Gao, Aqueous manganese-doped core/shell CdTe/ZnS quantum dots with strong fluorescence and high relaxivity. *J. Phys. Chem. C* 117, 18752 (2013).
175. B. Lin, X. Yao, Y. Zhu, J. Shen, X. Yang, H. Jiang, and X. Zhang, Multifunctional manganese-doped core–shell quantum dots for magnetic resonance and fluorescence imaging of cancer cells. *New. J. Chem.* 37, 3076 (2013).
176. V. K. Sharma, S. Gokyar, Y. Kelestemur, T. Erdem, E. Unal, and H. V. Demir, Manganese doped fluorescent paramagnetic nanocrystals for dual-modal imaging. *Small* 10, 4961 (2014).
177. F. Zhang, F. He, X.-W. He, W.-Y. Li, and Y.-K. Zhang, Aqueous synthesis of highly luminescent surface Mn^{2+}-doped CdTe quantum dots as a potential multimodal agent. *Luminescence* 29, 1059 (2014).
178. K. Ding, L. Jing, C. Liu, Y. Hou, and M. Gao, Magnetically engineered Cd-free quantum dots as dual-modality probes for fluorescence/magnetic resonance imaging of tumors. *Biomaterials* 35, 1608 (2014).
179. I. F. Li and C.-S. Yeh, Synthesis of Gd doped CdSe nanoparticles for potential optical and MR imaging applications. *J. Mater. Chem.* 20, 2079 (2010).
180. W. Guo, W. Yang, Y. Wang, X. Sun, Z. Liu, B. Zhang, J. Chang, and X. Chen, Color-tunable Gd–Zn–Cu–In–S/ZnS quantum dots for dual modality magnetic resonance and fluorescence imaging. *Nano Res.* 7, 1581 (2014).
181. F. Zhang, T.-T. Sun, Y. Zhang, Q. Li, C. Chai, L. Lu, W. Shen, J. Yang, X.-W. He, Y.-K. Zhang, and W.-Y. Li, Facile synthesis of functional gadolinium-doped CdTe quantum dots for tumor-targeted fluorescence and magnetic resonance dual-modality imaging. *J. Mat. Chem. B* 2, 7201 (2014).
182. W. Yang, W. Guo, X. Gong, B. Zhang, S. Wang, N. Chen, W. Yang, Y. Tu, X. Fang, and J. Chang, Facile synthesis of Gd–Cu–In–S/ZnS bimodal quantum dots with optimized properties for tumor targeted fluorescence/MR *in vivo* imaging, *ACS Appl. Mater. Interfaces* 7, 18759 (2015).
183. A. K. Saha, P. Sharma, H.-B. Sohn, S. Ghosh, R. K. Das, A. F. Hebard, H. Zeng, C. Baligand, G. A. Walter, and B. M. Moudgil, Fe doped CdTeS magnetic quantum dots for bioimaging. *J. Mat. Chem. B* 1, 6312 (2013).
184. S. Aime, M. Fasano, and E. Terreno, Lanthanide(III) chelates for NMR biomedical applications. *Chem. Soc. Rev.* 27, 19 (1998).
185. E. J. Werner, A. Datta, C. J. Jocher, and K. N. Raymond, High-relaxivity MRI contrast agents: Where coordination chemistry meets medical imaging. *Angew. Chem. Int. Ed.* 47, 8568 (2008).
186. M. Port, J.-M. Idée, C. Medina, C. Robic, M. Sabatou, and C. Corot, Efficiency, thermodynamic and kinetic stability of marketed gadolinium chelates and their possible clinical consequences: A critical review. *Biometals* 21, 469 (2008).
187. J.-M. Idée, M. Port, I. Raynal, M. Schaefer, S. Le Greneur, and C. Corot, Clinical and biological consequences of transmetallation induced by contrast agents for magnetic resonance imaging: A review. *Fundam. Clin. Pharmacol.* 20, 563 (2006).
188. C. de Haën, Conception of the first magnetic resonance imaging contrast agents: A brief history. *Top Magn. Reson Imaging* 12, 221 (2001).
189. P. Hermann, J. Kotek, V. Kubicek, and I. Lukes, Gadolinium(iii) complexes as MRI contrast agents: Ligand design and properties of the complexes. *Dalton Trans.* 3027–3047 (2008).
190. G.-P. Yan, L. Robinson, and P. Hogg, Magnetic resonance imaging contrast agents: Overview and perspectives. *Radiography* 13, e5 (2005).
191. P. Caravan, Protein-targeted gadolinium-based magnetic resonance imaging (MRI) contrast agents: Design and mechanism of action. *Acc. Chem. Res.* 42, 851 (2009).
192. L. Moriggi, C. Cannizzo, E. Dumas, C. R. Mayer, A. Ulianov, and L. Helm, Gold nanoparticles functionalized with gadolinium chelates as high-relaxivity MRI contrast agents. *J. Am. Chem. Soc.* 131, 10828 (2009).
193. W. J. M. Mulder, G. J. Strijkers, G. A. F. van Tilborg, A. W. Griffioen, and K. Nicolay, Lipid-based nanoparticles for contrast-enhanced MRI and molecular imaging. *NMR in Biomed.* 19, 142 (2006).
194. Z. Zhou and Z.-R. Lu, Gadolinium-based contrast agents for magnetic resonance cancer imaging. *Wiley Interdiscip Rev. Nanomed. Nanobiotechnol.* 5, 18 (2013).
195. K. B. Ghaghada, M. Ravoori, D. Sabapathy, J. Bankson, V. Kundra, and A. Annapragada, New dual mode gadolinium nanoparticle contrast agent for magnetic resonance imaging. *Plos One* 4, e7628 (2009).
196. E. Karathanasis, J. Park, A. Agarwal, V. Patel, F. Zhao, A. V. Annapragada, X. Hu, and R. V. Bellamkonda, MRI mediated, non-invasive tracking of intratumoral distribution of nanocarriers in rat glioma. *Nanotechnology* 19, 315101 (2008).
197. F. Erogbogbo, C.-W. Chang, J. L. May, L. Liu, R. Kumar, W.-C. Law, H. Ding, K. T. Yong, I. Roy, M. Sheshadri, M. T. Swihart, and

P. N. Prasad, Bioconjugation of luminescent silicon quantum dots to gadolinium ions for bioimaging applications. *Nanoscale* 4, 5483 (2012).

198. W. J. M. Mulder, R. Koole, R. J. Brandwijk, G. Storm, P. T. K. Chin, G. J. Strijkers, C. de Mello Donegá, K. Nicolay, and A. W. Griffioen, Quantum dots with a paramagnetic coating as a bimodal molecular imaging probe. *Nano Lett.* 6, 1 (2006).

199. R. Koole, M. M. van Schooneveld, J. Hilhorst, K. Castermans, D. P. Cormode, G. J. Strijkers, C. de Mello Donegá, D. Vanmaekelbergh, A. W. Griffioen, K. Nicolay, Z. A. Fayad, A. Meijerink, and W. J. M. Mulder, Paramagnetic lipid-coated silica nanoparticles with a fluorescent quantum dot core: A new contrast agent platform for multimodality imaging. *Bioconjugate Chem.* 19, 2471 (2008).

200. L. Liu, W.-C. Law, K.-T. Yong, I. Roy, H. Ding, F. Erogbogbo, X. Zhang, and P. N. Prasad, Multimodal imaging probes based on Gd-DOTA conjugated quantum dot nanomicelles. *Analyst.* 136, 1881 (2011).

201. P. Verwilst, S. Park, B. Yoon, and J. S. Kim, Recent advances in Gd-chelate based bimodal optical/MRI contrast agents. *Chem. Soc. Rev.* 44, 1791 (2015).

202. Q. Zhou, K. Mu, L. Jiang, H. Xie, W. Liu, Z. Li, H. Qi, S. Liang, H. Xu, Y. Zhu, W. Zhu, and X. Yang, Glioma-targeting micelles for optical/magnetic resonance dual-mode imaging. *Int. J. Nanomedicine* 10, 1805 (2015).

203. W. J. M. Mulder, K. Castermans, J. R. van Beijnum, M. G. A. Oude Egbrink, P. T. K. Chin, Z. A. Fayad, C. W. G. M. Löwik, E. L. Kaijzel, I. Que, G. Storm, G. J. Strijkers, A. W. Griffioen, and K. Nicolay, Molecular imaging of tumor angiogenesis using $\alpha v\beta 3$-integrin targeted multimodal quantum dots. *Angiogenesis* 12, 17 (2009).

204. W. M. Mulder, K. Castermans, J. van Beijnum, M. A. Oude Egbrink, P. K. Chin, Z. Fayad, C. G. M. Löwik, E. Kaijzel, I. Que, G. Storm, G. Strijkers, A. Griffioen, and K. Nicolay, Molecular imaging of tumor angiogenesis using $\alpha v\beta 3$-integrin targeted multimodal quantum dots. *Angiogenesis* 12, 17 (2009).

205. G. A. F. van Tilborg, W. J. M. Mulder, P. T. K. Chin, G. Storm, C. P. Reutelingsperger, K. Nicolay, and G. J. Strijkers, Annexin A5-conjugated quantum dots with a paramagnetic lipidic coating for the multimodal detection of apoptotic cells. *Bioconjugate Chem.* 17, 865 (2006).

206. J. Savill and V. Fadok, Corpse clearance defines the meaning of cell death. *Nature* 407, 784 (2000).

207. R. L. M. Haas, D. de Jong, R. A. Valdés Olmos, C. A. Hoefnagel, I. van Den Heuvel, S. F. Zerp, H. Bartelink, and M. Verheij, *In vivo* imaging of radiation-induced apoptosis in follicular lymphoma patients. *Int. J. Radiat. Oncol. Biol. Phys.* 59, 782 (2004).

208. H. Yang, S. Santra, G. A. Walter, and P. H. Holloway, Gd^{III}-functionalized fluorescent quantum dots as multimodal imaging probes. *Adv. Mater.* 18, 2890 (2006).

209. C.-Y. Cheng, K.-L. Ou, W.-T. Huang, J.-K. Chen, J.-Y. Chang, and C.-H. Yang, Gadolinium-based CuInS2/ZnS nanoprobe for dual-modality magnetic resonance/optical imaging. *ACS Appl. Mater. Inter.* 5, 4389 (2013).

210. W. B. Tan and Y. Zhang, Multifunctional quantum-dot-based magnetic chitosan nanobeads. *Adv. Mater.* 17, 2375 (2005).

211. G. J. Stasiuk, S. Tamang, D. Imbert, C. Poillot, M. Giardiello, C. Tisseyre, E. L. Barbier, P. H. Fries, M. de Waard, P. Reiss, and M. Mazzanti, Cell-permeable Ln(III) chelate-functionalized inp quantum dots as multimodal imaging agents. *ACS Nano* 5, 8193 (2011).

212. G. J. Stasiuk, S. Tamang, D. Imbert, C. Gateau, P. Reiss, P. Fries, and M. Mazzanti, Optimizing the relaxivity of Gd(iii) complexes appended to InP/ZnS quantum dots by linker tuning. *Dalton Trans.* 42, 8197 (2013).

213. L. W. E. Starmans, M. B. Kok, H. M. H. F. Sanders, Y. Zhao, C. de Mello Donegá, A. Meijerink, W. J. M. Mulder, H. Grüll, G. J. Strijkers, and K. Nicolay, Influence of cell-internalization on relaxometric, optical and compositional properties of targeted paramagnetic quantum dot micelles. *Contrast Media Mol. Imaging.* 6, 100 (2011).

214. X. Xing, B. Zhang, X. Wang, F. Liu, D. Shi, and Y. Cheng, An "imaging-biopsy" strategy for colorectal tumor reconfirmation by multipurpose paramagnetic quantum dots. *Biomaterials* 48, 16 (2015).

215. J. Shen, Y. Li, Y. Zhu, X. Yang, X. Yao, J. Li, G. Huang, and C. Li, Multifunctional gadolinium-labeled silica-coated Fe_3O_4 and $CuInS_2$ nanoparticles as a platform for *in vivo* tri-modality magnetic resonance and fluorescence imaging. *J. Mater. Chem. B* 3, 2873 (2015).

216. M. F. Ferreira, G. Pereira, A. F. Martins, C. I. O. Martins, M. I. M. Prata, S. Petoud, E. Toth, P. M. T. Ferreira, J. A. Martins, and C. F. G. C. Geraldes, Ln[DO3A-N-[small alpha]-(pyrenebutanamido)propionate] complexes: Optimized relaxivity and NIR optical properties. *Dalton Trans.* 43, 3162 (2014).

8 CONCLUSÕES GERAIS

- Os *quantum dots* foram conjugados eficientemente à transferrina e mostraram-se como promissoras sondas fluorescentes sítio-específicas para o estudo dinâmico do TfR em células cancerígenas;
- As células HeLa e as DBTRG apresentaram quantidades similares de TfRs e uma maior expressão desse receptor quando comparadas às células U87. Além disso, as células DBTRG se mostraram mais eficientes na reexpressão do TfR na membrana e isto pode estar relacionado com às características do câncer em situações recorrentes, uma vez que as células DBTRG são originadas de um glioblastoma recidivo, enquanto que as células U87 são originadas de um tumor primário;
- Os *quantum dots* conjugados à transferrina se mostraram como potenciais sistemas para serem aplicados para a compreensão da biologia celular do câncer, como também para auxiliar na elucidação de mecanismos biológicos para fins de aprimoramento de terapias via receptor de transferrina;
- Os *quantum dots* também foram eficientemente conjugados a nanopartículas magnéticas de óxido de ferro, originando sondas bimodais estáveis e com elevada fluorescência, além de apresentarem alta magnetização de saturação;
- Os resultados indicaram que aproximadamente oito QDs foram conjugados em cada nanopartícula de óxido de ferro, caracterizada como magnetita (Fe_3O_4), e essas BNPs apresentaram características superparamagnéticas e um tamanho médio aproximado de 17 nm;
- As nanopartículas bimodais (BNPs) mostraram-se como eficientes sondas inespecíficas de baixa toxicidade para marcação de células por fluorescência, além de potenciais agentes de contrastes para aquisição de imagens ponderadas em T_2;
- As BNPs foram eficientemente conjugadas à transferrina, originando sondas multimodais com especificidade para o TfR;
- Os resultados indicaram que praticamente toda a transferrina (98%) foi conjugada às nanopartículas bimodais. Além disso, essas sondas multimodais (BNPs-Tf) apresentaram baixa citotoxicidade, podendo ser aplicadas para estudo de processos celulares *in vivo* em pequenos animais;

- As sondas multimodais mostraram-se bastante eficientes para marcação sítio-específica por fluorescência e com potencial para melhorar o contraste na IRM, uma vez que forneceram valores maiores de relaxividade transversal (r_2) quando comparados às BNPs sozinhas.
- Por fim, esses sistemas multimodais podem ser aplicados para ampliar a compreensão da biologia celular do câncer em sistemas *in vitro* e *in vivo*, podendo auxiliar em métodos de diagnósticos e terapêuticos, além de poderem ser utilizados para biosseparação e hipertermia;

9 PERSPECTIVAS

- Como perspectivas de curto prazo objetiva-se: (1) aplicar os QDs-Tf no estudo de receptores de transferrina em outros tipos de células cancerígenas, tais como mama e próstata e pulmão; (2) utilizar as sondas multimodais obtidas para aquisição de imagens por ressonância magnética de células marcadas por esses sistemas;
- Sondas multimodais podem ser aplicadas no estudo e para aprimoramento do diagnóstico por mais de uma modalidade de imagem em outras células cancerígenas, a exemplo destas, estão às células de câncer de pulmão e de glioblastoma, pois estas células são originadas em órgãos estratégicos para aquisição das imagens por ressonância magnética nuclear;
- Em médio prazo pretende-se formar novas sondas multimodais através da conjugação das BNPs, desenvolvidas nesta tese, a outras biomoléculas, tais como lectinas e o ácido fólico, a fim de elucidar processos relacionados ao câncer, bem como auxiliar em métodos de diagnósticos e terapias destinados a sistemas biológicos *in vivo* e *in vitro* que tenham não somente o TfR como alvo, mas outras moléculas e outros receptores que também sejam críticos para o seu metabolismo.

ANEXO A

ANEXO A – ARTIGO PUBLICADO EM PARALELO

Journal of Luminescence 174 (2016) 17–21

Contents lists available at ScienceDirect

Journal of Luminescence

journal homepage: www.elsevier.com/locate/jlumin

Full Length Article

A pH dependence study of CdTe quantum dots fluorescence quantum yields using eclipsing thermal lens spectroscopy

C. Estupiñán-López [a], C. Tolentino Dominguez [a,d], P.E. Cabral Filho [a,b], B.S. Santos [a,c], A. Fontes [a,b,*], R.E. de Araujo [a,**]

[a] Laboratory of Biomedical Optics and Imaging, Federal University of Pernambuco, Recife, PE, Brazil
[b] Biophysics and Radiobiology Department, Federal University of Pernambuco, Recife, PE, Brazil
[c] Pharmaceutical Sciences Department, Federal University of Pernambuco, Recife, PE, Brazil
[d] Centre for Telecommunication Studies, Pontifical Catholic University of Rio de Janeiro, Rio de Janeiro, RJ, Brazil

ARTICLE INFO

Article history:
Received 13 June 2015
Received in revised form
29 December 2015
Accepted 30 December 2015
Available online 29 January 2016

Keywords:
Quantum dots
Thermal lens
Quantum efficiency
Emission spectroscopy

ABSTRACT

In this study we evaluated the absolute fluorescence quantum yield (Φ) of hydrophilic CdTe QDs in function of different pHs, modified from the alkaline to acid, by using two different chemicals compounds, the mercaptosuccinic acid (MSA-the stabilizing agent of the QDs synthesis) or hydrochloric acid (HCl). The pH control of QDs suspensions is essential for the use of fluorescent nanoparticles in biological systems. We used the eclipsing thermal lens spectroscopy technique to determine the absolute fluorescence quantum yield values. The results showed variations on the Φ values as a function of the pH, which allowed a better understanding of QDs emission characteristics, establishing parameters for their use in biomedical applications such as optical images of biological systems, immunoassays, flow cytometry, biosensors and others.

1. Introduction

In life sciences, the development and characterization of new materials are of great importance, specifically those that enable their innovation and improvement for purposes related to biological process comprehension, diagnosis and therapies. In this context, fluorescence based techniques such as microscopy for imaging living cells, tissues and small animals; flow cytometry; fluoroimmunoassay and optical biosensors [1–4], which explore fluorescent probes, have been shown to be important tools to understand biological mechanisms [5]. Fluorescent probes allow the development of fluorescence based assays with high sensibility, which can provide the identification and quantification of biomolecules with high specificity. Among the fluorescent probes, the Quantum Dots (QDs) present valuable advantages, which have allowed us to enjoy the full potential of fluorescence. QDs are fluorescent colloidal nanocrystals composed by semiconductor materials, with dimensions ranging from 2 to 10 nm, which present unique optical properties, as: (1) broad absorption bands, allowing the excitation of multiple QDs' colors by a single light source. This advantage is also interesting for experiments with QDs as FRET (Forster Resonance Energy Transfer) donors for minimizing the possibility of direct excitation of the acceptor [6]; (2) high resistance to photobleaching, approximately 100 times higher than organic fluorophores, allowing to follow in time several long and lasting biological processes, and (3) narrow emission spectra, permitting multiplex analysis [7–9]. Due to these special properties, QDs have been applied as fluorescent probes for molecular, cellular and *in vivo* imaging; cytometry and fluoroimmunoassays; for biosensors and also, more recently, as photosensitizers in photodynamic therapy (PDT) [10].

QDs have a complex structure where the core, responsible for the fluorescence emission, is coated with a passivation layer that offers the photostability and provides the quality of the emission of these nanocrystals. Besides, hydrophilic QDs present a functionalization layer conferred by the stabilizing agents that contains chemical functional groups, which also allow QDs conjugation with biomolecules. The bioconjugation provides specificity to the optical fluorescence techniques, leading to particular interactions between QDs and biological systems. The conjugation can be performed by adsorption or by covalent bound. In order to apply bare QDs or conjugated QDs, it is always required adjustments of physical and chemical conditions, as temperature and pH, in order to have nanocrystals suspensions appropriated for biological applications [11]. It is known that these adjustments, especially for

* Correspondence to: Departamento de Biofísica e Radiobiologia, CCB, UFPE, Av. Prof. Moraes Rego, s/n, 50670-901 Recife, PE, Brazil.
** Correspondence to: Departamento de Eletrônica e Sistemas, Centro de Tecnologia, UFPE, R. Acadêmico Hélio Ramos, s/n, 50740-530 Recife, PE, Brazil.
E-mail addresses: adriana.fontes.biofisica@gmail.com (A. Fontes), renato.earaujo@ufpe.br (R.E. de Araujo).

http://dx.doi.org/10.1016/j.jlumin.2015.12.052
0022-2313/

ıjugation, can modify the fluorescence efficiency of these ıocrystals [12]. These changes can be quantified by absolute ɔrescence quantum yield (Φ) measurements, which evaluate efficiency of fluorophores to emit radiation [13].

Fluorescence quantum yield is defined as the ratio of the ımber of emitted photons by the number of absorbed photons by luorophore. There are still few works that evaluate changes in ɔlute quantum yields and they are usually related to hydro-ɔbic QDs [14,15]. Moreover, different techniques have been ɔlored to measure fluorescence quantum yield. These techni-ɛs can be classified into absolute and relative method [15,16]. efly, relative techniques, that compare fluorescence emission ɛctra, use reference materials with known quantum yield values quantify the fluorescence efficiency of a new sample. The need reference materials limits the use of relative methods. Besides, ɔlute methods, exploring integrated sphere or thermal lens ɛctroscopy (TLS), can directly provide quantum yield quantifi-ion without the use of standard samples. In particular, TLS erges as a technique which presents more accurate results for values when compared with methods that directly explore ative and absolute fluorescence analyses [16,17].

This study aimed to evaluate the absolute fluorescence quan-n yield of Cadmium Telluride (CdTe) QDs, synthesized in aqu-ıs medium, according to different pHs adjusted by the addition mercaptosuccinic acid (MSA) or hydrochloric acid (HCl), which two chemical compounds usually explored on the pH control QDs suspensions [18,19]. For example, the pH of hydrophilic s soon after the synthesis is usually around 10.0, the pH of logical samples is around 7.0 and the pH to perform covalent ıjugation by using the most applied coupling agents, EDC and fo – NHS (1-Ethyl-3-(3-dimethylaminopropyl)carbodiimide and ıydroxysulfosuccinimide sodium salt), is around 6.0 [20]. CdTe s are the most used hydrophilic nanocrystals for biological ɔlications.

In order to calculate the Φ values for the samples, we used the ɛrmal lens (TL) spectroscopy in single-beam configuration and ipsing mode detection (S-ETL), which joins the higher sensi-ity of the eclipsing mode (when compared to conventional TL ıdes) with the more accurate results of Φ provided by TL hniques (when compared to other methods that explore rela-ɛ and absolute fluorescence analysis) [21,22]. These results can ɔvide a better understanding of processes that modify the QDs' ission characteristics, when the pH values of the suspension is ınged, helping to establish parameters and specific limits for proving their applications in life sciences.

Experimental procedures

Samples preparation

CdTe QDs were synthesized in aqueous medium with adapta-ns of the method described by Andrade and co-authors [19]. efly, QDs were prepared by adding reduced tellurium, Te^{2-}, in a ution containing $Cd(ClO_4)_2$ (cadmium perchlorate) at pH > 10 in presence of MSA, which acts as stabilizing and functionalizing ɛnt, in a molar ratio of 5:1:6.0 Cd:Te:MSA. The reaction pro-ɛded for 5 h at 80 °C, in inert atmosphere and under constant ɛring. All reagents were obtained from Sigma Aldrich. The Te^{2-} ıeous solution was prepared by reducing metallic tellurium ɛh $NaBH_4$ at a high pH (using 100 μL of NaOH, 2 mol L^{-1}), also ɛder heating and in inert nitrogen atmosphere. Finally, the sus-ısion was diluted in a proportion of 1:6 (QDs:Water – v/v), ulting in samples with a final pH=10.3 and absorbance less ın 0.1 at the wavelength of 532 nm.

Two groups of samples were prepared. A first group with the pHs adjusted by the addition of the stabilizing agent, MSA (4.9%), obtaining samples with pHs: 9.8; 9.1; 8.4; 7.3; 6.2 and 5.3. A second group of samples with pHs: 9.8; 9.1; 8.4 and 8.0, with values adjusted using HCl (1 mol L^{-1}). All samples were prepared to reach equal molar concentrations, and therefore the samples absorbance remains the same for all pH values. All samples were prepared and analyzed in quintuplicate, for each pH suspension.

Thermal lens spectroscopy

When a laser beam travels through an absorbing sample, the illuminate region suffers a local increase of its temperature, which is generated by energy absorption followed by a non-radiative energy decay in the material. The last process produces a sample heating that in turn induces localized changes in its refractive index (n). The localized changes in n result on an optical lens behavior of the sample, known as thermal lens (TL) effect [13,23].

In order to create the TL effect, the light from a Gaussian beam laser is focused on an absorbing sample and the temporal intensity dynamics of the transmitted beam is evaluated. The most acceptable theoretical model that explains the TL effect in a single-beam configuration is based on a Gaussian beam propagation theory and Fresnel diffraction. The model was developed by Sheldon and collaborators [24]. The analytical expression for the temporal behavior of the intensity of transmitted beam is:

$$I = I_0\left[1-\frac{\theta}{2}\tan^{-1}\left(\frac{2V}{\left[9+V^2\right]\left(\frac{t_c}{2t}\right)+3+V^2}\right)\right]^2 \quad (1)$$

where I_0 is the beam intensity at $t=0$, θ is the thermal phase shift and V is given by

$$V = \frac{z}{z_R}+\left(\frac{z_R}{z_2}\right)\left[1+\left(\frac{z}{z_R}\right)^2\right] \quad (2)$$

Considering the position of the beam waist as the origin of the z coordinate, z is the position of the sample and z_2 is the distance of the sample to the photodetector; z_R is the Rayleigh length; t_c is the characteristic heat diffusion time, given by $t_c=\omega_{ex}/4D$, being $D=\kappa/\rho C_P$ the thermal diffusivity, ρ is the volumetric density and C_P the specific heat of the sample and ω_{ex} the excitation beam waist.

The amplitude of θ, in Eq. (1), is determined from Eq. 3:

$$\theta = -\frac{\varphi P_{abs}}{k\lambda_{ex}}\frac{dn}{dT} \quad (3)$$

being φ the fraction of absorbed energy converted in thermal energy, also called absolute nonradiative quantum yield; λ_{ex} is the excitation wavelength; κ is the thermal conductivity of solvent; dn/dT the thermo-optic coefficient and P_{abs} is the laser power absorbed by the sample, which is obtained from $P_{abs}=P_{ex}(1-e^{-\alpha L})$, α is the linear absorption coefficient at the excitation wavelength (λ_{ex}), P_{ex} the incident excitation power and L is the optical path length of the sample.

The nonradiative quantum yield, φ, for fluorescent materials is given by.

$$\varphi = 1-\Phi\frac{\lambda_{ex}}{\langle\lambda_{em}\rangle} \quad (4)$$

Thus, the Φ of the sample can be obtained analyzing the temporal dynamics of the laser beam that passes through the sample, determining the power absorbed (P_{abs}) and by using Eqs. (1), (3) and (4).

2.3. Experimental set-up

QDs suspensions were characterized by UV–vis electronic absorption spectroscopy (Shimadzu, model 1800 UV–vis). After the pH adjustment, the emission spectra for all QDs systems were immediately obtained using $\lambda_{exc}=532$ nm, excitation slit of 15 nm and emission slit of 2.5 nm, in a fluorescence spectrofluorometer (PerkinElmer, LS55).

The experimental scheme to evaluate the quantum yield of the CdTe nanostructures is shown in Fig. 1. Single beam eclipse TL was explored due to its high sensitivity and set-up simplicity. As excitation source it was used a CW laser (Nd: YAG; Compass 215M-20, Coherent Inc.) emitting at 532 nm. QDs suspensions were placed in a glass cuvette with $L=1$ mm. A lens (L_3 in Fig. 1) of 10 cm of focal length was used to focus the laser beam on the sample. A chopper was used to control the laser exposure time on the sample (duty cycle=0.05, frequency=110 Hz). An opaque circular mask blocking the central region of the propagating beam was placed between the sample and the detector to increase the sensitivity of the TL technique [21]. The incident laser power on the samples was maintained in 9 mW, the spot size of the incident laser beam (ω_{ex}) was 5 mm, the Rayleigh length (z_R) was 1.1 mm and the detector was placed 65 cm (z_2) from the sample, and that sample was placed at $z\sim1.16$ mm. Typical values for the parameters dn/dT, C_P, κ and ρ can be found in the literature [25].

3. Results and discussions

Fig. 2 shows the absorption spectra of the CdTe QDs suspension used in the experiments at the original pH of 10.3. One can observe the first absorption peak at about 552 nm, indicating an average diameter of approximately 3 nm for the nanoparticles [26,27]. Furthermore using the Beer–Lambert equation and molar coefficient extinction proposed by Yu et al. [28], it was estimated the QDs concentration as 4.8 μmol L^{-1} for the original suspension. After dilution in water at 1:6 (v/v), the final concentration used in the experiments was 0.8 μmol L^{-1}. The adjustment of the pHs, by using HCl or MSA, did not change the absorption spectra.

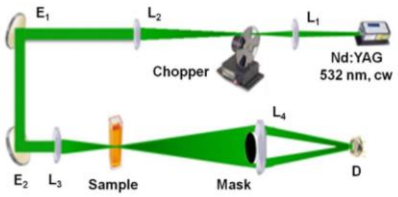

Fig. 1. Experimental scheme of the thermal lens arrangement in the eclipsing mode. L_1, L_2, L_3 and L_4 are biconvex lenses; M_1, M_2 are aluminum mirrors; D is the photodetector, the black circle represents a spatial mask.

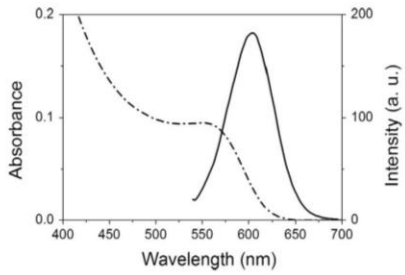

Fig. 2. Absorption (dashed line) and emission (full line) spectrum of CdTe QDs suspension. $\lambda_{exc}=532$ nm.

The QDs maximum emission peak was about 604 nm at original alkaline pH and the full width half maximum (FWHM) was approximately 58 nm, at $\lambda_{exc}=532$ nm. Fig. 3 shows the emission spectra of the QD suspension with different pH values. When HCl was applied on the sample pH adjustment (see Fig. 3a) a significant change on the QDs emission was observed. By lowering the sample pH, from 10.3 to 7.9, with HCl an 8.7 times reduction of the emission peak was observed (Fig. 3a). Fig. 3b shows the QD emission spectrum for two different pH obtained using MSA. One can observe a slightly change of the spectrum peak intensity and a blue shift, about 7 nm, probably indicating an improvement of the QDs passivation layer.

The analyses of the fluorescence emission spectra showed that adjustments on the pH of QDs suspensions induce changes on the fluorescence properties of the nanostructures. Fig. 4 shows the behavior of the integrated emission intensity (that is proportional to quantum yield) for samples with pH adjusted by MSA and HCl. When the suspension pH was reduced by using HCl, we observed a decrease on the QDs emission intensity. In Fig. 4 one can identify a decrease about 7.5 times of the QDs emission, when the pH was changed from 10.3 to 7.9 for HCl samples. Moreover, when the pH was adjusted to a value smaller than 7.9 with HCl, the QDs suspension precipitated. Two main processes are accounted for this observation: the increase in the acid solution, by adding H^+ ions, which induces the removal of the nanocrystals stabilizing/passivation layer (1) and decreases the negative charge of QDs surface (2). By lowering the sample pH using MSA, the integrated emission intensity of the QDs suspension increased.

On the evaluation of the fluorescence quantum yield, the eclipsing TL spectroscopy was explored. Fig. 5 shows a typical result obtained by the thermal-lens technique. In Fig. 5 one can observe a temporal behavior of the collected light on the TL experimental arrangement. The transient behavior of the light intensity reaching the photodetector indicates the shaping of the thermal lens in the sample. The red curve represents the theoretical fit adjusted to the experimental data, by using the Eq. (1). With the theoretical fit adjustment we were able to obtain a fluorescence quantum yield value for all samples used.

Fig. 6 shows the variation of quantum yield values when the pH was adjusted with MSA (stars) or HCl (circles). By adding MSA to the sample, Φ changes from ~62% to ~68% were obtained with pHs going from 7.3 to 5.0. When the MSA was used, the QD passivation layer was improved. MSA participate actively in the formation of this layer, by the association of thiol groups on the nanocrystals surface, minimizing the defects related with unpaired Cd^{2+} ions. Furthermore, using the MSA solution to pH adjustment the samples remained stable and without precipitation. The fluorescence quantum yield values present an uncertainty of approximately 5%, rising mainly from the fitting adjustment of Eq. (1) on the TL experimental curves. A ~10% change was also observed by evaluating the integrated emission intensity, for the same pH range. Moreover, suspensions with pH higher than 7.5 are less fluorescent. MSA samples with high pH are expected to contain emitting and non-emitting nanocrystals and therefore the Φ values presented are smaller (~50%). In this case, for non-homogeneous samples, the values of Fig. 6 should be considered as collective scale Φ, rather than an individual quantum yield, due to the TL spectroscopy limitations. TL spectroscopy and fluorescent intensity analysis techniques are more appropriated for homogeneous samples [29].

When the samples pHs were changed using HCl, the Φ values decreased. Pilla et al. reported similar behavior using hydrophobic re-dispersed CdSe/ZnS QDs [14]. By adding HCl for pH adjustment, stronger population inhomogeneities, consisted by the presence of

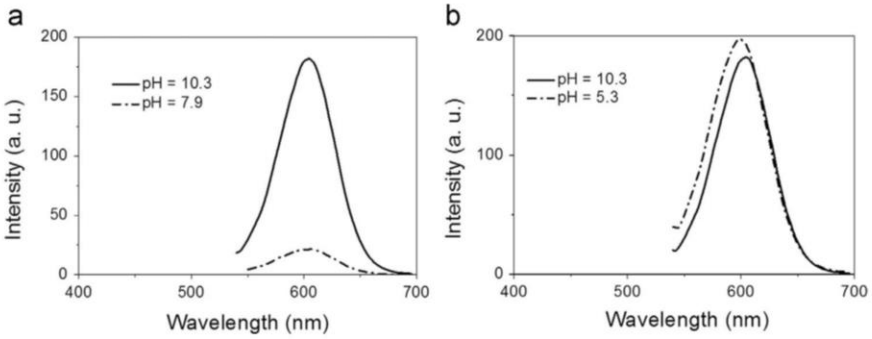

Fig. 3. Emission spectrum of CdTe QDs with pH adjusted with (a) HCl and (b) MSA. The excitation wavelength was 532 nm.

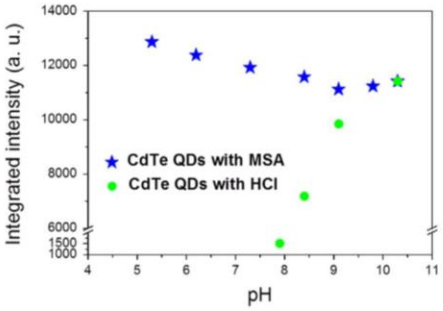

Fig. 4. Integrated emission intensity of QD suspensions with pH adjusted with MSA (stars) and HCl (circles).

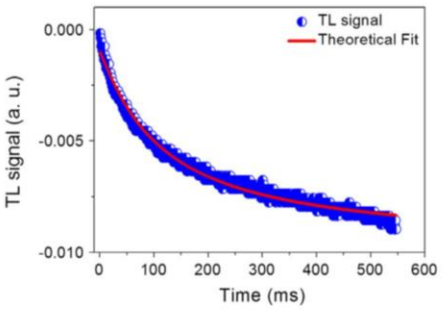

Fig. 5. TL signal (blue curve) and theoretical fit (red line) for CdTe QDs at the pH = 10.3. (For interpretation of the references to color in this figure legend, the reader is referred to the web version of this article.)

higher amounts of low fluorescent as well as non-fluorescent nanocrystals, can be achieved. Moreover samples, adjusted with HCl and with pH equal or lower than 7.9, showed flocculation and phase separation one day after the pH adjustment. This behavior is attributed probably to the remotion or degradation of the QDs stabilizing/passivation layer by the HCl, and consequently defects on the surface was exposed, reducing the efficiency of the electron-hole recombination and also the suspension stability. Therefore, for those inhomogeneous samples, the fluorescence intensity method and TL spectroscopy are limited showing a high discrepancy in their results (Figs. 6 and 4).

4. Conclusions

It is well known the expanding use of QDs in biological applications. When these nanocrystals are applied in biological systems a special care must be taken to the experimental procedures performed on

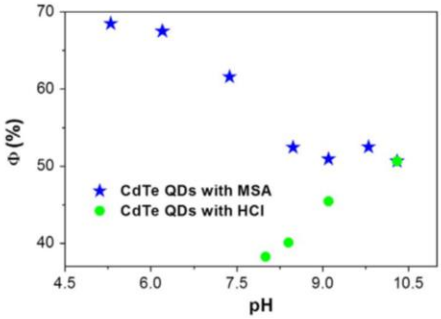

Fig. 6. Quantum yield of CdTe QDs whose pH was adjusted with MSA (stars) or HCl (circles).

different pH regimes of the original systems (usually obtained and kept at pH > 10 for hydrophilic procedures). A neutral pH (close to the physiological) or acid pH (for bioconjugation) will be imposed to the nanocrystals suspension and their optical properties may vary greatly from their original description. We observed significant changes on the fluorescence quantum yield of CdTe QDs by adjusting the suspension pH using HCl or MSA. The absolute quantum yield of CdTe QDs was measured using the TL technique in the eclipsing mode and the QDs fluorescence spectra were also analyzed. We showed that stabilizing agents should be preferred for adjusting the pH QDs suspensions, leading to a stable suspension with a high quantum yield. Moreover, the results allow a better understanding of the pH effects on the emission characteristics of QDs, establishing parameters for their use in biomedical applications.

Acknowledgments

Authors are grateful to Coordenação de Aperfeiçoamento de Pessoal de Nível Superior (CAPES), Conselho Nacional de Desenvolvimento Científico e Tecnológico (CNPq), Fundação de Amparo à Ciência e Tecnologia do Estado de Pernambuco (FACEPE) for financial supports and student fellowships. We are also grateful to the National Institute of Science in Photonics (INFo) for financial resources.

References

[1] A.M. De Grand, J.V. Frangioni, Technolo. Cancer Res. Treat. 2 (2003) 553.
[2] C. Szymanski, H. Yi, J. Liu, E. Wright, C. Payne, Imaging intracellular quantum dots: fluorescence microscopy and transmission electron microscopy, in: S. J. Rosenthal, D.W. Wright (Eds.), NanoBiotechnology Protocols, Humana Press, New York, 2013, pp. 21–33.
[3] M.R. Loken, A.M. Stall, J. Immunol. Methods 50 (1982) R85.
[4] S.A. Khan, G.T. Smith, F. Seo, A.K. Ellerbee, Biosens. Bioelectron. 64 (2015) 30.

[5] T.J. Deerinck, Toxicol. Pathol. 36 (2008) 112.
[6] I.L. Medintz, H. Mattoussi, Phys. Chem. Chem. Phys. 11 (2009) 17.
[7] A. Sukhanova, I. Nabiev, Expert Opin. Med. Diagn. 2 (2008) 429.
[8] X. Michalet, F.F. Pinaud, L.A. Bentolila, J.M. Tsay, S. Doose, J.J. Li, G. Sundaresan, A.M. Wu, S.S. Gambhir, S. Weiss, Science 307 (2005) 538.
[9] I.L. Medintz, H.T. Uyeda, E.R. Goldman, H. Mattoussi, Nat. Mater. 4 (2005) 435.
[10] S. Shukla, Adv. Mater. Rev. 1 (2014) 10.
[11] P. Guo, C. Wei, Nanomed. Nanotechnol. Biol. Med. 1 (2005) 122.
[12] Y. Zhang, T.-H. Wang, Theranostics 2 (2012) 631.
[13] J.H. Brannon, D. Magde, J. Phys. Chem. 82 (1978) 705.
[14] V. Pilla, L.P. Alves, J.F. de Santana, L.G. da Silva, R. Ruggiero, E. Munin, J. Appl. Phys. 112 (2012) 104704.
[15] R.A. Cruz, V. Pilla, T. Catunda, J. Appl. Phys. 107 (2010) 083504.
[16] G.A. Crosby, J.N. Demas, J. Phys. Chem. 75 (1971) 991.
[17] C. Würth, M. Grabolle, J. Pauli, M. Spieles, U. Resch-Genger, Anal. Chem. 83 (2011) 3431.
[18] R.B. Lira, A.T. de Sales Neto, K.K.H.G. Carvalho, E.S. Leite, J.A.G. Brasil, D.P.L. Azevedo, P.E. Cabral Filho, M.B. Cavalcanti, A.J. Amaral, P.M.A. Farias, B.S. Santos, A. Fontes, Biocompatible water soluble quantum dots as new bio-photonic tools for hematologic cells: applications for flow cell cytometry, in, 2010, pp. 75750P-75750P-75755.
[19] C.G. Andrade, P.E. Cabral Filho, D.P.L. Tenório, B.S. Santos, E.I.C. Beltrão, A. Fontes, L.B. Carvalho, Int. J. Nanomed. 8 (2013) 4623.
[20] G.T. Hermanson, Chapter 3-zero-length crosslinkers, in: G.T. Hermanson (Ed.), Bioconjugate Techniques, second ed.,Academic Press, New York, 2008, pp. 213–233.
[21] C. Estupiñán-López, C.T. Dominguez, R. de Araujo, Opt. Express 21 (2013) 18592.
[22] R.D. Snook, R.D. Lowe, Analyst 120 (1995) 2051.
[23] C. Hu, J.R. Whinnery, Appl. Opt. 12 (1973) 72.
[24] S. Sheldon, L. Knight, J. Thorne, Appl. Opt. 21 (1982) 1663.
[25] C. Estupiñán-López, C.T. Dominguez, P.E. Cabral Filho, A. Fontes, R.E. de Araujo, Quantum Dots Fluorescence Quantum Yield Measured by Thermal Lens Spectroscopy. Quantum Dots: Applications in Biology, in: Springer, New York, 2014, pp. 93–101.
[26] A.L. Rogach, T. Franzl, T.A. Klar, J. Feldmann, N. Gaponik, V. Lesnyak, A. Shavel, A. Eychmüller, Y.P. Rakovich, J.F. Donegan, J. Phys. Chem. C 111 (2007) 14628.
[27] P. Dagtepe, V. Chikan, J. Jasinski, V.J. Leppert, J. Phys. Chem. C 111 (2007) 14977.
[28] W.W. Yu, L. Qu, W. Guo, X. Peng, Chem. Mater. 15 (2003) 2854.
[29] J. Laverdant, W.D. de Marcillac, C. Barthou, V.D. Chinh, C. Schwob, L. Coolen, P. Benalloul, P.T. Nga, A. Maître, Materials 4 (2011) 1182.

ANEXO B

ANEXO B – TEMPLATE PARA FORMATAÇÃO DO ARTIGO A SER SUBMETIDO PARA A REVISTA *"JOURNAL OF MATERIALS CHEMISTRY B"*

Please do not adjust margins

Journal Name

ARTICLE

Title

A. N. Authorname,[a] A. N. Authorname[b] and A. N. Authorname[c]

Received 00th January 20xx,
Accepted 00th January 20xx

DOI: 10.1039/x0xx00000x

www.rsc.org/

Abstract text goes here. The abstract should be a single paragraph that summarises the content of the article

A Headings are the primary heading type e.g. Introduction, Results and discussion, Experimental

B Headings should always be subordinate to A headings e.g. Synthetic procedures, Materials and methods, Crystallography.

C headings should always be subordinate to B headings e.g. General procedure for synthesis of compound X. The main paragraph text follows directly on here.

The main text of the article should appear here with headings as appropriate.

Conclusions

The conclusions section should come in this section at the end of the article, before the acknowledgements.

Acknowledgements

The acknowledgements come at the end of an article after the conclusions and before the notes and references.

Notes and references

‡ Footnotes relating to the main text should appear here. These might include comments relevant to but not central to the matter under discussion, limited experimental and spectral data, and crystallographic data.

[a] *Address here.*
[b] *Address here.*
[c] *Address here.*

† Footnotes relating to the title and/or authors should appear here.
Electronic Supplementary Information (ESI) available: [details of any supplementary information available should be included here]. See DOI: 10.1039/x0xx00000x

§
§§
etc.

1 Citations should appear here in the format A. Name, B. Name and C. Name, *Journal Title*, 2000, **35**, 3523; A. Name, B. Name and C. Name, *Journal Title*, 2000, **35**, 3523.
2 ...

Formatting – please delete this box prior to submission

- Graphics, including tables, will be located at the top or bottom of the column following their first citation in the text during production (unless they are equations, which appear in the flow of the text). They can be single column or double column as appropriate and require appropriate captions.
- Text is not wrapped around any of the graphics.
- During production, sufficient space will be inserted around graphics for clarity of reading; a horizontal bar will also be used to separate all inserted graphics, tables and their captions from the text:

- Please consult the Styles menu for recommended formatting for all text, including footnotes, references, tables, images and captions.

Please do not adjust margins

ANEXO C

ANEXO C – TEMPLATE PARA FORMATAÇÃO DO ARTIGO EM PREPARAÇÂO PARA A REVISTA *"COLLOIDS AND SURFACES B: BIOINTERFACES"*

COLLOIDS AND SURFACES B: BIOINTERFACES
An International Journal Devoted to Fundamental and Applied Research on Colloid and Interfacial Phenomena in Relation to Systems of Biological Origin

AUTHOR INFORMATION PACK

TABLE OF CONTENTS

ISSN: 0927-7765

DESCRIPTION

Colloids and Surfaces B: Biointerfaces is an international journal devoted to fundamental and applied research on colloid and interfacial phenomena in relation to systems of biological origin, having particular relevance to the medical, pharmaceutical, biotechnological, food and cosmetic fields.

Each Editor of Colloids and Surfaces B has specific fields of expertise. To ensure a smooth and rapid refereeing process, please submit your article to the Editor related to the topic of your research (you can select the correct editor in the drop down menu in our online submission system: http://ees.elsevier.com/colsub):

John Brash
•Interactions of biomolecules (proteins, enzymes, peptides, polysaccharides, DNA) at the solid-solution and air-solution interfaces;
•Surface/interfacial interactions of tissue and blood; Biomaterials development and interfacial properties;
•Drug delivery/controlled release

Henk Busscher
•Physico-chemical mechanisms of microbial adhesion, biofilm formation and tissue cell interaction to surfaces
•Microbial adhesion and biofilm formation
•Role of surface characteristics, surface modification and protein adsorption on microbial adhesion and biofilm formation
•Physico-chemical mechanisms providing biolubrication to surfaces

Dganit Danino
•Self-assembly and molecular assemblies (proteins, polymers, peptides, surfactants)
•Structure of biological fluids
•Drug delivery vehicles at nano and meso scales
•1D structures - fibrils, ribbons, nanotubes
•Milk proteins

Li-Qun Wang
•Surface modification including structured surfaces;
•Biocompatible materials;
•Anti-fouling materials;

•Bio-detection/bio-imaging materials;
•Interactions of biomolecules and cells at interfaces.

Submissions that: (1) deal solely with biological phenomena and do not describe the physico-chemical or colloid-chemical background and/or mechanism of the phenomena, and (2) deal solely with colloid/ interfacial phenomena and do not have appropriate biological content or relevance, are outside the scope of the journal and will not be considered for publication.

The journal publishes regular research papers, reviews, short communications and invited perspective articles, called BioInterface Perspectives. The BioInterface Perspective provide researchers the opportunity to review their own work, as well as provide insight into the work of others that inspired and influenced the author. Regular articles should have a maximum total length of 6,000 words. In addition, a (combined) maximum of 8 normal-sized figures and/or tables is allowed (so for instance 3 tables and 5 figures). For multiple-panel figures each set of two panels equates to one figure. Short communications should not exceed half of the above. It is required to give on the article cover page a short statistical summary of the article listing the total number of words and tables/figures.

AUDIENCE

Colloid and Surface Chemists, Chemical Engineers, (Bio) Pharmaceutical, Cosmetic and Food Chemists, Physical Chemists, Polymer Chemists, Biological and Bioengineers, Organic Chemists, Microbiologists, Medicinal Chemists.

IMPACT FACTOR

2015: 3.902 © Thomson Reuters Journal Citation Reports 2016

ABSTRACTING AND INDEXING

Chemical Abstracts
Current Contents/Physics, Chemical, & Earth Sciences
EMBASE
INSPEC
PASCAL/CNRS
Applied Polymers Literature
APOLLIT
Scopus
EMBiology

EDITORIAL BOARD

C. Gao, Hangzhou, Zhejiang Province, China
T.A. Horbett, Seattle, Washington, USA
K. Ishihara, Tokyo, Japan
K.D. Jandt, Jena, Germany
L. Jiang, Haidian, Beijing, China
K. Kataoka, Tokyo, Japan
J. Kizhakkedathu, Vancouver, British Columbia, Canada
R. Leblanc, Coral Gables, Florida, USA
C. Leidy, Bogota, Colombia
K. Makino, Tokyo, Japan
W. Norde, Wageningen, Netherlands
H. Ohshima, Tokyo, Japan
T. Okano, Tokyo, Japan
K. Park, West Lafayette, Indiana, USA
W. Pitt, Provo, Utah, USA
K. Prasad, Bhagalpur, India
B. Ratner, Seattle, Washington, USA
G. Reid, London, Ontario, Canada
C.A. Siedlecki, Hershey, PA, Pennsylvania, USA
P. Tengvall, Linköping, Sweden
W-B. Tsai, Taipei, Taiwan
N. Tufenkji, Montreal, Quebec, Canada
H.C. van der Mei, Groningen, Netherlands
S. Wang, Beijing, China
G. M. Whitesides, Cambridge, Massachusetts, USA
X. Zhang, Beijing, China

GUIDE FOR AUTHORS

Your Paper Your Way

We now differentiate between the requirements for new and revised submissions. You may choose to submit your manuscript as a single Word or PDF file to be used in the refereeing process. Only when your paper is at the revision stage, will you be requested to put your paper in to a 'correct format' for acceptance and provide the items required for the publication of your article.
To find out more, please visit the Preparation section below.

INTRODUCTION

Colloids and Surfaces B: Biointerfaces is an international journal devoted to fundamental and applied research on colloid and interfacial phenomena in relation to systems of biological origin, having particular relevance to the medical, pharmaceutical, biotechnological, food and cosmetic fields.

Each Editor of Colloids and Surfaces B has specific fields of expertise. To ensure a smooth and rapid refereeing process, please submit your article to the Editor related to the topic of your research (you can select the correct editor in the drop down menu in our online submission system: http://ees.elsevier.com/colsub):

John Brash
•Interactions of biomolecules (proteins, enzymes, peptides, polysaccharides, DNA) at the solid-solution and air-solution interfaces;
•Surface/interfacial interactions of tissue and blood; Biomaterials development and interfacial properties;
•Drug delivery/controlled release

Henk Busscher
•Physico-chemical mechanisms of microbial adhesion, biofilm formation and tissue cell interaction to surfaces
•Microbial adhesion and biofilm formation
•Role of surface characteristics, surface modification and protein adsorption on microbial adhesion and biofilm formation
•Physico-chemical mechanisms providing biolubrication to surfaces

Hong Chen
•Surface modification including structured surfaces;
•Biocompatible materials;
•Anti-fouling materials;
•Bio-detection/bio-imaging materials;
•Interactions of biomolecules and cells at interfaces.

Dganit Danino
•Self-assembly and molecular assemblies (proteins, polymers, peptides, surfactants)
•Structure of biological fluids
•Drug delivery vehicles at nano and meso scales
•1D structures - fibrils, ribbons, nanotubes
•Milk proteins

Submissions that: (1) deal solely with biological phenomena and do not describe the physico-chemical or colloid-chemical background and/or mechanism of the phenomena, and (2) deal solely with colloid/interfacial phenomena and do not have appropriate biological content or relevance, are outside the scope of the journal and will not be considered for publication.

The journal publishes regular research papers, reviews, invited perspective articles, called BioInterface Perspectives, and Protocols (see below). The BioInterface Perspective provide researchers the opportunity to review their own work, as well as provide insight into the work of others that inspired and influenced the author. Regular articles should have a maximum total length of 6,000 words. In addition, a (combined) maximum of 8 normal-sized figures and/or tables is allowed (so for instance 3 tables and 5 figures). For multiple-panel figures each set of two panels equates to one figure. Short communications should not exceed half of the above. It is required to give on the article

cover page a short statistical summary of the article listing the total number of words and tables/ figures. Short Communications submitted to this journal will be re-directed to the journal Colloid and Interface Science Communications, which is the dedicated letters journal in our family of colloid titles.

Cover Letter

A cover letter is mandatory and should give the justification of the submission, highlights of the article, and a general impact statement. A short statistical summary of the article listing the total number of words and tables/figures is also required.

Protocols

Protocols of methods are welcome to the journal, but these articles have special formatting requirements. Protocols should deal with fundamental and applied research on colloid and interfacial phenomena in relation to systems of biological origin. Protocols should be relevant to the medical, pharmaceutical, biotechnological, food or cosmetic fields. Protocols will offer expert research guidelines on how to use an experimental set-up. The descriptions must be in great detail and troubleshooting tips to solve problems need to be included. These protocols contain a summary, introduction, materials, methods (with crucial steps highlighted), analyzing procedure (if necessary), expected results and conclusions. Figures and flow charts can be included where necessary. You are encouraged to use video material, animation sequences and interactive plots to support the procedure of your protocol, please see the author information pack for detailed information. Title: describe the method in the title. Abstract: give a summary of the procedure rather than a summary of the results. Introduction: introduce the technique and for which applications it is and can be used. Compare the technique with other techniques if possible and discuss advantages and disadvantages of the different techniques. Materials and preparatory procedures applied are divided in Reagents used, Equipment used (all equipment you need for the whole protocol), Preparatory procedures applied (buffers, suspensions etc.), Equipment set-up (specific equipment). For reagents and equipment give information of the make and company. Methods according to protocol: give a step by step description of the procedure, number every step. Write it as in a protocol, the active tense, full sentences are not necessary. Highlight critical steps in which you can describe the points for an optimal performance of your experiment, but also trouble shooting points. The protocol needs to be written in such a case that it is accessible for non-specialists, use a flow diagram if this clarifies the multistep process. If there are multiple routes to perform the procedure, mention it and give suggestions when to choose which route. Expected results: Give some examples of results and analysis of the results which will give the reader an impression what to expect.

End with Future Prospects: in which you describe possible new developments (max 150 words).

BEFORE YOU BEGIN

Ethics in publishing

Please see our information pages on Ethics in publishing and Ethical guidelines for journal publication.

Human and animal rights

If the work involves the use of human subjects, the author should ensure that the work described has been carried out in accordance with The Code of Ethics of the World Medical Association (Declaration of Helsinki) for experiments involving humans; Uniform Requirements for manuscripts submitted to Biomedical journals. Authors should include a statement in the manuscript that informed consent was obtained for experimentation with human subjects. The privacy rights of human subjects must always be observed.

All animal experiments should comply with the ARRIVE guidelines and should be carried out in accordance with the U.K. Animals (Scientific Procedures) Act, 1986 and associated guidelines, EU Directive 2010/63/EU for animal experiments, or the National Institutes of Health guide for the care and use of Laboratory animals (NIH Publications No. 8023, revised 1978) and the authors should clearly indicate in the manuscript that such guidelines have been followed.

Declaration of interest

All authors are requested to disclose any actual or potential conflict of interest including any financial, personal or other relationships with other people or organizations within three years of beginning the submitted work that could inappropriately influence, or be perceived to influence, their work. More information.

Submission declaration
Submission of an article implies that the work described has not been published previously (except in the form of an abstract or as part of a published lecture or academic thesis or as an electronic preprint, see 'Multiple, redundant or concurrent publication' section of our ethics policy for more information), that it is not under consideration for publication elsewhere, that its publication is approved by all authors and tacitly or explicitly by the responsible authorities where the work was carried out, and that, if accepted, it will not be published elsewhere including electronically in the same form, in English or in any other language, without the written consent of the copyright-holder.

Contributors
Each author is required to declare his or her individual contribution to the article: all authors must have materially participated in the research and/or article preparation, so roles for all authors should be described. The statement that all authors have approved the final article should be true and included in the disclosure.

Changes to authorship
Authors are expected to consider carefully the list and order of authors **before** submitting their manuscript and provide the definitive list of authors at the time of the original submission. Any addition, deletion or rearrangement of author names in the authorship list should be made only **before** the manuscript has been accepted and only if approved by the journal Editor. To request such a change, the Editor must receive the following from the **corresponding author**: (a) the reason for the change in author list and (b) written confirmation (e-mail, letter) from all authors that they agree with the addition, removal or rearrangement. In the case of addition or removal of authors, this includes confirmation from the author being added or removed.
Only in exceptional circumstances will the Editor consider the addition, deletion or rearrangement of authors **after** the manuscript has been accepted. While the Editor considers the request, publication of the manuscript will be suspended. If the manuscript has already been published in an online issue, any requests approved by the Editor will result in a corrigendum.

Copyright
Upon acceptance of an article, authors will be asked to complete a 'Journal Publishing Agreement' (see more information on this). An e-mail will be sent to the corresponding author confirming receipt of the manuscript together with a 'Journal Publishing Agreement' form or a link to the online version of this agreement.

Subscribers may reproduce tables of contents or prepare lists of articles including abstracts for internal circulation within their institutions. Permission of the Publisher is required for resale or distribution outside the institution and for all other derivative works, including compilations and translations. If excerpts from other copyrighted works are included, the author(s) must obtain written permission from the copyright owners and credit the source(s) in the article. Elsevier has preprinted forms for use by authors in these cases.

For open access articles: Upon acceptance of an article, authors will be asked to complete an 'Exclusive License Agreement' (more information). Permitted third party reuse of open access articles is determined by the author's choice of user license.

Author rights
As an author you (or your employer or institution) have certain rights to reuse your work. More information.

Elsevier supports responsible sharing
Find out how you can share your research published in Elsevier journals.

Role of the funding source
You are requested to identify who provided financial support for the conduct of the research and/or preparation of the article and to briefly describe the role of the sponsor(s), if any, in study design; in the collection, analysis and interpretation of data; in the writing of the report; and in the decision to submit the article for publication. If the funding source(s) had no such involvement then this should be stated.

Funding body agreements and policies
Elsevier has established a number of agreements with funding bodies which allow authors to comply with their funder's open access policies. Some funding bodies will reimburse the author for the Open Access Publication Fee. Details of existing agreements are available online.

Open access

This journal offers authors a choice in publishing their research:

Open access
• Articles are freely available to both subscribers and the wider public with permitted reuse.
• An open access publication fee is payable by authors or on their behalf, e.g. by their research funder or institution.
Subscription
• Articles are made available to subscribers as well as developing countries and patient groups through our universal access programs.
• No open access publication fee payable by authors.

Regardless of how you choose to publish your article, the journal will apply the same peer review criteria and acceptance standards.

For open access articles, permitted third party (re)use is defined by the following Creative Commons user licenses:

Creative Commons Attribution (CC BY)
Lets others distribute and copy the article, create extracts, abstracts, and other revised versions, adaptations or derivative works of or from an article (such as a translation), include in a collective work (such as an anthology), text or data mine the article, even for commercial purposes, as long as they credit the author(s), do not represent the author as endorsing their adaptation of the article, and do not modify the article in such a way as to damage the author's honor or reputation.

Creative Commons Attribution-NonCommercial-NoDerivs (CC BY-NC-ND)
For non-commercial purposes, lets others distribute and copy the article, and to include in a collective work (such as an anthology), as long as they credit the author(s) and provided they do not alter or modify the article.

The open access publication fee for this journal is **USD 3100**, excluding taxes. Learn more about Elsevier's pricing policy: https://www.elsevier.com/openaccesspricing.

Green open access
Authors can share their research in a variety of different ways and Elsevier has a number of green open access options available. We recommend authors see our green open access page for further information. Authors can also self-archive their manuscripts immediately and enable public access from their institution's repository after an embargo period. This is the version that has been accepted for publication and which typically includes author-incorporated changes suggested during submission, peer review and in editor-author communications. Embargo period: For subscription articles, an appropriate amount of time is needed for journals to deliver value to subscribing customers before an article becomes freely available to the public. This is the embargo period and it begins from the date the article is formally published online in its final and fully citable form.

This journal has an embargo period of 24 months.

Elsevier Publishing Campus
The Elsevier Publishing Campus (www.publishingcampus.com) is an online platform offering free lectures, interactive training and professional advice to support you in publishing your research. The College of Skills training offers modules on how to prepare, write and structure your article and explains how editors will look at your paper when it is submitted for publication. Use these resources, and more, to ensure that your submission will be the best that you can make it.

Language (usage and editing services)
Please write your text in good English (American or British usage is accepted, but not a mixture of these). Authors who feel their English language manuscript may require editing to eliminate possible grammatical or spelling errors and to conform to correct scientific English may wish to use the English Language Editing service available from Elsevier's WebShop.

Submission

Our online submission system guides you stepwise through the process of entering your article details and uploading your files. The system converts your article files to a single PDF file used in the peer-review process. Editable files (e.g., Word, LaTeX) are required to typeset your article for final publication. All correspondence, including notification of the Editor's decision and requests for revision, is sent by e-mail.

For submitting your manuscript to Colloids and Surfaces B: Biointerfaces please go to our Elsevier Editorial System (EES) Website at: http://ees.elsevier.com/colsub/ .

Referees

Please submit, as part of the covering letter with the manuscript, the names, affiliation and email addresses of four potential Referees. Appropriate Referees should be knowledgeable about the subject but have no close connection with any of the authors. In addition, Referees should be from institutions other than (and preferably countries other than) those of any of the Authors.

PREPARATION

NEW SUBMISSIONS

Submission to this journal proceeds totally online and you will be guided stepwise through the creation and uploading of your files. The system automatically converts your files to a single PDF file, which is used in the peer-review process.
As part of the Your Paper Your Way service, you may choose to submit your manuscript as a single file to be used in the refereeing process. This can be a PDF file or a Word document, in any format or lay-out that can be used by referees to evaluate your manuscript. It should contain high enough quality figures for refereeing. If you prefer to do so, you may still provide all or some of the source files at the initial submission. Please note that individual figure files larger than 10 MB must be uploaded separately.

References

There are no strict requirements on reference formatting at submission. References can be in any style or format as long as the style is consistent. Where applicable, author(s) name(s), journal title/book title, chapter title/article title, year of publication, volume number/book chapter and the pagination must be present. Use of DOI is highly encouraged. The reference style used by the journal will be applied to the accepted article by Elsevier at the proof stage. Note that missing data will be highlighted at proof stage for the author to correct.

Formatting requirements

There are no strict formatting requirements but all manuscripts must contain the essential elements needed to convey your manuscript, for example Abstract, Keywords, Introduction, Materials and Methods, Results, Conclusions, Artwork and Tables with Captions.
If your article includes any Videos and/or other Supplementary material, this should be included in your initial submission for peer review purposes.
Divide the article into clearly defined sections.

Figures and tables embedded in text

Please ensure the figures and the tables included in the single file are placed next to the relevant text in the manuscript, rather than at the bottom or the top of the file.

Use of word processing software

Regardless of the file format of the original submission, at revision you must provide us with an editable file of the entire article. Keep the layout of the text as simple as possible. Most formatting codes will be removed and replaced on processing the article. The electronic text should be prepared in a way very similar to that of conventional manuscripts (see also the Guide to Publishing with Elsevier). See also the section on Electronic artwork.
To avoid unnecessary errors you are strongly advised to use the 'spell-check' and 'grammar-check' functions of your word processor.

Subdivision - unnumbered sections

Divide your article into clearly defined sections. Each subsection is given a brief heading. Each heading should appear on its own separate line. Subsections should be used as much as possible when cross-referencing text: refer to the subsection by heading as opposed to simply 'the text'.

Introduction
State the objectives of the work and provide an adequate background, avoiding a detailed literature survey or a summary of the results.

Material and methods
Provide sufficient detail to allow the work to be reproduced. Methods already published should be indicated by a reference: only relevant modifications should be described.

Results
Results should be clear and concise.

Discussion
This should explore the significance of the results of the work, not repeat them. A combined Results and Discussion section is often appropriate. Avoid extensive citations and discussion of published literature.

Conclusions
The main conclusions of the study may be presented in a short Conclusions section, which may stand alone or form a subsection of a Discussion or Results and Discussion section.

Appendices
If there is more than one appendix, they should be identified as A, B, etc. Formulae and equations in appendices should be given separate numbering: Eq. (A.1), Eq. (A.2), etc.; in a subsequent appendix, Eq. (B.1) and so on. Similarly for tables and figures: Table A.1; Fig. A.1, etc.

Essential title page information

• ***Title.*** Concise and informative. Titles are often used in information-retrieval systems. Avoid abbreviations and formulae where possible.
• ***Author names and affiliations.*** Please clearly indicate the given name(s) and family name(s) of each author and check that all names are accurately spelled. Present the authors' affiliation addresses (where the actual work was done) below the names. Indicate all affiliations with a lower-case superscript letter immediately after the author's name and in front of the appropriate address. Provide the full postal address of each affiliation, including the country name and, if available, the e-mail address of each author.
• ***Corresponding author.*** Clearly indicate who will handle correspondence at all stages of refereeing and publication, also post-publication. **Ensure that the e-mail address is given and that contact details are kept up to date by the corresponding author.**
• ***Present/permanent address.*** If an author has moved since the work described in the article was done, or was visiting at the time, a 'Present address' (or 'Permanent address') may be indicated as a footnote to that author's name. The address at which the author actually did the work must be retained as the main, affiliation address. Superscript Arabic numerals are used for such footnotes.

Abstract

A concise and factual abstract is required. The abstract should state briefly the purpose of the research, the principal results and major conclusions. An abstract is often presented separately from the article, so it must be able to stand alone. For this reason, References should be avoided, but if essential, then cite the author(s) and year(s). Also, non-standard or uncommon abbreviations should be avoided, but if essential they must be defined at their first mention in the abstract itself.

The abstract should be no longer than 250 words

Graphical abstract
A Graphical abstract is mandatory for this journal. It should summarize the contents of the article in a concise, pictorial form designed to capture the attention of a wide readership online. Authors must provide images that clearly represent the work described in the article. Graphical abstracts should be submitted as a separate file in the online submission system. Image size: please provide an image with a minimum of 531 × 1328 pixels (h × w) or proportionally more. The image should be readable at a size of 5 × 13 cm using a regular screen resolution of 96 dpi. Preferred file types: TIFF, EPS, PDF or MS Office files. You can view Example Graphical Abstracts on our information site.
Authors can make use of Elsevier's Illustration and Enhancement service to ensure the best presentation of their images also in accordance with all technical requirements: Illustration Service.

Highlights
Highlights are mandatory for this journal. They consist of a short collection of bullet points that convey the core findings of the article and should be submitted in a separate editable file in the online submission system. Please use 'Highlights' in the file name and include 3 to 5 bullet points (maximum 85 characters, including spaces, per bullet point). You can view example Highlights on our information site.

Keywords
Immediately after the abstract, provide a maximum of 6 keywords, using American spelling and avoiding general and plural terms and multiple concepts (avoid, for example, 'and', 'of'). Be sparing with abbreviations: only abbreviations firmly established in the field may be eligible. These keywords will be used for indexing purposes.

Acknowledgements
Collate acknowledgements in a separate section at the end of the article before the references and do not, therefore, include them on the title page, as a footnote to the title or otherwise. List here those individuals who provided help during the research (e.g., providing language help, writing assistance or proof reading the article, etc.).

Formatting of funding sources
List funding sources in this standard way to facilitate compliance to funder's requirements:

Funding: This work was supported by the National Institutes of Health [grant numbers xxxx, yyyy]; the Bill & Melinda Gates Foundation, Seattle, WA [grant number zzzz]; and the United States Institutes of Peace [grant number aaaa].

It is not necessary to include detailed descriptions on the program or type of grants and awards. When funding is from a block grant or other resources available to a university, college, or other research institution, submit the name of the institute or organization that provided the funding.

If no funding has been provided for the research, please include the following sentence:

This research did not receive any specific grant from funding agencies in the public, commercial, or not-for-profit sectors.

Nomenclature and Units
The use of nomenclature and symbols adopted by IUPAC is recommended (Quantities, Units and Symbols in Physical Chemistry, Blackwell Scientific, Oxford, 1988).

Math formulae
Please submit math equations as editable text and not as images. Present simple formulae in line with normal text where possible and use the solidus (/) instead of a horizontal line for small fractional terms, e.g., X/Y. In principle, variables are to be presented in italics. Powers of e are often more conveniently denoted by exp. Number consecutively any equations that have to be displayed separately from the text (if referred to explicitly in the text).

Footnotes
Footnotes should be used sparingly. Number them consecutively throughout the article. Many word processors can build footnotes into the text, and this feature may be used. Otherwise, please indicate the position of footnotes in the text and list the footnotes themselves separately at the end of the article. Do not include footnotes in the Reference list.

Artwork
Electronic artwork
General points
• Make sure you use uniform lettering and sizing of your original artwork.
• Embed the used fonts if the application provides that option.
• Aim to use the following fonts in your illustrations: Arial, Courier, Times New Roman, Symbol, or use fonts that look similar.
• Number the illustrations according to their sequence in the text.
• Use a logical naming convention for your artwork files.
• Provide captions to illustrations separately.
• Size the illustrations close to the desired dimensions of the published version.
• Submit each illustration as a separate file.

A detailed guide on electronic artwork is available.
You are urged to visit this site; some excerpts from the detailed information are given here.
Formats
If your electronic artwork is created in a Microsoft Office application (Word, PowerPoint, Excel) then please supply 'as is' in the native document format.
Regardless of the application used other than Microsoft Office, when your electronic artwork is finalized, please 'Save as' or convert the images to one of the following formats (note the resolution requirements for line drawings, halftones, and line/halftone combinations given below):
EPS (or PDF): Vector drawings, embed all used fonts.
TIFF (or JPEG): Color or grayscale photographs (halftones), keep to a minimum of 300 dpi.
TIFF (or JPEG): Bitmapped (pure black & white pixels) line drawings, keep to a minimum of 1000 dpi.
TIFF (or JPEG): Combinations bitmapped line/half-tone (color or grayscale), keep to a minimum of 500 dpi.
Please do not:
• Supply files that are optimized for screen use (e.g., GIF, BMP, PICT, WPG); these typically have a low number of pixels and limited set of colors;
• Supply files that are too low in resolution;
• Submit graphics that are disproportionately large for the content.

Color artwork
Please make sure that artwork files are in an acceptable format (TIFF (or JPEG), EPS (or PDF), or MS Office files) and with the correct resolution. If, together with your accepted article, you submit usable color figures then Elsevier will ensure, at no additional charge, that these figures will appear in color online (e.g., ScienceDirect and other sites) regardless of whether or not these illustrations are reproduced in color in the printed version. **For color reproduction in print, you will receive information regarding the costs from Elsevier after receipt of your accepted article**. Please indicate your preference for color: in print or online only. Further information on the preparation of electronic artwork.

Figure captions
Ensure that each illustration has a caption. Supply captions separately, not attached to the figure. A caption should comprise a brief title (**not** on the figure itself) and a description of the illustration. Keep text in the illustrations themselves to a minimum but explain all symbols and abbreviations used.

Tables
Please submit tables as editable text and not as images. Tables can be placed either next to the relevant text in the article, or on separate page(s) at the end. Number tables consecutively in accordance with their appearance in the text and place any table notes below the table body. Be sparing in the use of tables and ensure that the data presented in them do not duplicate results described elsewhere in the article. Please avoid using vertical rules.

Citation in text
Please ensure that every reference cited in the text is also present in the reference list (and vice versa). Any references cited in the abstract must be given in full. Unpublished results and personal communications are not recommended in the reference list, but may be mentioned in the text. If these references are included in the reference list they should follow the standard reference style of the journal and should include a substitution of the publication date with either 'Unpublished results' or 'Personal communication'. Citation of a reference as 'in press' implies that the item has been accepted for publication.

Reference links
Increased discoverability of research and high quality peer review are ensured by online links to the sources cited. In order to allow us to create links to abstracting and indexing services, such as Scopus, CrossRef and PubMed, please ensure that data provided in the references are correct. Please note that incorrect surnames, journal/book titles, publication year and pagination may prevent link creation. When copying references, please be careful as they may already contain errors. Use of the DOI is encouraged.

A DOI can be used to cite and link to electronic articles where an article is in-press and full citation details are not yet known, but the article is available online. A DOI is guaranteed never to change, so you can use it as a permanent link to any electronic article. An example of a citation using DOI for an article not yet in an issue is: VanDecar J.C., Russo R.M., James D.E., Ambeh W.B., Franke M.

(2003). Aseismic continuation of the Lesser Antilles slab beneath northeastern Venezuela. Journal of Geophysical Research, http://dx.doi.org/10.1029/2001JB000884i. Please note the format of such citations should be in the same style as all other references in the paper.

Reference management software
Most Elsevier journals have their reference template available in many of the most popular reference management software products. These include all products that support Citation Style Language styles, such as Mendeley and Zotero, as well as EndNote. Using the word processor plug-ins from these products, authors only need to select the appropriate journal template when preparing their article, after which citations and bibliographies will be automatically formatted in the journal's style. If no template is yet available for this journal, please follow the format of the sample references and citations as shown in this Guide.

Users of Mendeley Desktop can easily install the reference style for this journal by clicking the following link:
http://open.mendeley.com/use-citation-style/colloids-and-surfaces-b-biointerfaces
When preparing your manuscript, you will then be able to select this style using the Mendeley plug-ins for Microsoft Word or LibreOffice.

Reference formatting
There are no strict requirements on reference formatting at submission. References can be in any style or format as long as the style is consistent. Where applicable, author(s) name(s), journal title/book title, chapter title/article title, year of publication, volume number/book chapter and the pagination must be present. Use of DOI is highly encouraged. The reference style used by the journal will be applied to the accepted article by Elsevier at the proof stage. Note that missing data will be highlighted at proof stage for the author to correct. If you do wish to format the references yourself they should be arranged according to the following examples:

Reference Style

1. All references made to publications in the text should be presented in a list of references following the text of the manuscript. The manuscript should be carefully checked to ensure that the information given in the text is exactly the same as that given in the reference list.
References to the literature should be made according to the numerical system described below.
2. In the text refer to the subject or to the author's name (without initial), followed by the reference number in square brackets.
3. If reference is made in the text to publications written by more than two authors, the name of the first author should be used, followed by "et al.". Note that in the reference list the names of authors and co-authors should be given in full.
4. References should be arranged in the order in which they appear in the text.
5. Use the following system for arranging the references:
(i) For journals
N. Levy, N. Garti and S. Margdassi, Colloids Surfaces A: Physicochem. Eng. Aspects, 97 (1995) 91.
(ii) For monographs
B.E. Conway, Ionic Hydration in Chemistry and Biophysics, Elsevier, Amsterdam, 1981.
(iii) For edited books
R.D. Thomas, in E. Buncel and J.R. Jones (Eds.), Isotopes in the Physical and Biomedical Sciences, Vol. 2, Elsevier, Amsterdam, 1991, Chapter 7.
For conference proceedings, symposia etc.
A.G. Marshall, in P.G. Kistemaker and N.M.M. Nibbering (Eds.), Advances in Mass Spectrometry, Proc. 12th International Mass Spectrometry Conference, Amsterdam, 26-30 August 1991, Elsevier, Amsterdam, 1992, p. 37.
6. Abbreviations of journal titles should conform to those adopted by the Chemical Abstract Service (Bibliographic Guide for Editors and Authors, The American Chemical Society, Washington, DC, 1974). If the correct abbreviation is not known, the title should be given in full.
7. Reference to a personal communication should be followed by the year, e.g. A.N. Other, personal communication, 1989.

Journal abbreviations source
Journal names should be abbreviated according to the List of Title Word Abbreviations.

Video
Elsevier accepts video material and animation sequences to support and enhance your scientific research. Authors who have video or animation files that they wish to submit with their article are strongly encouraged to include links to these within the body of the article. This can be done in the same way as a figure or table by referring to the video or animation content and noting in the body text where it should be placed. All submitted files should be properly labeled so that they directly relate to the video file's content. In order to ensure that your video or animation material is directly usable, please provide the files in one of our recommended file formats with a preferred maximum size of 150 MB. Video and animation files supplied will be published online in the electronic version of your article in Elsevier Web products, including ScienceDirect. Please supply 'stills' with your files: you can choose any frame from the video or animation or make a separate image. These will be used instead of standard icons and will personalize the link to your video data. For more detailed instructions please visit our video instruction pages. Note: since video and animation cannot be embedded in the print version of the journal, please provide text for both the electronic and the print version for the portions of the article that refer to this content.

Supplementary material
Supplementary material can support and enhance your scientific research. Supplementary files offer the author additional possibilities to publish supporting applications, high-resolution images, background datasets, sound clips and more. Please note that such items are published online exactly as they are submitted; there is no typesetting involved (supplementary data supplied as an Excel file or as a PowerPoint slide will appear as such online). Please submit the material together with the article and supply a concise and descriptive caption for each file. If you wish to make any changes to supplementary data during any stage of the process, then please make sure to provide an updated file, and do not annotate any corrections on a previous version. Please also make sure to switch off the 'Track Changes' option in any Microsoft Office files as these will appear in the published supplementary file(s). For more detailed instructions please visit our artwork instruction pages.

Database linking
Elsevier encourages authors to connect articles with external databases, giving readers access to relevant databases that help to build a better understanding of the described research. Please refer to relevant database identifiers using the following format in your article: Database: xxxx (e.g., TAIR: AT1G01020; CCDC: 734053; PDB: 1XFN). More information and a full list of supported databases.

AudioSlides
The journal encourages authors to create an AudioSlides presentation with their published article. AudioSlides are brief, webinar-style presentations that are shown next to the online article on ScienceDirect. This gives authors the opportunity to summarize their research in their own words and to help readers understand what the paper is about. More information and examples are available. Authors of this journal will automatically receive an invitation e-mail to create an AudioSlides presentation after acceptance of their paper.

3D molecular models
You can enrich your online articles by providing 3D molecular models (optional) in PDB, PSE or MOL/MOL2 format, which will be visualized using the interactive viewer embedded within the article. Using the viewer, it will be possible to zoom into the model, rotate and pan the model, and change display settings. Submitted models will also be available for downloading from your online article on ScienceDirect. Each molecular model will have to be uploaded to the online submission system separately, via the '3D molecular models' submission category. More information.

Interactive plots
This journal enables you to show an Interactive Plot with your article by simply submitting a data file. Full instructions.

Submission checklist
The following list will be useful during the final checking of an article prior to sending it to the journal for review. Please consult this Guide for Authors for further details of any item.

Ensure that the following items are present:

One author has been designated as the corresponding author with contact details:
- E-mail address
- Full postal address

All necessary files have been uploaded, and contain:
- Keywords

• All figure captions
• All tables (including title, description, footnotes)
Further considerations
• Manuscript has been 'spell-checked' and 'grammar-checked'
• References are in the correct format for this journal
• All references mentioned in the Reference list are cited in the text, and vice versa
• Permission has been obtained for use of copyrighted material from other sources (including the Internet)
Printed version of figures (if applicable) in color or black-and-white
• Indicate clearly whether or not color or black-and-white in print is required.
For any further information please visit our Support Center.

AFTER ACCEPTANCE

Online proof correction

Corresponding authors will receive an e-mail with a link to our online proofing system, allowing annotation and correction of proofs online. The environment is similar to MS Word: in addition to editing text, you can also comment on figures/tables and answer questions from the Copy Editor. Web-based proofing provides a faster and less error-prone process by allowing you to directly type your corrections, eliminating the potential introduction of errors.
If preferred, you can still choose to annotate and upload your edits on the PDF version. All instructions for proofing will be given in the e-mail we send to authors, including alternative methods to the online version and PDF.
We will do everything possible to get your article published quickly and accurately. Please use this proof only for checking the typesetting, editing, completeness and correctness of the text, tables and figures. Significant changes to the article as accepted for publication will only be considered at this stage with permission from the Editor. It is important to ensure that all corrections are sent back to us in one communication. Please check carefully before replying, as inclusion of any subsequent corrections cannot be guaranteed. Proofreading is solely your responsibility.

Offprints

The corresponding author will, at no cost, receive a customized Share Link providing 50 days free access to the final published version of the article on ScienceDirect. The Share Link can be used for sharing the article via any communication channel, including email and social media. For an extra charge, paper offprints can be ordered via the offprint order form which is sent once the article is accepted for publication. Both corresponding and co-authors may order offprints at any time via Elsevier's Webshop. Corresponding authors who have published their article open access do not receive a Share Link as their final published version of the article is available open access on ScienceDirect and can be shared through the article DOI link.

AUTHOR INQUIRIES

Track your submitted article
Track your accepted article
You are also welcome to contact the Elsevier Support Center.